EXPERIMENTAL INVESTIGATION OF TRANSVERSE ACOUSTIC INSTABILITIES

A Dissertation
Presented to
The Academic Faculty

by

Travis Edward Smith

In Partial Fulfillment
of the Requirements for the Degree
Doctor of Philosophy in the
School of Aerospace Engineering

Georgia Institute of Technology
December 2017

EXPERIMENTAL INVESTIGATION OF TRANSVERSE ACOUSTIC INSTABILITIES

Approved by:

Dr. Tim Lieuwen, Advisor
School of Aerospace Engineering
Georgia Institute of Technology

Dr. Wenting Sung
School of Aerospace Engineering
Georgia Institute of Technology

Dr. Jerry Setizman
School of Aerospace Engineering
Georgia Institute of Technology

Dr. Devesh Ranjan
Mechanical Engineering
Georgia Institute of Technology

Dr. Suresh Menon
School of Aerospace Engineering
Georgia Institute of Technology

Date Approved: October 30, 2017

To my Lord and Savior, Jesus Christ.

ACKNOWLEDGEMENTS

This work would not have been possible without the support of many people. I would like to thank you all for how you have helped me reach this point in my career. First, I would like to thank my family for how wonderful they have been. To my wife, Kelly, thank you for your love, support, and patience during the PhD process. This was not easy on you and would not have been possible without you. Secondly, I would like to thank my parents, Wharton and Annette Smith, for providing me with the freedom and education to pursue this degree. I would also like to thank them and my wife's parents, Dr. Ed and Pat Frazelle, for their encouragement, support, and guidance during the process.

A special thank you goes to my advisor, Tim Lieuwen, and the mentoring team of Bobby Noble and Ben Emerson. Without these people, the work would never have reached this point. Their guidance through this time and their compassion during life's difficulties made it possible to finish this work. I am eternally grateful for their compassion and understanding when life threw a curveball at my wife and me. I would also like to thank David Wu, Seth Hutchins, and Kristopher Manion for their support in the more day-to-day tasks related to facilities and running an experiment.

I would also like to thank the many members of the Combustion Lab community, both past and present, for teaching, aiding, and supporting this work. A special thank you goes to Jackie O'Connor for taking me on as an undergraduate student many years ago. She showed me it was possible to do this and sparked my interest in the field. I would like to thank those who were senior to me and set a great example before me, a very tough act to follow: Sai Thumuluru, Vishal Acharya, Andrew Marshall, Prabhaker Venkateswaran,

Chris Foley, Ben Wilde, Nick Magina, Mike Aguilar, Michael Malanoski, Nishant Jain, Sampath Adusumilli, Brandon Sforzo, and Luke Humphrey. A special thank you goes to my officemates, Brandon and Ianko, for keeping me sane during parts of the process. Next I would like to thank the undergraduates and graduate students who helped me in my experiment: Dan Moeggenberg, Benjamin Marquis, Rafiya Tasnim, Jamie Lim, Rajeev Atluri, Aaron Prakash, and most recently Raghul Kumar. I would also like to thank the graduate students who were my peers in many classes: Julia Lundrigan, Andrew Irby, Anna Hotle, Alex Miller. Many thanks goes out to the rest of the community as well: Debolina Dasgupta, Nick Rock, Hanna Ek, Chris Douglas, Matthew Sirignano, Vedanth Nair, and the many younger graduate students. This Combustion Lab community has been fantastic and incredibly supportive. The culture of aiding and teaching each other through collaboration is responsible for this work. I hope to find a culture like this wherever I go.

TABLE OF CONTENTS

LIST OF TABLES

LIST OF FIGURES

LIST OF SYMBOLS AND ABBREVIATIONS

$\left(\widehat{\ }\right)$	Fourier coefficient of quantity
$(\ )'$	Fluctuating component
ρ	Density
A	Area of nozzle exit
A_{nf}	Amplitude of response of n times the harmonic
A_m	Representative helical mode
$\widehat{\boldsymbol{B}}_m$	Periodic azimuthal mode coefficient
$\hat{B}_{ref,m}$	Periodic azimuthal mode coefficient predicted from forcing function
$\bar{B}_{j,m}$	Radially integrated magnitude of coefficient in j-direction
$\hat{B}_{m,s}$	Anti-symmetric component of disturbance
$\hat{B}_{m,s}$	Symmetric component of disturbance
$\bar{c}$	Flame progress variable contour
c	Speed of sound
$\hat{C}_m$	Sample helical mode coefficient

D Nozzle outer diameter

E Energy

E_a Acoustic energy density

f_0,ω_0 forcing frequency

$\hbar_R$ Heat release per unit mass

IP In-Phase

ISL Inner shear layer

JC Jet core

J_m Bessel function of the second kind

$\widehat{K}$ Integrated fluctuating kinetic energy

k Axial wavenumber

m Periodic azimuthal mode number

OP Out-of-Phase

OSL Outer shear layer

p Pressure

$\hat{q}$ Fluctuating heat release

Q	Global heat release
r/D	Normalized radial direction
R_f	Flame edge
$\hat{R}_m$	Flame edge periodic azimuthal mode (non-dimensional)
$r_{i,annulus}$	Inner radius of annulus
$r_{o,annulus}$	Outer radius of annulus
$r_{i,nozzle}$	Radius of nozzle centerbody
$r_{o,nozzle}$	Outer radius of nozzle annular exit
R^2	Coefficient of fit quality
s/D	Normalized nozzle spacing
S_n	Swirl number
s_c^u	Flame consumption speed
U_0	Bulk velocity
u_{ref}	Reference velocity
$\boldsymbol{u}$	Velocity field

$u_{z,0}$	Time-average axial velocity
$\hat{u}_{ant}$	Anti-symmetric component of velocity disturbance
$\hat{u}_{sym}$	Symmetric component of velocity disturbance
$\hat{v}$	Acoustic velocity
z/D	Normalized axial direction
r,z,θ	Cylindrical coordinate system
x,y,z	Cartesian coordinate system

SUMMARY

This work investigates acoustic instabilities in transversely forced swirl flames. The presence of transverse forcing on this naturally unstable flow both influences the natural instabilities, as well as amplifies disturbances that may not necessarily manifest themselves during natural oscillations. By manipulating the structure of the acoustic forcing field, both axisymmetric and helical modes are preferentially excited away from the frequency of natural instability. Additionally, forced and self-excited transverse acoustic instability studies to date have strong coupling between the transverse and axial acoustic fields near the flame. This is significant, as studies suggest that it is not the transverse disturbances themselves, but rather the induced axial acoustic disturbances, that control the bulk of the heat release response. This work utilizes 5 kHz stereo PIV and OH PLIF measurements as well as OH* and CH* chemiluminescence measurements to investigate transverse instabilities with and without induced axial acoustics.

The work presents a method for spatially interpolating the phase locked r-z and r-θ planar velocity and flame position data, extracting the full three-dimensional structure of the helical disturbances. These helical disturbances are also decomposed into symmetric and antisymmetric disturbances about the jet core, showing the subsequent axial evolution (in magnitude and phase) of each of these underlying disturbances. It is shown that out-of-phase acoustic forcing excites $m = \pm 1$ modes, but the flow field preferentially amplifies the counter-winding, co-rotating helical disturbance over the co-winding, counter-rotating helical disturbance. This causes the flow and flame to transition from a transverse flapping near the jet exit to a precessing motion further downstream. In contrast, in-phase forcing

with induced axial acoustics promotes axisymmetric $m = 0$ disturbances which dominate the flow field over the entire axial domain. In both cases, the amplitudes of the antisymmetric disturbances about the jet core grow with downstream distance before saturating and decaying, while the symmetric disturbances appear nearly negligible. It is suggested that this saturation and decay is due to linear effects (e.g., a negative spatial growth rate), rather than nonlinear interactions.

Experiments performed with essentially the same transverse acoustic wave field, but with and without axial acoustics, show that significant heat release oscillations are only excited in the former case. The results show that the axial disturbances at the nozzle exit are the dominant cause of the heat release oscillations. These observations support the theory that the key role of the transverse motions is to act as the "clock" for the instability, setting the frequency of the oscillations while having a negligible direct effect on the actual heat release fluctuations. They also show that transverse instability heat release can be damped by either actively canceling the induced axial acoustics in the nozzle (rather than the much larger energy transverse combustor disturbances), or by passively tuning the nozzle impedance to drive an axial acoustic velocity node at the nozzle outlet.

CHAPTER 1. INTRODUCTION

1.1 Motivation

Due to climate change, there has been a movement to reduce manmade greenhouse gas emissions. For aeroderivative engines used in power generation, the most common emissions reducing solution, running a fuel-lean mixture, places the engine in an operational regime where combustion instabilities are more prevalent [1, 2]. Specifically the issue of combustion dynamics arises, the process by which acoustics and heat release oscillations add energy to each other [3]. This coupling process results in a reduced lifetime for engine hardware and the occasional catastrophic failure of engine components. To illustrate this point, Figure 1 shows a picture of a can combustor both before and after having experienced combustion dynamics. The picture on the left shows a clean perforated plate around the fuel injectors while the picture on the right shows the plate having been corroded and destroyed by combustion dynamics [4]. There are several strategies to mitigate existing engine problems with combustion dynamics [5, 6], but the best strategy is prevention through design. This study aims to improve the understanding of combustion dynamics so that future multi-nozzle combustors will have reduced emissions and an expanded operability regime.

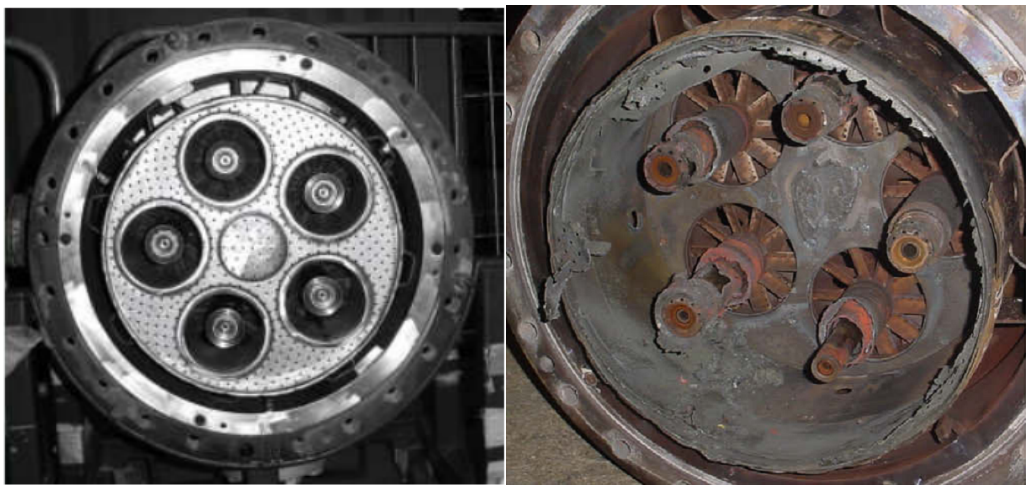

Figure 1 - Before-and-after images of a can combustor nozzle geometry that demonstrates the effect of combustion dynamics [4].

1.2 History of Combustion Instability/Dynamics

Combustion instabilities and combustion dynamics have been studied for many years. One of the earliest observations of the coupling between heat release and acoustics occurred in 1859 with Professor Rijke. He observed that if a heat source were placed at approximately one quarter length inside of a vertical tube with two open ends, a tone was generated that "was so loud that it could be easily heard two or three rooms from the laboratory where the experiment was being performed [7]." The sound generation was attributed to the successive expansion and contraction of the air inside the tube lining up with it's acoustic mode. The heat source caused the air to expand after which the walls of the tube cooled down the air, causing the contraction.

Later in 1878, Lord Rayleigh theorized that in general the relative phasing of heat release oscillations to acoustic oscillations could either inhibit or encourage acoustics:

> "If heat be periodically communicated to, and abstracted from, a mass of air vibrating (for example) in a cylinder bounded by a piston, the effect

> produced will depend upon the phase of the vibration at which the transfer of heat takes place. If heat be given to the air at the moment of greatest condensation, or taken from it at the moment of greatest rarefaction, the vibration is encouraged. On the other hand, if heat be given at the moment of greatest rarefaction, or abstracted at the moment of greatest condensation, the vibration is discouraged [8]."

In other words, acoustic pressure fluctuations and heat release oscillations within a system are sustained or amplified when the two are in phase. The converse is also true in that the fluctuations are damped when out of phase with each other. This is known as the Rayleigh Criterion for combustion instability and can be expressed as

$$\frac{1}{T}\int p'(t)q'(t)dt > 0, \tag{1.1}$$

where $p'(t)$ represents the acoustic pressure fluctuations and $q'(t)$ represents heat release fluctuations. The Rayleigh criterion is the foundation for the current understanding of combustion dynamics.

In the 1950s, combustion dynamics and instabilities became a huge problem in practical applications, specifically rocket engines [9-11]. Rocket engines experiencing instabilities were observed to have "more-or-less-violent oscillations of the chamber conditions [12]." Additionally, two different types of combustion instability became apparent: a low frequency mode called "chugging" and a high frequency mode called "screaming" or "screech." Both modes caused damage to the hardware, sometimes exploding the rocket engine. The chugging mode could mostly be explained by a feedback

mechanism called “injector coupling” [13], which will be discussed later, while the higher frequency modes were much less understood but still studied [9, 11].

Decades later, modern systems still experience combustion dynamics and instability. It is not uncommon to see this in refinery flares [14], jet engines, or aeroderivative power generation engines. As mentioned in the Section 1.1, the operating regime for reduced emissions coincides with increased combustion instabilities, as the engines are more sensitive to coupling between acoustics and heat release [1]. Next we examine possible coupling mechanisms that cause or contribute to combustion dynamics.

1.3 Physical Coupling Mechanisms in Combustion Devices

There are many different pathways for acoustic and heat release oscillation coupling, as summarized by Figure 2. In general terms, the flow field, the geometry or hardware, acoustics, heat release, turbulent mixing rates, and mixture properties can couple in almost any combination. This particular figure is discussed in more detail in Ducruix et al. [15].

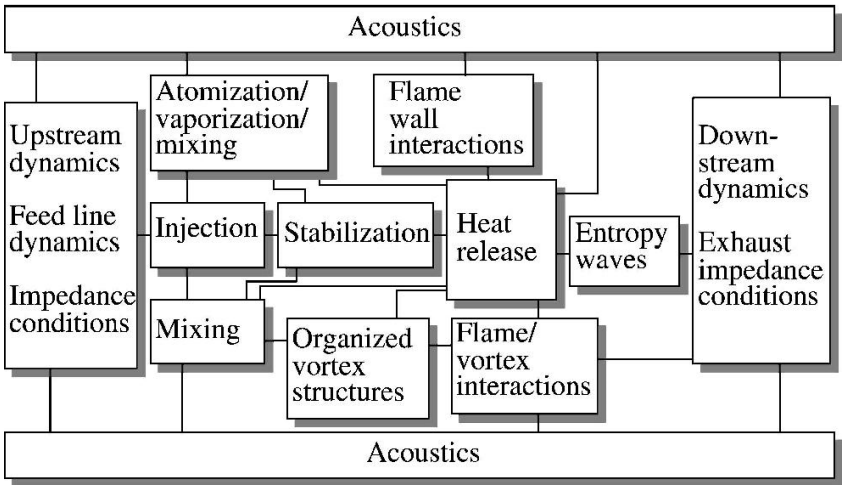

Figure 2- Basic interactions leading to combustion instabilities[5].

To demonstrate this point, consider a feedback cycle within a typical aeroderivative combustion chamber, as shown in Figure 3. The chamber consists of a mixing section or nozzle with a fuel injector and an air injector, a section where the combustion takes place, and an area contraction at the exit of the combustion chamber. The flame in the combustion chamber generates entropy waves that convect with the mean flow from the flame location to the exit of the chamber. The waves interact with the exit walls and reflect as acoustic pressure waves that then convect upstream. The acoustic waves then interact with the flame and generate entropy waves and fluctuating heat release. Additionally, a second pathway exists where the acoustic waves move past the flame and generate fluctuations in the fuel or air flow rate. These fluctuations in the mixture convect downstream to the flame and create oscillatory heat release and entropy waves. If the acoustic waves are in phase with the heat release oscillations of the flame due to any part of this cycle, the cycle will grow stronger, as described by Rayleigh's criterion. Typically the dominant combustion dynamics mechanisms are the ones that result in the heat release and pressure fluctuations being in phase [15]. As can be seen from this example, many different processes can couple to create a combustion dynamic cycle. The specific coupling processes this work focuses on are those of feed line coupling, flame-vortex interactions, and acoustic velocity flame response.

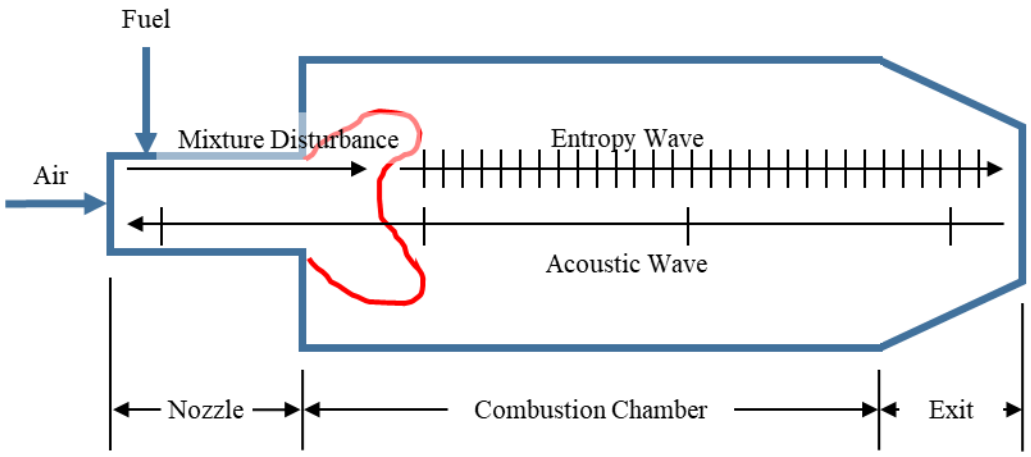

Figure 3 - Schematic of a combustion chamber demonstrating a feedback cycle.

Feed line coupling occurs when the natural acoustic modes of the combined combustor and feed line cause oscillations in fuel and/or air mass flow rates as described in the example above. This results in an oscillatory equivalence ratio flowing to the flame and a subsequent oscillation in heat release [16-19]. The time it takes for the equivalence ratio disturbance to convect from the injector to the flame can cause the heat release disturbance at the flame to be either in-phase or out-of-phase with the acoustics at the flame location. It has been experimentally observed that the feed line coupling cycle generates strong fluctuations when the combustor is running at a lower equivalence ratio, as the heat release is more sensitive to perturbations in the mixture at lower time-averaged equivalence ratios. Unfortunately, these conditions are also where NO_x emissions are reduced [2]. This mechanism is fairly well understood, and is mentioned because any experiment desiring to study other mechanisms needs to mitigate this one. This experiment mitigates feed-line coupling by making the convective time constant very long so that mixing processes can homogenize the mixture before it reaches the flames.

The other two mechanisms, flame/vortex interactions and acoustic velocity flame response, are more broadly referred to as velocity-coupled flame responses and are the focus of this study. Figure 4 schematically shows the velocity-coupled feedback cycle. Both vortices and acoustic velocity disturbances interact with the flow field into which the flame propagates. Acoustic disturbances create periodic flow fluctuations which in turn create periodic displacements of the flame, as demonstrated by the analysis of Acharya et al. [20]. The local displacements of the flame, depending on the geometry of the flame surface (for example an inverted cone), can increase or decrease the overall surface area and overall fuel consumption rates, which then result in fluctuating heat release. The fluctuating heat release then adds to the acoustics or flow field fluctuations to complete the cycle.

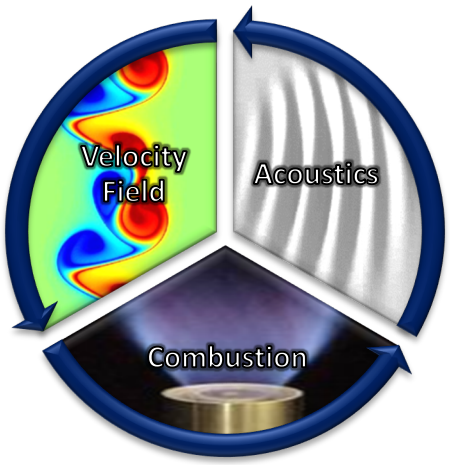

Figure 4 - Velocity-coupled flame response feedback cycle.

The frequencies associated with velocity-coupled feedback cycles can come from multiple sources, from the inherent acoustics or from hydrodynamic modes of the flow field. Additionally Silva et al. [21] has shown that a thermoacoustic instability can have its own frequency independent of the acoustics or flow field. However, most instabilities

occur at or near the acoustic frequencies of the combustor. Consider the simple geometry shown in Figure 5 representative of annular combustors. The geometry is characterized by three dimensions: an internal radius, an external radius, and a length. The distance between the external and internal radii is usually small in comparison to the average radius of the annulus. Acoustic modes can be oriented in multiple directions through this geometry: longitudinally (in the direction of the axis), transversely (in the θ direction), and radially, as well as any combination of these directions. Radial modes are typically not significant in combustion dynamics as the small annular width is associated with a very high frequency, and flames typically do not show a strong response at these frequencies. The longitudinal and transverse modes have much lower characteristic frequencies and are more important to combustion dynamics; typically, the acoustic wavelengths of these modes are far greater than the flame dimension, making the flame acoustically compact. This thesis focuses on the acoustically compact flame response to transverse acoustics.

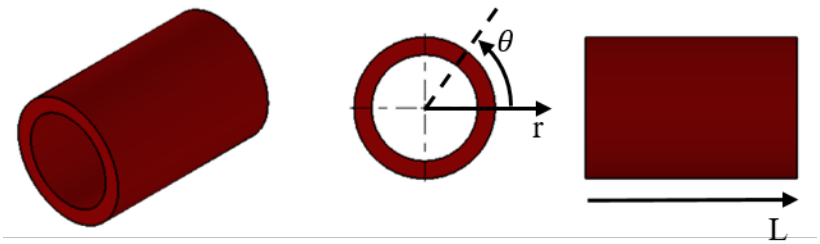

Figure 5 - General annular geometry with cylindrical coordinates.

A key feature of the transverse acoustic problem not shared by the longitudinal acoustic problem is the periodic boundary conditions. Longitudinal acoustic boundary conditions result in an approximately one-dimensional standing wave in the longitudinal direction, while the periodic boundary condition allows for travelling or standing wave solutions. This means that a longitudinal mode inside of an annulus results in all nozzles

feeling the same acoustic field; while in a transverse acoustic mode, different nozzles/flames experience different parts of the acoustic wave and can respond differently [22-25]. An additional difference between the longitudinal and transverse problems is that a longitudinal wave typically excites only an axisymmetric flow/flame disturbance while the transverse waves excite intrinsically three-dimensional, helical flow/flame disturbances [26]. The excited multidimensional flow disturbances result in different hydrodynamic modes appearing in the flow field [22, 23]. Additionally, the acoustic response of the nozzle varies depending on how the transverse acoustic wave encounters it [27]. For example, a flame located at a pressure node within a standing transverse wave will respond differently than a flame experiencing a traveling transverse wave [27-29]. However, the response of the flame and flow field to the traveling transverse wave appears similar to that of a flame located at a pressure antinode within a standing acoustic wave.

Given the complex relationship between acoustics and heat release in a combustor, the velocity-coupled flame response is typically characterized with a low order model. These models assume a specific input for the acoustics such as upstream velocity disturbances or transverse velocity disturbance and acoustic field type. The output from these models is a global heat release fluctuation. The typical models are a linear Flame Transfer Function (FTF) and a non-linear, amplitude-dependent Flame Describing Function (FDF) [30-35]. The FTF can be defined as the ratio of output normalized heat release to input normalized velocity disturbance:

$$FTF = \frac{q'/Q_0}{u'/U_0}. \tag{1.2}$$

The FDF on the other hand is a function of the input amplitude and captures non-linear mechanisms such as the saturation of the flame response. Example flame response saturation mechanisms are vortex roll-up and unsteady flame liftoff, both of which reduce the flame surface area [36-38]. FTFs and FDFs are usually measured experimentally by a combination of velocity measurements and chemiluminescence measurements [34, 38, 39]. Additionally there have been many efforts at modeling the FTF using the G-equation for various flame shapes and disturbance shapes [40-49].

Measurements of the FTF have been performed for both longitudinal and transverse inputs [35-38, 50-57]. The unconfirmed consensus has been that the longitudinal modes create the dominant flame response and that the transverse modes play a negligible part until non-linearities arise due to large amplitude disturbances [26, 58]. Work by O'Connor has investigated the relationship between the transverse acoustics and the flame response function [26]. Figure 6 shows a diagram detailing the mechanisms leading from azimuthal or transverse disturbances to flame response [26]. Note the pathway leading from transverse to longitudinal acoustics. O'Connor theorized that the dominant flame response was due to this pathway, but did not isolate different pathways in her measurements. Rather, she measured the coupled pathway and attempted to measure the coupling between the transverse and axial acoustics.

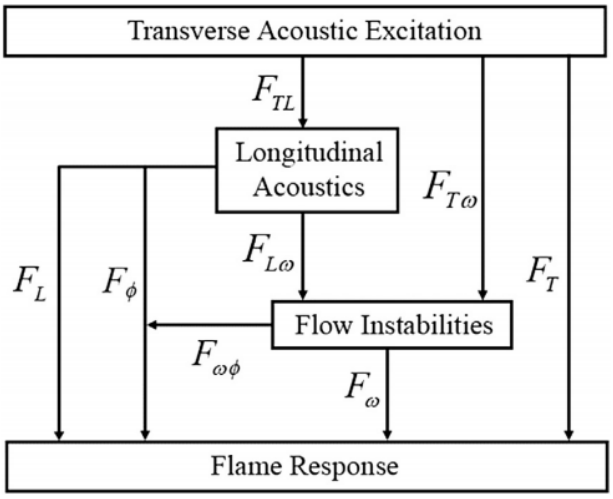

Figure 6 - Pathways from transverse acoustics to flame response [26].

The work of Blimbaum et al. [27] shows that the transverse acoustic wave induces a multi-dimensional acoustic field at the nozzle. These acoustic fields are demonstrated in Figure 7. The pressure node shows the multidimensional velocity disturbances out of the nozzle as alternating arrows on either side of the centerline. The pressure antinode, on the other hand, results in strong longitudinal acoustics and strong uniform axial disturbances, depending on the nozzle impedance at the transverse frequency.

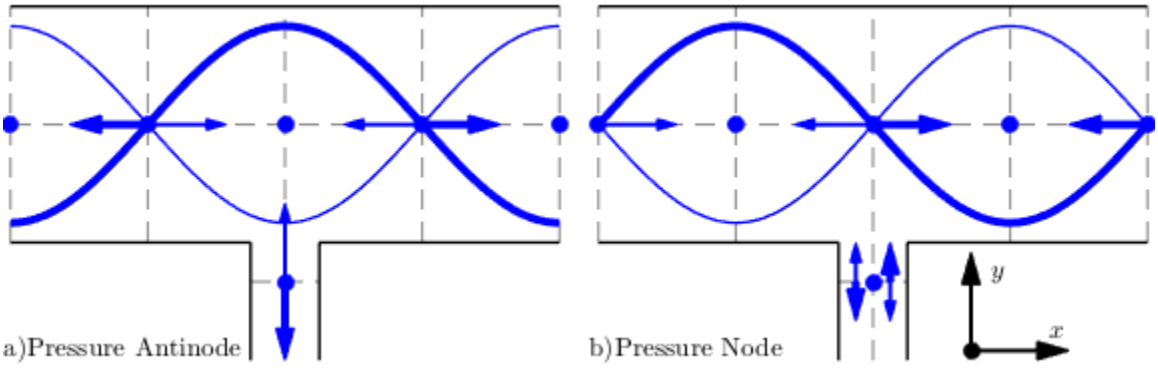

Figure 7 - Example transverse (left) pressure antinode and (right) pressure node field about the nozzle with arrows demonstrating acoustic velocity.

Figure 8 shows the longitudinal coupling for a pressure node and pressure antinode in a different form. The x-axis shows the magnitude of the transverse disturbance, and the y-axis shows the magnitude of the axial disturbance. Having a nozzle located at a pressure node results in little induced axial acoustics; however a pressure antinode results in a strong coupling between the axial and transverse acoustic fields. The nozzle impedance determines the slope of the line representing the pressure antinode. Nearly every pressure antinode measurement to date has included a contribution from the longitudinal disturbance. The aim of this work is to decouple the acoustics and make the pressure antinode line collapse onto the pressure node line. This work uses simultaneous longitudinal and transverse forcing to accomplish this and studies the response of a swirling flame and flow field to only the transverse acoustics.

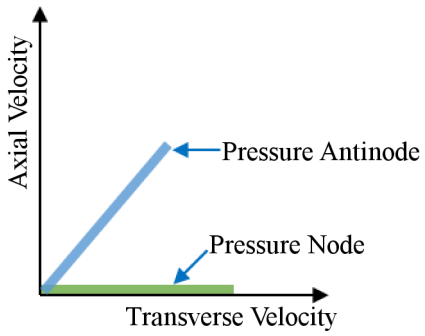

Figure 8 - Diagram showing longitudinal coupling for different forcing configurations.

1.4 Swirling Flow Dynamics

This work describes measurements and analysis of the forced dynamics of a swirling, premixed flame. Both reacting and nonreacting swirling jet flows exhibit a variety of unsteady features associated with underlying hydrodynamic instabilities. In particular,

high swirl flows exhibit vortex breakdown above a critical swirl number, leading to a pocket of central recirculating flow [59-61]. The instantaneous center of rotation of the swirling flow precesses around the geometric center of rotation, known as the precessing vortex core (PVC). The basic mechanism of vortex breakdown is still the subject of debate and has been related both to concepts of absolute instability and to criticality in the flow field state, where disturbances in a supercritical flow convect only downstream from the point of breakdown [62].

In addition to the substantial influence of vortex breakdown on both time-averaged and unsteady flow features, swirling flows generally have shear in both the radial and azimuthal direction. For example, flows with a centerbody are quite common and have two separating shear layers which are subject to the Kelvin-Helmholtz instability, leading to the concentration of vorticity originating from the separating boundary layers into helical structures as illustrated in Figure 9. The mechanism responsible for the occurrence of these helical structures is quite distinct from that of vortex breakdown and the PVC, although they are strongly coupled. There is an enormous literature on vortex precession and/or helical flow disturbances in swirl flows, for both non-reacting and combustion flows [6, 63-71]. Comprehensive reviews and reference lists are given by Syred [66] and Candel et al. [72].The helical disturbance found in the flow field, described by m, depends strongly on the swirl number and “wake-like” or “jet-like” features of the flow [73]. For example, the experiment of Liang and Maxworthy [73] showed that a swirling jet without a centerbody after vortex breakdown had a dominant co-rotating, counter-winding $m = +1$ mode with a weaker $m = +2$ counter-winding mode.

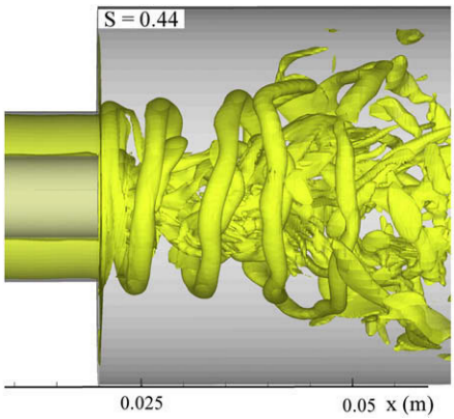

Figure 9 - Iso-vorticity surface demonstrating the Kelvin-Helmholtz instability manifested as a helical mode in a swirling flow [74].

In order to fix some notation, we use the same conventions of Oberleithner et al. [75] and denote a helical disturbance, A, indexed by the azimuthal mode number m as a function of frequency, ω (defined to be positive), in a polar coordinate system (r, θ, z), as

$$A_m = \hat{C}_m(r, z)\exp[i(\omega t - m\theta - kz)] \tag{1.3}$$

where $\hat{C}_m$ is the complex coefficient, the hat denoting a complex number, and k is the axial wavenumber. The $m = 0$ mode is axisymmetric while the $m > 0$ and the $m < 0$ modes denote counter-clockwise and clockwise rotations of iso-phase surfaces within an r-θ plane. The mean swirl is counter-clockwise and positive θ is in the counter-clockwise direction, so that the $m > 0$ and $m < 0$ modes refer to co- and counter-rotating modes respectively. The co- and counter-winding terms refer to the direction the helix winds with respect to the mean swirl, as shown in Figure 10. A co-winding direction is expressed as $k/m < 0$ while a counter-winding disturbance is $k/m > 0$. The velocity measurements presented here denote the temporal Fourier transform of the velocity vector, $\boldsymbol{u}(r, \theta, z, t)$ (using the $\exp(i\omega t)$ convention) by $\widehat{\boldsymbol{u}}'$ and decompose the complex velocity into azimuthal modes, indexed by m:

$$\widehat{\boldsymbol{u}}'(r,\theta,z,\omega) = \sum_{m=-\infty}^{\infty} \widehat{\boldsymbol{B}}_m(r,z,\omega)e^{-im\theta} \tag{1.4}$$

where $\widehat{\boldsymbol{B}}_m$ is the complex coefficient of the helical mode m containing the spatial amplitude of the mode and the spatial phase information including the $\exp(-ikz)$ term in Eqn. (3).

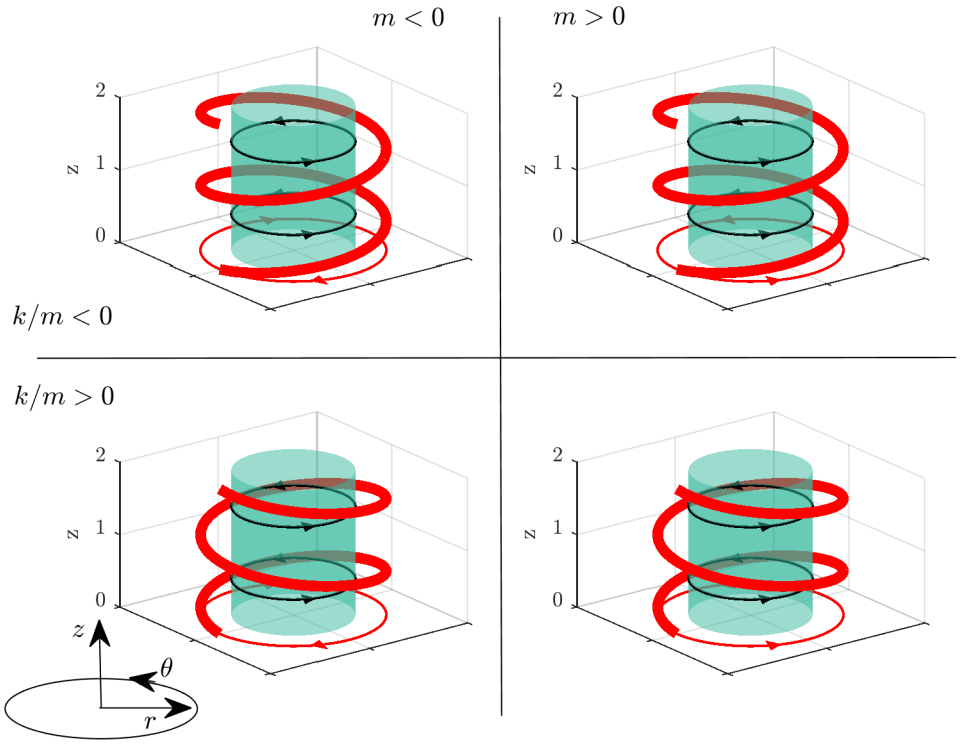

Figure 10 - Diagram demonstrating winding and rotation direction of helical $|\boldsymbol{m}| = 1$ iso-phase surface shown in red. Black arrows denote mean swirl direction, and red arrows denote rotation direction of iso-phase surface in $\boldsymbol{r}$-$\boldsymbol{\theta}$ plane.

The particular focus of this study is on flows with external transverse forcing. The presence of transverse forcing on this naturally unstable flow can both influence these natural instabilities, as well as amplify disturbances that may not necessarily manifest themselves during natural oscillations. This occurs because these swirling jet flows have a variety of different underlying modes with different spatio-temporal growth rates. For example, the axisymmetric shear layer mode is strongly excited in the presence of axial

forcing, even in situations where the natural instability of the flow manifests itself as a strong helical disturbance. Numerous observations of combustors undergoing axial thermoacoustic oscillations note the suppression of the strong helical structures in the flow in this case, as the forcing of the underlying axisymmetric mode is so strong [76].

1.5 Forced Helical Modes

In addition to helical vortices and modes in an unforced swirl flame, the transverse acoustic field is highly multidimensional and excites helical modes from the nozzle. In order to illustrate this point, decompose the velocity vector, $\boldsymbol{u}(r,\theta,z,t)$, into frequency space and azimuthal disturbance modes, indexed by m:

$$\widehat{\boldsymbol{u}}'(r,\theta,z,\omega) = \sum_{m=-\infty}^{\infty} \widehat{\boldsymbol{B}}_m(r,z,\omega)e^{-im\theta} \tag{1.5}$$

where $\widehat{\boldsymbol{u}}'$ is the Fourier transform of the fluctuating velocity field, and $\widehat{\boldsymbol{B}}_m$ is the complex coefficient of the helical mode m. The $m = 0$ mode is axisymmetric while the $m > 0$ and the $m < 0$ modes denote co- and counter-swirling helical modes assuming counter-clockwise swirl. In order to demonstrate how different helical modes were excited at different points in the standing wave structure, O'Connor et al. [26] expanded a transverse acoustic wave into helical mode coefficients in an (r,θ,z) coordinate system centered at a nozzle using a Jacobi-Anger expansion,

$$e^{ikx} = \sum_{m=-\infty}^{\infty} \hat{B}_{ref,m}(kr)e^{im\theta}, \tag{1.6}$$

where x denotes the propagation direction of the transverse wave and $k = \omega/c$ denotes the acoustic wave number. They showed that for a flame located at a pressure node/velocity antinode, the acoustic disturbance excited odd hydrodynamic modes as

$$\hat{B}_{ref,m} = i^{m-1} J_m(kr), \tag{1.7}$$

with the $m = \pm 1$ modes being dominant, where r denotes the radial cylindrical coordinate; even modes are not excited. In contrast, even modes are excited as

$$\hat{B}_{ref,m} = i^{m} J_m(kr), \tag{1.8}$$

for a flame located at a pressure antinode with the $m = 0$ mode being dominant; odd modes are not excited. Finally, for a traveling wave, both even and odd modes are excited as

$$\hat{B}_{ref,m} = i^{m} J_m(kr). \tag{1.9}$$

While this decomposition of the acoustic wave into nozzle-centered helical modes provides insight into how different hydrodynamic disturbances are excited by the acoustic field, it does not show how they affect the spatially integrated heat release oscillations or which mode will become dominant. Nonetheless, this expansion provides useful insight into several experimental studies. For example, the results of O'Connor *et al.* showed that when there is an acoustic pressure antinode at the nozzle, the $m = 0$ mode (manifested as an axisymmetric vortex) was the dominant mode of flow response, exciting axisymmetric flame wrinkling [26]. In contrast, when the transverse acoustic mode has a velocity antinode at the nozzle, the dominant response was in the $m = \pm 1$ modes. Aguilar *et al.* [77] similarly studied a transversely forced configuration, comparing the response of a single and triple nozzle configuration. They also showed strong excitation of the $m = 0$

mode in both single and triple nozzle cases when the nozzle was located at the pressure anti-node, and the $m = \pm 1$ modes when the nozzle was located at a pressure node.

1.6 Modeling and Measurements of the FTF for Swirl Flames

Modeling efforts of the FTF have proven fruitful, as the physics governing the linear heat release response of the flame are usually simple. For example, the heat release from a premixed flame, $\dot{Q}(t)$, can be described by [3]

$$\dot{Q}(t) = \int_{flame} \rho^u s_c^u \hbar_R dA, \tag{1.10}$$

where ρ_u represents the density of the unburned reactants, s_c^u the flame consumption speed, and $\hbar_R$ the heat release per unit mass of reactants. This equation shows that $\dot{Q}(t)$ can be effected by a change in $\hbar_R$ through equivalence ratio variations, by a change in mass consumption of the flame $\rho^u s_c^u$, or by an increase in the flame surface area [54, 78].

The flame sheet, and thus its surface area, is commonly modeled with a simple convection equation called the G-equation. Schuller et al. [79] explains how this method is used in modeling both v-flames and conical flames. Previous work using the G-equation has proven useful in predicting the linear response of a flame to flow disturbances for v-flames, cone flames, and inverted cone flames [42, 44, 79-84]. Work by Preetham et al. [42, 44, 81, 84] used the G-equation formulation to look at a bluff-body flame's sensitivity to harmonic forcing, unsteady stretch effects, and the effects of turbulence on the harmonic response. Palies et al. [45] and Moeck et al. [46] used the G-equation to explain the observed responses of swirl flames to different acoustic perturbations. More recently Acharya used a G-equation formulation to perform multiple studies on the sensitivity of a

swirling, inverted-conical flame to hydrodynamic disturbances and what happens when the flame becomes asymmetric [47-49, 82, 83].

Swirl flame G-equation studies have shown that the flame has a sensitivity of its own to the spatio-temporal structure of the disturbance velocity; i.e., the response of the flame cannot be simply characterized by a single reference velocity, and it responds differently to, say, an $m = +1$ disturbance than it does an $m = -1$ disturbance of equal magnitudes. For example, the following helical mode with index, m_0, excites the largest amplitude of flame flapping:

$$m_0 = \left(\frac{f}{\Omega}\right)\left(\frac{U_0 \cos^2(\psi)}{U_c} - 1\right) \tag{1.11}$$

as detailed in Acharya et al. [47], where ψ is the flame angle, U_c is the disturbance convection speed, f is the frequency, Ω is the angular rotation rate of the swirl flow, and U_0 is the bulk flow velocity in the axial direction. This expression shows that usually $m \neq 0$ flow perturbations result in the largest local flame motion and response.

While m_0 describes the mode exciting the largest magnitude of flame sheet flapping, a different mode, m_1, generally excites the largest amplitude of spatially integrated heat release, and a third mode, m_2, leads to the largest free field acoustic emissions from the flame [83]. For example, for flames that are axisymmetric in the absence of excitation, $m_1 = 0$; in fact, it is only the $m = 0$ mode that excites spatially integrated heat release, as the integral of $m \neq 0$ modes about an axisymmetric flame results in phase cancellation and no net contribution to global heat release. In other words, the only mode for which $\int e^{im\theta} d\theta$ between 0 and 2π does not equal 0 is the $m = 0$ mode, and

thus the $m = 0$ mode is responsible for the global flame response [46, 47]. To summarize, the hydrodynamic mode responsible for the largest local flame response, usually $m \neq 0$, is not always the mode responsible for the global heat release response, $m = 0$.

This modeling result is well-supported by experiments. Measurements by Worth and Dawson [23] of self-excited transverse oscillations in an annular combustor showed that the heat release depended on the position of the flame with respect to the acoustic wave. Similarly, Paschereit's group observed a similarity in flame response, as observed by OH* chemiluminescence, to a transverse traveling wave and to a transverse pressure antinode at the nozzle [28, 29]. This observation is consistent with modeling results that suggest that the dominant flame response comes from the axisymmetric, $m = 0$ mode, which is excited for both traveling waves and pressure antinode cases [46, 47]. In addition, previous work by Acharya et al. observed that the measured helical modes of the flow field minimally changed the measured global heat release fluctuations due to the near symmetry of their flame [85]. However, they did find that the axisymmetric modes contributed strongly to global heat release.

Given the importance of the $m = 0$ mode to the spatially integrated flame response, it is important to better understand the mechanisms responsible for its excitation. The discussion below closely follows the review paper by O'Connor et al. [26]. First, it is important to note that the word "transverse mode" or "transverse excitation" is itself an approximation of the more complex reality, where the combustor system is intrinsically multidimensional. This conceptualization is useful to understand dominant features controlling the acoustic mode shape and frequency of the system. In combustion systems with transverse modes, however, there are intrinsically some axial motions excited in

regions where three-dimensional geometric effects occur – of particular interest to this study is at premixing nozzles. Transverse modes lead to axial acoustic flow motions in the nozzle, which are a wave diffraction effect, as the dominantly transverse mode leads to an oscillatory pressure field across the nozzle. These axial flow oscillations are a dominant excitation source for $m = 0$ hydrodynamic modes. The relative amplitude of these axial flow oscillations is controlled by two factors – the transverse wave structure, and the nozzle impedance. In particular, strong axial oscillations are excited when the transverse wave has a pressure anti-node, which leads to a strongly oscillating axial pressure gradient in the flow direction [27]. The nozzle impedance, defined as the ratio of the unsteady pressure to axial velocity at the nozzle outlet, also has a significant effect on this transverse to axial coupling for pressure anti-node and traveling wave acoustic excitation.

1.7 Transverse Acoustics Studies

Previous transverse acoustic studies have been performed on both single nozzle and multi-nozzle experiments to study the swirling flow field and the effects of transverse and axial acoustic forcing [54, 86-88]. A comprehensive review of the literature is given in O'Connor et al. [26]. Here the transverse literature is divided into several sections: high frequency acoustics, unforced acoustically compact flames, and forced acoustically compact flames.

High-frequency acoustics take into account the local interactions of the flame front and the acoustic field [9-11, 86, 89-92]. The work of Rogers [9] and Blackshear [11] looked at mechanisms responsible for screech within a rocket engine. They found that screech was due to a mechanism where the high-frequency acoustics coupled with the vortex shedding

off the flame holder, which then displaced the flames. The resulting heat release oscillations were in-phase with the acoustic pressure field and fulfilled the Rayleigh criterion. More recently, Schwing et al. [86, 89, 90, 93] has looked at the high frequency flame-acoustic coupling in a swirl flame, developing a model to simulate the local interactions between the flame and disturbance field. The predicted flame transfer functions are based off spatially integrating the local Rayleigh index throughout the can combustor.

Self-excited annular studies show frequencies on the order of hundreds of Hz, where the flames are acoustically compact [22, 23, 88, 94-99]. These studies have focused on the flame shapes and interactions. Specifically Worth and Dawson, mentioned previously, observed different modal structures within their heat release measurements depending on the location of the flame within the acoustic field [22-24, 56]. They saw strong heat release fluctuations at a pressure antinode and negligible heat release fluctuations at a pressure node. They also observed that if the peak heat release spatially coincides with a net swirl around the annulus, the acoustic wave will spin in that direction about the annulus [22]. In addition to Worth and Dawson, Bourgouin et al. [88, 95, 97] have looked at self-excited annular instabilities. Specifically, they have analyzed the flame shapes inside of an annular combustor experiencing a combination of transverse and longitudinal fluctuations.

The remaining studies are those of acoustically-compact, transversely-forced flames that have come from within this group [57, 85, 100-109] and other groups [28, 29, 110-113]. Hauser et al. [110, 111] studied transverse acoustic forcing on the inlet flow, and found that acoustics in that region created convecting swirl fluctuations resulting in heat

release response. Saurabh et al. [28, 29, 112] measured the effects of transverse standing and traveling waves in the combustion region on flame response, assuming that the axial acoustics contribute to the flame response, but not isolating the effects of transverse acoustics. For example, in a recent work, Saurabh and Paschereit [112] measured the flame transfer function of combined axial and transverse acoustic forcing. They found that the superposition of a transverse pressure antinode and axial acoustics increased the flame response compared to only axial acoustics while the superposition of a pressure node detracted from it. However, they did not look at adjusting the phase of the axial signal, and thus their results are not general. O'Connor [100, 101, 103-105] analyzed the transverse disturbance field and its interactions with the flow field thoroughly through her work, proposing a flame transfer function model that included a term for axial coupling [102]. However, the term was estimated from measurements of the coupled acoustic field. Later, O'Connor and Acharya [106] presented further measurements and modeling of the coupled flame transfer function for a swirling flame, but the individual contributions due to the transverse and axial acoustics were not separated. This work aims to further these studies by isolating the contribution of axial and transverse acoustics to flame response for an acoustically compact swirling flame, as shown in Figure 6 and Figure 8.

1.8 Scope of Work

This study is motivated by the fact that previous forced and self-excited transverse studies have not controlled for the induced axial motions at the nozzle. While Saurabh et al. [28, 29, 112] and O'Connor et al. [102, 106] looked at the combined effects, they did not attempt to isolate them. This work decouples these effects, by forcing the system both transversely and axially, similar to Saurabh et al. [112], but with control of their relative

phases and amplitudes. The flow field and flame response to the decoupled acoustic fields are compared to the effects of the coupled acoustic fields in order to elucidate the physics behind the response to both.

In addition to isolating the transverse acoustics, this work develops a new method for interpolating experimental data over a large domain. Previously, experimental measurements were limited to either small tomographic volumes with large uncertainties or planar measurements. By combining different measurement planes, the entire domain of interest is interpolated and enables a well-resolved calculation of the growth of hydrodynamic modes using minimal experimental data.

The rest of the thesis is organized as follows. Chapter 2 presents the experimental facility and diagnostics as well as the efforts to decouple the longitudinal acoustics from the transverse acoustics. It also discusses the efforts to interpolate the experimental data throughout the entire flow field. Chapter 3 presents the time-average flow field as well as an analysis of the flow field disturbances measured in the r-z plane for each test case. The decomposition of the flow field into helical modes is shown to better explain the behavior in the r-z plane. Chapter 4 presents the development of the novel helical mode interpolation method and describes an analysis of the results. Chapter 5 will looks at the effects of the transverse acoustics on the heat release and shows that the heat release response is actually a function of the excited axisymmetric mode rather than the axial acoustics. The end chapter presents conclusions and recommendations for future work on the subject.

CHAPTER 2. EXPERIMENT OVERVIEW

The aim of this chapter is to introduce the facility, diagnostics, and longitudinal minimization process to set the stage for the analyses performed in Chapters 3-5. As such, this chapter first introduces the experimental facility, describing the thought process behind its design as well as how the resonant frequencies were identified. Next the diagnostics utilized in the study are presented in detail: their set-up, uncertainty, and processing. Finally the efforts to perform axial minimization are presented along with the effects on the exit profile out of the nozzle.

2.1 Facility and Flow Conditions

Figure 11 displays a cut-section of the multi-nozzle combustor facility, similar to O'Connor and Lieuwen [100] and Aguilar et al. [77]. The combustor is designed to excite nominally one-dimensional transverse modes and represents an unwrapped annular sector containing three nozzles. The nozzle conditions are independently controlled, allowing for multiple flame configurations within the same combustor. Windows on the front and the back of the combustor make the center nozzle and nozzle interaction regions visible. A third window located between the exhaust ports gives a top-down view of the center nozzle. Additionally, there is a laser port on the side of the combustor allowing a laser sheet to bisect all three nozzles.

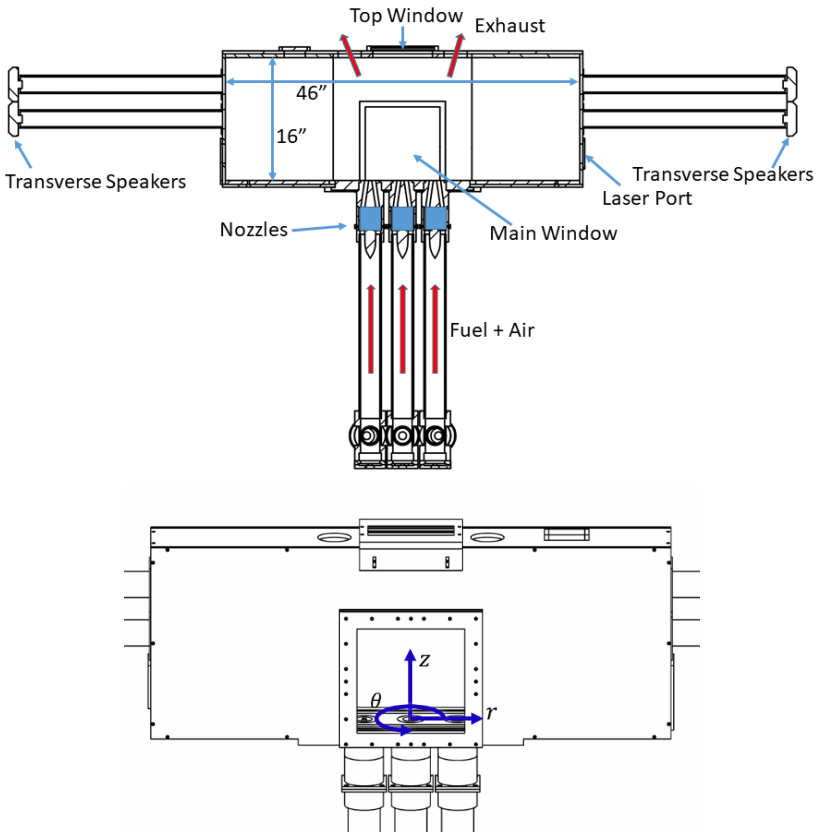

Figure 11 - Diagram of combustor flow path in red. Coordinate system shown on bottom in blue.

Figure 12 shows a schematic of the fuel and air flow paths to the combustor. The natural gas flows from the 30 psi supply line to a subcritical orifice where the flow rate is metered with a static pressure and differential pressure measurement. These flow measurements have an uncertainty of 2-3% of their instantaneous values. The flow then splits into three lines going to the mixing pipes of each nozzle. The individual flow rates are controlled by needle valves and then metered using subcritical orifices with corresponding measurements. Two default-closed solenoids are placed on the line, one near the wall and one just before the split, to provide on/off flow control for both normal operation and emergencies.

Air from the 125 psi line is regulated down to 75-80 psi before cooling air and control air split from the main line. The main air flow rate is measured through a subcritical orifice before passing through the heater and splitting between the nozzles. The individual flow to each nozzle is controlled using a globe valve and metered with pressure and temperature measurements using the critical orifice shown in Figure 13. The seeding air is added prior to metering, thus the flow contribution of seeding air is measured. The preheat temperature is measured just upstream of the combustor after the fuel and air have mixed.

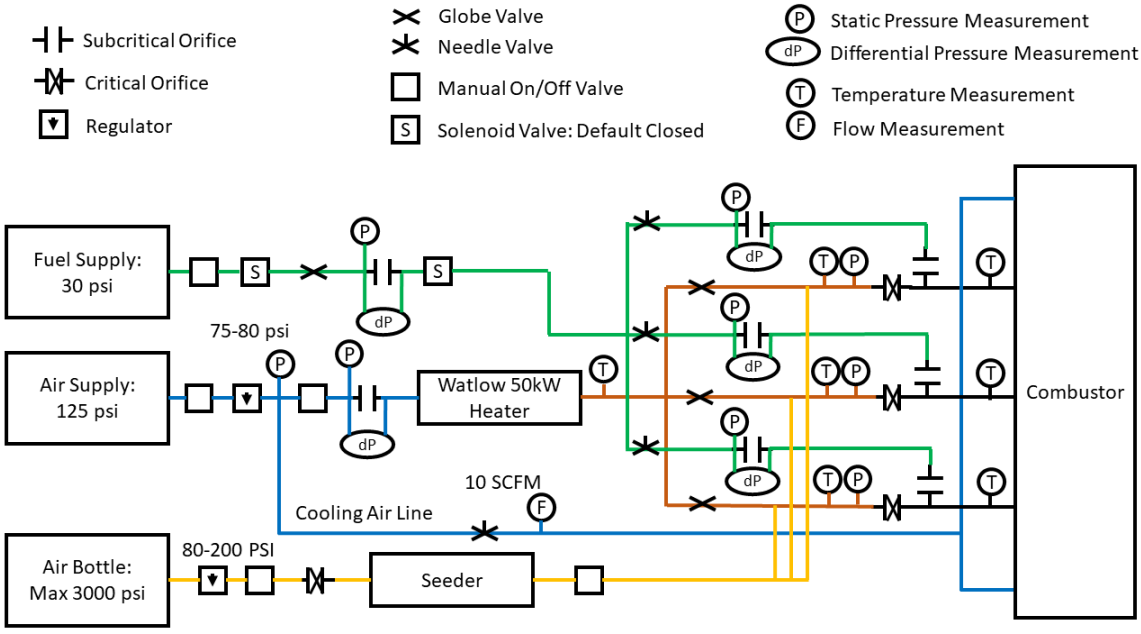

Figure 12 - Schematic of flow paths.

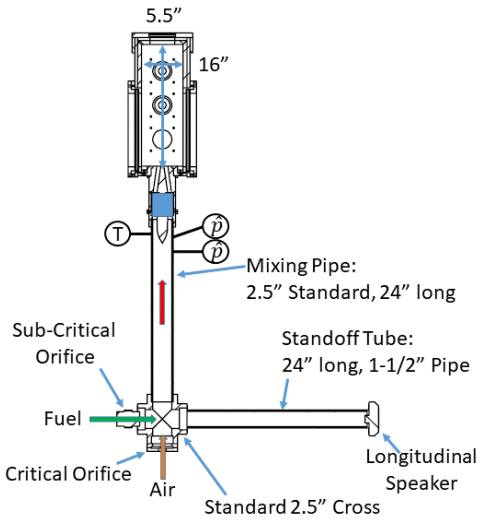

Figure 13 – Cut-section of mixing pipe and combustor.

Figure 14 shows a cut-section of the nozzle design. Premixed natural gas and air flow through a pipe to a flow diverger with an axisymmetric hyperbolic tangent profile to ensure a smooth entry into the annular passage with inner and outer radii of $r_{i,annulus} =$ 18 mm and $r_{o,annulus} = 31$ mm, respectively. Next, the flow passes through an axial swirler with a geometric swirl number of 0.6. The annular passage then converges over an axial distance of 88.9 mm, to $r_{o,nozzle} = 18.5$ mm and $r_{i,nozzle} = 5$ mm, so that the annular area is reduced by 50%. The swirl number of the flow exiting the nozzle, S_n, calculated from a stereoscopic Particle Image Velocimetry (sPIV) measurement is approximately 0.5, calculated as the ratio of the tangential to axial momentum assuming constant density [114]

$$S_n = \frac{\int_0^{D/2} \bar{u}_\theta \bar{u}_Z r^2 dr}{\frac{D}{2}\int_0^{D/2} \bar{u}_Z^2 r dr}. \tag{2.1}$$

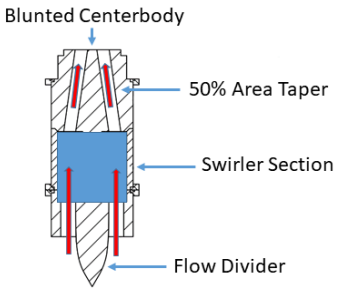

Figure 14 - Diagram of the nozzle with units in mm, flow path in red.

The nozzles are spaced 2.9 diameters apart and all have equal air mass flow, measured at the upstream critical orifice. The nominal bulk velocity of the air entering the combustor was 25 m/s and increased to about 28.8 m/s with the addition of seeding air and fuel. The air velocity varied between cases by ± 0.25 m/s, well within the flow measurement error, 2-3%. The preheat temperature, measured just upstream of each nozzle, was 500 K $\pm$ 10K. The equivalence ratios of the methane-air mixtures were 0.94 and 0.63 for the center and outer nozzles, respectively, with an uncertainty of 3% in the measured fuel mass flow rate. The different fuel/air ratios simulate lean outer nozzles with a center piloting nozzle. The richer center nozzle stabilized the outer flames, which would not stabilize without it; thus, the outer flames appear substantially lifted from their nozzles, as shown in Figure 15. The outer flames are dimmer due to their lower equivalence ratios. Other flow conditions were measured but are not presented for this work; they are listed in Appendix A.

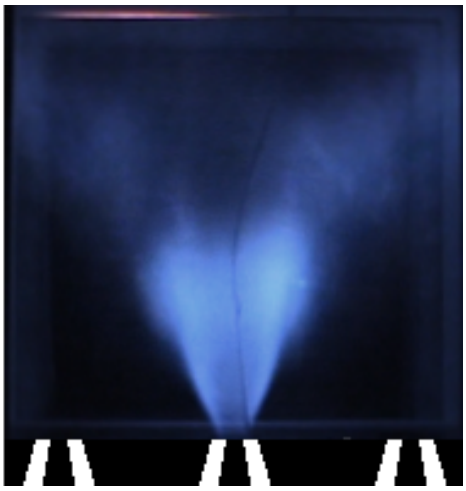

Figure 15 - Luminescence image of flame with nozzle positions overlaid.

The transverse acoustic forcing tubes with speakers are shown in Figure 16. The speakers were calibrated to have an equal amplitude response based on an impedance tube measurement prior to diagnostic measurements. This calibration did not account for differences in the phase response of the speakers, measured as a 7 degree range at 390 Hz and 20 degrees at 1170 Hz. The transverse excitation signal amplitude is constant for each transverse speaker, with a phase difference between the left and right speaker signals of either 0° and in-phase (IP) or 180° and out-of-phase (OP). These conditions create either a pressure antinode or a velocity antinode at the center nozzle respectively, as verified previously [107] and through cold flow measurements.

Ten acoustic pressure sensors monitor the system acoustics, 4 located on the transverse acoustic tubes 1 inch from the inside of the combustor box (PCB 113b28) and the other 6 (PCB 112a05) split evenly between the 3 mixing pipes, as shown in Figure 16. The side sensors are more sensitive while the mixing pipe sensors have a higher operational temperature range. Using the two mixing pipe sensors, we can estimate the acoustic

velocity in the mixing pipe at the sensor location. However, the sensor location is too far away from the dump plane to estimate the acoustic fluctuations at the nozzle exit.

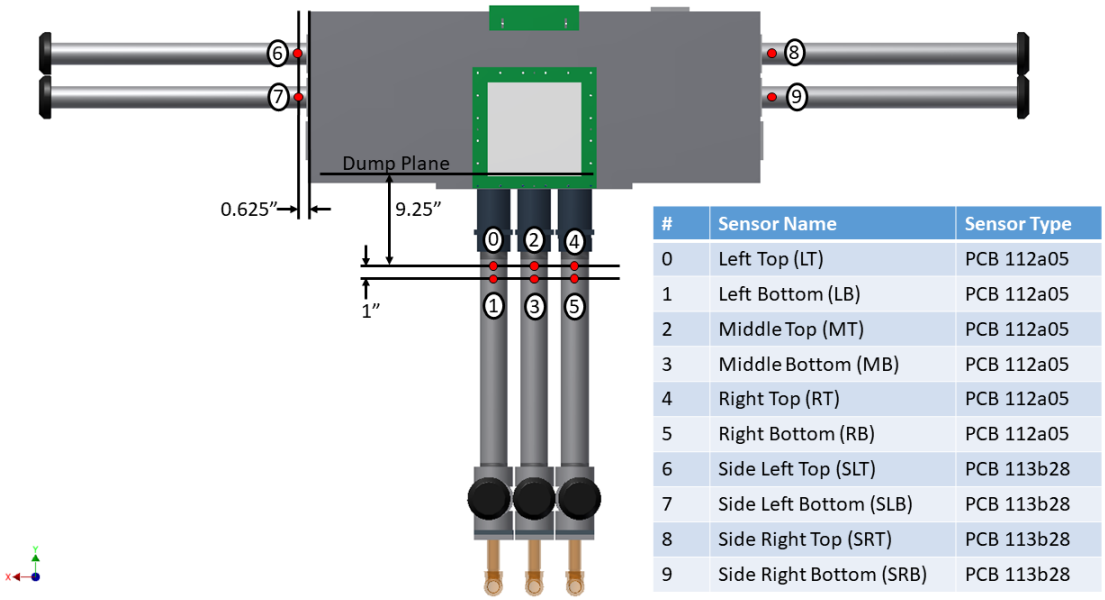

#	Sensor Name	Sensor Type
0	Left Top (LT)	PCB 112a05
1	Left Bottom (LB)	PCB 112a05
2	Middle Top (MT)	PCB 112a05
3	Middle Bottom (MB)	PCB 112a05
4	Right Top (RT)	PCB 112a05
5	Right Bottom (RB)	PCB 112a05
6	Side Left Top (SLT)	PCB 113b28
7	Side Left Bottom (SLB)	PCB 113b28
8	Side Right Top (SRT)	PCB 113b28
9	Side Right Bottom (SRB)	PCB 113b28

Figure 16 - Acoustic sensor locations (red dots) within the combustor.

2.1.1 Characterization of Acoustic Forcing and Combustor Acoustic Response

In order to identify the frequencies of interest, the author performed a frequency sweep within a COMSOL simulation of the combustor geometry; the COMSOL analysis was then validated using experimental measurements. Included in the domain of the COMSOL analysis were the interior of the combustor box, the transverse forcing tubes, and only the center inlet pipe, shown in Figure 17c. It was assumed that the combustor was filled with air that has a spatially varying temperature profile, shown in Figure 17a and in Figure 17b, to approximate the local variations in speed of sound. The exhaust ducts, located on top of the combustor, were treated as a pressure release condition, and all other boundaries but the speakers were rigid wall. The speakers were modeled as a normal

acceleration condition, and the speakers on the right and left sides were placed either in-phase or 180° out-of-phase with each other.

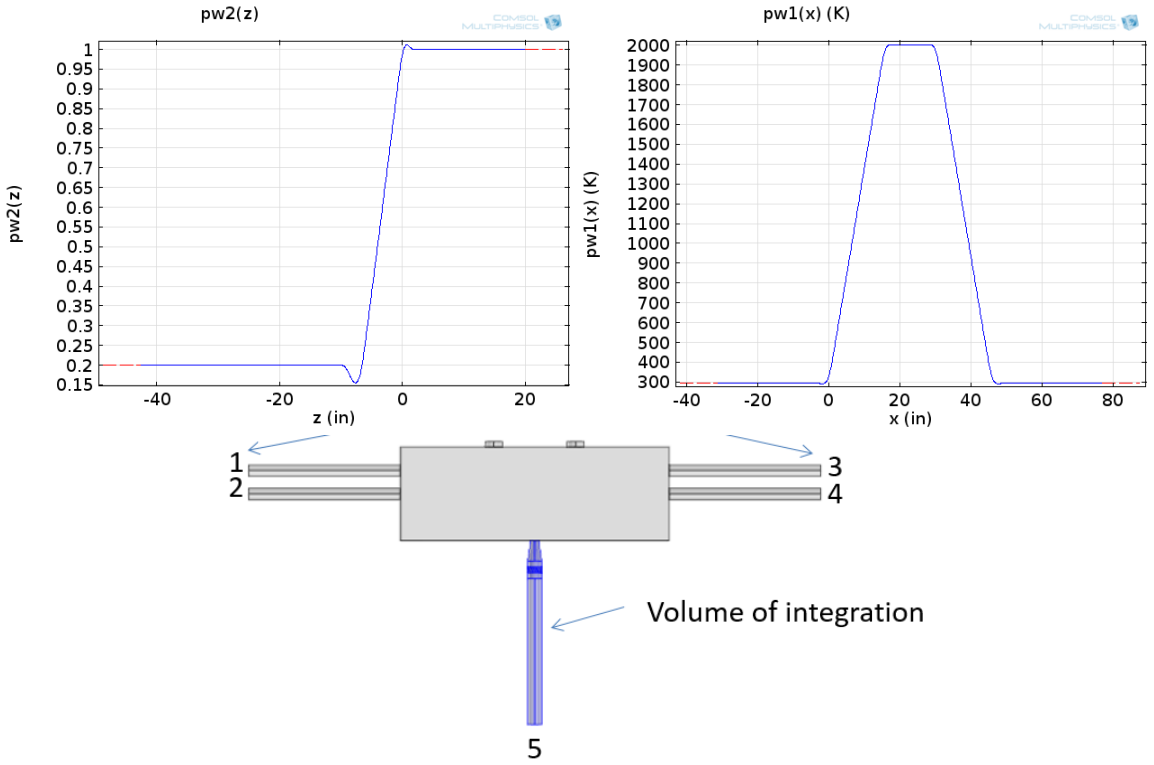

Figure 17 – (top-left) Axial temperature profile, (top-right) Transverse temperature profile, and (bottom) geometry of calculation with the inlet pipe highlighted in blue.

A computational frequency study with constant amplitude IP forcing was performed, and pressure measurements were taken at two points—the side acoustic tube where experimental measurements would be taken and a point above the center nozzle representative of the flame. Frequencies from 100 Hz to 3000 Hz in steps of 10 Hz were used in the calculations, and a pseudo spectrum was created, shown in Figure 18. The spectrum shows peaks at 250, 390, 610, 900, 1170 Hz and higher. The frequencies above approximately 1300 Hz showed a non-1D transverse structure in the combustor box and were thus ignored. The peak frequency of the combustor occurred at 390 Hz, the design frequency which corresponds to the resonant frequency of the box and inlet pipe.

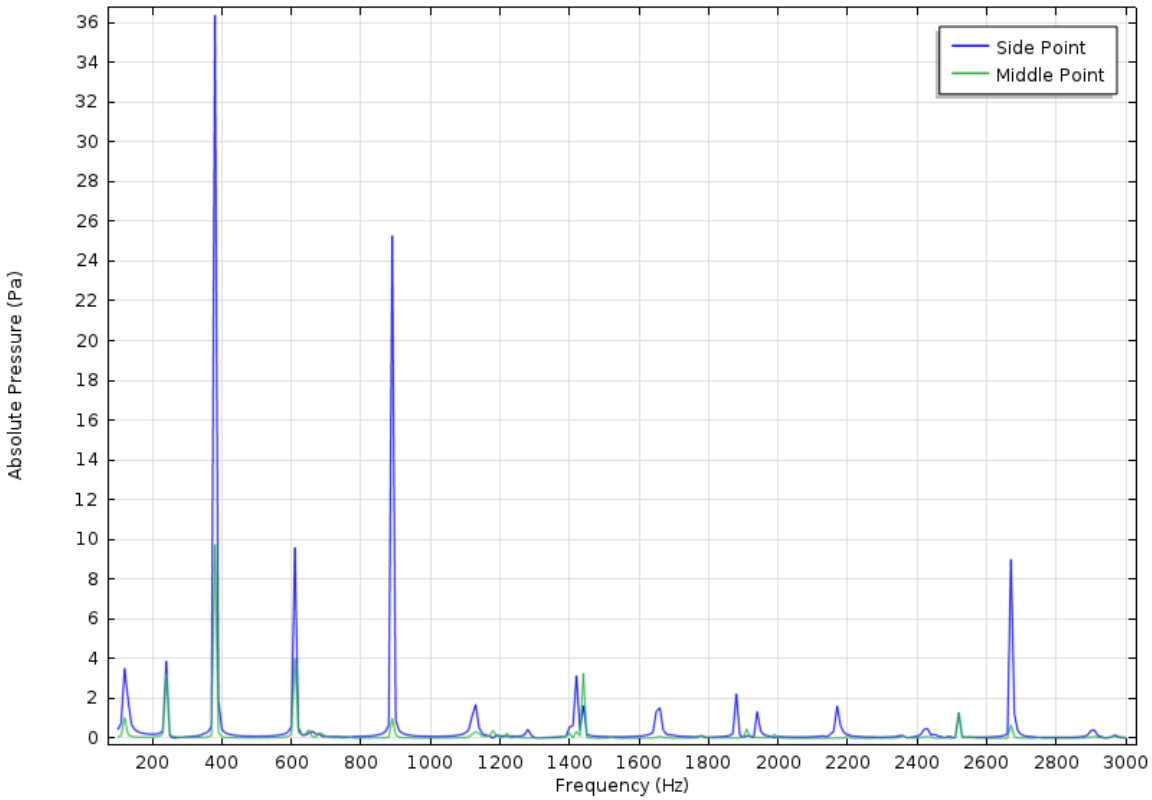

Figure 18 - Pseudo spectrum calculated from COMSOL frequency sweep of IP forcing. "Side Point" is the SRB sensor, and "Middle Point" is at the flame location.

The acoustic response inside of the combustor was experimentally measured for a single flame configuration. The forcing signal sent to the speakers and the acoustic signal from a pressure sensor were simultaneously sampled at 20kHz, with a low pass filter on the acoustic signal using a cutoff frequency of 5kHz. The acoustic signal was measured in the lower of the two side acoustic tubes, one inch from the combustor box. The forcing signal was a 30 second, constant amplitude, frequency sweep from 100Hz to 3kHz. The test method was as follows: ignite the flame, begin the 35 second recording, turn on the function generator channel, trigger the frequency sweep, and wait until the recording is finished to turn off the function generator. The 30 second signal within the 35 second recording was located by identifying the sudden transition from a 3kHz signal to a 100 Hz

signal at the end of the frequency sweep. Figure 19 shows the Hilbert transform of the pressure signal as a function of frequency, which has been correlated with time. Based on this study and on the COMSOL analysis of the modes, 250, 390, 500, and 1180 Hz were chosen as frequencies for further study as they allow for stronger forcing with less input due to resonances. The 600 and 900 Hz frequency peaks were rejected as COMSOL showed that these were acoustic modes of the side tubes and inlet pipes but not the box. After the initial data campaign using only a single nozzle, the frequencies were narrowed down again to 390 and 1180 Hz as these showed a strong response for both IP and OP forcing. For the data sets used in this study, the 1180 Hz frequency was identified as the third harmonic of the 390 Hz frequency and corrected to 1170 Hz. Thus the final frequencies of interest are 390 Hz and 1170 Hz.

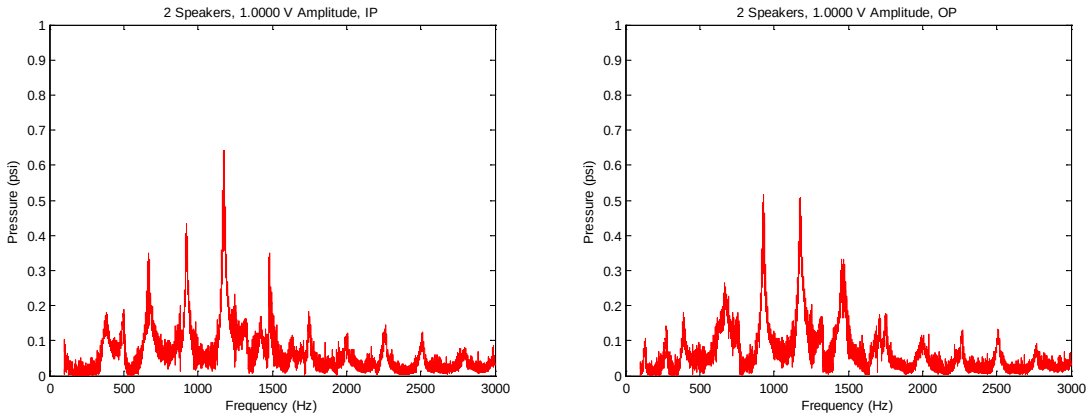

Figure 19 - Pseudo-spectrum calculated from the combustor acoustic response to a frequency sweep measurement.

Figure 20 shows the spatially integrated power spectra from the measured velocity field (sum of the magnitude of each velocity component squared) over the region $-0.75 < r/D < 0.75$ and $0.1 < z/D < 1.2$, taken in the r-z plane. The details of the local spectra calculation are described in Section 2.2.5, “Post Processing Techniques.” The spectra

shown below is the spatial integration of the fluctuating kinetic energy, $\widehat{K}$, of every point within the designated region. The figure shows that the frequency response is clearly discernible for all forcing cases and that the OP case is an order of magnitude larger than the IP case for 390 Hz, while the 1170 IP and OP cases are of comparable response magnitude for the two flow fields.

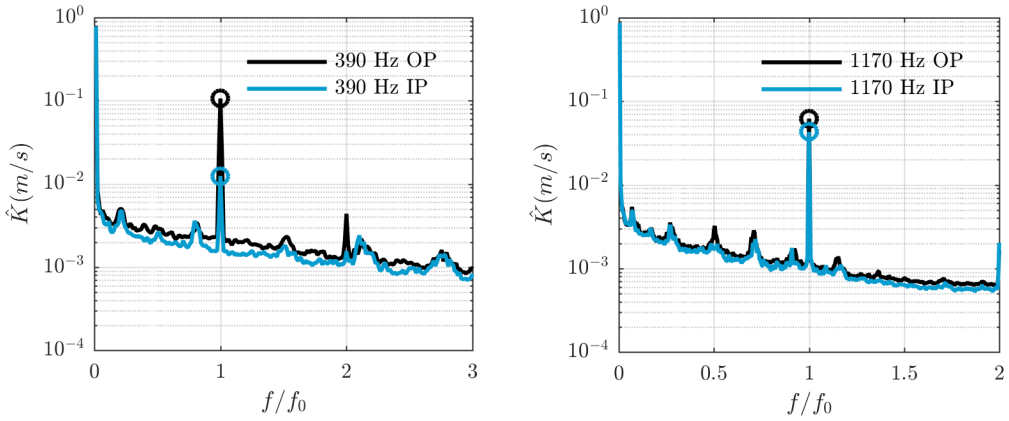

Figure 20 - Spectra of the fluctuating kinetic energy for the acoustically forced cases calculated from the sPIV velocity fields.

2.2 Diagnostic Techniques and Post-Processing

Multiple diagnostic techniques were utilized to study the flame and flow response. Specifically, simultaneous stereoscopic Particle Image Velocimetry (sPIV) and OH Planar Laser Induced Fluorescence (OH-PLIF) were taken to characterize the flame and flow field response while OH* and CH* chemiluminescence measurements were taken to characterize the heat release. An additional technique, two-component PIV, characterized the nozzle acoustic response at the forcing frequency during the axial acoustic minimization procedure.

This work considers two measurement planes: a horizontal plane parallel to the dump plane centered about the middle nozzle and a vertical plane bisecting the three nozzles. These measurement planes are referred to as the r-θ and r-z planes respectively. The plane nomenclature is in reference to a cylindrical coordinate system centered on the middle nozzle with the axial direction in-line with the axis of the nozzle, as shown by Figure 11. All measurements were taken in the r-z plane/orientation, but only the planar sPIV and OH-PLIF measurements were taken in the r-θ plane.

2.2.1 Simultaneous sPIV and OH PLIF

Simultaneous OH Planar Laser Induced Fluorescence (OH PLIF) and Stereoscopic Particle Image Velocimetry (sPIV) were taken at 5 kHz. A double-pulsed laser with a wavelength of 527 nm, supplying 12 Watts per laser head, was used to place a laser sheet through the test section for sPIV. Two CMOS cameras with an interframe time of 400 ns were placed at equal angles to the plane containing the laser sheet and filtered to capture the scatter from the 0.5-1 micron TiO_2 particles. For the r-z plane measurement, the PIV laser pulses were tested at 5, 10, and 14 μs apart, with 14 μs being chosen. This time spacing best balanced loss of particles due to out of plane motion and sufficient in-plane particle motion, allowing the fastest particles to move approximately 6 pixels between laser pulses. Similarly the r-θ measurement plane tested 3, 5, and 8 μs between laser pulses with 8 μs being chosen. The OH PLIF technique was performed using a dye laser system tuned to 283.4502 nm pumped by an Nd:YAG laser at 532nm. The OH fluorescence was captured using an additional high speed CMOS camera coupled to a gated high speed intensifier using a 45mm UV CIRCA lens. Background flame chemiluminesecne was blocked using

a custom made narrowband interference filter (>80% transmission). Three cylindrical lenses (collimating: $f = 50$ mm diverging and $f = 200$ mm converging, thickness: $f = 750$ mm converging) were used on each of the lasers to create and condition the laser sheets before they were combined and passed into the combustor. The PIV laser sheet was approximately 2mm thick as measured by moving an index card with a traverse through the beam path, and the OH-PLIF laser sheet was approximately 0.5mm.

The laser sheets for the *r-z* plane passed through the laser port on the side of the combustor and was observed through the front window. The sPIV cameras were set at an angle of 35 degrees to the normal of the laser sheet and captured both forward and backscatter. The intensified PLIF camera was perpendicular to the laser sheet. Figure 21 shows a schematic of the camera setup.

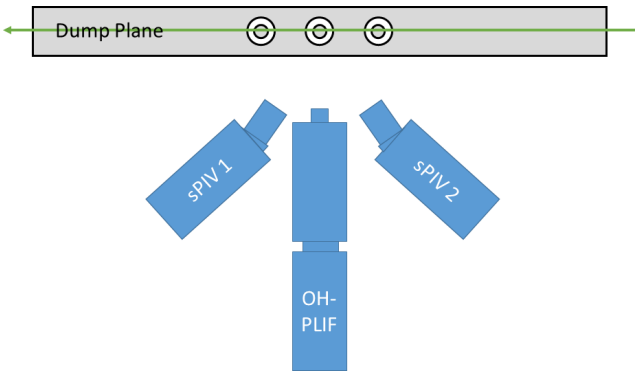

Figure 21 - Schematic of camera setup in r-z plane with the vertical laser sheet in green.

For the *r-θ* plane, the laser sheet passed through the front window of the combustor and out the back window. The two coplanar PIV cameras were set at 55 degrees from the normal of the laser sheet, looking down, and capturing both forward and back scatter from the particles in the flow. The intensified PLIF camera looked at a UV coated mirror reflecting the dump plane through the top window located between the exhaust ports.

Measurements in the r-θ planes were obtained at axial heights of $z/D = 0.15, 0.67, 1.2,$ and 1.7. The jet merging occurs around $z/D = 2$, so most of these measurement domains are upstream of the flow field and shear layer merging. Figure 22 shows a schematic of the camera setup for this plane.

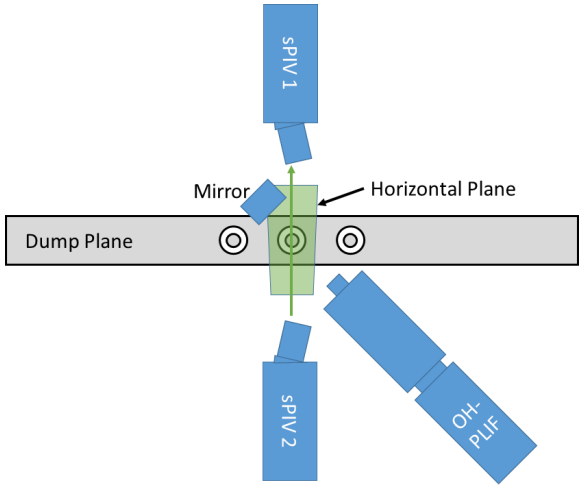

Figure 22 - Schematic of camera setup in r-θ plane with laser sheet in green.

Figure 23 shows the overlap of filtered PLIF and raw Mie scattering (sPIV) images for both the r-z and r-θ measurement planes. The more visible region of the Mie scattering image (yellow) contains more seeding particles and corresponds to the reactant jet exiting the annular nozzle. The region in blue shows where OH was present in the image and corresponds to where the products of the reaction can be found. The density jump across the flame is reflected in the change in number of seeding particles from the reactant jet to the blue product region, resulting in fewer visible particles in the product region. These images show that the flame is located in the inner shear layer of the seeded reactant jet. The nozzle exit can also be seen in the r-θ image- note that its center is offset from the center of the blue OH PLIF region because the sPIV viewing cameras are set at an angle and measuring a plane above the nozzle.

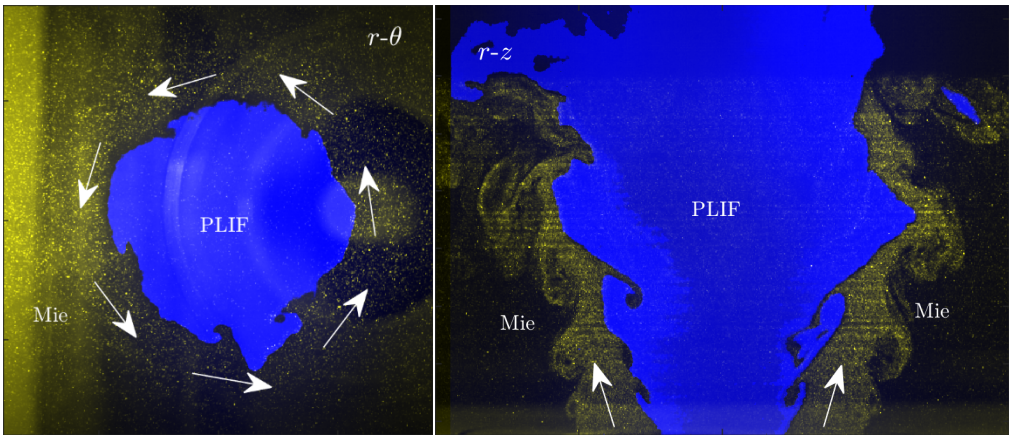

Figure 23 - Mie scattering (yellow) and filtered OH-PLIF image (blue) overlayed for r-θ and r-z planes, $dt/2$ apart.

The two sets of image pairs acquired from the sPIV technique were processed using the DaVis 8.3 software from Lavision. The background was accounted for by subtracting a sliding minimum in time, which also reduced reflections in the images but did not account for laser power variations. The calculation then used a particle normalization prior to applying a multi-pass, decreasing size correlation calculation. The initial passes contained no overlap and used a square window while the final pass used a Gaussian round window. After each correlation calculation, the vectors were filtered using the median filter that removes, then reinserts the vector values based on the rms of their neighbors. The specific processing parameters for each measurement plane are shown in Table 1.

Table 1 - sPIV processing settings for each plane.

Plane	**Initial Step**	**Final Step**	**Intermediate Filter**	**Post-processing Filter**
r-z	48x48 pix, 1 pass	16x16 pix, 50% overlap, 3 passes	2x (Remove >2.1 rms Reinsert <1.7 rms)	2x (Remove >1.8 rms Reinsert <1.6 rms)
r-θ, z/D=0.15	32x32 pix, 1 pass	24x24 pix, 50% overlap, 4 passes	2x (Remove >3 rms Reinsert <1.8 rms)	2x (Remove >3 rms Reinsert <2 rms)
r-θ, z/D=0.67	48x48 pix, 1 pass	24x24 pix, 50% overlap, 3 passes	2x (Remove >3 rms Reinsert <2 rms)	4x (Remove >2 rms Reinsert <1.2 rms)
r-θ, z/D=1.2	64x64 pix, 1 pass	32x32 pix, 75% overlap, 3 passes	2x (Remove >2.5 rms Reinsert <1.6 rms)	4x (Remove >2.1 rms Reinsert <1.6 rms)
r-θ, z/D=1.7	48x48 pix, 1 pass	32x32 pix, 75% overlap, 3 passes	4x (Remove >1.7 rms Reinsert <1.2 rms)	4x (Remove >1.9 rms Reinsert <2.1 rms)

There are multiple sources of error within PIV measurements. First particles might not track the flow field reliably. The particles used in this experiment were TiO_2 with a mean diameter of 0.5 μm, which were able to track the vortices within the flow field. Secondly out-of-plane motion can cause loss of pairs between image shots. The large swirl number of the flow meant that there was significant out-of-plane motion between laser pulses; however, the dt was chosen so that the particles would move approximately a quarter of the sheet thickness, minimizing the loss of pairs between images. Even with this dt, the measurements of the jet nearest the nozzle exit experienced bias errors because the high azimuthal velocity caused significant loss of pairs and cut off the higher end of the velocity distribution. This is apparent in the measured r-z plane; the axial velocity appears to accelerate out of the nozzle and achieves a maximum approximately 0.1 diameters downstream. The rest of the r-z plane is dominated by the error associated with sub-pixel interpolation. In other words, the instantaneous velocity vectors have an in-plane uncertainty on the order of 1-2 m/s. The out-of-plane velocity has a larger uncertainty than the in-plane components due to the angle of the cameras.

LaVision performed several studies on identifying the uncertainty from PIV measurements [115, 116]. They found that correlation statistics provided the best means of estimating the uncertainty. The DaVis software calculates an uncertainty estimate using this method. Table 2 shows a summary of median uncertainties of instantaneous velocities, as calculated by DaVis. These median uncertainties are on the same order of magnitude as uncertainties associated with errors in sub-pixel interpolation and show that the out-of-plane measurement contains the highest error, as expected.

Table 2 - Median random uncertainties of instantaneous velocities for each measurement plane and for the horizontal (u), vertical (v), and out-of-plane (w) velocity components.

Plane	$u\ (m/s)$	$v\ (m/s)$	$w\ (m/s)$
r-z	1.1	0.9	1.8
r-θ, $z/D = 0.15$	0.6	0.4	0.7
r-θ, $z/D = 0.67$	0.7	0.5	0.8
r-θ, $z/D = 1.2$	1.2	0.9	1.4
r-θ, $z/D = 1.7$	1.2	0.8	1.2

The PLIF images give a measure of the instantaneous density field as well as the location of the flame edge. Knowing that the region where there is OH signal represents products and the region of no signal represents reactants, the instantaneous PLIF image is filtered and then binarized between zero (no signal) and one (signal). These instantaneous, binarized images can be averaged to obtain a progress variable field, $\bar{c}$, that represents the probability of flame products being present in a given region. The $\bar{c} = 0.5$ iso-contour provides a convenient reference location to denote as the average position of the flame. Both phase-averaged and time-averaged progress variables were calculated.

2.2.2 Two Component PIV

The two-component PIV was performed at 5 kHz and focused on the nozzle exit. Two laser pulses from a dual pulsed Nd:YLF laser (527 nm) were set 3.36 μs apart, and the scatter off of TiO_2 particles (0.5-1 micron) was captured using a high speed CMOS camera with an interframe time of 300 ns. The region of interest was approximately 25 mm x 25 mm (256x256 pixels).

Figure 24 shows a sample image focused on the right half of the nozzle exit with a 1-inch-tall laser sheet. 2500 image pairs were taken, corresponding to 0.5 seconds of data. The images were preprocessed by using the built-in pixel normalization with a setting of 2

pixels. A single pass of a 32x32 interrogation window with 25% overlap was used, and the vector post- processing used the iterative “strongly remove and replace” filter 2 times with settings of 2.2 and 1.8 for the remove and replace options respectively. The calculated instantaneous velocities have an uncertainty of 1 m/s, based on the sub-pixel interpolation. The specific settings of the calculation method used in DaVis did not permit the convenient uncertainty calculation.

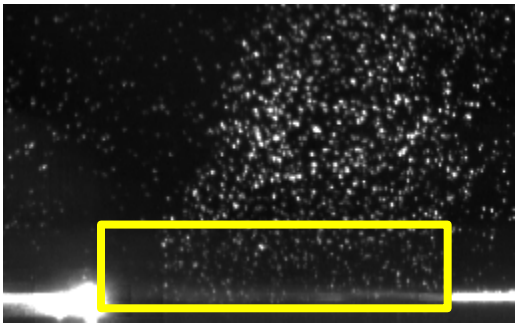

Figure 24 - Mie scattering image showing region of calculation for 2 component PIV technique.

2.2.3 OH Chemiluminescence*

OH* measurements were taken at 50kHz over a span of 2 seconds using a photo multiplier tube (PMT). OH* was chosen as it can be considered a representation of the heat release in the system [117]. It should be noted that broadband CO_2* emission contaminates the OH* signal, but has a near negligible contribution [118]. Additionally, the intensity of both light emissions are linearly related to the heat release; thus, this metric still works. A Hamamatsu H5784-04 PMT with a 10 mm window on the front, was placed inside of a box to eliminate any noise from background light. A bulkhead optical fiber connector was placed on the box, co-axially with the PMT sensor, to allow a directional measurement. In between the connector and the PMT was a Newport band pass filter with a center frequency

of 310nm and a half width of 10nm. Figure 25 shows the distances that determine the viewing angles. The maximum half angle based only on the measurements of the bulkhead connector and assuming no internal reflections is approximately 8.4 degrees, while the half angle based on the 10 mm PMT sensor dimension and distance from the opening of the connector is 7.25 degrees. However, the effective diameter of the sensor is 8 mm which gives a half angle of 6.12 degrees. The box containing the PMT was placed approximately 36 in. away from the center of the test section, aligned with the center of the window, and captured the majority of the 9.7x9.7 inch window.

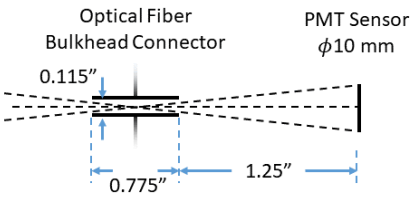

Figure 25 – Diagram showing relative distances of PMT sensor for calculating half angles.

2.2.4 CH Chemiluminescence*

CH* chemiluminescence images were taken at 5 kHz with simultaneous 50kHz OH* PMT and acoustic measurements. A subregion of the window was captured using a CMOS camera (Photron SA-3) filtered by a 2” CH* filter (center frequency of 434 nm with a 17 nm bandwidth) coupled to the High Speed IRO gated intensifier from Lavision with an exposure time of $10\mu s$ and a gain setting of 70. The CH* measurement was contaminated by a significant contribution from CO_2*; however both of these light emission are linear with heat release[118]. A Nikon 45mm lens with f=2.8 was used on the front of the intensifier. The image resolution was 352x384 pixels with a corresponding size of roughly 80x86 mm. Figure 26 shows a sample image from this measurement. Some of

the chemiluminescence occurs outside of the measurement region; however, the majority of the lost chemiluminescence appears downstream and is not due to structures flowing out of the side of the image. Additionally, reflections from the OH filter used for simultaneous OH-PLIF appear in the measurement within the region $z/D \in (0.5,1.3)$. The reflections skew local statistics within this region to a higher value. This is discussed in Section 0.

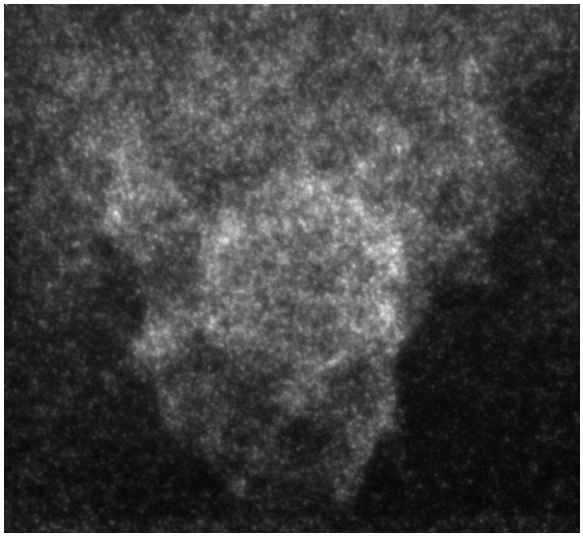

Figure 26 - Sample CH* image.

2.2.5 Post-Processing

The output velocity vectors from DaVis were in Cartesian coordinates, so the first post-processing step was to convert the vectors into the cylindrical coordinate system shown in Figure 11. For the r-z plane, this was a trivial task. For the r-θ plane, the instantaneous velocity vectors were interpolated, using a cubic interpolation, onto a polar grid where the radial spacing was roughly equal to the Cartesian grid point spacing. The origin of the polar grid was chosen as the point which maximized the time-average flow field axisymmetry The instantaneous velocity components were then transformed into the cylindrical coordinate system.

A Fourier transform of the vector fields was performed at each point in the grid giving a frequency spectrum at each spatial location for each component of velocity. Each spectrum was estimated using Welch's method with a window size of 0.2 seconds and a 75% overlap, resulting in 27 ensembles and a spectral resolution of 5 Hz. The phase angles were calculated using a similarly averaged cross-power spectral density estimation with respect to the signal at the location of the maximum axial velocity standard deviation.

For the r-θ plane, the Fourier coefficients, minus the estimated acoustic contribution, were decomposed into periodic azimuthal modes. Eqn. (2.2), seen below, shows the spatial decomposition of the frequency domain velocity measurements into periodic azimuthal modes:

$$\widehat{\boldsymbol{B}}_m(r,z,\omega) = \frac{1}{2\pi}\int_0^{2\pi} \widehat{\boldsymbol{u}}'(r,\theta,z,\omega)e^{-im\theta}d\theta. \tag{2.2}$$

Note that the choice of sign convention of the periodic azimuthal modes was set such that $m < 0$ is counter-swirling, and $m > 0$ is co-swirling for this particular flow. This sign convention assumes that the azimuthal disturbance is of the form

$$A_m = \hat{C}_m\,(r)\exp[i(\omega t - m\theta)] \tag{2.3}$$

where $\hat{C}_m$ is the complex coefficient whose hat denotes a complex number, and assumes that the mean swirl is in the counter-clockwise direction.

The OH-PLIF edges were similarly treated to decompose them into azimuthal modes. First, the phase-averaged $\bar{c} = 0.5$ position was parameterized by the function, $R_f(\theta, z, t^*)$, where t^* represents the phase in the acoustic cycle. The Fourier coefficient of

the r-θ flame edge, $\hat{R}_f$, is calculated by performing a convolution of the phase averaged flame edge and $\exp(i\omega t)$ and can then be decomposed into azimuthal modes as

$$\hat{R}_f(\theta, z, \omega) = \int_{-\infty}^{\infty} \sum_{m=-\infty}^{\infty} \hat{R}_m(z, \omega) e^{\mathrm{i}(\omega \mathrm{t} - m\theta)} d\omega, \tag{2.4}$$

where $\hat{R}_m(z, \omega)$ represents the azimuthal mode coefficients at the given axial location and frequency.

While the azimuthal coefficients of the flame edge only depend on the axial location, the azimuthal coefficients from the velocity data are multidimensional in nature. Thus various approaches were used to reduce the dimensionality of the data sets to facilitate data presentation. First, the helical mode magnitudes are integrated as follows:

$$\overline{\boldsymbol{B}}_m(\omega, z) = \int_0^R \left|\widehat{\boldsymbol{B}}_m(\omega, z, r)\right| r dr, \tag{2.5}$$

where the outer limit of the integration R is the outer edge of the time-averaged outer shear layer in the r-z plane, defined as

$$\frac{\partial\left(\bar{u}_Z(R, z)\right)}{\partial r} \equiv 0.5 * \min\left(\frac{\partial\left(\bar{u}_Z(r, z)\right)}{\partial r}\right). \tag{2.6}$$

$\overline{\boldsymbol{B}}_m$ is the area weighted integral of the coefficient magnitudes from the centerline to the edge of the outer shear layer. This approach works well for identifying which modes are dominant at each axial location but hides the spatial distribution of these modes. In order to also reduce the dimensionality of the velocity data, while presenting some information about both its radial and axial distributions, reference lines in the r-z plane are defined. First, reference inner shear layer (ISL) and outer shear layer (OSL) lines were defined, where the largest axial velocity fluctuations occur in these shear layers. The ISL and OSL

are calculated as the location of minimum and maximum mean azimuthal vorticity, respectively, as a function of axial distance. An additional reference line, the jet core (JC) is calculated as the line of maximum velocity magnitude in the r-z plane. Figure 27 shows the locations of these three lines on a sample time-averaged r-z flow field where the colour represents the azimuthal velocity normalized by a reference bulk axial velocity out of the nozzle, $u_{ref} = 28.8\ m/s$.

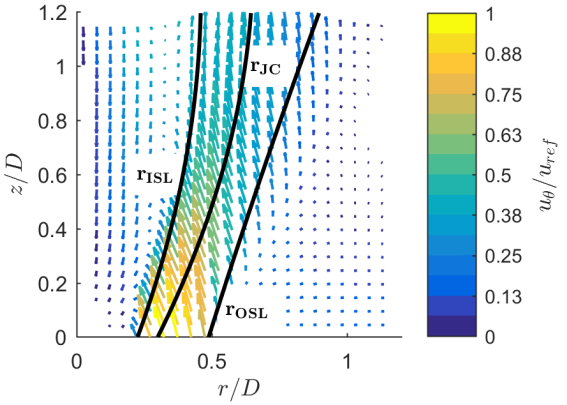

Figure 27 - Sample time-average r-z plane showing shear layers and jet core locations.

2.3 Minimizing Induced Axial Acoustics

In order to decouple the transverse and longitudinal acoustics, a feasibility study using COMSOL was performed on the combustor geometry. This study showed that it was possible to suppress induced axial acoustics during transverse excitation and provided the methodology used to find the optimal parameters for minimizing the induced axial acoustics. Using this methodology, the optimal longitudinal forcing parameters were found that minimize the axial coupling for the 390 Hz forcing but not 1170 Hz. The results from both the computational study and the experimental mapping procedure are presented here.

2.3.1 COMSOL Simulation

The COMSOL simulation mentioned in Section 2.1.1 was modified to include a speaker for axial forcing. This speaker was controlled independently of the transverse speakers, and the amplitude of its fluctuations, Q, was a ratio with respect to the transverse amplitude. Unlike the actual experiment, the axial speaker was located at the bottom of the inlet pipe, oriented upwards; whereas in the actual experiment, the axial speaker is located at the end of a pipe perpendicular to the bottom of the inlet. The transverse speakers were forced either in-phase or out-of-phase; however, it was found that the analysis did not make sense for the OP forcing condition due to the pressure node located at the nozzle exit and the resulting lack of acoustics in the inlet pipe.

The study aimed to show how best to cancel or minimize the acoustic energy inside of the inlet pipe and how best to measure it. The acoustic energy in the inlet pipe was calculated by integrating Eqn. (2.6) over the highlighted domain in Figure 17c

$$E_{tube} = \iiint 0.5 * \rho_0 * \left[\left(\frac{|p'|}{\rho_0 c} \right)^2 + \left(\frac{\left| \frac{dp'}{dz} \right|}{\rho_0 \omega} \right)^2 \right] dV \tag{2.7}$$

The parameter space defined by the longitudinal phase and amplitude was mapped out with a resolution of 10 degrees and 0.05 in Q. The calculated acoustic energy inside of the pipe is shown in Figure 28a. This shows that at a phase of 180 degrees and an amplitude ratio of 0.55, we can obtain a minimum in the acoustic energy inside of the pipe.

Additionally, the simulation placed measurement probes at existing pressure sensor locations. The resulting measurements, not shown, revealed that the sensors on the inlet pipes were placed in the wrong location to perform real-time measurements of the induced

axial acoustic minimization for both frequencies. In other words although a pressure node at either sensor location corresponded well with the minimized axial acoustics for 390 Hz, a pressure node at the same location did not minimize the induced axial acoustics at 1170 Hz. However, the results showed that the acoustic velocity at the nozzle exit, as shown in Figure 28b, corresponded well with the acoustic energy inside of the inlet pipes for both frequencies. The optimal phase was in agreement with the minimal acoustic energy phase while the amplitudes agreed closely, with the nozzle exit velocity amplitude at $Q = 0.45$.

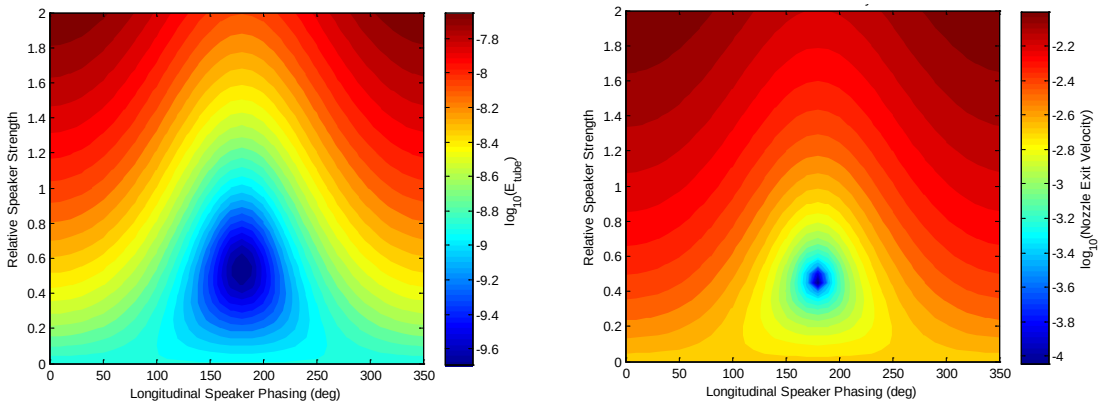

Figure 28 – (left) Acoustic energy inside of inlet pipe as a function of axial speaker forcing conditions and (right) nozzle exit velocity fluctuation magnitude at given frequency as a function of axial speaker settings for 390 Hz IP forcing.

The axial acoustics inside of the inlet pipe could not be cancelled completely within the COMSOL simulation. The reason for this is simple; the transverse acoustics in the absence of axial forcing places a pressure antinode at the axial speaker location while the axial forcing imposes a velocity fluctuation at the same location. Because the pressure and velocity are 90 degrees out of phase, their superposition will never be able to cancel out all of the acoustics for the given model.

Figure 29 shows the calculated mode shapes along the combustor centerline for the cases with and without axial minimization. The discontinuity in the lines is due to the solid

centerbody falling on the measurement line. This shows that the magnitude of both the pressure and velocity fluctuations are decreasing in the inlet pipe as expected, confirming the reduction in the axial acoustics.

Given that the conditions that minimize the axial acoustic energy and the axial acoustics at the nozzle exit were close, the goal becomes to minimize the acoustic field at the nozzle exit, a much simpler task to measure. Additionally the nature of the responses in Figure 28 suggests a path towards experimentally optimizing the minimization parameters: 1) perform a constant amplitude phase sweep to identify the optimal phase, then 2) perform an amplitude sweep at the identified phase.

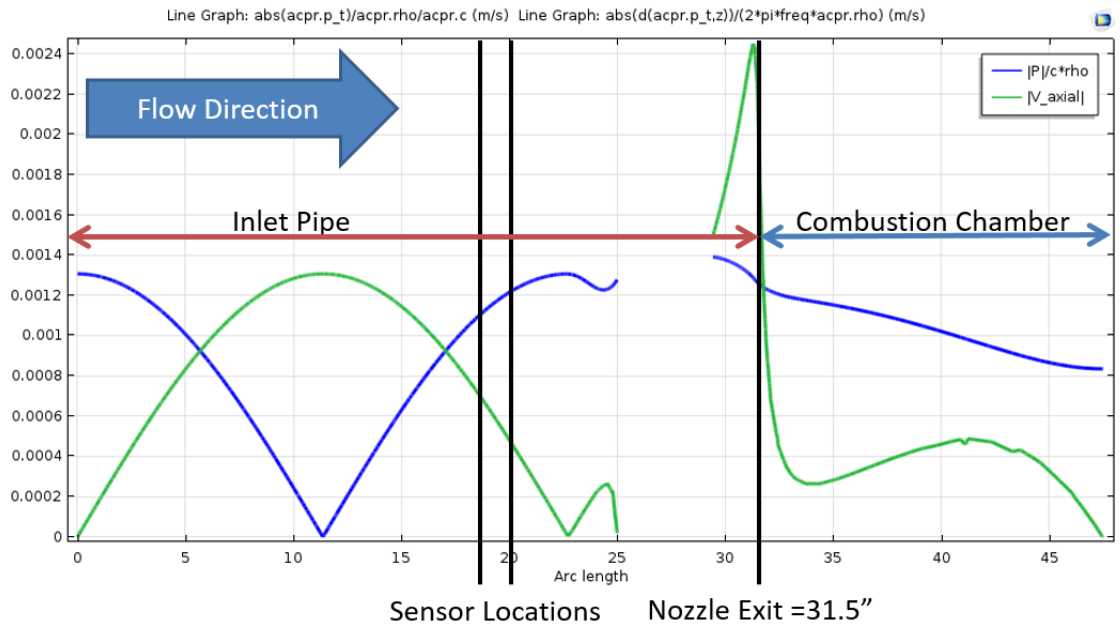

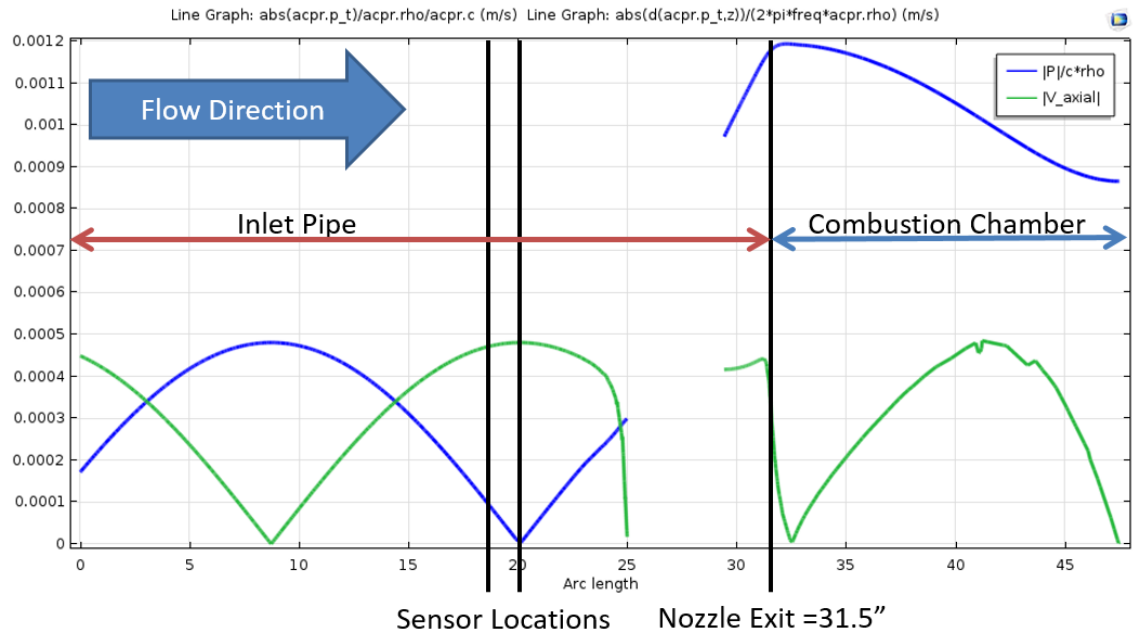

Figure 29 - Mode shapes for (top) axially unforced and (bottom) inlet pipe acoustic energy minimum conditions for the simulated 390 Hz IP forcing case.

2.3.2 Experimental Mapping of Cancellation Parameters

Two-component PIV was performed to measure the effect of the axial forcing during the phase and amplitude sweeps. From the PIV measurement, the average axial velocity fluctuation magnitude across the nozzle was calculated, given by

$$\overline{|\hat{u}_z(\omega_0)|} = \frac{1}{r_{o,nozzle} - r_{i,nozzle}} \int_{r_{i,nozzle}}^{r_{o,nozzle}} |\hat{u}_z(\omega_0, r)| dr \qquad (2.8)$$

where $r_{i,nozzle}$ and $r_{o,nozzle}$ are the centerbody and nozzle radii respectively. The signal-to-noise ratio (SNR), defined as the ratio of the velocity fluctuation magnitude at the forcing frequency to the magnitude at adjacent frequencies, measures how well the coherent signal is resolved from the noise, and values near unity have a higher uncertainty. For the non-minimized case, the SNR across this region was on the order of 10.

For both the amplitude and phase sweeps, the transverse speakers were excited with a $1V$ and 0° phase reference signal. Figure 30 shows the results of the axial speaker phase sweep and subsequent amplitude sweep for the 390 Hz IP forcing condition. The phase sweep shown in Figure 30a, performed with the axial speaker amplitude at 1V, shows the expected periodic trend as the axial phase is varied from 0° to 350°. The minimum phase from the sweep was at 50°, which corresponded with the minimum of the average SNR of 5 ocurring at 40°. The axial speaker was then set at a constant phase of 50°, and the amplitude was swept from 0 to 2V. The response is shown in Figure 30b with the minimum response occuring at an axial amplitude of 0.6V. The average SNR once again followed the same trend as the axial response and reached a minimum of approximately 3 at 0.7V, meaning the coherent signal was nearly indistinguishable from the noise and that the measurement had a higher uncertainty.

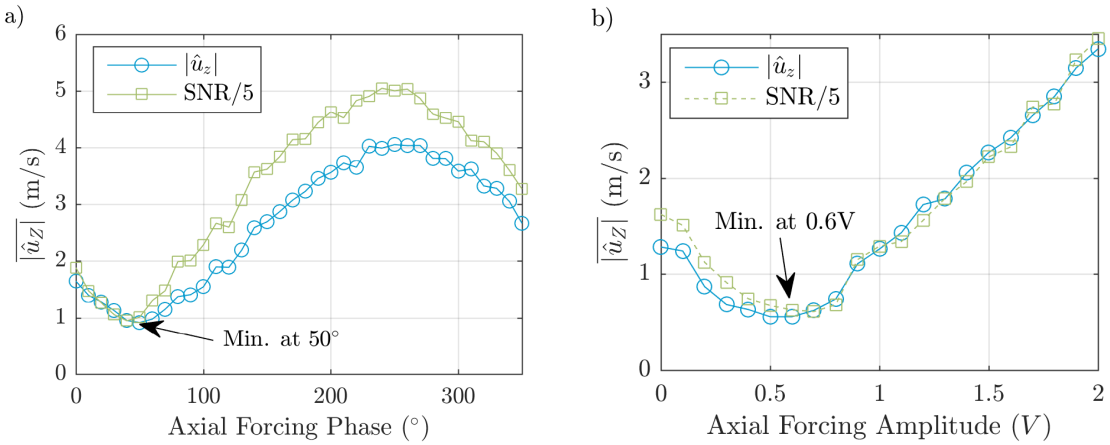

Figure 30 – (left) Average axial velocity response at forcing frequency across nozzle holding transverse forcing constant and sweeping phase of axial speaker and (right) average axial velocity response at forcing frequency across nozzle holding transverse forcing constant and sweeping amplitude of axial speaker.

The above sweeps were performed twice to ensure repeatability with the optimal phase and amplitude only deviating by an incremental step. A refining sweep of both phase and amplitude was then performed twice around the 40°, 0.6V setting. The results of the two refining sweeps are shown in Figure 31. The optimal axial forcing parameters were calculated as 0.6V and 40° for the central axial speaker at 390 Hz.

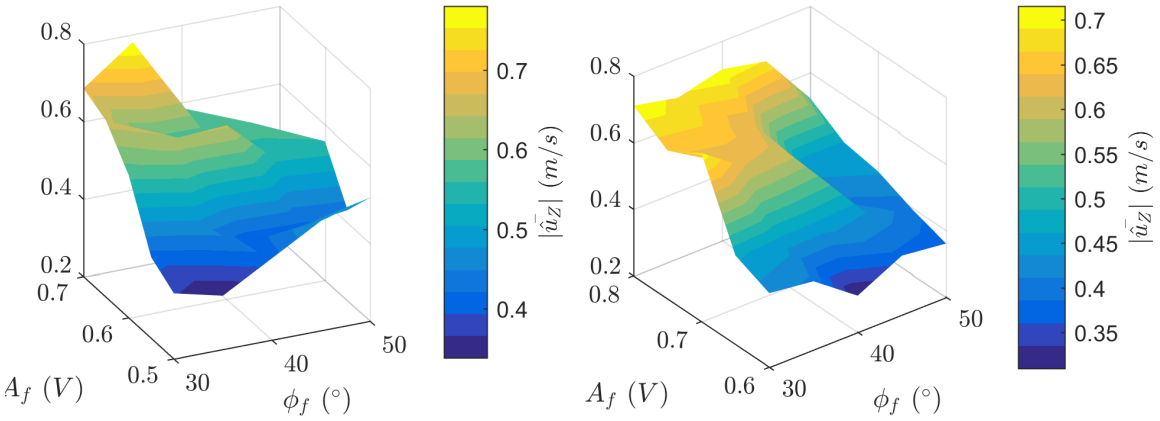

Figure 31 - Parameter sweeps around the identified optimal axial forcing condition for minimum nozzle exit velocity fluctuations for the 390 Hz IP forcing case.

This same procedure was also attempted at another frequency where significant transverse forced response data were previously obtained, 1170 Hz. However, the measurements did not identify a repeatable optimal condition. The minimum axial speaker phase varied by more than 20° between runs, and the phase sweep did not show the periodic shape. It is suspected that this lack of repeatability is due to the sensitivity of the high frequency acoustic field to the slightly transient nature of the thermal conditions within the combustor. In other words as, the combustor heated up, the acoustic field changed significantly more for the higher frequency than for the lower frequency. As a result of the 1170 Hz investigation, it was decided to force a pressure node at the sensor location on the

inlet pipe. The idea was that this forcing would cause a repeatable change within the flow field.

The measured axial velocity fluctuation profiles at the nozzle exit are shown in Figure 32. The baseline profiles show a peak in the inner shear layer at $r/D = 0.18$ (associated with vortical velocity), a lower amplitude but more spatially constant jet core fluctuation (due to acoustic velocity), as well another amplitude peak in the outer shear layer. When the minimization is introduced for the 390 Hz IP forcing, the inner shear layer axial fluctuations as well as the acoustic axial fluctuations are greatly reduced. The axial fluctuations are reduced by a factor of 1-2 across the jet and a factor of approximately 5 at the inner shear layer. These results demonstrate that the axial acoustic minimization procedure is effective at cancelling the axial disturbances out of the nozzle for the 390 Hz IP case. However, the 1170 Hz IP minimization did not result in a repeatable flow field response despite the non-minimized case being repeatable. This is most likely due to the same reasons that the frequency and phase sweep were not repeatable. However, Figure 32 shows that the minimization, while not consistent, did in fact reduce the flow field response. This means that combining acoustic characterizations and heat release characterizations on a case-by-case basis for the minimized 1170 case can still give meaningful insight into flow phenomenon.

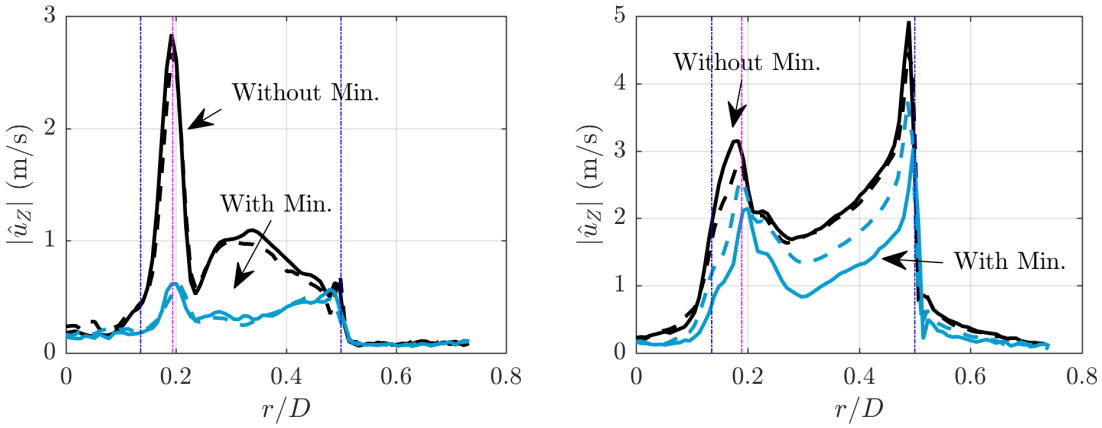

Figure 32 - Magnitude of axial velocity fluctuations at an axial height of 0.04 z/D for the 390 Hz IP case (left) and 1170 Hz IP case (right) with and without axial minimization. Blue, dash-dot lines denote the inner and outer edges of the annulus, and the magenta line denotes the location of the inner shear layer. Duplicate data is shown.

CHAPTER 3. FLOW STRUCTURES AND FLOW RESPONSE

This chapter introduces the flow field and the effects of acoustic forcing. First it is shown that the acoustic forcing has little effect on the time-average flow field, which suggests a linear response to acoustic forcing. Next the forced cases are analyzed in the r-z plane after a qualitative discussion of each: first the pressure node cases (OP), then the pressure antinode (IP) cases without and with axial minimization. It is shown that the locations, such as specific shear layers, within the flow field that respond to a particular frequency are consistent whether the forcing is IP or OP. Additionally it is shown that all disturbances convect with nearly the same phase speed. Lastly the pressure antinode cases with axial minimization are discussed, and it is shown that they consistently reduce the near nozzle helical mode content and the overall response.

3.1 Time-Averaged Flow Field

Figure 33 shows contour plots of the time-average, unforced flow field with the zero velocity contours overlaid in white, the ISL, OSL, and JC overlaid in black, and the time average flame, $\overline{c} = 0.5$, overlaid in red. This particular data set was taken from the Triple Nozzle Data set from June 2016, as detailed in Appendix B, and focuses on the center nozzle. The axial velocity profile shows that the jet cross-section leaving the annulus appears as two diverging regions of high axial momentum due to a combination of centrifugal forces and gas expansion, with gas expansion as the dominant effect as shown by comparing the reacting and non-reacting profiles (shown later). Inside the annular jet, there is a strong recirculation region that begins at the centerbody and closes further downstream. The peak reverse flow occurs at an axial distance of $z/D \approx 1.4$. Additionally,

there are much weaker reverse flow regions between the center nozzle and the adjacent nozzles, which are spaced approximately 2.9 s/D apart.

The radial velocity contours of Figure 33 capture the jet expansion as well as the closure of the recirculation region. The presence of the radial stagnation contour near the centerline shows that the measured flow is slightly asymmetric, as expected in a real flow due to geometric misalignments and measurement offsets from the centerline. Additionally, the entrainment of mass into the swirling jet is shown by the regions of negative radial velocity outside of the OSL. The azimuthal velocity does not add much information to the picture; however, it should be noted that the region of strongest azimuthal velocity is near the nozzle exit. This region corresponds to the location within the r-z PIV field with the highest uncertainty as the increased azimuthal velocity results in loss of pairs from within the PIV measurement. Additionally, the apparent acceleration of the axial and radial velocity out of the nozzle exit are due to the bias error introduced by the high azimuthal velocity at the nozzle exit, as discussed in Chapter 2. However, at further downstream distances, the uncertainty is much lower, and the loss of pairs becomes negligible.

The last component of the flow field is the density, as demonstrated by the $\overline{c}$ contours in Figure 33. The $\overline{c} = 0.5$ contour shows that the time-average flame is anchored on the centerbody, in the wake region, and extends out into the jet. For this unforced case, the flame completely crosses the jet at a downstream distance of approximately $z/D = 2.3$. However, the axial spread of the distribution suggests that this jet crossing point is dynamic in nature. PLIF measurements show that this region is dominated by the combination of intermittent flames traveling upstream as well as large flame structures coupled to vortices

crossing the jet. Lastly notice that low axial distances and higher axial distances show noise in the time-average profile; this is due to the laser sheet intensity being approximately quadratic axially with a peak intensity around $z/D \approx 1.2$. Thus the signal to noise ratio in these regions is poorer than in the middle of the measurement domain.

The question remains of whether acoustic excitation causes any changes to the time-average flow field. Figure 34 shows a comparison of the velocity profiles taken at several different heights. These profiles show that there are no substantial differences in the time-average velocities or time-average flame progress variable when forcing is introduced. Also as expected from the contour plots, both the radial and azimuthal profiles go to zero at the centerline. The flame progress variable profile shows noise at low axial distances due to the laser sheet intensity variations. Additionally, comparing the progress variable on the right side of the measurement plane to that of the left shows the effect of experimental asymmetries on the flame.

The lack of any significant changes to the flow field is an argument against a non-linear response within the flow field. To illustrate this point, first expand the incompressible 2D u-momentum equation about a baseflow profile, denoted by subscript 0, using $u = u_0 + u_1$, $v = v_0 + v_1$, and $p = p_0 + p_1$. The subscript 1 denotes the harmonic response at the forcing frequency. This gives:

$$\begin{aligned} &\frac{\partial u_0}{\partial t} + u_0\frac{\partial u_0}{\partial x} + v_0\frac{\partial u_0}{\partial y} + \left(\frac{\partial u_1}{\partial t} + u_0\frac{\partial u_1}{\partial x} + v_0\frac{\partial u_1}{\partial y} + u_1\frac{\partial u_0}{\partial x} + v_1\frac{\partial u_0}{\partial y}\right) \\ &\qquad + \left[u_1\frac{\partial u_1}{\partial x} + v_1\frac{\partial u_1}{\partial y}\right] \\ &\qquad = -\frac{1}{\rho}\frac{\partial p_0}{\partial x} + \nu\frac{\partial^2 u_0}{\partial x^2} + \nu\frac{\partial^2 u_0}{\partial y^2} + \left(-\frac{1}{\rho}\frac{\partial p_1}{\partial x} + \nu\frac{\partial^2 u_1}{\partial x^2} + \nu\frac{\partial^2 u_1}{\partial y^2}\right). \end{aligned} \tag{3.1}$$

Here the first order terms are in parenthesis and the higher order terms are in brackets. Assuming that the baseflow is time invariant and taking the time-average of the equation, denoted by an overbar, gives the following expression:

$$u_0 \frac{\partial u_0}{\partial x} + v_0 \frac{\partial u_0}{\partial y} + \left[\overline{u_1 \frac{\partial u_1}{\partial x}} + \overline{v_1 \frac{\partial u_1}{\partial y}}\right] = -\frac{1}{\rho}\frac{\partial p_0}{\partial x} + \nu \frac{\partial^2 u_0}{\partial x^2} + \nu \frac{\partial^2 u_0}{\partial y^2}. \qquad (3.2)$$

This equation says that the time-average flow contains contributions from the perturbations. The fact that the flow field profiles shown in Figure 34 do not substantially vary despite the different forcing conditions suggests that the perturbations are very small, and that the linearity assumption may apply.

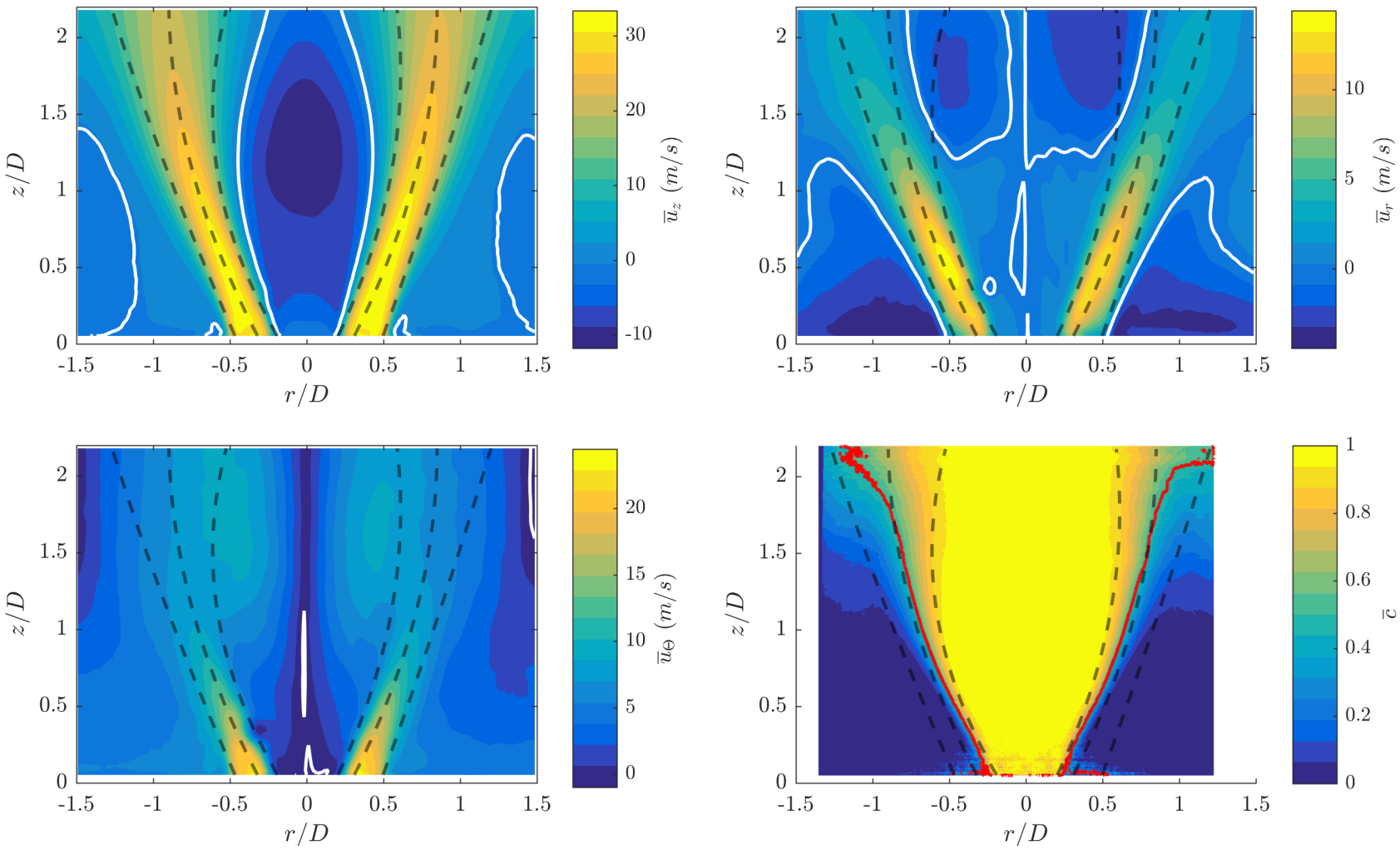

Figure 33 - Unforced *R-Z* time-average flow field at 25 m/s with ISL, OSL, and JC lines overlaid in dashed black, 0 contours in white, and $\overline{c} = 0.5$ in red.

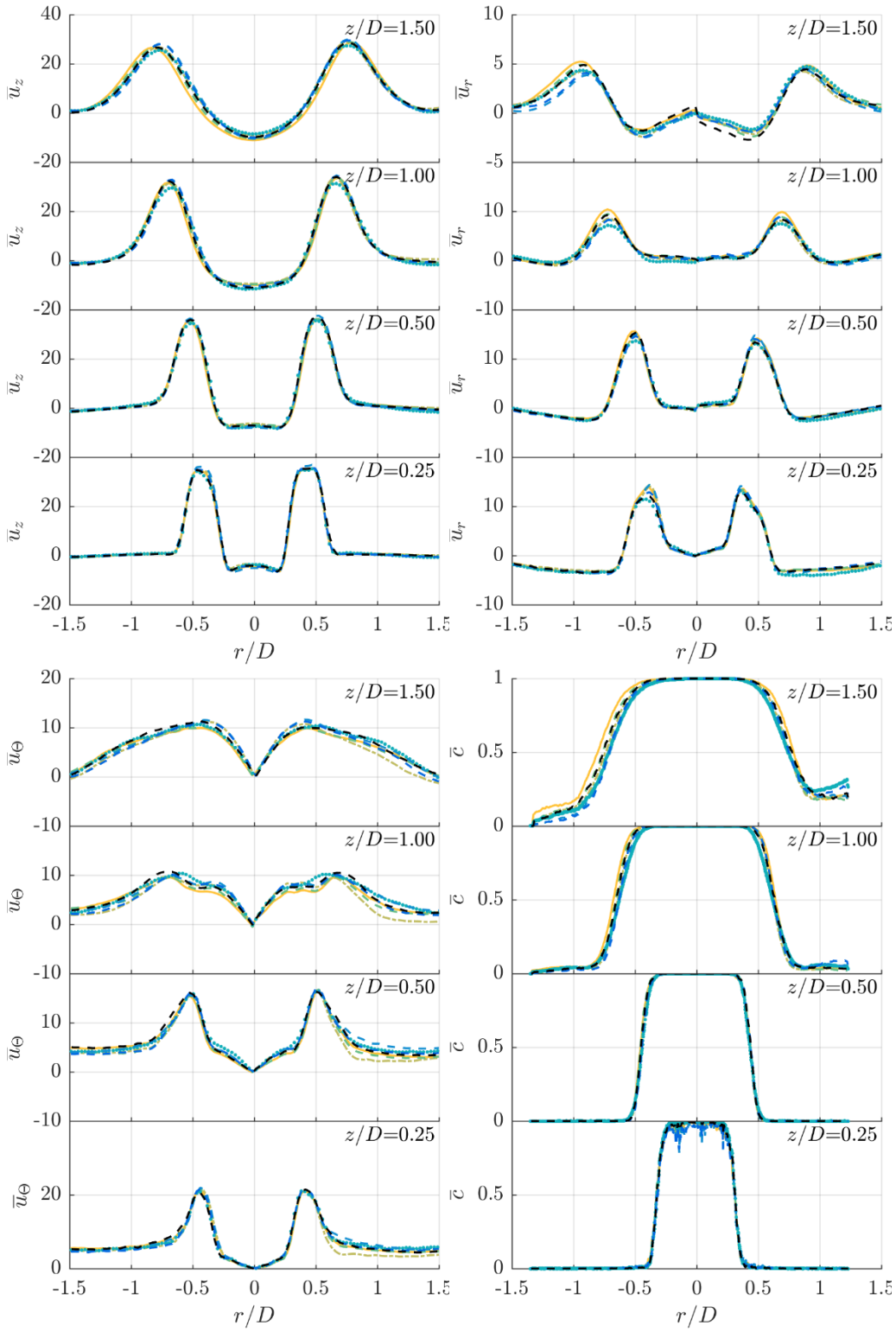

Figure 34 - Velocity and flame progress variable profiles for all forced cases at selected heights.

Figure 34 also shows that the azimuthal component of velocity does not go to zero at the approximate midpoint between nozzles ($r/D = 1.45$). One might initially expect the azimuthal velocity at the midpoint between two nozzles to go to zero (e.g., see Boehm *et al.*[119]) by symmetry arguments. However, this is only true if the nozzle flows are identical, which they are not due to the lifted nature of the outer flames; i.e., the outer two jets act as non-reacting jets in the near nozzle region. As shown in Figure 35, a key difference between the reacting and nonreacting jet is the wider jet spreading angle. This pushes the swirling flow outward in the reacting case.

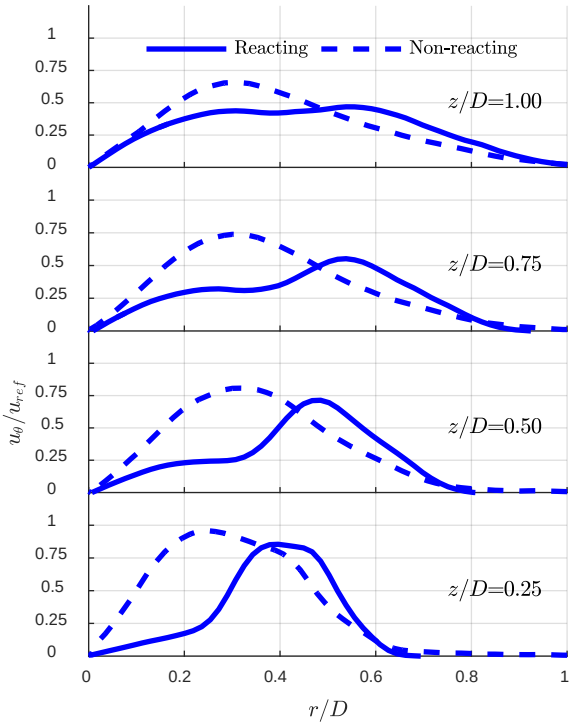

Figure 35 - Left-side azimuthal velocity profiles at multiple heights for unforced single nozzle configuration reacting and non-reacting conditions.

3.2 Forced Response for a Pressure Node

Having provided a description of the time-average r-z flow field, this section looks at the forced response of the swirl flow for the pressure node configuration (OP) for both the low (390 Hz) and high frequency (1170 Hz) cases. This section begins with a qualitative description of the flow response, then moves on to a quantitative analysis in r-z.

3.2.1 Qualitative Description

Figure 36a shows a series of instantaneous flame edges with the flow field overlaid for the 390 Hz OP forcing case. Figure 36b shows the same condition, but this time with phase-averaging of the flame and flow field from instantaneous data with a bin size of 10 degrees resulting in 138 samples averaged. The phase-averaged flame clearly shows the flapping motion caused by the forcing as alternating undulations on the left and right sides of the flame. The downstream convection of the flame wrinkles is also evident in the phase-averaged images. The large motion of the flame edge causes the jet to oscillate, and the region of large axial velocity to move in and out of the shear layer. This should result in large axial oscillations appearing in the shear layer. The instantaneous images are much less clear; however, as the flame edges contain many wrinkles due to turbulent, acoustic, and hydrodynamic content at all frequencies.

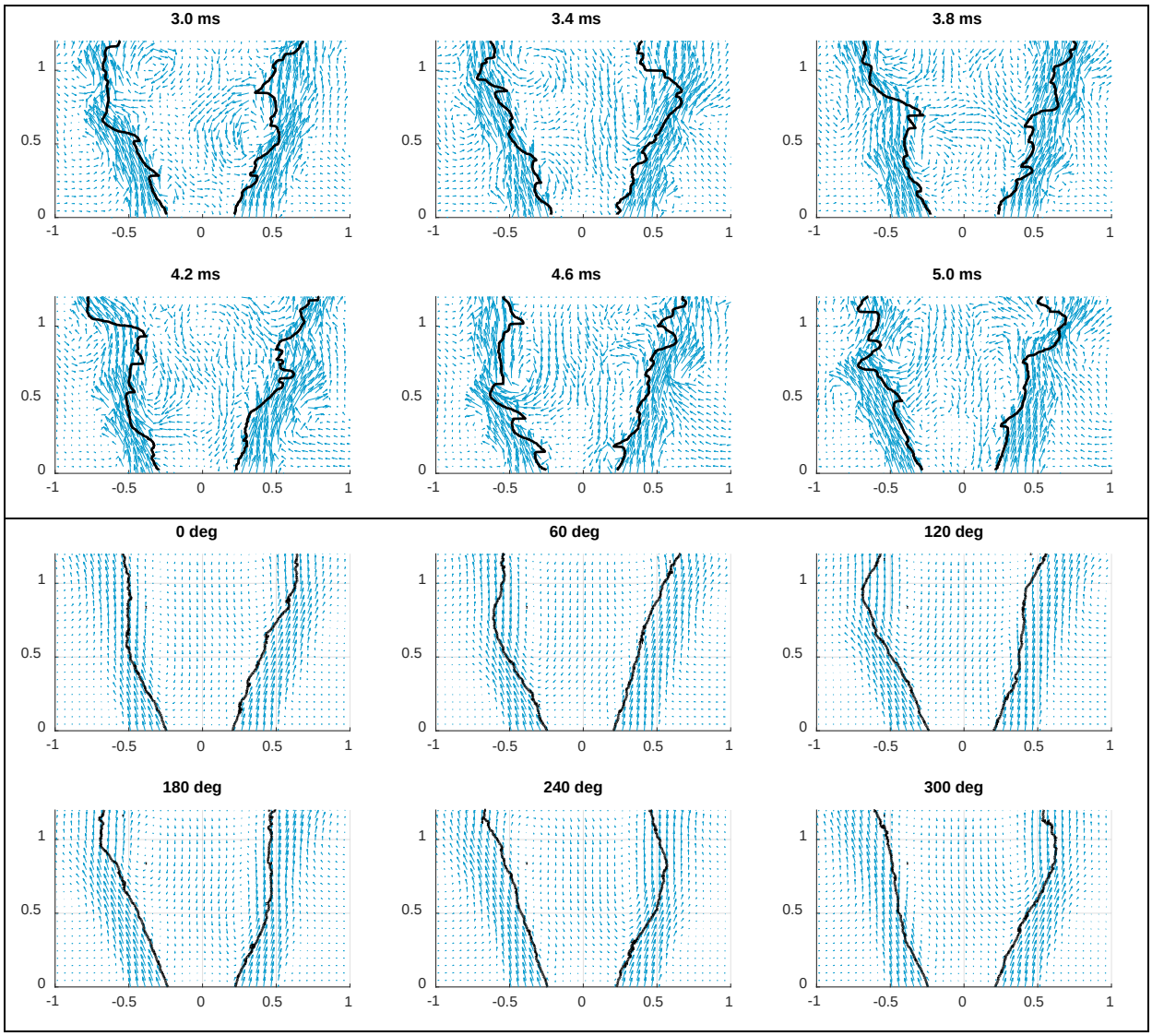

Figure 36 - Triple nozzle 390Hz OP forcing (top) instantaneous flame edge and velocity vectors (bottom) phase-averaged $\bar{c}$=0.5 and velocity vectors.

When viewed in the r-θ plane, the strong flapping motion from the r-z plane becomes a strong side-to-side movement of the jet. Figure 37 shows sequential overlaid OH PLIF and vector field images for the 390 Hz OP forcing case with the green line representing the outline of the OH signal at a time instant approximately half a cycle earlier (168 degrees). Near the nozzle exit the two lines are nearly coincident and circular, due to the flame nearly conforming to the shape of the circular centerbody where it is attached. Farther downstream, the strong side-to-side flapping of the flame and flow field is evident.

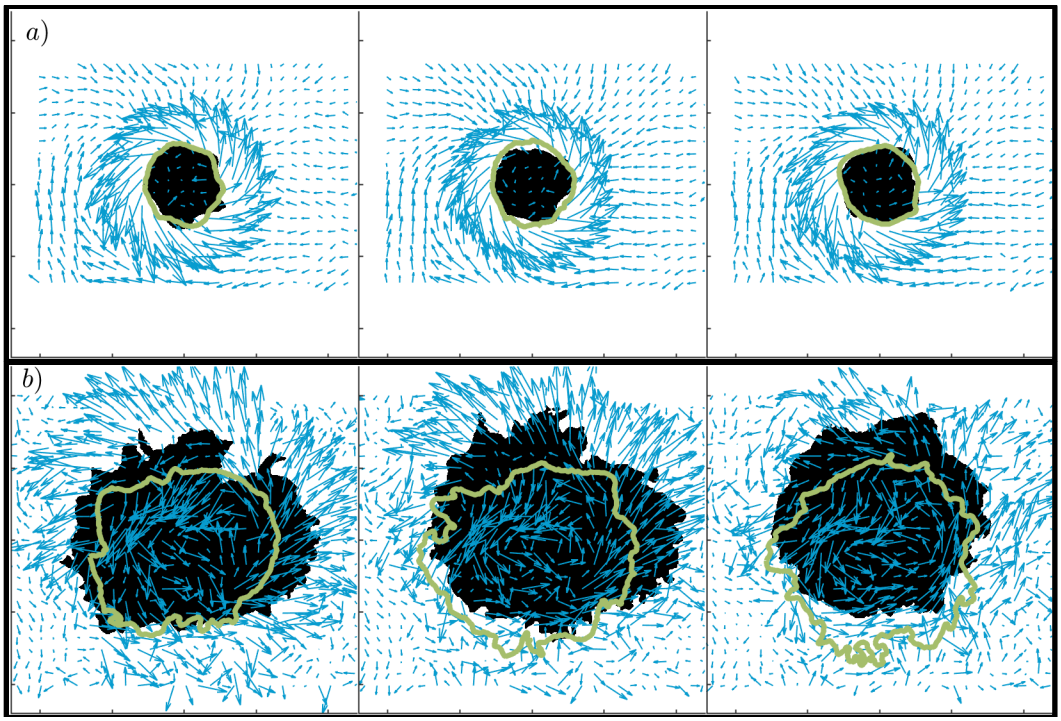

Figure 37 - Sequential OP forcing images in r-θ for (top) $z/D = 0.15$ and (botom) $z/D = 1.2$ showing velocity vectors and OH PLIF. The black region denotes the current OH PLIF signal while the green lines denotes its outline at a time instant 168 degrees earlier.

The strong side-to-side flapping motion is a manifestation of dominant $m = \pm 1$ modes, as quantified in Figure 38 and consistent with the discussion in the Introduction. Additionally shown are radially integrated reference coefficients, $\bar{B}_{ref,m}$, calculated from

$$\bar{B}_{ref,m} = \int_0^R \left|\hat{B}_{ref,m}\right| r dr, \tag{3.3}$$

where $\hat{B}_{ref,m}$ is calculated from a Jacobi-Anger decomposition taken from O'Connor et al. [26] and mentioned in Section 1.5. These helical disturbances manifest themselves as staggered vortices and asymmetric flapping of the flame sheet. Note how the amplitude of the higher order helical disturbances, such as $m = \pm 3$, are slightly larger than predicted by the model velocity field. Again, this is likely a manifestation of the fact that the data are taken at $z/D = 0.15$, where they have had some time to spatially develop. Additionally

this could be due to the random fluctuations associated with turbulence being captured by the decomposition. Finally, note the small but nonzero $m = 0$ mode, due to some inherent axial motions induced at the nozzle exit.

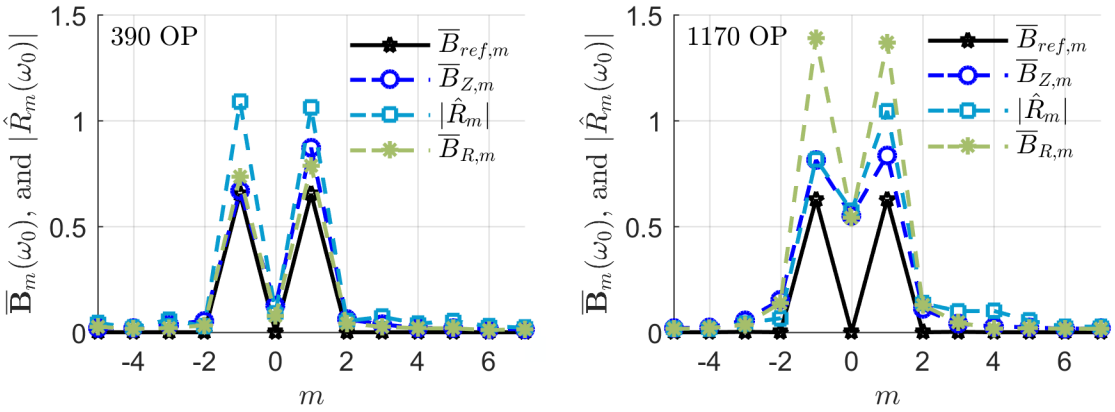

Figure 38 - Radially integrated helical mode coefficients of velocity fluctuations ($\overline{B}_m$) for the 390 Hz OP (left) and 1170 Hz OP (right) forcing cases ($z/D = 0.15$) and a scaled flame edge helical mode coefficient magnitude ($\widehat{R}_m$) compared to the scaled reference velocity function from the introduction integrated over the domain.

3.2.2 Quantitative Analysis in r-z

Having shown qualitatively the OP flame motion from both the r-z and r-θ perspectives and having established that this motion can be decomposed into helical modes, let us next look at the spatial distributions of the disturbances in the r-z plane.

Figure 39 shows the disturbance amplitude of the axial velocity, the radial velocity, the vorticity, and the progress variable field for the 390 Hz OP forcing case. Superposed on these fields are the time-average shear layer reference lines and time-average flame edge. The axial velocity shows clear disturbances within both the ISL and OSL. Not shown in this figure, the ISL and OSL axial disturbances act 180° out of phase from each other so that as the ISL increases, the OSL decreases. This phasing is consistent with the motion of

a flapping jet. Next look at the structure of the radial disturbances: disturbances appear in the ISL, OSL, and further downstream in the JC. The ISL and OSL disturbances at lower axial distances are vortical in nature, as displayed by the vortical disturbance map. Interference effects in the radial disturbance map between vortical disturbances and the acoustic disturbances are manifested as a decrease in the disturbance field response at $z/D = 1$, specifically the low amplitude regions outside of the OSL where destructive interference occurs. Beyond this axial location, the radial disturbances in the JC are primarily dilatational in nature as shown by the weak vorticity disturbance at these downstream locations. Dilatational disturbances are seen primarily in the radial component because the flame causes dilatation normal to its nearly vertical surface. Disturbances in the progress variable field follow the time-average flame edge and fall within the time-average shear layers, as expected as this region contains the reactants into which the flame is propagating. The smoothly growing width and amplitude of the disturbance region suggests that interference effects on the flame edge are not pronounced. The region of maximum amplitude, and potentially the most flame motion, occurs at an axial distance around $z/D = 1$. The flame edge will be presented later.

Figure 40 shows the same plot, but for the 1170 Hz OP forcing case. It is immediately apparent that the interference effects are important on the shown components of the velocity field; the axial velocity disturbances show broken structures due to the coupling of the vortical and acoustic disturbance fields while the radial component shows distinct nodal points on either side of the JC. For this case, the vorticity is located primarily in the OSL and then moves into the jet while the progress variable disturbances are located along the flame edge yet again. However, the progress variable disturbance regions show

a kink in width around $z/D = 0.6$ due to the interference effects between the acoustics and vortical disturbances. The lack of interference effects shown in the vorticity disturbance plot shows that acoustic interference effects may be reliably removed or ignored by looking at vorticity, showing only the underlying hydrodynamics of the flow field.

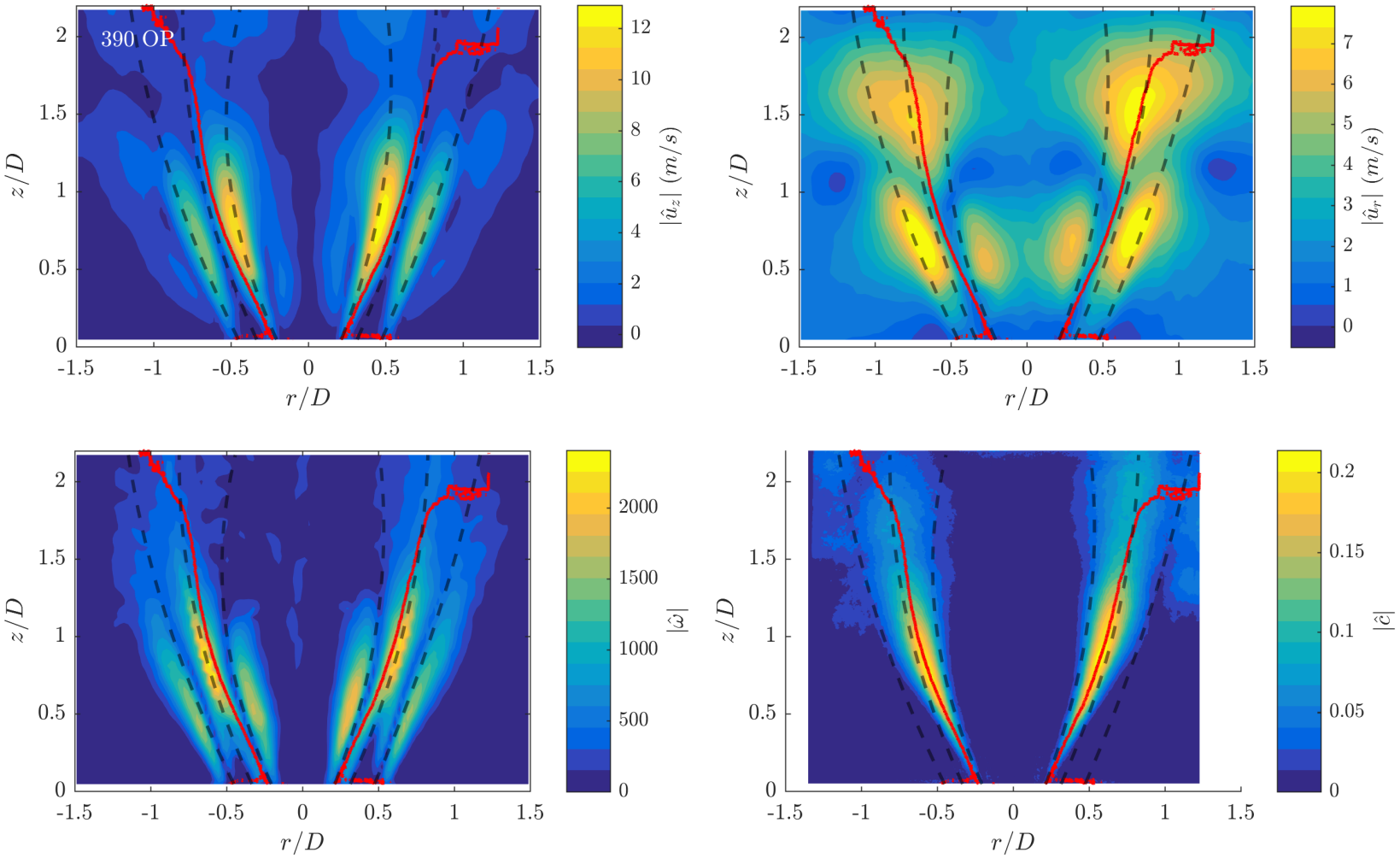

Figure 39 - 390 Hz OP disturbance field contours with time average ISL, OSL, JC overlaid in black and time-average flame edge in red.

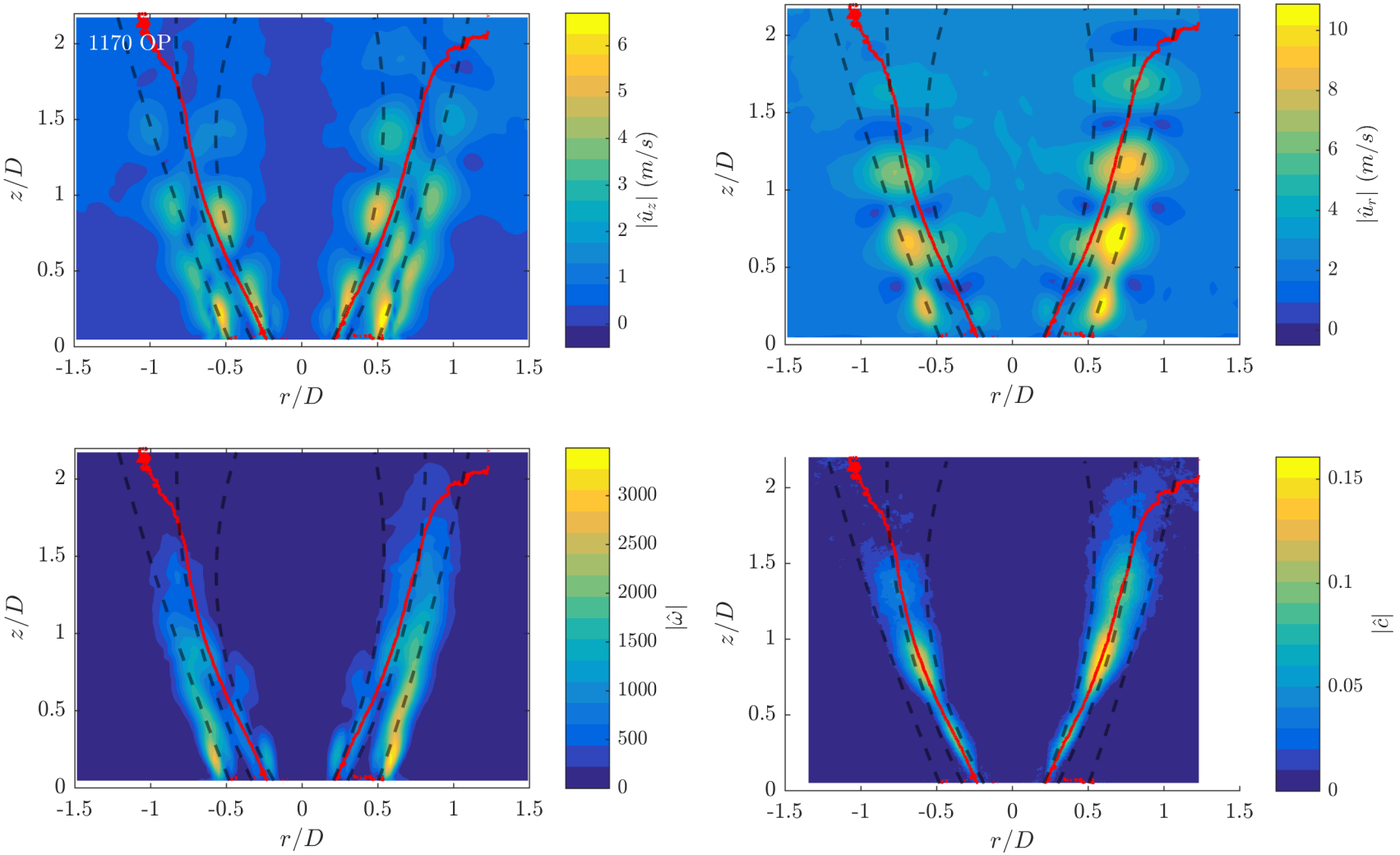

Figure 40 - 1170 Hz OP disturbance field contours with time average ISL, OSL, JC overlaid in black and time-average flame edge in red.

In order to look at the growth of mode shapes, a curve is fit to the maximum disturbance amplitudes for each disturbance on the left and right sides of the plane as a function of axial position. This gives an effective envelope for each disturbance. Figure 41 shows the disturbance magnitude envelopes of the axial, radial, vortical, and flame edge disturbances for the OP forcing cases. The 390 Hz forcing case, shown on the left, shows similar trends in the axial and vorticity envelopes, suggesting that the vorticity disturbances are the dominant contributions to the axial velocity disturbances. Additionally, as noted earlier, the radial disturbances show an interference pattern with a node near $z/D = 1$ due to the combination of the transverse acoustics and vortical disturbances. This interference node is present in the flame edge at a further downstream location, $z/D = 1.5$, suggesting a delay in the flame response to radial perturbations.

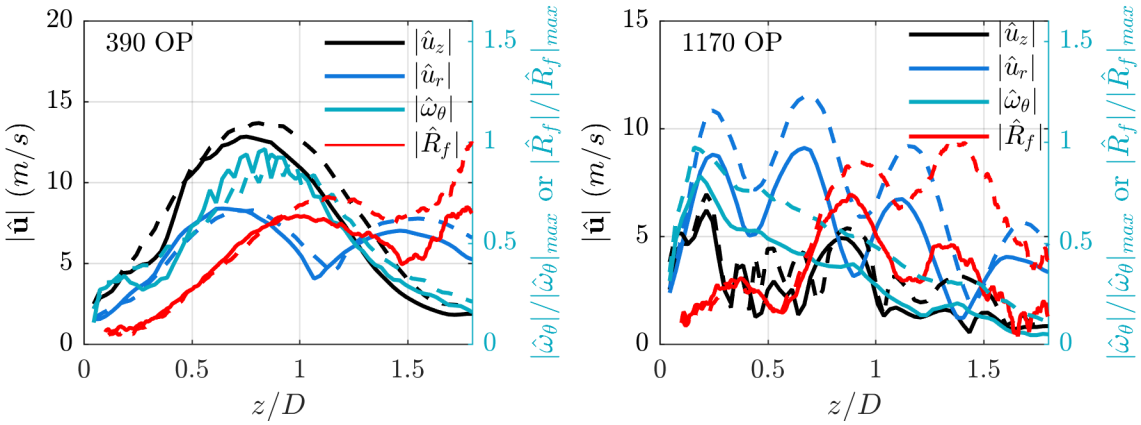

Figure 41 - Maximum disturbance amplitude for the left (solid) and right (dashed) sides of the r-z plane for the 390Hz OP (left) and 1170Hz OP (right) forcing cases.

The interference pattern is much more pronounced in the 1170 Hz OP forcing case shown on the right. The radial velocity profile and flame edge show peaks approximately every half diameter that are 180 degrees out of phase with each other. The magnitude of the vorticity disturbance monotonically decreases after a sharp peak at a low axial distances

($z/D = 0.15$) which corresponds to the height where the bias error of the flow out of the nozzle exit becomes negligible. The vorticity disturbance plot inherently ignores interference effects due to acoustics and shows that the amplitude disturbance of non-acoustic disturbances can be fairly well approximated using a simple function. Additionally, the left and right sides are not completely symmetric, suggesting that the flow field is experiencing an imperfect pressure node. Lastly, note that the axial disturbances have a noisy envelope in Figure 41 as there are no large-scale structures in Figure 40 for the maximum fit line to follow. In other words, the smoothed line of maximum disturbances jumps between structures in the contour plot and results in an incoherent axial velocity disturbance envelope.

Having considered the magnitude of the fluctuations, we next consider the axial dependence of their phase, as shown in Figure 42 along the disturbance envelope for the 390 Hz OP and 1170 Hz OP forcing cases. For 390 Hz OP, the phases all roughly fall along the same line with an average convection speed of approximately the mean flow velocity, 27 m/s, with the exception of the radial disturbance. The kink in the radial disturbance phase plot arises as the smoothed line fit to the maximum disturbance jumps between structures.

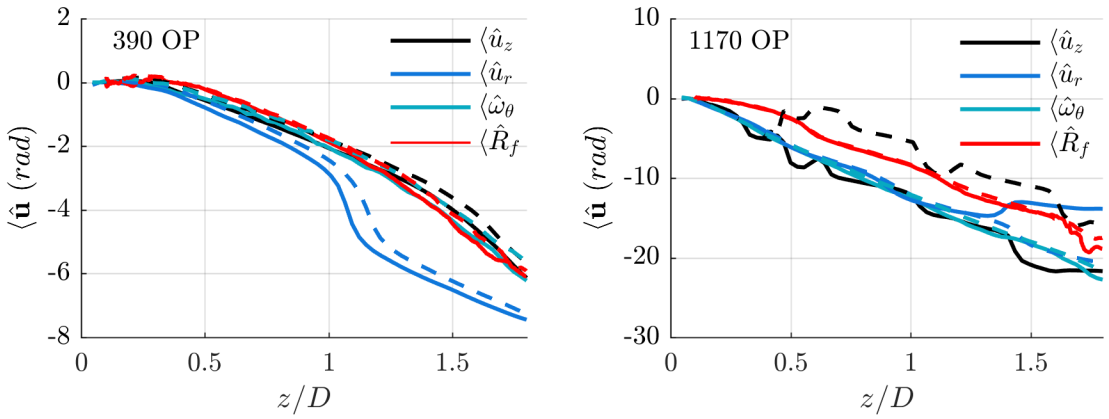

Figure 42 - Phase along maximum disturbance amplitude line for the left (solid) and right (dashed) sides of the r-z plane for the 390Hz OP (left) and 1170Hz OP (right) forcing cases.

To illustrate why the 390 Hz OP disturbances are convecting with the mean flow velocity, consider the jet to have a uniform velocity with a top-hat profile. The periodic flapping motion of the jet results in shear layer regions experiencing high axial velocity as the jet passes through that region. In other words, it is the periodic presence of the jet causing these disturbances. As these fluctuations are due to the inherent motion of the jet rather than any vortices, they convect with the mean flow velocity.

Next look at the phase plots of the 1170 Hz OP forcing case disturbances shown on the right in Figure 42. All of the phase lines show a near uniform phase speed of 21 m/s. The exception is the axial velocity which is not a coherent signal as discussed earlier. The fact that this phase speed is nearly constant and a fraction of the maximum jet velocity suggests that it originates from vorticity disturbances convecting in the shear layers. Figure 40 supports this hypothesis by showing a strong region of vorticity disturbance located exactly on the OSL, the same region picked up by all of the line fits. It is interesting to note that this phase speed is less than that of the 390 Hz OP, demonstrating that each mode has a frequency dependent convection speed. It also suggests that the two disturbances are

different in nature, possibly due to the 1170 OP vortical disturbances being stronger, as demonstrated by Figure 39 and Figure 40.

To briefly summarize this section, the pressure node, OP forcing cases experience a jet flapping motion. This motion can be described by a sum of $m = \pm 1$ helical disturbance modes. The vortical disturbances are strong and are located primarily in the shear layers and JC. Additionally, the flame edge can create dilatation disturbances, as in the 390 Hz OP case. Lastly the disturbance amplitude envelopes, once corrected for acoustics, show a simple growth and decay profile, and the disturbance phase speeds appear to be primarily linear.

3.3 Forced Response for a Pressure Anti-node without Axial Minimization

3.3.1 Qualitative Description

Next consider the pressure antinode, or IP, forcing case without any axial minimization. This forcing results in a symmetric pressure field across the nozzle and strong axial forcing of the nozzle acoustics (sometimes referred to as injector coupling), as described by Blimbaum et al. [27]. Additionally the motion induced on the flow field and flame edge are fundamentally different than the OP forcing case. Figure 43 shows a series of instantaneous flame edges take from OH PLIF images with the flow field overlaid for the 390 Hz IP forcing case. The behavior of the flame in the r-z plane seen in previous work is that the IP forcing case causes the two flame edges to move symmetrically towards and away from the centerline [26]. As the flame area modulates, the recirculation bubble also modulates and the left and right side OSL and ISL fluctuate in phase with each other.

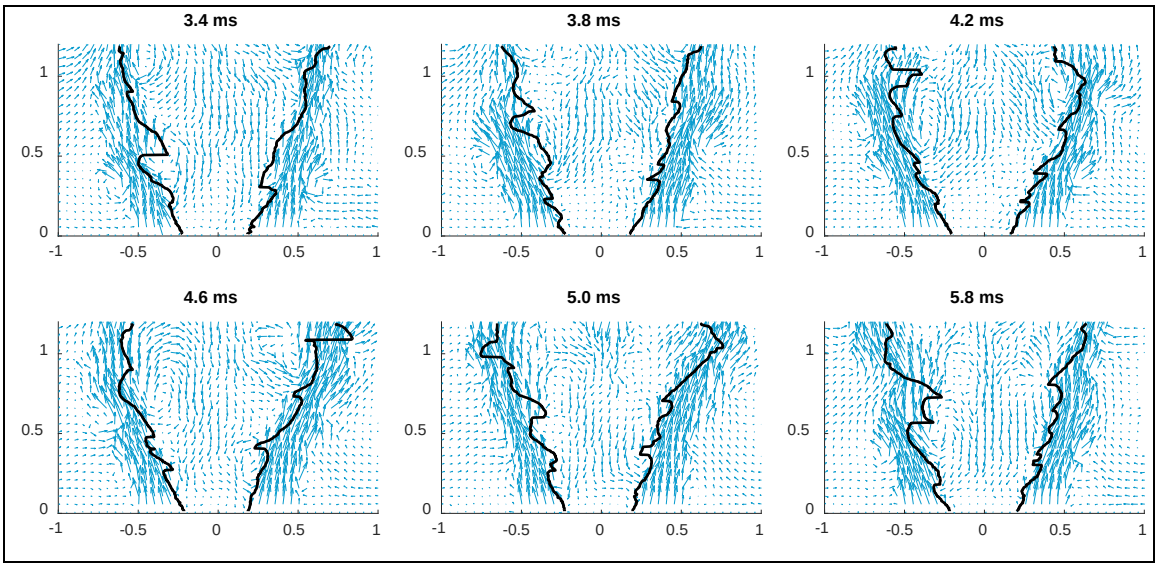

Figure 43 - Overlay of instantaneous flame edges and velocity vectors, triple nozzle configuration, 390Hz IP.

Consider this motion in the r-θ plane. Figure 44 plots a series of instantaneous vector fields and OH-PLIF images at different axial locations. The black region denotes the current OH-PLIF signal while the green line denotes the outline of the OH-PLIF region at a time instant roughly half a cycle earlier (more precisely, 168 degrees). The near coincidence of these two lines at the $z/D = 0.15$ location shows the relatively weak flame motion, due to flame attachment near the nozzle outlet. At the $z/D = 1.2$ location, however, the flame is clearly flapping in a nearly axisymmetric motion, as indicated by the significant differences in location between the two lines. In addition, there is clearly a significant degree of increased fine scale wrinkling.

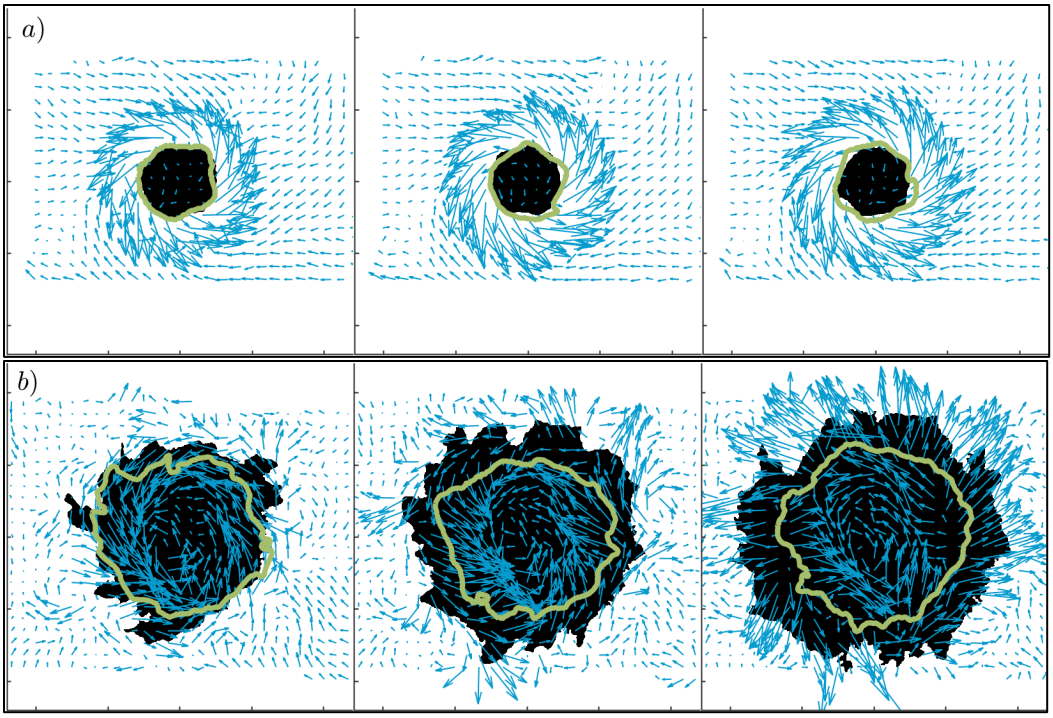

Figure 44 - Sequential IP forcing images in r-θ for (top) $z/D = 0.15$ and (bottom) $z/D = 1.2$ showing velocity vectors and binarized OH-PLIF. The black region denotes the instantaneous OH-PLIF signal while the green line denotes its outline at a time instant 168 degrees earlier.

Figure 45 shows the azimuthal mode decomposition of two velocity components, u_r and u_z, and the flame position, R_f, at a height of $z/D = 0.15$ for the IP forcing case from the non-interpolated data. Also overlaid for reference are radially integrated coefficients, $\bar{B}_{ref,m}$, from the Jacobi-Anger expansion shown in the earlier footnote.

These $\hat{B}_{ref,m}$coeffients give an estimate of the forcing provided by the acoustics to the hydrodynamic field. The data clearly shows the strong excitation of the $m = 0$ mode, consistent with prior measurements and predictions. The data also shows the presence of the weaker $m = \pm 2$ modes. While much weaker than the $m = 0$ mode, they are also much larger than suggested by the reference line, which is an indicator of the relative excitation that the acoustic disturbance provides to each mode. This may be a reflection of the fact

that these modes have had some spatial distance to develop (i.e., the data is taken $0.15D$ downstream from the nozzle outlet) or that there are "imperfections" of the acoustic excitation field relative to the model one-dimensional field, $\sin kx$, used for the reference coefficient calculation. The other azimuthal modes are nonzero, presumably a manifestation of the turbulent fluctuations in the flow. Nonetheless, it is the strong $m = 0$ oscillations which lead to axisymmetric disturbances convecting downstream in the shear layers, similarly causing strong axisymmetric wrinkling of the flame.

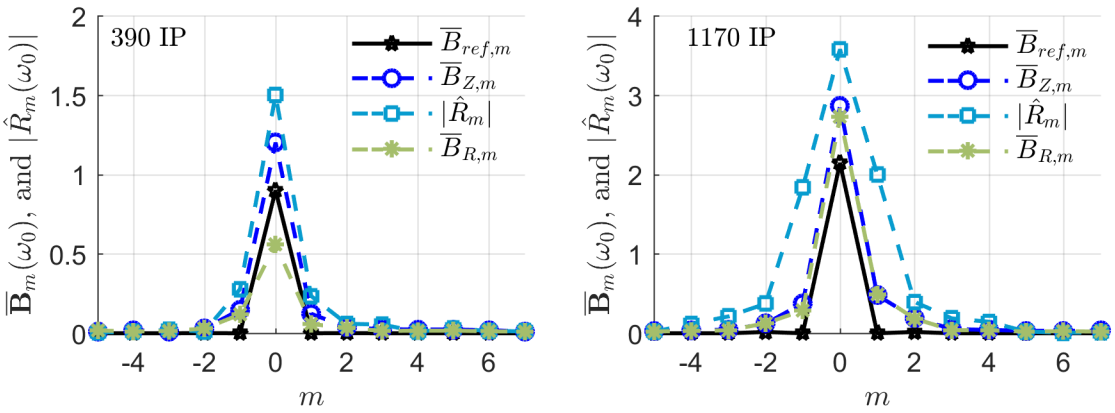

Figure 45 - Radially integrated helical mode coefficients of velocity fluctuations ($\overline{\mathbf{B}}_\mathbf{m}$) for the 390 Hz IP (left) and 1170 Hz IP (right) forcing cases ($\mathbf{z/D = 0.15}$) and a scaled flame edge helical mode coefficient magnitude ($\widehat{\mathbf{R}}_\mathbf{m}$) compared to the scaled reference velocity function from the introduction integrated over the domain.

The resulting heat release excited by these hydrodynamic flow disturbances depends strongly upon which helical mode is present. Phase cancellation from different azimuthal locations causes helical modes to excite minimal heat release oscillations when they are integrated azimuthally, even though they may excite strong flame flapping. Rather, the spatially integrated heat release is most affected by axisymmetric, $m = 0$ disturbances [47]. This can be seen by considering the integral $\int e^{im\theta} d\theta$ and noting that it is only

nonzero for $m = 0$. In other words, the dominant hydrodynamic mode exciting heat release oscillations and local flame wrinkling is different [22, 23, 28, 29].

3.3.2 Quantitative Analysis

Next consider the disturbance field maps for the 390 Hz IP forcing case shown in Figure 46. The expectation from the helical decomposition is that the disturbance fields should be dominated by axisymmetric disturbances appearing as symmetric disturbances on the left and right sides of the r-z plane. Clearly the symmetry does not appear in the axial and radial velocity fields. However, it should be noted from Figure 45 that there is content at the $m = \pm 1$ as well as at the $m = 0$ mode. The symmetric and antisymmetric components about the centerline can be decomposed into helical modes as

$$\begin{cases} \widehat{\boldsymbol{u}}_{sym} = \sum_{m=even} \widehat{\boldsymbol{B}}_m \exp(-im\theta) \\ \widehat{\boldsymbol{u}}_{ant} = \sum_{m=odd} \widehat{\boldsymbol{B}}_m \exp(-im\theta) \end{cases} \tag{3.7}$$

showing that the even modes, such as the $m = 0$ mode, are responsible for the symmetric response while the odd modes are responsible for the antisymmetric response. In other words the disturbance fields will not be perfectly symmetric due to the presence of the odd helical modes. Helical mode decompositions at higher axial locations confirm this by showing that the $m = \pm 1$ helical modes are on the same order of magnitude as the $m = 0$ mode.

Having noted the asymmetry of the disturbance fields in Figure 46, next look at their shapes. Similar to the OP forcing case at 390 Hz shown in Figure 39, the axial velocity disturbances are located within the shear layers while the radial component, due to

dilatation, is centered in the JC at further downstream locations. The vorticity disturbance and progress variable contour disturbances also take a similar shape to the OP case, suggesting that the mode shapes of the disturbances are more dependent on frequency than on the helical mode numbers describing the flow field.

Figure 47 shows the corresponding disturbance fields for the 1170 Hz IP forcing case. The first thing to notice is that the disturbance fields for this case are symmetric about the centerline. This suggests that the even modes are dominant throughout the entire flow field. Yet again, the disturbances in the IP forcing field are located in similar positions to those in the OP forcing field shown in Figure 40, but with fewer interference effects present. Specifically the vorticity disturbances and radial velocity disturbances are centered in the OSL with the radial disturbances showing a weak interference pattern, likely a manifestation of small deviations from the model IP acoustic field. Lastly the progress variable disturbance field does not show any interference pattern effects, unlike in the OP case. This is because the flame edge experiences weak radial disturbances due to the forced transverse acoustic velocity node.

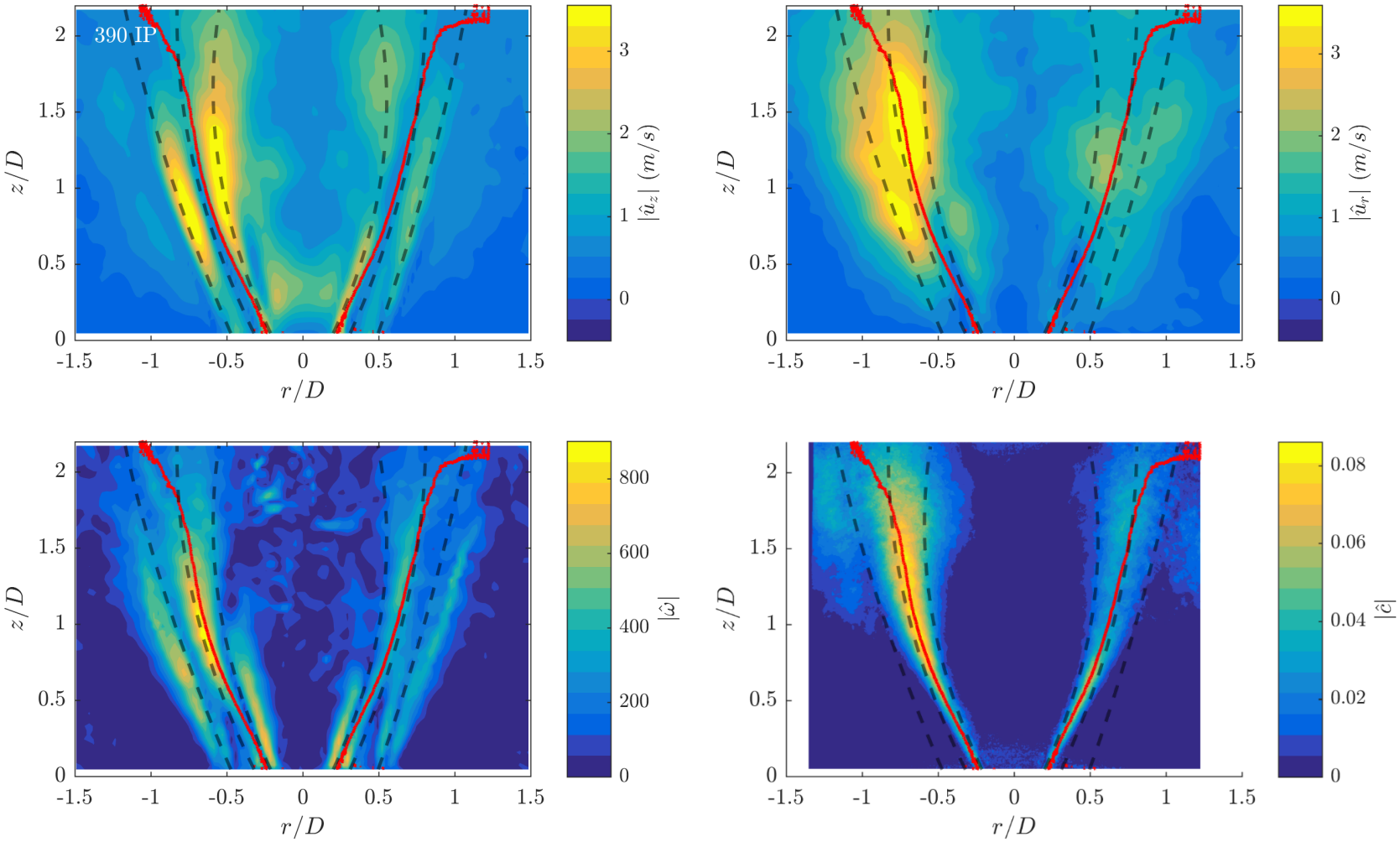

Figure 46 - 390 Hz IP without longitudinal minimization disturbance field contours with time average ISL, OSL, JC overlaid in black and time-average flame edge in red

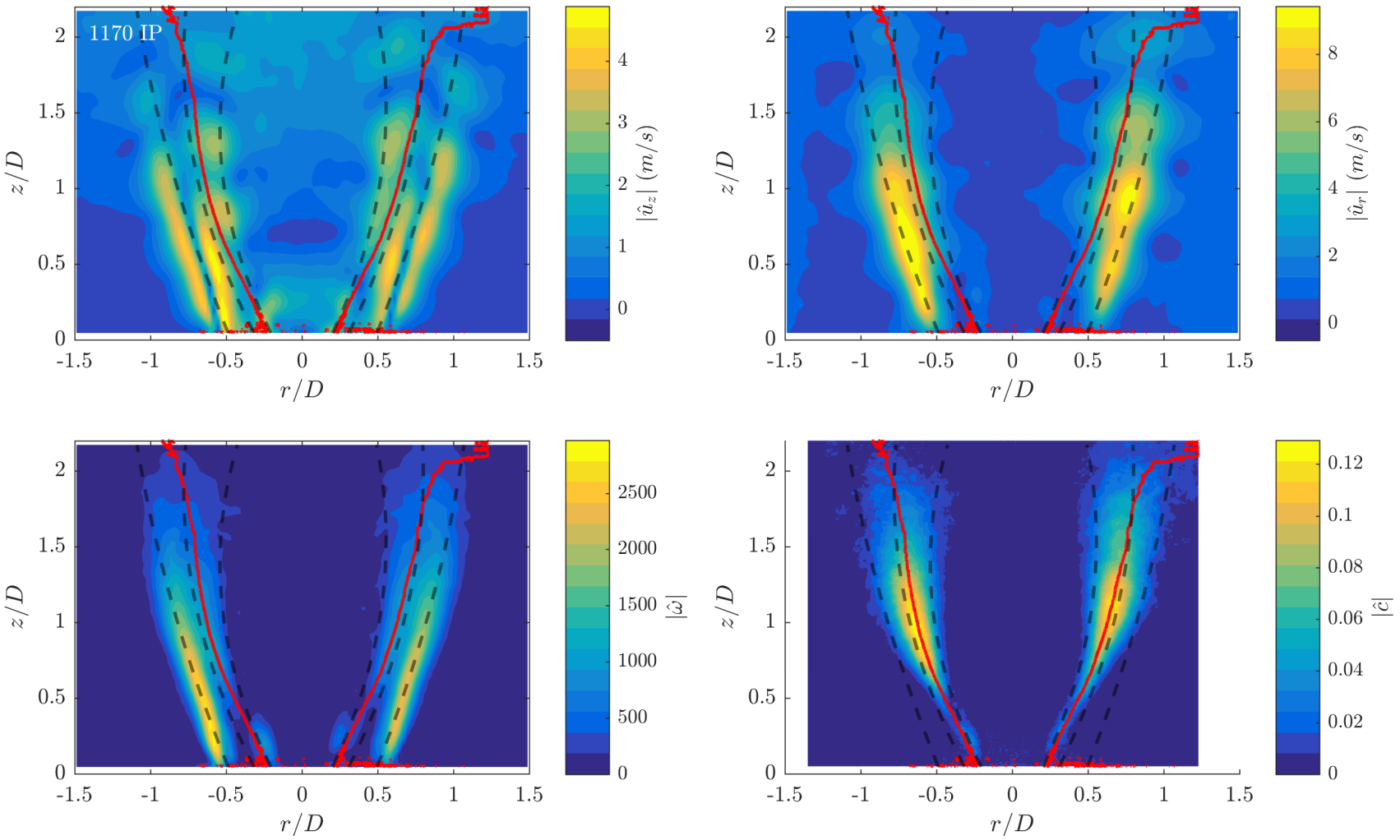

Figure 47 - 1170 Hz IP without longitudinal minimization disturbance field contours with time average ISL, OSL, JC overlaid in black and time-average flame edge in red.

Next consider the disturbance envelopes shown in Figure 48. As expected from the disturbance field plots in Figure 46, the 390 Hz IP envelopes are both chaotic and much stronger on the left side than the right side. Additionally the left side flame edge fluctuations show a much stronger oscillation than those of the right side, gradually increasing with downstream distance. The left side vorticity disturbance shows a decrease at $z/D = 0.6$ as it jumps between mode shapes, but stays nearly constant. The other disturbance envelopes are shown for completeness despite their incoherence.

The 1170 Hz IP case, however, is much better behaved. The radial velocity and normalized vorticity disturbances are nearly symmetric and show peaks at low axial distances after which they experience a gradual decay. This trend is similar to the one observed in Figure 41 for the 1170 Hz OP case but with smaller interference effects on the radial velocity. The axial velocity for this case, is much more coherent than for the previous case as well, with a more consistent profile even though the line switches between regions of high amplitude. The normalized flame edge fluctuations also show a drastic increase in magnitude, rather than a gradual increase as demonstrated by the 390 Hz IP case.

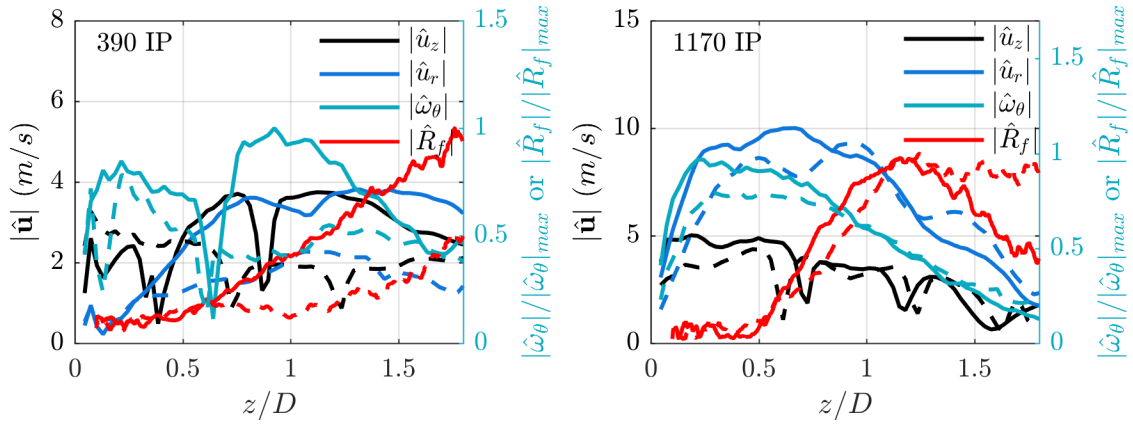

Figure 48 - Maximum disturbance amplitude for the left (solid) and right (dashed) sides of the *r*-*z* plane for the 390Hz IP (left) and 1170Hz IP (right) forcing cases both without axial minimization. Vorticity and flame edge fluctuations are normalized by their maximums.

Looking at the phase speeds in Figure 49, it is clear that both cases have a near constant phase speed. The sudden changes in phase are due to the line fit moving between regions of high amplitude disturbances. This is primarily a problem for the axial disturbances at both frequencies. For the 390 Hz IP case, the phase speed is approximately 17.1 m/s, and for 1170 Hz IP it is 21.1 m/s. These plots show that a simple function, such as a line, can be used to estimate the phase speeds where there is a coherent disturbance.

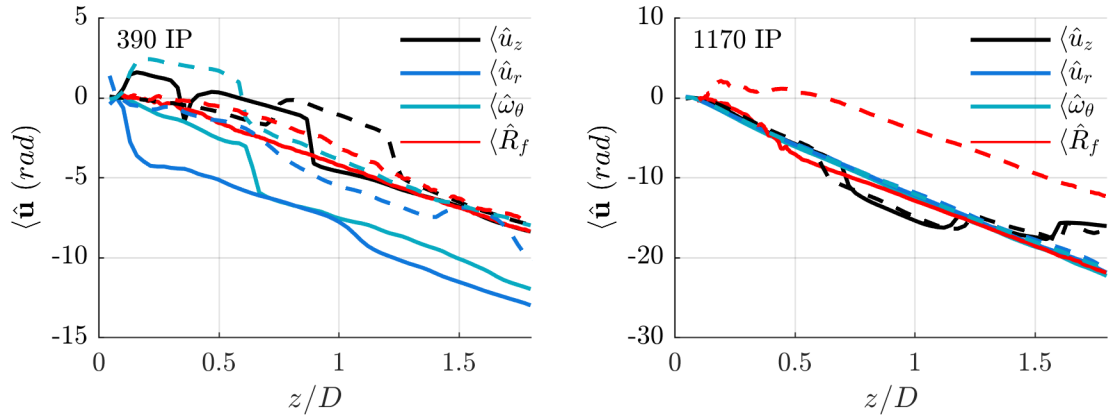

Figure 49 - Phase along maximum disturbance amplitude line for the left (solid) and right (dashed) sides of the *r*-*z* plane for the 390Hz IP (left) and 1170Hz IP (right) forcing cases both without axial minimization.

The disturbance fields show that the disturbances typically follow curvilinear lines in the r-z plane. When the interference effects are corrected for, the disturbance envelopes follow relatively simple trends. The phase plots for these disturbances also show that the phase can be approximated fairly well with a constant phase speed when there is a coherent disturbance. Finally, this section has shown that the spatial response of the flow field amplitude is similar between IP and OP forcing configurations. This suggests that each region of the flow field has its own sensitivity to external forcing; in other words, each shear layer has its own preferential frequency.

3.4 Forced Response for a Pressure Anti-node with Axial Minimization

The IP forcing case without axial minimization was characterized in the previous section. We showed that the measured helical mode content of that forcing case was primarily axisymmetric near the nozzle, and that it could be predicted in a straightforward way. Figure 50 shows the measured helical mode content for the axially minimized pressure antinode case at the two frequencies of interest near the nozzle exit compared to the non-minimized cases. It is apparent that the axisymmetric mode has been reduced for both cases in both the flow field and the flame while the other helical modes remain nearly unaffected. We noted in Chapter 2 that the 1170 Hz IP case with axial minimization was not repeatable; however, despite this fact, the figure shows that the minimization does in fact reduce the response at the nozzle exit.

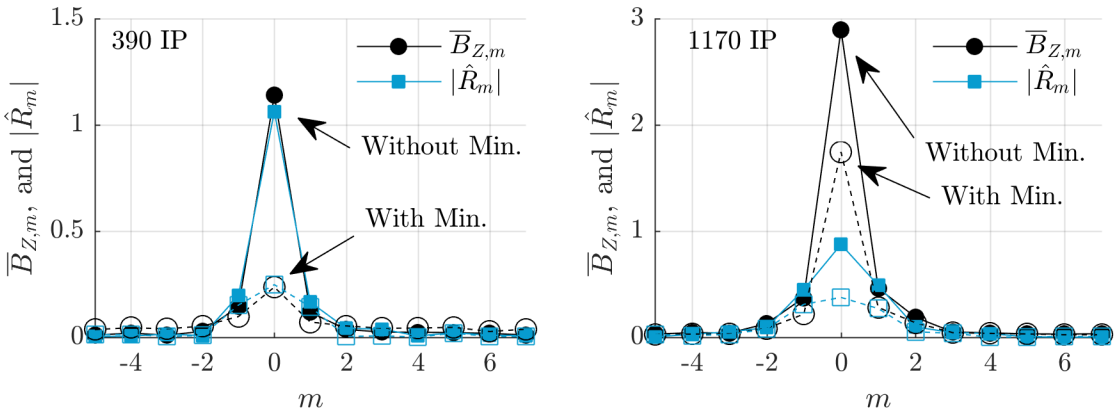

Figure 50 - Overlay of average axial PAM coefficient and scaled flame edge PAM coefficient with (dashed) and without (solid) minimization at an axial height of $0.15\ z/D$ for 390 Hz IP (left) and 1170 Hz IP (right).

Next look at the r-z disturbance fields in Figure 51 and Figure 52. As expected, these disturbance fields look similar to the IP forcing case without any axial minimization, but have a smaller amplitude. In other words, for the 390 Hz IP forcing Figure 46 showed axial disturbances with a maximum magnitude of approximately 3.5 m/s while Figure 51 shows axial disturbances with a maximum magnitude of approximately 1.8 m/s. The same is true for the 1170 Hz IP with axial minimization case despite its incomplete minimization.

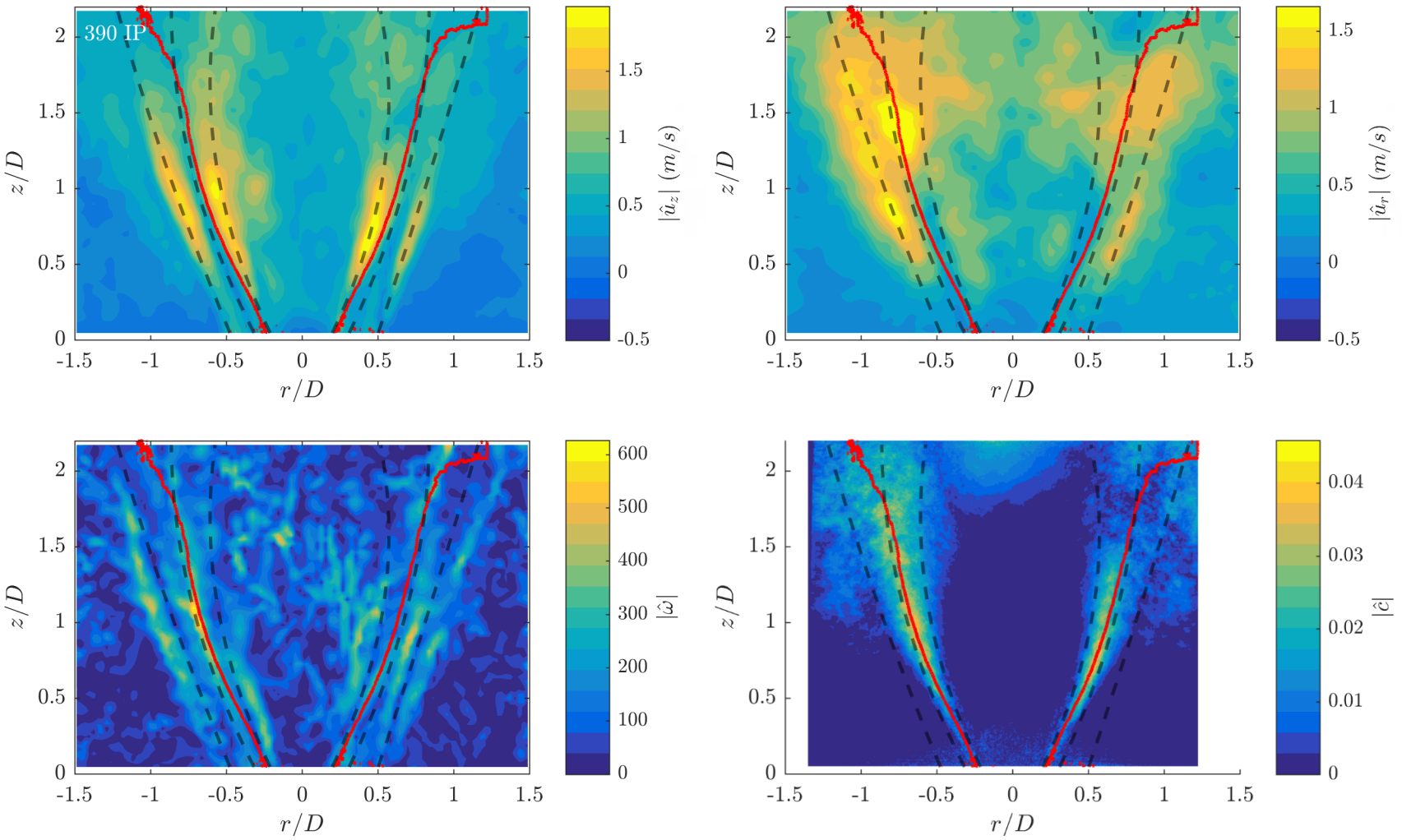

Figure 51 - 390 Hz IP with longitudinal minimization disturbance field contours with time average ISL, OSL, JC overlaid in black and time-average flame edge in red.

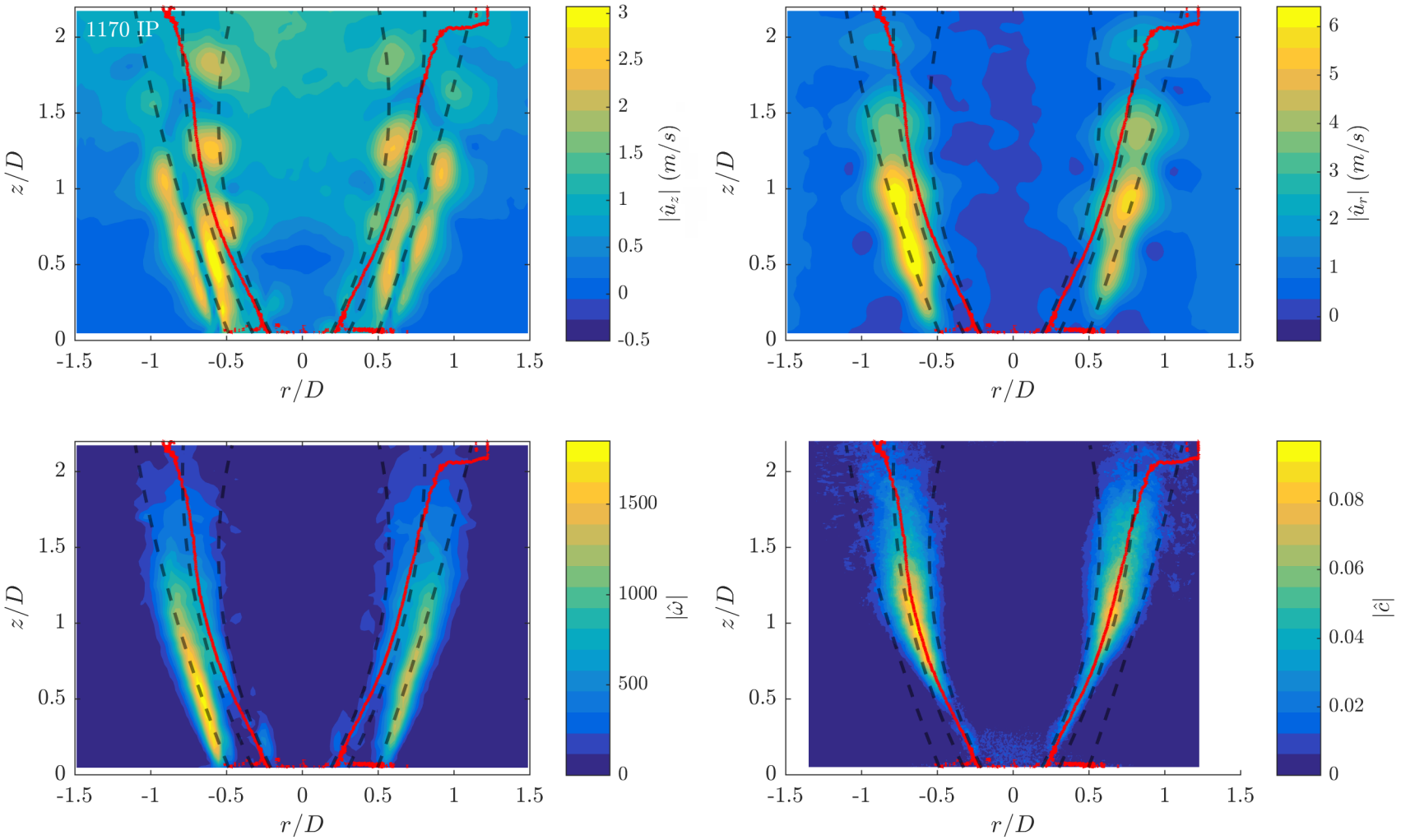

Figure 52 - 1170 Hz IP with longitudinal minimization disturbance field contours with time average ISL, OSL, JC overlaid in black and time-average flame edge in red.

This brief discussion of the axially minimized flow field shows two things. First it shows that the axially minimization reduces the axisymmetric response at the nozzle, as expected. The significance of the reduced axisymmetric response is that it should also reduce the heat release response of the flame and flow field. This is investigated further in Chapter 5. Second this section showed that the overall flow field response is reduced when axial minimization is introduced. This suggests that the longitudinal coupling has a strong impact on the flow field response to transverse acoustic waves.

3.5 Chapter Summary

This chapter presented the time-averaged swirl flow field and its response to acoustic forcing. It was shown that the effects of acoustic forcing were minimal on the time-averaged flow field, suggesting that the resultant perturbations are linear. The analysis of the pressure node forcing case showed that OP forcing resulted in odd helical modes and antisymmetric disturbances about the centerline. In contrast, the pressure antinode forcing case showed that IP forcing results in even helical modes, primarily the axisymmetric $m = 0$ mode, which are symmetric about the centerline. However, the measured response to IP forcing appeared to deviate from the symmetric prediction suggesting the presence of strong odd helical modes. Additionally, interference effects due to convecting vortical disturbances and acoustic disturbances were present in both the IP and OP forcing cases. It was shown through vorticity disturbances that when the interference effects are accounted for, the envelopes of the mode shapes take on simple profiles. Next it was shown that the phase of the convecting disturbances could be approximated by a linear function. Oddly, a comparison between the IP and OP forcing cases showed that the different forcing

configurations excited the same regions of the flow field for a given frequency. This suggests that these regions of the flow field are sensitive to the given frequencies or wavelengths of excitation. Finally it was observed that the effect of axial minimization was twofold: 1) the axisymmetric content was reduced throughout the flow field and 2) the entire flow field response was significantly reduced. These observations will be applied in the discussion of the novel interpolation technique of Chapter 4.

CHAPTER 4. A NOVEL HELICAL MODE INTERPOLATION METHOD

As mentioned in Chapter 2, sPIV and OH-PLIF measurements with the same forcing frequency were obtained along five planes – one r-z plane and four r-θ planes, as illustrated in Figure 53. The r-θ measurements are particularly useful, as they allow us to determine the amplitude and phase of all helical modes, $\widehat{\boldsymbol{B}}_m(r, z, \omega)$ at that z location. However, since these measurements are only obtained at four different z locations, there are also a number of questions about how these modes evolve between measurement planes. In contrast, the r-z planar measurement has information on the velocity field/flame position at every z location, but it is not possible to determine the relative amplitude of the different helical modes that are being superposed to give the resultant measurement. This section describes an interpolation approach to resolve the z distribution of the $\widehat{\boldsymbol{B}}_m(r, z, \omega)$ coefficients as well as its results for each forcing configuration, with the exception of the 1170 Hz IP with axial minimization case.

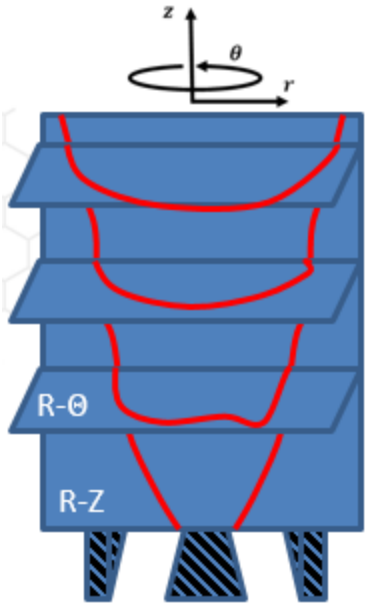

Figure 53 - Illustration of different measurement planes within a swirling, reacting flow field.

4.1 Interpolation Approach

4.1.1 Impact

With the overall goal of identifying and reconstructing helical modes within a volume, several methods have been used already in literature. The first method assumes an axisymmetric flow. Caux-Brisebois et al. [120] used a method that only requires measurements in the r-z plane. The idea is to take phase-reconstructed content and equate the phase with the azimuthal position of the measurement so that the r-z plane is rotated about the centerline of the combustor. This method was demonstrated on data from a single nozzle swirling flame within a cylindrical confinement, taken at the German DLR facility. The authors first used a proper orthogonal decomposition (POD) to remove the turbulent fluctuations from the velocity field. The flow field was then phase-averaged at the desired

frequency, and coherent structures were identified within the domain. The strength of this method lies in its simplicity; it only requires one measurement. However, this method is only applicable for axisymmetric flow fields and flames.

A second method utilizing only one r-z plane and one r-θ plane was developed in Oberleithner et al. [69]. This paper looked at an axisymmetric flow field, identified the azimuthal modes from within the r-θ plane, and then estimated their downstream growth through a linear stability analysis. This method is powerful as it is physics based and gives insight into the growth of these modes; however, this method is not truly data driven as the predicted axial modes do not necessarily capture the measured response in the r-z plane.

An additional method for interpolation that uses all of the data is a neural network learning algorithm. Pruvost et al. [121] demonstrated how this methodology could be applied to an experimental flow measured using PIV. However they used the PIV data to train the algorithm with only a two component r-z measurement and achieved very poor results. More recently, Ahmed et al. [122] analysed different adaptive learning methods in predicting the time-average flow and turbulent statistics of a swirl combustor. They used velocity field data taken using a direction sensitive laser Doppler velocimetry (LDV) measurement for both training and as the input. They found that the adaptive learning methods well predicted the turbulent statistics and mean flow profiles. This method is very promising for future work, but the downside is that some of the data needs to be sacrificed to properly train the neural network.

Interpolation methods based on the Navier-Stokes equations have also been used on various flow fields. For example, Acharya et al. [85] utilized this method to estimate all

velocity components from two-component PIV data in an r-z plane and r-θ planes for a swirling flow field. This method shows promise and is a robust physics based method for interpolating the data. However, it will be shown next that a simpler algorithm based on a linear least squares approach works very well.

The linear least squares method is a simple algorithm that can be adapted to any flow field. Assumptions can be added as needed, and with the proper model functions, it will capture the mean flow field and the flow field dynamics. Additionally this method allows for different data points to be considered with different weightings so that points with higher uncertainty have less effect. The methodology used in the next section makes the assumption that the appropriate basis functions for a swirling flow field are helical modes. These helical modes can capture deviations from axisymmetry in the mean flow field and in the phase-averaged flow field making this method applicable to non-cylindrical geometries. However, it is expected that expanding the methodology to multinozzle flows will introduce additional error; here only the center nozzle is interpolated. Additionally the axial basis functions utilized have a theoretical limit based on the number of r-θ planes, and the axial phase speeds of non-dominant helical modes are not well calculated. Lastly the fit is performed on a curvilinear coordinate system so that basic series can be used to describe the flow field, separating the axial and radial dependences. Despite these caveats, the linear least squares method proves to be a powerful tool that has advantages over all of the other methods.

4.1.2 Linear Least Squares Methodology

The measured velocity field can be decomposed into a time-averaged component, a coherent component at the forcing frequency and its harmonics, and the remaining, largely turbulent, component. The coherent component contains the superposition of acoustic and vortical (hydrodynamic) disturbances. Because the phase speeds of the acoustic and hydrodynamic disturbances are so different, their superposition manifests itself as clear interference patterns in the magnitude of the velocity fluctuations. To illustrate this, consider the sum of two disturbances with different axial phase speeds and amplitudes,

$$u'_{total} = \left[A_1\, e^{-ik_1 z} + A_2\, e^{-ik_2 z}\right] e^{i\omega t}. \tag{4.1}$$

If we take $A_1 = 1 - z^2$, $A_2 = 0.5$, $k_1 = 0.25$, and $k_2 = 10$, then the resultant envelope, $|u'_{total}|$, over the domain $z \in [-1,1]$ looks like Figure 54. The specific values were chosen as the acoustic disturbance has a long wavenumber and small but nearly constant amplitude while the convective wavenumber is smaller and has a spatially varying amplitude. Note that the peaks in the envelope of the total disturbance appear periodic.

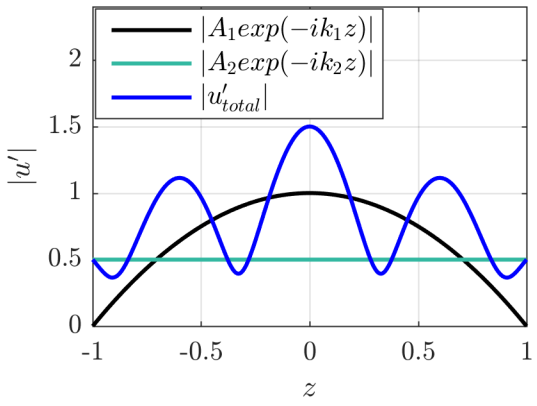

Figure 54 – Illustrated interference pattern.

In order to focus on the hydrodynamic disturbances, the acoustic contribution was estimated and subtracted from the Fourier coefficients, using a similar method to O'Connor

and Lieuwen [104]. Given that the IP forcing case measured the center nozzle at a velocity node, the transverse acoustic contribution to this case was negligible, and thus the technique was only applied to the transverse acoustics of the OP case. All OP data presented from this point forward will have the acoustic velocity component subtracted unless explicitly noted. As the transverse acoustic wave was nearly one-dimensional in nature, the transverse acoustic subtraction was only performed on the radial and azimuthal components of the flow field. The acoustic field was approximated by fitting a spatial sinusoidal function to the measured velocity field, at locations outside of the jet where the acoustic fluctuations dominated. Figure 55 shows the measured data and that with the acoustic subtraction performed on the OP case, showing the clear reduction of the interference pattern. The results are plotted along the shear layer lines and jet core defined in Chapter 2, Figure 27. The velocity envelopes in the shear layers still show some modulation, suggesting local deviations from the model acoustic field.

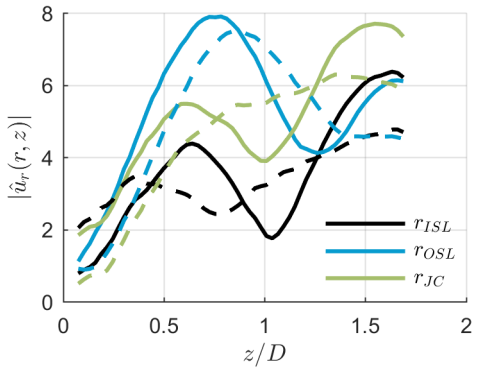

Figure 55 - Magnitude of transverse velocity fluctuations take from *r*-*z* data along ISL, OSL, and JC without (solid) and with (dashed) acoustic subtraction for the 390 Hz OP case.

The basic approach is to use a set of radial, azimuthal, and axial basis functions to fit the data (defined with respect to the coordinate system described below), and use a least

squares minimization approach to fit the data sets. The simplest option for these basis function is a linear combination of functions defined with respect to the (r, θ, z) coordinate system. The problem with that approach is that the flow streamlines are curved in the r-z coordinates, meaning that the velocity profiles in the z direction vary strongly as a function of r. This make the coordinate dependence of the basis functions inseparable. In order to separate the basis functions into a radial and axial component, we use a curvilinear coordinate system $(r^*, z/D)$ created by normalizing the radial direction with the radius of the jet core line at each axial location, $r^* = r/r_{JC}$. This is not a perfect decoupling, but works quite well as the disturbances and shear layers tend to fall along near constant r^*. The basis functions for the interpolation can then be written as

$$F(r^*, \theta, z) = \sum_i \sum_j \sum_k a_{ijk} f_i(r^*) g_j(z) h_k(\theta) \tag{4.2}$$

where $f_i(r^*)$ represents a radial basis function, $g_j(z)$ represents an axial basis function, $h_k(\theta)$ represents an azimuthal basis function, and a_{ijk} represents the fit coefficients for the combined terms. The following basis functions were chosen based upon extensive analysis of the measurements, with the objective of utilizing functions that naturally fit the measurements with a minimal number of coefficients:

$$\begin{aligned}
\sum_{l=1}^{N_r+1} f_l(r^*) &= 1 + \sum_{m=1}^{N_r} \sin\left(m\pi\left(\frac{r^*}{r^*_{\max}}\right)\right), \\
\sum_{l=1}^{N_z+2} g_l(z) &= 1 + \sum_{m=1}^{N_z+1} z^{m-1} \exp(i\phi(z)), \\
\sum_{l=1}^{2N_\theta+1} h_l(\theta) &= \sum_{m=-N_\theta}^{N_\theta} \exp(-im\theta).
\end{aligned} \tag{4.3}$$

Additional basis function sets for the radial and axial directions were attempted, specifically Chebyshev polynomials, monomials, Bessel functions, multiple types of Fourier series, and even Gaussian shaped functions. It was found that the radial shape could be best fit by the sine series, but that the axial function needed prior information to inform the basis set, such as the phase speed of the disturbance. Thus the function $\phi(z)$ in Eqn. (4.3) is a 2nd order polynomial fit to the phase lines in the shear layers as calculated from the r-z plane data, which allows the axial wavenumber of the dominant disturbances to be well approximated. This phase speed is calculated independently for each velocity component, but does not distinguish between different helical modes. This has the unfortunate side effect of not allowing different helical modes to have different phase speeds and loses the dispersion between modes. However as a result of the fit to the phase, the polynomial multiplying this term only has to capture the magnitude of the dominant helical disturbance. Finally, it should be noted that summing the axial and radial terms at a given axial-radial location gives the coefficients of the helical modes, i.e.

$$\widehat{\boldsymbol{B}}_m(r^*, z) = \sum_j \sum_k a_{jkl} f_j(r^*) g_k(z) \exp(im\theta). \tag{4.4}$$

The radial fit to the data was given by choosing $N_r = 15$. N_θ was chosen as 3 giving a total of 7 helical modes (note that the $|m|>3$ modes contain a negligible amount of the energy at the forcing frequency as shown later), with the lower amplitude $|m| \geq 2$ capturing the noise of the flow field. 4 different axial locations were measured allowing for 4 different axial terms to be used without introducing oscillations between axial locations. N_z was chosen as 2 so that the axial envelope of the helical modes could be

approximated by a 2rd order polynomial. Data outside of $z/D \in [0.05, 1.7]$ and $r^* \in [0, 2]$ were ignored during the fit.

The PIV Fourier coefficients from each measurement plane were phase locked to the r-z plane and placed into a large matrix. Each point used in the least squares fit was weighted by its representative measurement area ($dx * dy$). Each velocity component was fit separately, and Table 3 shows a summary of R^2 values for each data case and each interpolated velocity component compared to each plane. The largest R^2 value occurs for the r-z plane in all cases as the r-θ planes cause an increase in the number of data points at a given axial location, skewing the fit in their favor. Additionally, the axial velocity fit for the 1170 Hz cases was exceptionally poor as the equations shown above do not well approximate the more complex shape of the axial disturbances caused by interference effects. Additionally, the acoustic correction was applied solely to the transverse component, leaving the interference effects in the axial component. The 1170 Hz IP fit to the r-z plane was omitted as it gave a negative R^2 value. The radial component for the 1170 Hz cases had a much better fit as it contained a strong disturbance, however its fit to the r-z plane is poor so its results will not be presented. Lastly, the axially minimized cases are omitted from the interpolation as the 1170 Hz IP minimized forcing condition was not repeatable and the 390 Hz IP minimized case resulted in a poor fit due to weak disturbances.

Table 3 - R^2 values for fit to different planes from interpolation technique.

Forcing	Component	Total	*r-z*	$\frac{z}{D} = 0.15$	$\frac{z}{D} = 0.67$	$\frac{z}{D} = 1.2$	$\frac{z}{D} = 1.7$
390 OP	u_z	0.9515	0.9033	0.9119	0.9928	0.9905	0.9774
	u_r	0.9605	0.8940	0.9688	0.9896	0.9885	0.9917
390 IP	u_z	0.9144	0.6935	0.9540	0.9833	0.9803	0.9862

	u_r	0.9651	0.8312	0.9255	0.9710	0.9817	0.9881
1170 OP	u_z	0.4490	0.1830	0.9495	0.8131	0.6960	0.9219
	u_r	0.8315	0.7138	0.9743	0.9721	0.9519	0.9769
1170 IP	u_z	0.1537	--	0.8778	0.5440	0.0699	0.7205
	u_r	0.9077	0.7578	0.9865	0.9822	0.9722	0.9804

Due to the poor fit in the r-z plane for the 1170 Hz cases, and due to the poor fit of the axial component, the results of the interpolation technique will not be shown for these cases. Rather the discrete measurements taken from the r-θ planes will be used for further comparisons in Chapter 5. One possible reason that the high frequency case is not well captured is the Nyquist criterion. This says that in order to capture a harmonic disturbance, at least two measurement per cycle are required. The 1170 Hz case shows an interference pattern with a wavelength of $0.5D$, which roughly corresponds to the axial distance between measurement planes. The fit function to the phase, $\phi(z)$, tries to bypass this requirement; however, the interference patterns in the disturbance amplitude still require more measurements to be fully resolved. To capture the 1170 Hz disturbances appropriately, measurements would have to be taken approximately every $0.25D$. An additional possible reason for the poor fit to the 1170 Hz data may be that it is not repeatable for the same reasons that the axially minimized case is not repeatable. Essentially the standing acoustic wave is varying inside of the combustor as the boundary conditions, namely the temperature, inside of the combustor changes. Future recommended work for higher frequencies are to 1) address the issue of repeatability in the forcing configuration and 2) take more measurement planes in r-θ to better resolve the axial disturbances.

Figure 56 shows the fitted axial velocity and radial velocity magnitudes along the ISL and OSL compared to the original data for the 390 Hz OP case. The overall trends of the magnitudes and the relative amplitudes of the magnitudes are captured. The differences

are most notable in the OSL for the axial component and the ISL for the radial component. These differences are due to the fact that the fit is a compromise between the r-z and r-θ measured values.

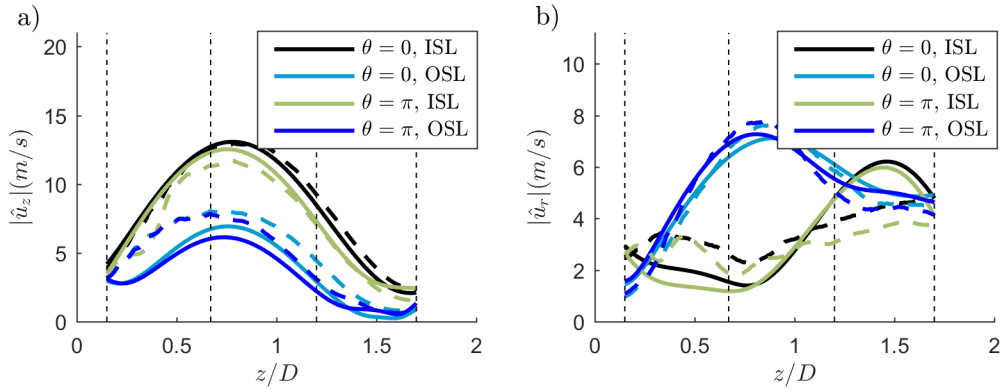

Figure 56 - Comparison of fit velocity magnitudes with r-z measured data along ISL and OSL for the 390 OP forcing case. Solid lines are interpolated data while dashed lines are measured from r-z plane.

4.2 Further Decomposition of Modes

As was shown in Chapter 3, the axial hydrodynamic modes consist of velocity fluctuations dominantly located in the shear layers, with different relative amplitudes and phases in the ISL and OSL, as shown notionally in Figure 57 (left). This suggests decomposing the ISL and OSL disturbances into those that are symmetrically and anti-symmetrically oscillating with respect to each other about the JC, as illustrated by Figure 57 (right). This was done using an even-odd decomposition in a coordinate system that is centered at the jet core, defined by $(r_2^*(z), z)$, using

$$\begin{cases} \widehat{\boldsymbol{B}}_{m,s}(r_2^*, z) = 0.5\left(\widehat{\boldsymbol{B}}_m(r_2^*, z) + \alpha\widehat{\boldsymbol{B}}_m(-r_2^*, z)\right), \\ \widehat{\boldsymbol{B}}_{m,a}(r_2^*, z) = 0.5\left(\widehat{\boldsymbol{B}}_m(r_2^*, z) - \alpha\widehat{\boldsymbol{B}}_m(-r_2^*, z)\right), \\ r_2^*(z) = r - r_{JC}(z), \end{cases} \tag{4.5}$$

where r_{ISL} is the location of the ISL, r_{JC} is the location of the JC, $\widehat{\boldsymbol{B}}_{m,s}$ is the symmetric component of the helical mode, $\widehat{\boldsymbol{B}}_{m,a}$ is the antisymmetric component of the helical mode, and α is a sign modifier equal to 1 for the axial component and -1 for the radial component. This decomposition is similarly motivated by hydrodynamic stability analysis of related velocity fields (i.e., annular, swirling flows with inner and outer shear layers) – e.g., Manoharan et al. [123] refers to the antisymmetric and symmetric shear layer modes as "sinuous" and "varicose" modes respectively.

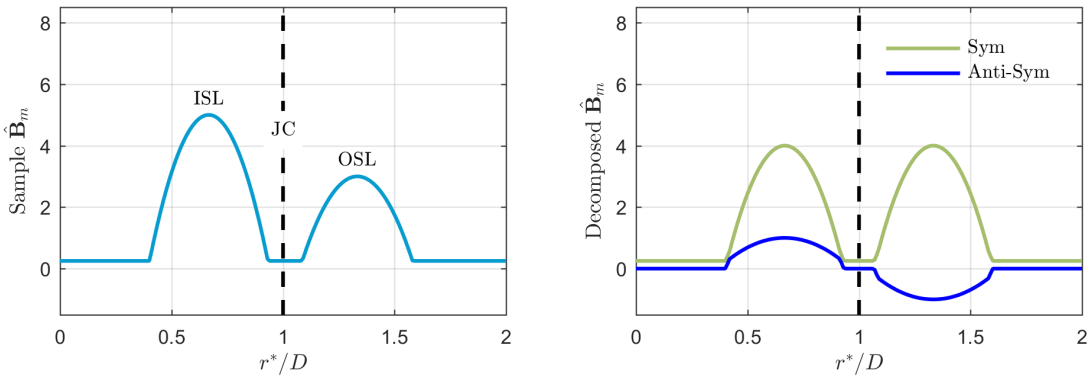

Figure 57 - Example (not data) azimuthal mode distribution illustrating symmetric and anti-symmetric decomposition of velocity disturbances about JC.

The physical manifestation of these symmetric and anti-symmetric disturbance modes for the $m = 0$ and 1 modes are illustrated in Figure 58. The anti-symmetric decomposition represents a flapping jet motion in 2D. Essentially the radial disturbance causes the jet to move across the time-average JC. This causes the axial velocity to increase in one shear layer and decrease in the other, the antisymmetric mode of the axial velocity. On the other hand the symmetric decomposition captures the modulation of the jet width. The radial disturbances compress or stretch the 2D jet, resulting in the symmetric axial velocity oscillations in the shear layers.

The helical mode number determines the periodicity of the decomposed modes about the centerline. If the mode is axisymmetric, $m = 0$, then the antisymmetric component represents the periodic expansion of the jet. Similarly the $m = 0$ symmetric component represents the periodic modulation of the jet annular width, which can represent mass flow oscillations. For the $m = \pm 1$ modes, the antisymmetric component represents the precession of the jet about the centerline while the symmetric component can represent local mass flow oscillations.

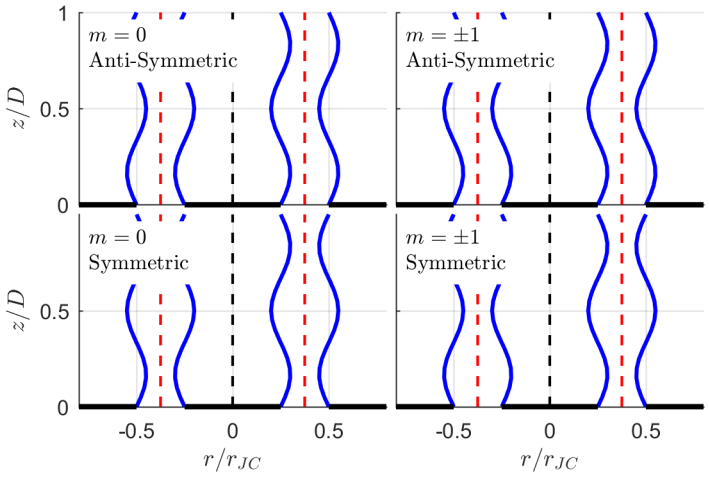

Figure 58 - Illustration of flow field manifestation of symmetric and antisymmetric modes as translation and expansion of annular jet due to radial disturbances in the ISL and OSL with the JC in red (dashed) and the centerline in black (dashed).

4.3 Results for 390 Hz

4.3.1 Characterization of Phase-Reconstructed Flow Field Using Volumetric Interpolation

Having shown the dominant features of the forced flame and flow, we next consider the spatial structure in more detail. Figure 59 shows the phase-reconstructed (defined as the sum of the time averaged component and component characterization of forced

response oscillating at the forcing frequency) velocity field streamlines overlaid on the phase-reconstructed vorticity disturbance field for the 390 Hz IP forcing case. The phase-reconstruction shown here uses the sum of helical coefficients for calculating the disturbance. Were only the $m = 0$ disturbance used, there would be little observable difference, because the other modes are negligible in comparison, as demonstrated earlier in Chapter 3. The phase-reconstructed vorticity disturbance fields show convective disturbances with a wavelength of approximately $0.5D$. Three vortical disturbance peaks are evident--one inside the ISL, one along the JC, and one outside of the OSL. As these vortical disturbances convect downstream, they are damped and amplified separately. For example, while the innermost disturbance has decayed in amplitude by $z/D = 1$, the middle disturbance along the JC continues to grow in strength.

It should also be noted that these vortical disturbances are distinct from the large region of rotating flow just inside the ISL that is shown by the full (i.e., sum of the time averaged and disturbance) flow field. Because the vortical disturbances in this particular case are weak compared to the time-averaged vorticity, they do not appear within the phase-reconstructed field as clear regions of rotation in the streamline. Instead, they act to capture the weak convective motion of the center of the large region of rotation. The phase-averaged flame edge, beginning in the shear layer and moving into the jet, is periodically deformed by the vortical disturbance field. While the disturbances may be small in magnitude, they have a significant effect on heat release as they are axisymmetric [124]. This will be explored more in Chapter 5.

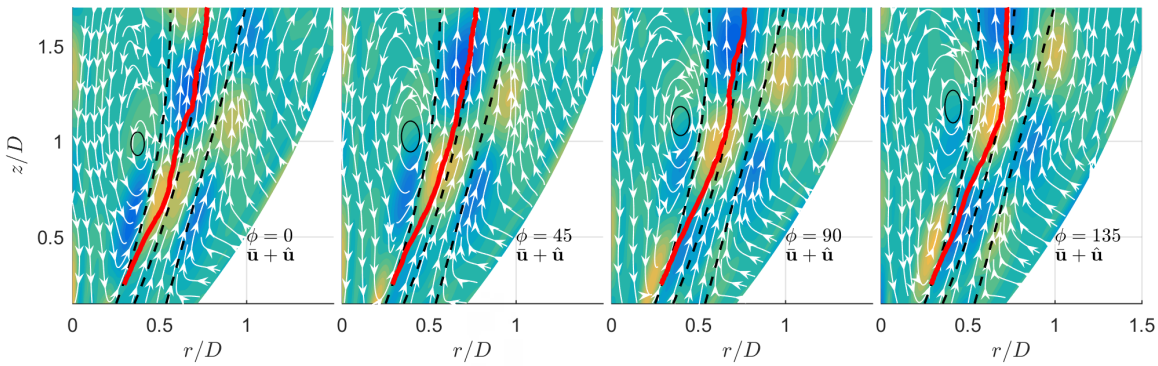

Figure 59 - 390 Hz IP phase-reconstructed flow field (superposition of time averaged and velocity field at the forcing frequency) overlaid on the vorticity disturbance field. Black dashed lines are the ISL, JC, and OSL, and the red line is the ensemble averaged flame edge.

Similarly, Figure 60 shows the phase-reconstructed velocity fields for the 390 Hz OP forcing case with the phase-averaged flame edge overlaid. The top row shows the velocity field reconstructed using the mean and the sum of the helical mode coefficients while the bottom two rows use only the $m = -1$ and $m = +1$ coefficients for the disturbance. The flame edge on each plot is the total disturbance, as it has not been decomposed. These two modes are analyzed individually as the analysis of Chapter 3 suggests that the dominant energy modes are in both the $m = \pm 1$ modes. This figure shows that at low axial distances ($z/D < 0.6$), both disturbances are of near equal amplitude, as shown by the color. While both modes grow axially, the $m = +1$ mode becomes stronger than the $m = -1$ mode. This shows that while the acoustics may excite the two modes nearly equally at the nozzle outlet, the flow field preferentially amplifies the $m = +1$ mode. Additionally this shows that the growth of the $m = +1$ mode does not occur at the expense of the $m = -1$ mode, showing that the two modes co-exist and that one mode does not necessarily suppress the other. Additionally the convection of the disturbances in the positive axial direction gives a positive k value (see Eq. 1) and means that the co-

rotating $m = +1$ mode is counter-winding while the counter-rotating $m = -1$ mode is co-winding.

Superposing the phase-averaged flame edge on the flow field adds insight into the velocity-flame interaction. At low axial heights the flame shows little disturbance; however, as the flow field disturbance amplitudes grow, the flame disturbance amplitude also grows and becomes noticeable beyond $z/D = 0.5$. The phase-averaged flame edge reaches the JC around an axial distance of $z/D = 0.8$ which corresponds with the location of maximum disturbance amplitude in the JC. This large flapping motion does not occur for the IP forcing case as the amplitude of the radial disturbances are weaker than the OP case. Additionally, the IP case forces an acoustic velocity node near the centerline, so the acoustic disturbance also does not aid in the flame propagation across the JC.

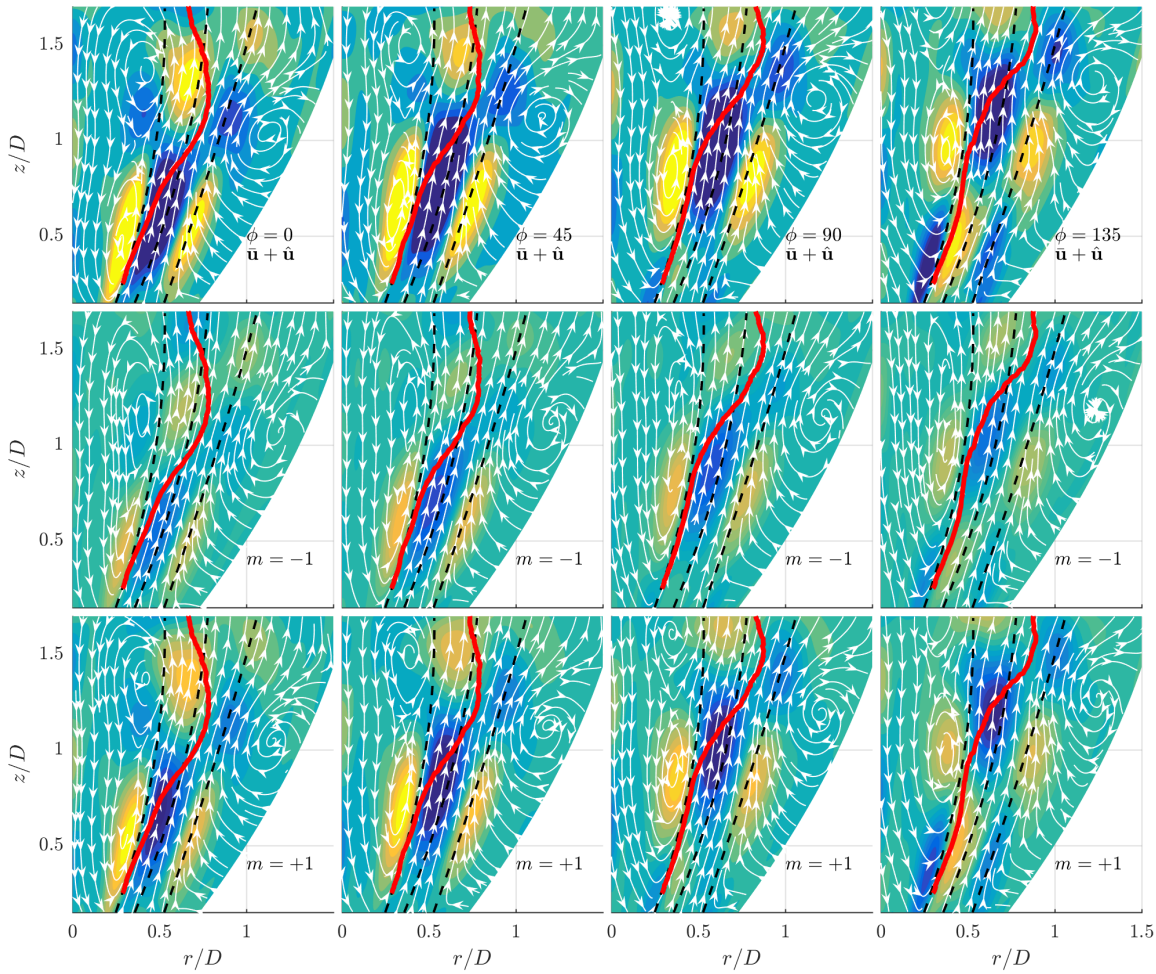

Figure 60 - (top) 390 Hz OP phase-reconstructed flow field and flame position overlaid on the vorticity disturbance field. (middle and bottom) Same data but only using $m = +1$ or $m = -1$ mode for reconstruction to show their separate contribution to the overall velocity shown in the top figure. Black dashed lines are the ISL, JC, and OSL, and the red line is the ensemble averaged flame edge.

Analyzing the IP forcing field showed that the superposition of the $m = 0$ mode on the time-averaged field resulted in convection of the region of rotation within the ISL and caused a small oscillatory expansion of the annular jet. The weak disturbances for this particular case meant that there were no large motions on the phase-reconstructed field. The OP forcing, however, experienced much stronger disturbances that were able to effect the phase-reconstructed flow field. The comparison of the $m = \pm 1$ disturbance fields

resulting from OP forcing shows that the $m = \pm 1$ modes grow together, with the co-rotating $m = +1$ mode preferentially amplified.

4.3.2 Axial Evolution of Disturbance Modes

This section further considers the relative amplitude and axial evolution of the hydrodynamic modes, using the symmetric-antisymmetric decomposition of Eqn. (8). Figure 61 shows the decomposition of the interpolated helical modes at multiple axial locations for the IP case. As noted before, the forced $m = 0$ mode is dominant throughout the flow field. Figure 61 also shows that, at the lowest height, $z/D = 0.15$, the symmetric axial mode is strong throughout the jet. This is likely a manifestation of bulk axial acoustic disturbances (as discussed earlier, no acoustic subtraction was attempted for the IP case), while the anti-symmetric axial disturbances are dominated by vortical disturbances in this region. The vortical disturbances shown in Figure 61 necessarily ignore this acoustic contribution. As the flow convects downstream, the anti-symmetric axial and radial disturbances grow in peak amplitude and spread out radially with the widening shear layer. The growing radial anti-symmetric disturbance is due to dilatational disturbances caused by the flame motion. The spread of the radial and axial modes is due to the presence of phase-jitter on the motion of the 2D cut-section of the jet, moving as illustrated in Figure 57. This shows that the transverse pressure antinode results in negligible oscillating mass fluctuations through the nozzle. Additionally the figure shows that the co-rotating, counter-winding $m = +1$ mode and counter-rotating, co-winding $m = -1$ modes grow downstream despite being negligible in amplitude near the nozzle exit. The flow amplifies

both of these modes, particularly the co-rotating, counter-winding $m = +1$ mode which peaks around $z/D = 0.7$.

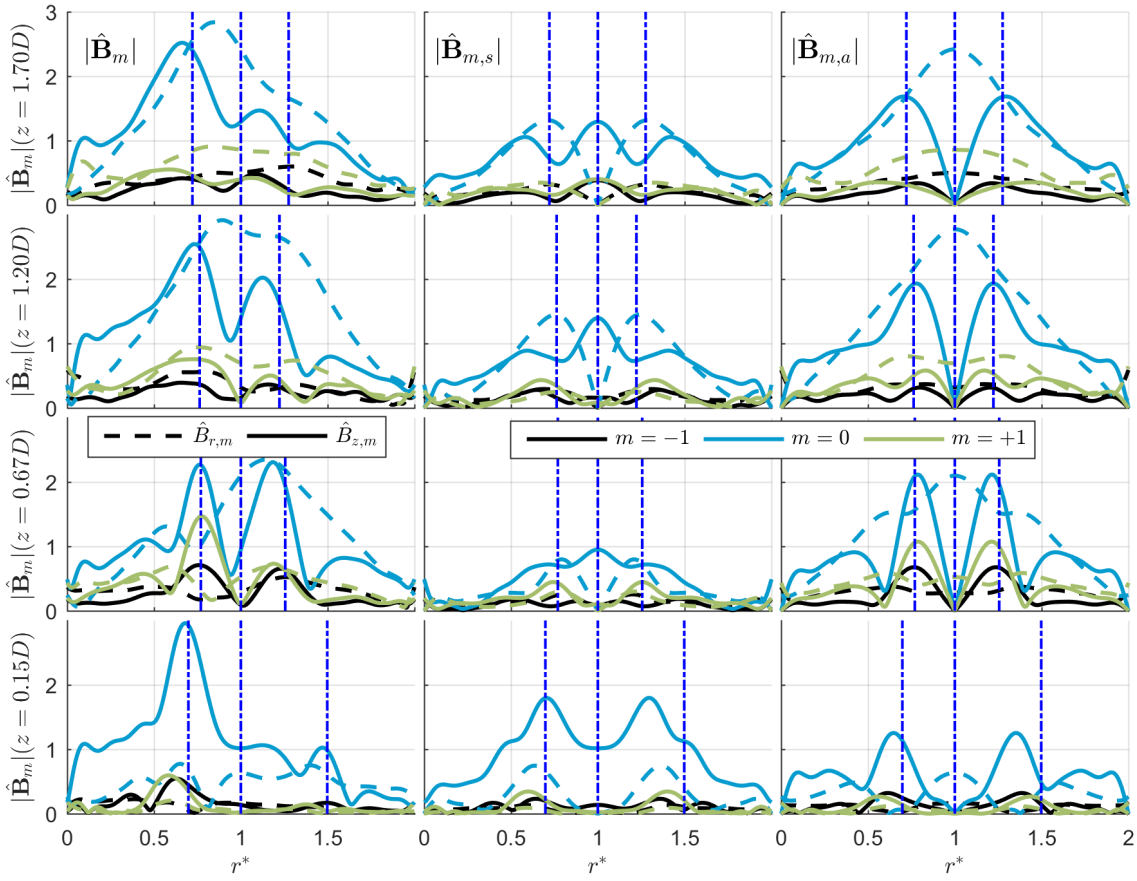

Figure 61 - Helical mode profiles and decomposition about the JC for both axial (solid) and radial (dashed) velocity components for the 390 Hz IP forcing case. JC, ISL, and OSL lines (dash-dot) are shown for reference.

Figure 62 plots the radially integrated energy of the $m = 0$ mode over the decomposition domain, $\boldsymbol{E}_m = \int \left|\widehat{\boldsymbol{B}}_m\right|^2 rdr$. The black line represents the total energy of the interpolated mode shape, the blue line represents the integrated energy of the symmetric mode, and the green line represents the integrated energy of the anti-symmetric mode. It is clear from this plot that the $m = 0$ mode is dominated by the combination of the axial and radial anti-symmetric modes about the JC. It is expected that the most dominant radial

mode is anti-symmetric as the acoustic excitation results in a transverse anti-symmetric disturbance about the JC. Additionally, the peak of this mode occurs at $z/D = 1.4$, which coincides with where the jet stops expanding and where the recirculation zone begins to close. The axial phase taken at a single normalized radius shows a constant convection speed for the dominant anti-symmetric modes – the slope of these lines correspond to a disturbance convection speed of 14.6 m/s. Additionally the radial and axial antisymmetric modes act approximately 90 degrees out of phase with each other, and the phase of the flame envelope follows the $m = 0$ modes quite well.

The flame edge envelope from the $\theta = 0$ plane is also shown. The envelope grows initially with the disturbances, then deviates near an axial distance of $z/D = 0.7$. This is due to the weak $m = 0$ perturbations experienced by the flame and to interference effects from the other helical modes.

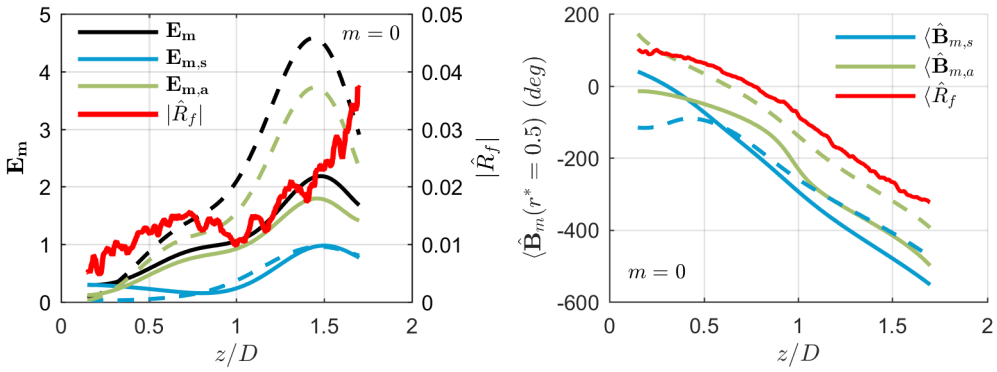

Figure 62 – (left) Radial integration of total energy, symmetric mode energy, and antisymmetric energy for both axial (solid) and radial (dashed) velocity components for the 390 Hz IP $m = 0$ mode with the flame envelope and (right) the corresponding phase plots of the decomposition maintaining the original phase reference.

Figure 63 shows the spatial decomposition of the interpolated helical modes for the 390 OP forcing case. The axial disturbances are strongly anti-symmetric and located in the

shear layers, while the radial disturbances are dominated by anti-symmetric disturbances throughout the entire jet. This combination for the $m = \pm 1$ modes represents the precession of the annular jet about the geometric centre of the flow field. When the two precession motions are of equal amplitude, the superposition of the two results in the side-to-side flapping of the jet. However, at further downstream locations, the $m = +1$ anti-symmetric mode becomes dominant. This shows that the motion of the annular jet transitions from a flapping motion to a precession motion in the swirl direction. Additionally, note that at further downstream locations, the axial disturbances lose their sharpness and amplitude due to the combination of phase-jitter and amplitude decay while the radial disturbances continue to grow. This growth in the radial structure is due to the dilatational disturbance created by the flapping flame. Consistent with this trend, Figure 64 shows that the energy of the anti-symmetric radial mode is constantly growing throughout most of the domain and peaks near the downstream end of the domain.

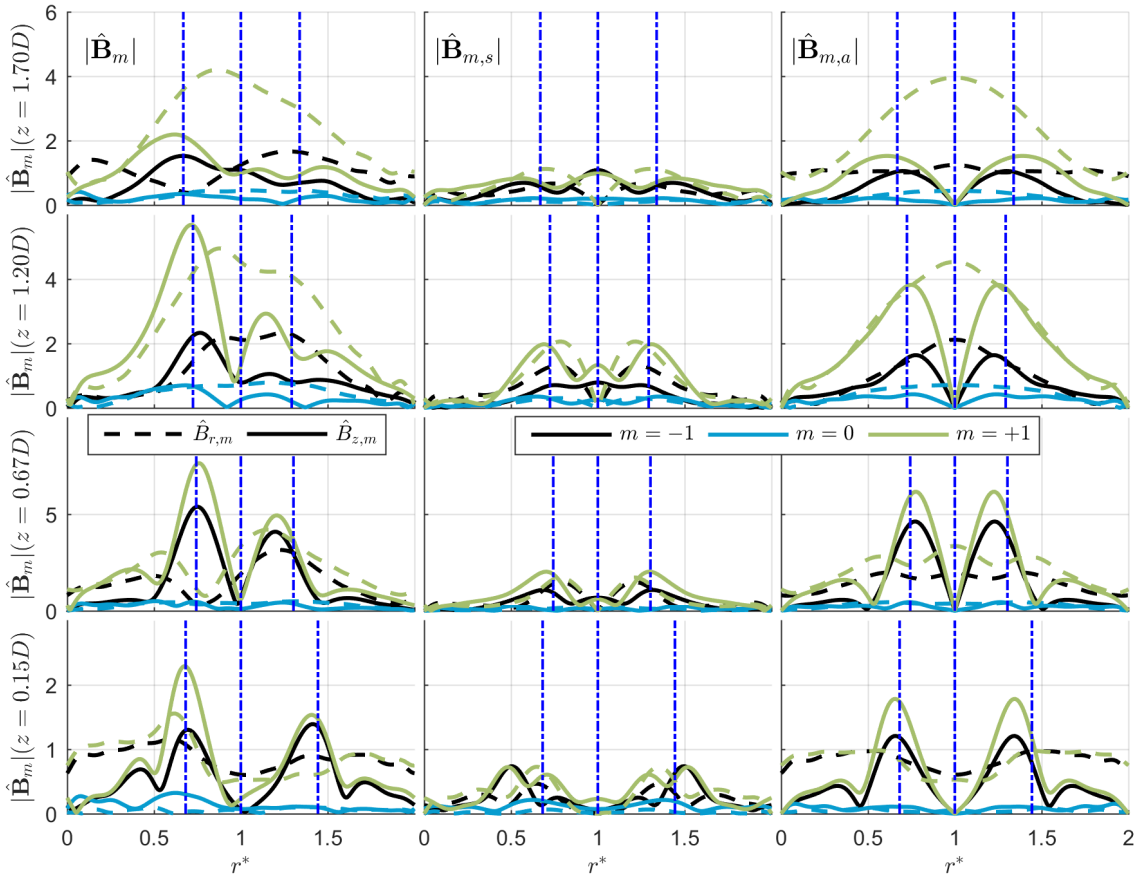

Figure 63 - Interpolated helical mode profiles and decomposition about the JC for both axial (solid) and radial (dashed) velocity components for the 390 Hz OP forcing case. JC, ISL, and OSL lines (dash-dot) are shown for reference.

Figure 64 shows the radially integrated data for the OP forcing case. First, note the difference in mode envelopes between the axial and radial velocity components: the radial envelope shows a bimodal structure peaking around $z/D = 0.8$ and $z/D = 1.5$ while the axial profile only peaks around $z/D = 0.8$. This is because the axial fluctuations and axial velocity are decaying as they progress downstream while the transverse modes are switching from a vortical disturbance to a strong dilatational disturbance due to the flame flapping. The flame edge fluctuations grow, following the $m = +1$ radial fluctuations, and reach a near maximum around $z/D = 1.1$ where the flame crosses the jet periodically. As mentioned earlier, the flame moves out of the inner shear layer around $z/D = 0.8$,

corresponding to the peak axial fluctuation and suggesting that the axial fluctuations are tied to baroclinic torque provided by the density stratification of the flame. Additionally, the phase plots show that the anti-symmetric axial and radial modes are approximately 90 degrees out-of-phase with each other, which is expected for the motion this decomposition describes. The energy in the symmetric modes is primarily a result of the fit to the spatial noise not captured by the anti-symmetric component, therefore its phase plots do not look coherent. Note that the phase speed of the flame edge fluctuations tends to match the $m = -1$ modes better than the $m = +1$ modes despite the $m = +1$ mode being dominant.

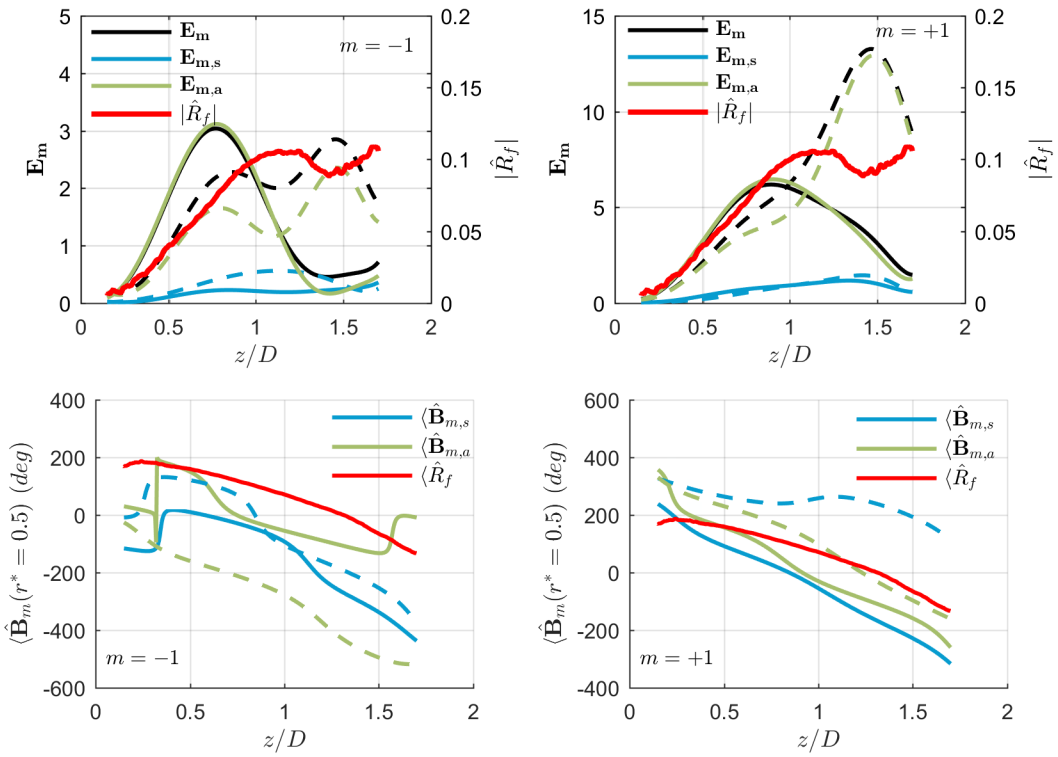

Figure 64 - Radial integration of total energy, symmetric mode energy, and antisymmetric energy for both axial (solid) and radial (dashed) velocity components for the 390 Hz OP (top-left) $m = -1$ and (top-right) $m = +1$ modes with the flame envelope and the corresponding phase plots of the decomposition maintaining the original phase reference for (bottom-left) $m = -1$ and (bottom-right) $m = +1$.

The above data all show growth, followed by decay of the disturbance modes. An important question to address is the relative role of linear and nonlinear processes in leading to the saturation and decay of these disturbances. Next, we briefly consider the significance of nonlinear effects. Self-excited global modes are characterized by narrowband instabilities that grow in time until linear and nonlinear dissipation balance growth, resulting in limit-cycle oscillations. On the other hand, forced modes can derive energy from external forcing and need not rely on temporal feedback for growth, instead extracting energy from the forcing in some region and developing spatially as the flow convects away. This allows forced modes to exhibit linear spatial growth, so long as the amplitude of the oscillation remains small enough for nonlinear effects to be insignificant (which may not be true for all of the domain). A key signature of nonlinear effects is the presence of harmonics and/or subharmonics of the forcing frequency. Figure 65 shows the envelopes of vorticity disturbances along the JC taken from the r-z plane Fourier coefficients, $\widehat{\boldsymbol{u}}'$, at the forcing frequency and its first two harmonics. These results were obtained from the 390 Hz OP forcing case as it shows the larger response amplitude and should, therefore, exhibit the largest non-linear effects. This JC line was selected because the line of maximum amplitude disturbances at the forcing frequency passes through the JC. Figure 65 clearly shows that there is a strong response at the forcing frequency, A_f, and a minimal response at the harmonics, A_{2f} and A_{3f}, which falls into the noise level of the spectra at each axial location. These results strongly suggest that nonlinearities do not play an important role in controlling the flow dynamics for these reported cases.

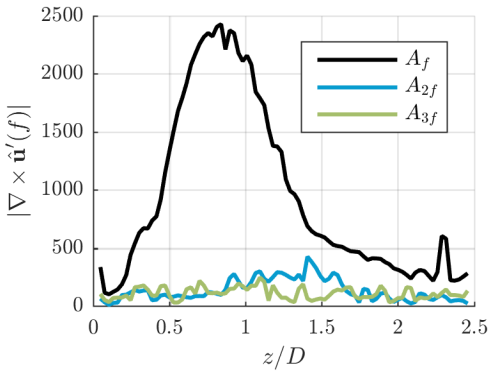

Figure 65 - Envelope of vorticity disturbance amplitude along the left-side JC for the 390 Hz OP case taken directly from un-interpolated r-z data for the forcing frequency and its harmonics.

We close this section by summarizing a few key observations. As noted, the $m = +1$, co-rotating, counter-winding mode grows more rapidly than the $m = -1$, counter-rotating, co-winding mode. Although the acoustic forcing excites both modes at the nozzle outlet equally, the co-rotating mode is apparently more strongly amplified as it convects along the flow. As argued above, there is little evidence of significant nonlinear effects, and so this preferential amplification appears to be a linear effect – i.e., that the spatial growth rate of the $m = +1$ mode is larger than that of the $m = -1$ mode. Moreover, this difference clearly must be due to an asymmetry induced by swirl.

Another important point this work demonstrates is the fact that forced flows of this nature, at least for amplitudes and/or spatial regimes where the dynamics are linear, can exhibit multiple hydrodynamic modes at the same time, In agreement with other studies [69, 73, 125]. These modes can include both co- and counter-winding helical modes, as well as symmetric and antisymmetric jet column disturbances. In contrast, unforced but globally unstable systems, where the limit cycle motion is a clear indication of strong

nonlinear effects, appear to be dominated by a single mode [73, 126] possibly due to saturation.

4.4 Results for 1170 Hz

As previously mentioned, the 1170 Hz cases have a poor least squares fit. This section demonstrates the usefulness of analyzing the r-θ planes without any interpolation. The helical modes can be decomposed into symmetric and antisymmetric modes at the measurement location; however, disturbance envelopes are unresolved and phase speeds cannot be shown for individual helical modes. This section presents these results for the measured r-θ planes.

4.4.1 1170 Hz IP without Axial Minimization

Figure 66 shows the radial and axial helical coefficient magnitudes decomposed into their symmetric and antisymmetric components for the 1170 Hz IP case. The far left shows the magnitude of the helical mode coefficient as a function of the normalized radial coordinate. In agreement with the qualitative discussion from Chapter 3 for the IP case, the figure shows that the $m = 0$ mode is dominant throughout the flow field. Also in agreement with the results shown in Chapter 3, the radial and axial peaks begin in the OSL and move towards to the JC. The radial profile shows a single peak in the OSL, a product of a convecting vortical disturbance as it creates a radial, in-phase disturbance across the shear layer. The axial helical mode profile, on the other hand, shows two peaks on either side of the OSL line, consistent with the strong convecting vortical disturbance as it induces oppositely phased axial disturbances on either side of its center with no axial fluctuation at its center.

Near the nozzle, axial fluctuations are present across the jet with peaks in or near the shear layers due to the induced axial acoustics and convecting vortices. When decomposed, the near nozzle fluctuations show a combination of symmetric and antisymmetric contributions. However at further downstream distances the antisymmetric mode becomes dominant, similar to the 390 Hz case. This motion represents the flapping of the jet. A similar transition occurs for the radial component of velocity, from a combined symmetric-antisymmetric mode near the nozzle to a dominant antisymmetric mode further downstream. However, the combined mode is due to a strong peak radial fluctuation located only in the OSL. Thus the transition from combined to antisymmetric can be interpreted as the OSL showing strong oscillations that induce a large scale jet flapping at further downstream distances as the vortical disturbance travels into the jet.

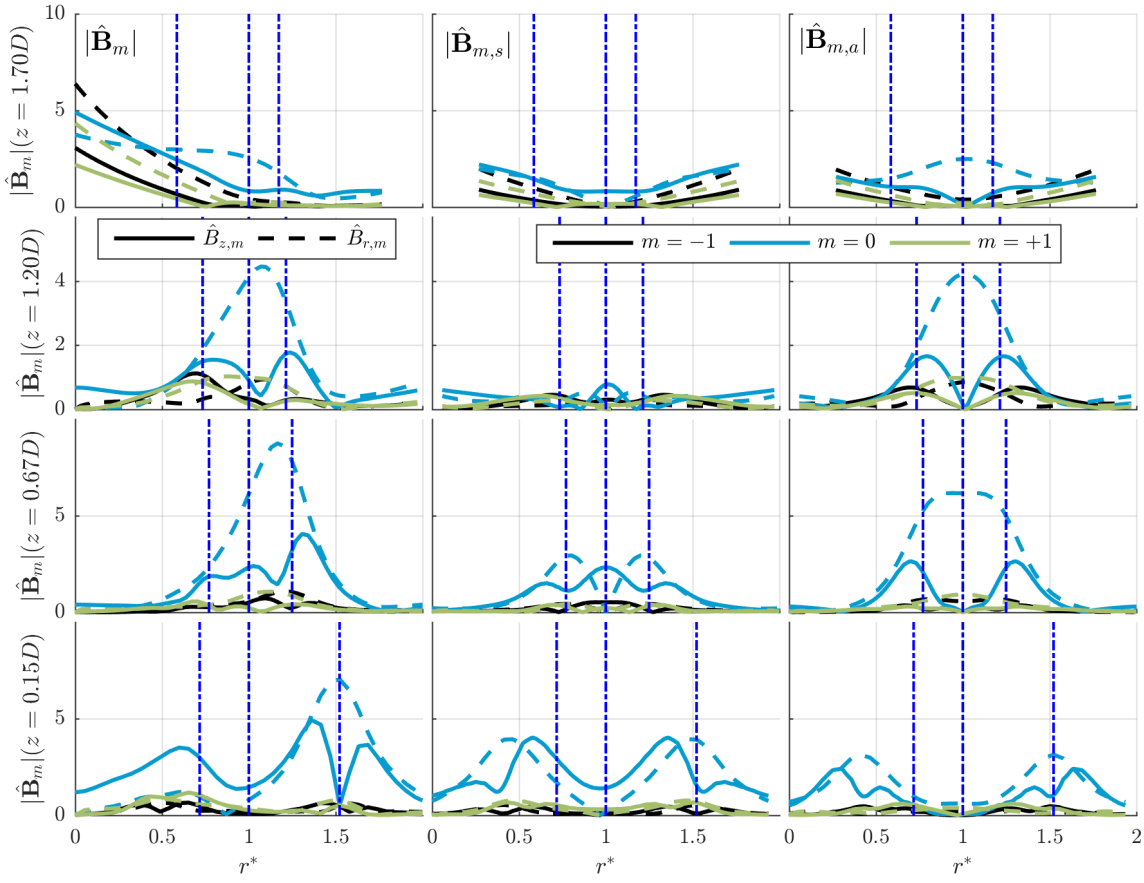

Figure 66 - Helical mode profiles and decomposition about the JC for both axial (solid) and radial (dashed) velocity components for the 1170 Hz IP forcing case. JC, ISL, and OSL lines (dash-dot) are shown for reference.

Figure 67 shows the average helical mode coefficient at each measured height for the 1170 Hz IP forcing case without any axial minimization. This figure primarily shows that the flow response to the forcing condition is fairly repeatable up until a height of approximately $z/D = 1.7$. It is not unexpected that the highest measurement height would show a lack of repeatability. Essentially the amplitude of response at this height is the integral of the growth rates throughout a vortical disturbance's passage time, meaning that the longer the passage time, the more room for variability in the measurement.

Figure 67 clearly shows a dominant $m = 0$ mode for both the axial and radial coefficients. The forcing condition results in these two components initially having an average axial helical mode coefficient on the same order of magnitude. The axial mode demonstrates the significant acoustic coupling near the nozzle. The radial component, however shows the strength of the vortical disturbance in the OSL. The vortical disturbance follows the envelope of the radial disturbance with an initial increase in the average coefficient followed by a steady decline. This trend follows the observed radial and vortical trends taken from the r-z plane in Chapter 3, Figure 47. The good repeatability and the agreement with the trend from the r-z planes suggests that the interpolation should work for this case.

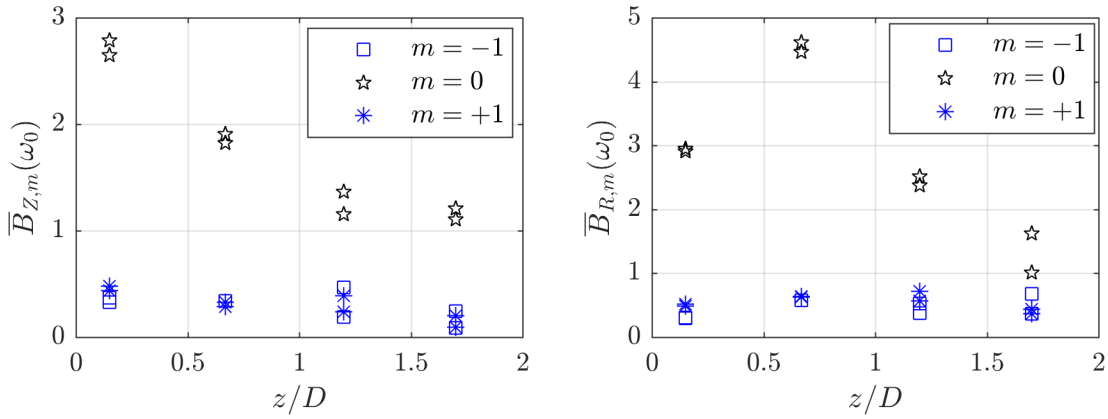

Figure 67 - 1170 Hz IP without axial minimization average helical mode coefficients for each data set with duplicate data sets shown.

4.4.2 1170 Hz OP

Next we look at the 1170 Hz OP forcing case in Figure 68 where the helical mode profiles from each r-θ measurement have been decomposed into the symmetric and antisymmetric components. The left most plots show that the flow field is dominated by $m = \pm 1$ modes in both the radial and axial directions, as expected from Chapter 3.

Additionally near the nozzle the locations of the peaks in the radial and axial mode shapes are the same as that of the 1170 Hz IP case shown in Figure 66. Similar to the 1170 Hz IP case, the radial peak begins in the OSL and move towards the JC, while the axial disturbance shows peaks in both shear layers with a two peaks on either side of the radial peak. Also similar to the 1170 Hz IP case, the radial disturbances are much stronger than the axial disturbances except near the nozzle. The decomposition further reveals that these modes are primarily antisymmetric for both the axial and radial disturbances away from the nozzle. The $m = +1$ mode then becomes dominant meaning that the jet profile begins to transition from a strong flapping of the annular jet to a swirling motion, as demonstrated by Figure 58. Lastly all regions of the flow, even those outside of the jet, experience strong side-to-side motions even at $z/D = 1.7$, evident by the equal amplitude $m = \pm 1$ helical modes.

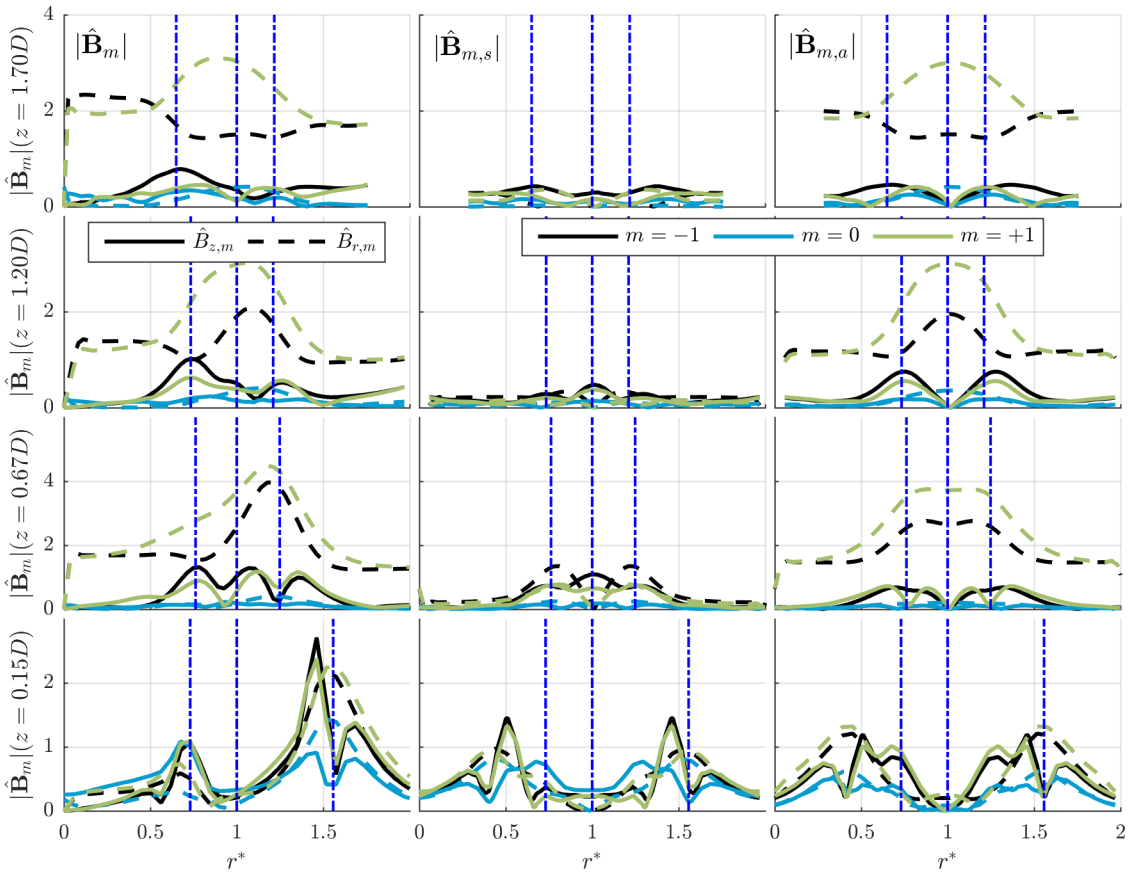

Figure 68 - Helical mode profiles and decomposition about the JC for both axial (solid) and radial (dashed) velocity components for the 1170 Hz OP forcing case. JC, ISL, and OSL lines (dash-dot) are shown for reference.

Looking at the average helical mode coefficient magnitudes in Figure 69 shows that the $m = +1$ mode is consistently more amplified in the radial component, but that the axial component does not show the same preference. Unlike the 1170 Hz IP case, the axial component is small compared to the radial component. Near the nozzle the response of the radial component to acoustic forcing is consistent between duplicate data sets with a near equal $m = \pm 1$ response. As the flow moves downstream, the $m = +1$ radial helical mode shows a quick increase to a peak at $z/D = 0.67$ followed by a consistent decrease. The $m = -1$ radial mode also consistently shows this trend, but with a weaker amplitude.

As the flow moves away from the nozzle, the discrepancy between duplicate measurements increases. This shows that the response is not completely repeatable at further downstream conditions. As mentioned in Chapter 2, it is expected that the changing temperature of the combustor during a run changes the thermal boundary conditions and the speed of sound throughout the combustor. Because this frequency has a smaller wavelength than the 390 Hz acoustic wave, the 1170 Hz acoustic field is more sensitive to fluctuations in the speed of sound.

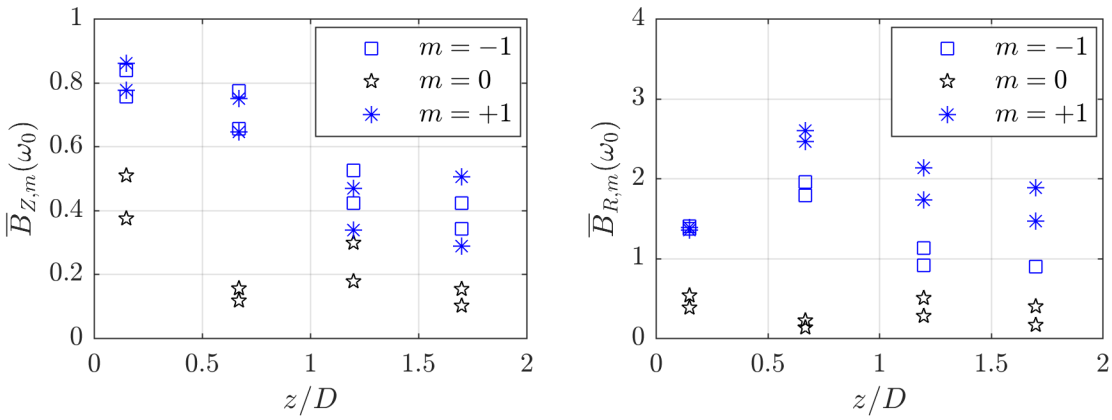

Figure 69 - 1170 Hz OP average helical mode coefficients for each data set with duplicate data sets shown.

This section has shown that similar to the 390 Hz cases, the 1170 Hz cases preferentially excite the antisymmetric modes. This shows that the annular jet has a tendency to transition to a global flapping motion. Additionally this section has shown that the 1170 Hz OP case tends to excited the $m = +1$ mode over the $m = -1$ mode, while the 1170 Hz IP case excited the $m = 0$ mode, as expected. This means that despite the different excitations shapes and frequencies between the 390 Hz and 1170 Hz cases, the flow acts consistently. Additionally we showed in this section that the variation in the flow field response increases with downstream distance as the convection allows for more

amplification of differences in growth rate. Without the interpolation, the envelopes of the average coefficient magnitude are not spatially resolved making any estimate of growth rates impossible. Additionally this lack of spatial resolution prevents the estimation of the phase speeds for each helical mode.

4.5 Chapter Summary

This chapter has shown how phase-locked results from multi-plane (both r-z and r-θ) measurements can be combined to elucidate the three dimensional disturbance structure of a periodically forced, swirling, reacting jet. In particular, by using a volumetric interpolation approach, the velocity and vorticity field were decomposed into its various azimuthal modes. The azimuthal modes were then decomposed into symmetric and antisymmetric disturbances about the jet core with good spatial resolution. Given that the overall velocity field is a superposition of modes with different azimuthal periodicities, and jet core symmetries, such a decomposition lends considerable additional insight into the velocity field than can be obtained by looking at a single plane. Additionally, the technique enables spatially resolved estimates of phase speeds and growth rates for each helical modes.

Measurements showed that the dominant forced helical modes can evolve axially in a quite different manner, particularly for the 390 Hz OP forcing case where the $m = \pm 1$ modes start at near equal amplitude but soon diverge as the co-rotating, counter-winding $m = +1$ mode is preferentially amplified. The counter-rotating, co-winding $m = -1$ mode is still significant, but does not interact with the co-rotating mode. This makes the flow and flame transition from a transverse flapping motion to a precessing motion at further

downstream distances. It was hypothesized that the $m = +1$ mode was preferentially amplified because it was counter-winding, based upon some results from temporal stability theory. As for the 390 Hz IP forcing case, the axisymmetric $m = 0$ modes dominated throughout the entire flow field, as this mode was the most strongly excited. The presence of the $m = \pm 1$ modes were also detected, but their effect on the flow field was minimal in comparison to the $m = 0$ mode. Additionally, the symmetric/antisymmetric decomposition of the flow field shows that the motions in the shear layers that are anti-symmetric or sinuous about the jet core are most amplified; these are the modes associated with transverse motions of the annular jet. This trend holds for all azimuthal modes for the given transverse forcing cases which raises the question of whether axial forcing would also see this same trend.

Despite their poor fit to the basis functions, the 1170 Hz cases were analyzed to show the limitations of planar measurements. The decomposition was possible, as was showing axial envelopes of the helical modes, but the spatial resolution was prohibitive towards estimating phase speeds or growth rates of helical modes. However, the decomposition did show that for the 1170 Hz cases, the antisymmetric modes were dominantly amplified despite starting with a similar order of magnitude as the symmetric disturbances. Despite the poor spatial resolution, the envelopes of the helical mode coefficients at 1170 Hz were discussed, showing the preferential excitation of the $m = +1$ mode for OP forcing and $m = 0$ mode for IP forcing.

CHAPTER 5. HEAT RELEASE RESPONSE TO TRANSVERSE ACOUSTICS

The focus of this chapter is on the heat release response of the swirl flame to transverse acoustic forcing. Chapter 3 showed the flow response to pure transverse waves. This information will now be leveraged to better understand the effects of transverse forcing without the presence of axial acoustics.

A paper by Acharya et al. [47] demonstrated analytically that an axisymmetric flame shows little to no global heat release response to helical disturbances. The reasoning is that when a helical disturbance on the flame is integrated azimuthally, the net disturbance is zero. In other words

$$\int_0^{2\pi} \exp(im\theta)\, d\theta = 0, \text{ for } m \neq 0. \tag{5.1}$$

The caveats on this finding are that the flame needs to be axisymmetric and that the flame disturbance needs to have a small amplitude and be devoid of non-linearities. Additionally O'Connor et al. [26] showed that the imposed transverse acoustic field could be decomposed into helical modes, with the result that a pressure antinode is characterized by a strong $m = 0$ mode while a pressure node is characterized by strong $m = \pm 1$ modes and a non-existent $m = 0$ mode. Chapters 3 and 4 confirmed that these are the dominant modes throughout the measured flow fields at the forcing frequencies, thus the conclusion is that the pressure antinode case shows a strong response in heat release at the acoustic frequency while the pressure node forcing has a negligible response.

Additionally Chapter 3 showed that the effect of the axial minimization on the pressure antinode case is to reduce the magnitude of the $m = 0$ mode within the flow field. The expectation then is that the global heat release response will be diminished as well. Therefore, if the pressure node forcing case and the pressure antinode forcing case, neither with axial acoustics, show no response at the acoustic frequency, then the transverse acoustics induce no response on the flame and the induced axial acoustics are responsible for the flame response. This chapter investigates the theory presented by Acharya et al. [47] by first looking at the global flame response, then looking at the local or axial flame response compared to the helical mode content. The pressure node, pressure antinode, and pressure antinode without axial coupling are all studied in order to generalize these results.

5.1 Global Heat Release Response to Transverse Acoustic Forcing

Figure 70 shows the global heat release response, as estimated from the integrated OH* chemiluminescence PMT measurement detailed in Chapter 2. The left plot overlays the unforced spectra and the 390 Hz pressure node (OP) spectra with duplicate data. The plot on the right shows the pressure antinode (IP) response for 390 Hz with and without axial minimization. The figure demonstrates that the 390 Hz IP forcing case, the case with significant $m = 0$ excitation, creates a strong response at the forcing frequency while the axial minimization successfully minimized the heat release. In contrast, the spectra of the unforced and 390 Hz pressure node cases are virtually identical around the forcing frequency, showing that the energy at 390 Hz is on the order of the noise. This is in agreement with the theory presented above. The two peaks at 80 Hz and 195 Hz are caused by the natural dynamics of the system. The duplicate IP forcing cases were not shown as there was significant experimental error with the forcing condition for these sets. The side

acoustic sensors for the duplicate cases were significantly out of phase with each other, a maximum of 60 degrees phase difference, while the shown cases showed phase measurements within 10 degrees of each other.

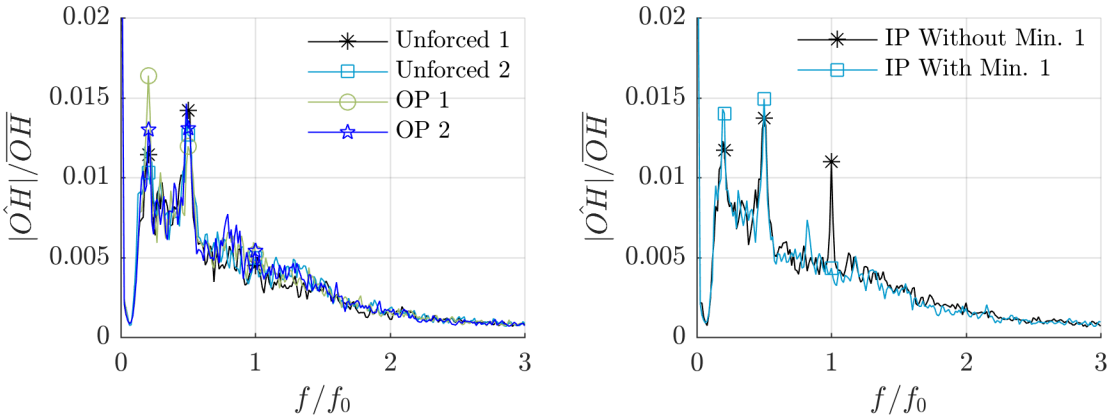

Figure 70 – (left) Normalized OH* chemiluminescence PSD estimate showing the unforced case and the 390 Hz pressure node forcing, and (right) 390 Hz pressure antinode forcing with and without axial minimization.

The excitation signal was recorded simultaneously with the acoustics and heat release. The cross-coherences of the heat release to the excitation signal for the OP cases are on the order of 0.2 while the IP case with axial minimization has a cross-coherence of 0.5. The poor coherence shows that the response at the frequency is partly due to the excitation signal and partly due to background noise within the flow field.

Figure 71 shows the corresponding measurements at 1170 Hz. On the left are the pressure node and unforced measurements, and on the right are the pressure antinode measurements. Clearly the unforced heat release does not naturally respond at 1170 Hz. Unlike the 390 Hz forcing however, all forcing cases show a response. The values of the heat release response do not appear to be repeatable except in the case of the pressure node.

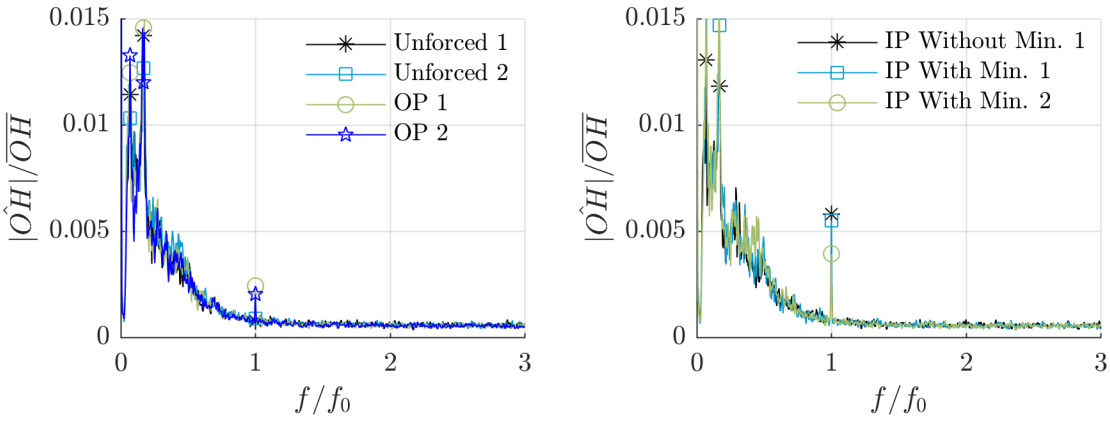

Figure 71 – (left) Normalized OH* chemiluminescence PSD estimate showing the unforced case and the 1170 Hz pressure node forcing, and (right) 1170 Hz pressure antinode forcing with and without axial minimization.

We next desire to calculate a transfer function. The response of the heat release is a sensitive function of the acoustic field both within the combustor and upstream in the mixing chamber. The temperature field determines the local speed of sound, and when combined with the acoustic boundary conditions also determines the resonant acoustic frequencies and corresponding mode shapes. The shape of the acoustic field is important as the sensitivity of the flow field to external forcing is spatially dependent. As shown by Tammisola and Juniper [127], the nozzle exit region is the most sensitive region to velocity disturbances, so having an axial velocity antinode at this location should increase the heat release response. Changes in the boundary conditions change the locations of pressure nodes and antinodes, potentially placing a velocity node at the nozzle exit. This means that as the axial forcing is introduced to minimize the induced axial acoustics, the velocity and pressure nodes change locations as well. This leads to the question, is the heat release more sensitive to the acoustic power in the upstream pipes or due to the mode shape? The proper transfer function should take this into account when considering the input.

Additionally using the power spectra calculations in developing a transfer function gives a poor estimate of the response as it includes power from both the coherent and incoherent parts of the signal. The coherent part of the signal is thus estimated by performing a discrete Fourier transform at the forcing frequency over a 0.1 second window and averaging 15 ensembles phase referenced to the same point in time. Because the excitation signal contains no phase drift, averaging the complex coefficients brings out the coherent content of the signal while the incoherent part of the signal containing phase drift is averaged out due to phase cancellation. An infinite recording would cause the incoherent noise to go to zero while the coherent signal remains. Figure 72 shows a comparison between the power spectra estimate and the ensemble averaged complex Fourier coefficients for a recording of 1.5 seconds on the left and a recording of 60 seconds on the right. The PMT measurement has a cross coherence of 0.06 over the 60 second window and a cross coherence of 0.04 over the 1.5 second window. On the left, the incoherent signal has been significantly reduced, but the coherent signal has not been fully recovered. On the right, the 60 seconds has fully recovered the coherent part while eliminating the incoherent parts of the signal. The heat release data was calculated over a 2 second span, meaning that data points with low coherence will have poorer estimates of the coherent response.

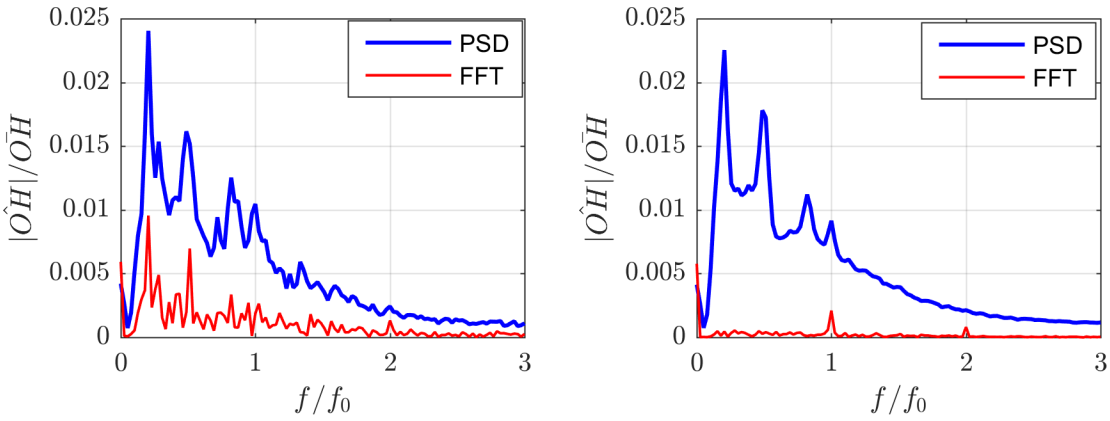

Figure 72 - Comparison of ensemble averaged Fast Fourier Transform (FFT) and estimated power spectrum (PSD) on normalized response of heat release over 1.5 seconds (left) and 60 seconds (right) for 390 Hz OP data set.

Having developed the tools needed for calculating a transfer function, let us consider possible inputs. Figure 73 shows different acoustic measurements from the upstream pipe of the middle nozzle as a function of the normalized heat release for both the 390 Hz and 1170 Hz cases. Specifically the figure shows the magnitude of the Fourier coefficients from the middle nozzle top acoustic sensor, $\hat{p}_{MT}$, the middle nozzle bottom acoustic sensor, $\hat{p}_{MB}$, and their difference, $\hat{p}_{MT} - \hat{p}_{MB}$. The top sensor is located approximately 9.25 inches upstream of the nozzle exit, and the bottom sensor is located one inch further upstream.. The 390 Hz points are grouped into two collections: the 3 points on the left are the OP and IP with minimization cases and the one point on the right is the IP case without minimization. The points on the left have a low coherence and thus a higher uncertainty in position. Additionally due to the poor coherence of the measurements and lack of measurements with a strong response, no good correlation can be made from this data set for 390 Hz. The 1170 Hz data on the other hand shows a good correlation between the heat release and both the bottom sensor and sensor differential. The top sensor has values that appear near zero as the axial minimization attempted to place a pressure node

at that condition. Given that the 1170 Hz data shows a strong correlation, a good transfer function can be calculated using just the bottom sensor, but that transfer function would not be able to capture the response to different axial acoustic mode shapes.

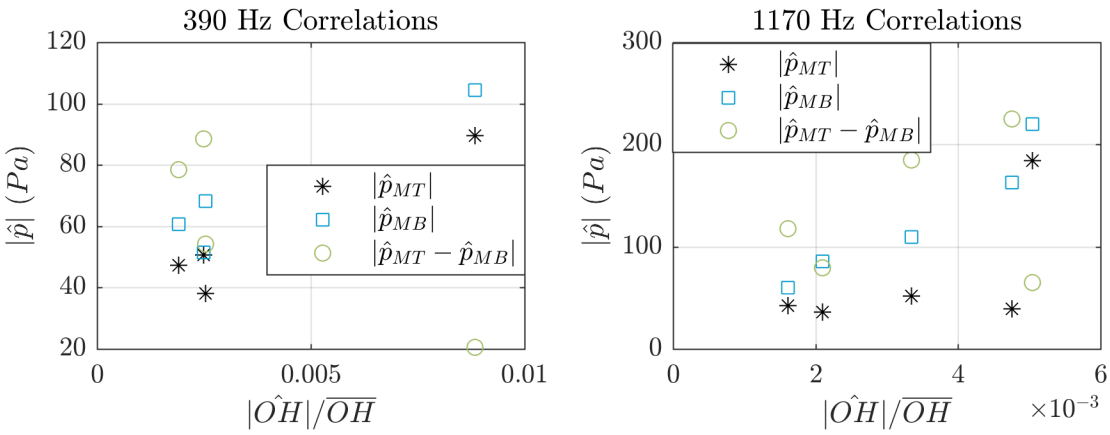

Figure 73 - Different acoustic measurements as a function of normalized heat release.

A different metric can be used to account for the different axial acoustic mode shapes: the acoustic energy density. The acoustic energy density takes into account all of the acoustic measurements from Figure 73, which should ignore any mode shape effects on the measurement.. The acoustic energy density, E_a, is estimated as

$$E_a = \frac{1}{2}\left(\frac{|\hat{p}|^2}{\rho_0 c_0^2} + \rho_0 |\hat{v}|^2\right), \tag{5.2}$$

where the pressure is the averaged pressure coefficient from the two measurements, the density (ρ_0) and speed of sound (c_0)are estimated based on the mixture with seeding air, and the acoustic velocity is estimated using a linearized 1D Euler equation. Specifically the acoustic velocity, $\hat{v}$, is estimated as

$$\hat{v} = \frac{-i}{\omega \rho_0} \frac{\hat{p}_{MT} - \hat{p}_{MB}}{\delta x}. \tag{5.3}$$

This velocity estimate is susceptible to noise as the difference amplifies the noise found in either pressure signal.

Figure 74 shows the acoustic energy density plotted as a function of the normalized heat release. The figure shows no trend for the 390 Hz cases, and similarly shows a large spread in the data points for the 1170 Hz cases. The three points on the left of the 390 Hz plot are the OP and the IP with axial minimization cases, which all have a low coherence and large uncertainty in their normalized chemiluminescence measurements. Because the metric independent of the mode shape shows a poor trend for both frequencies, the heat release response must be a strong function of the axial acoustic mode shape.

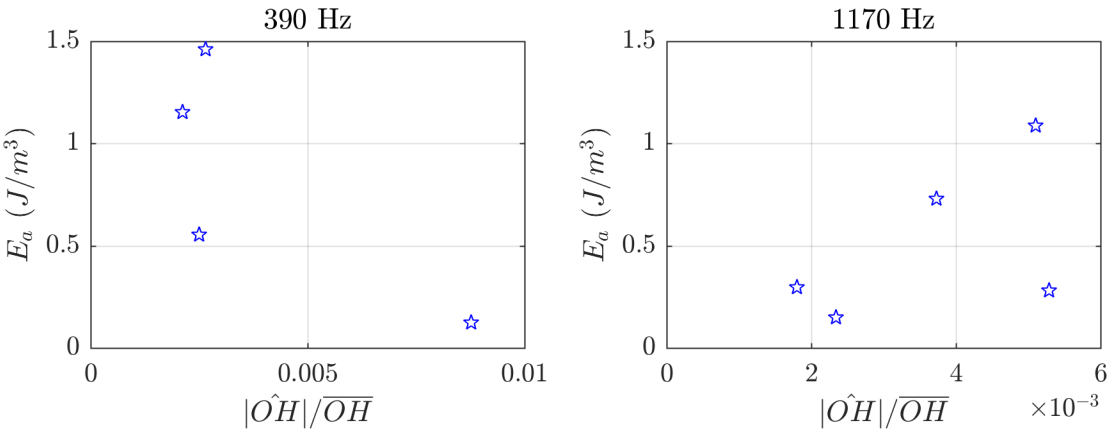

Figure 74 - Normalized heat release vs. estimated acoustic energy density.

As mentioned earlier, Tammisola and Juniper [127] showed that the nozzle exit is the most sensitive region to acoustic forcing. Additionally it was shown in Chapter 2 that the axial minimization reduced the nozzle exit velocity fluctuations and in Chapter 3 that this reduced the $m = 0$ mode. Here have shown that acoustic measurements taken at a different location do not well predict the flame response even when the mode shape is ignored. Given this information, a logical conclusion is that the proper input to the transfer

function is the axial velocity fluctuation at the nozzle exit due to an axisymmetric disturbance.

Figure 75 shows the relationship between the average $m = 0$ mode coefficient and the heat release for the 390 Hz cases. The case to the far left is the OP case. The case in the middle is the IP case with axial minimization, and the case on the far right is the IP case without any minimization. This plot clearly shows that the $m = 0$ mode works well as the input to the transfer function. Additionally the plot shows that a line fit to the data points does not pass through the origin as expected. This could be due to non-linearity within the flow field or uncertainty in the data measurement. Given the small recording time and low cross-coherence of the heat release measurements, it is most likely the latter. The 1170 Hz case is not shown because the heat release measurements were not taken simultaneously with the PIV measurements and because there is an issue with the repeatability of the acoustic field.

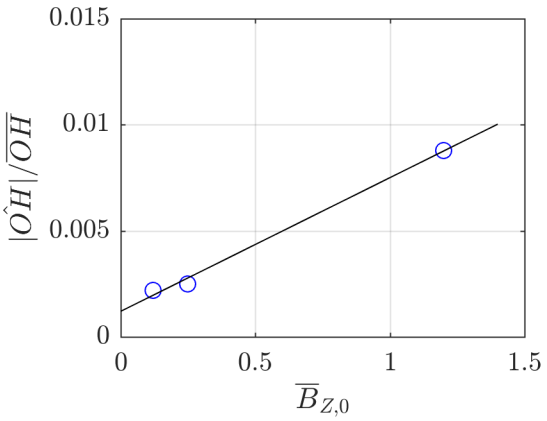

Figure 75 - Normalized heat release plotted as a function of the average axisymmetric axial disturbance measured at $z/D = 0.15$.

5.2 Local Comparison between Helical Modes and Heat Release

Having shown that the global heat release response is a strong function of the $m = 0$ mode near the nozzle exit, we next look at the impact of the $m = 0$ mode on the local heat release. Figure 76 shows a plot of the discretely measured axisymmetric mode data with duplicates and the envelope of heat release fluctuations as a function of downstream distance. The IP forcing case without any minimization, as expected, shows a stronger helical mode content and a stronger heat release profile. The radial helical mode content peaks around an axial distance of 1.2 while the heat release peaks around a distance of 1.4. This peak is related to the reflection of the flame from the OH filter on the other side of the combustor, and no direct conclusions can be drawn from it. As mentioned in Section 2.2.4, measurements in the region $z/D \in (0.5,1.33)$ are contaminated by the reflection, resulting in higher values and potentially non-local measurements. Despite this contamination, the heat release profile contains a bimodal structure due to interference patterns on the flame edge between convecting vortical disturbanes and the acoustic field. The first peak shows a 180 degree phase shift from the trend seen in the downstream heat release response, most likely related to the switch between dominant axial and radial modes. The cross coherence is strong throughout the flow field (> 0.8), except at nodal points in the interference pattern and at further downstream distances ($z/D > 1.7$). The nodal region occurs within the reflection; however the reflection would not have distorted the measurement in such a way to create this node. In other words, the reflection would not have created the approximately π radian phase jump between the first coherent axial section and the section coherent axial section. The main effects of the reflection would be to change the nodal location, the peak location, and their relative amplitudes.

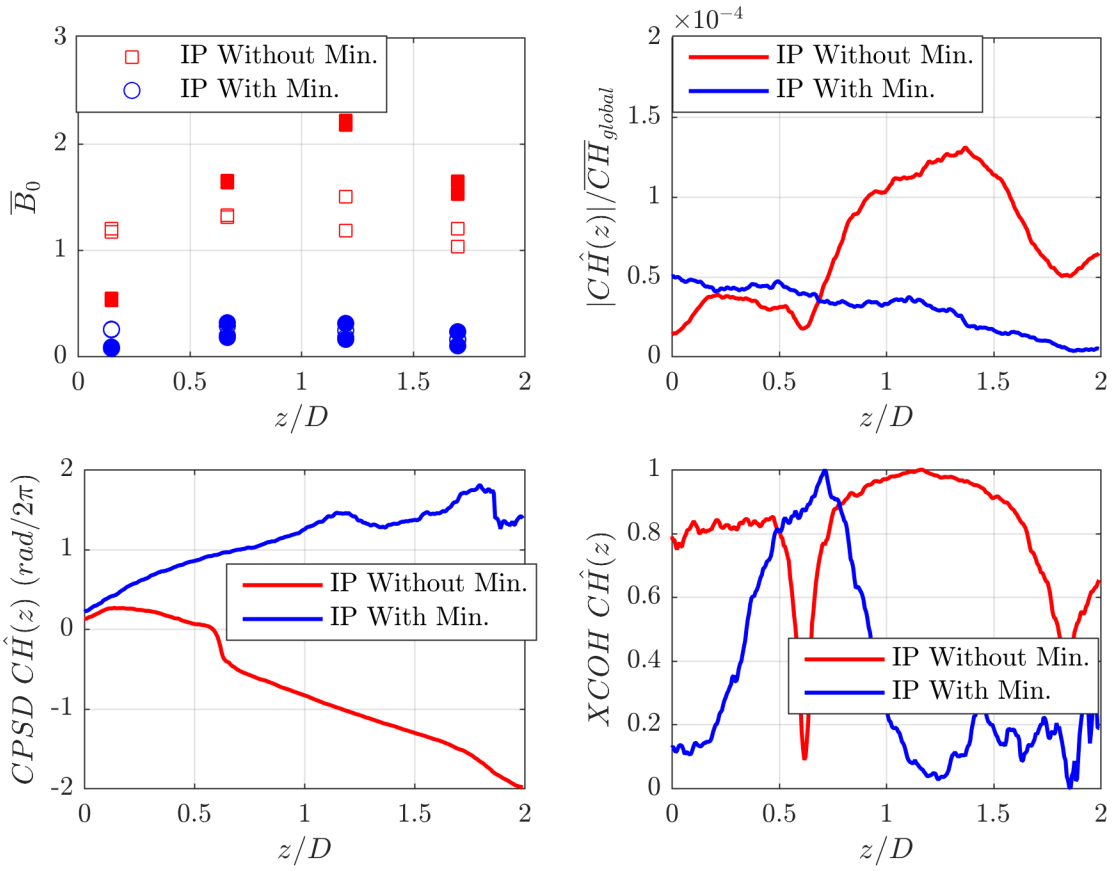

Figure 76 - Axisymmetric mode content (top-left) for axial (open) and radial (filled) modes from the 390 Hz IP cases with and without minimization and (top-right) normalized heat release response as a function of axial distance. (bottom-left) angle of cross power spectral density (CPSD) estimate of heat release fluctuations at the forcing frequency referenced to the same point as (bottom-right) cross-coherence of heat release fluctuations at forcing frequency.

On the other hand, the IP case with minimization in Figure 76 shows little coherent response as the cross coherence decays rapidly away from the chosen location. The envelope shows no peaks, and the angle of the heat release disturbance shows a trend moving upstream. Given the poor coherence of the signal, this line likely has no physical meaning. Figure 76 strongly supports the idea that a stronger axisymmetric mode leads to stronger heat release response both locally and globally.

5.3 Chapter Summary

This chapter has considered the question of how a transverse acoustic field without induced axial acoustics effects the heat release. It was shown that the induced axial acoustics inside of the nozzle are not a good predictor of the response of a swirl flame, but rather that the axisymmetric velocity at the nozzle exit was the proper input for a transfer function because this location is the most sensitive region of the flow field to velocity perturbations. Therefore, the response to transverse acoustics is due primarily to this region of the flow field. Global heat release responses occur when the axisymmetric mode is induced here, which can be caused by strong induced axial acoustics or a weak axial acoustic antinode.

The local heat release response is also strongly a function of the axisymmetric mode. The heat release envelope showed similar trends to the measurements of the axisymmetric mode at discrete locations, following the radial axisymmetric mode quite well. However, the contamination of the CH* measurement means that this may have been caused by the captured reflection. When the axisymmetric mode was reduced at the nozzle exit, it was successively reduced throughout the flow field resulting in an incoherent flame response.

This chapter proves that the $m = 0$ mode is responsible for the heat release. Cases without significant $m = 0$ modes showed a heat release response that was indistinguishable from the noise. Additionally it shows that the transverse to axial coupling matters when it results in an axial velocity antinode at the nozzle exit. This coupling excites the $m = 0$ hydrodynamic mode responsible for the heat release.

Therefore, the role of transverse acoustics in the heat release response is to induce an axial acoustic field in the upstream pipe that creates an axisymmetric velocity disturbance at the nozzle exit. This chapter showed that when this condition is not met, the flame does not respond coherently to the transverse excitation.

CHAPTER 6. CONCLUSIONS AND FUTURE WORK

Previous work on swirl flames within a transverse acoustic field did not attempt to isolate the effects of the transverse acoustic field from the axial acoustic field. Their measurements of transverse transfer functions inherently captured the coupling between the two fields. The first aim of this work was to experimentally isolate the transverse acoustic field for an acoustically compact flame and study its impact on the flow and flame structures and response. A method of isolating the transverse acoustics was created, using simultaneous axial and transverse forcing combined in such a way that the axial forcing counters the induced axial acoustics of the transverse forcing. The flow field and flame response were studied for this forcing configuration. Second, this work developed a novel interpolation approach using helical modes as a basis function to calculate the flow field response of the volume from planar measurements. The work demonstrated the effectiveness of this method on the aforementioned transversely forced flow fields.

6.1 Conclusions

The first major contribution of this work is to show the effects of pure transverse forcing on an acoustically compact flame and flow field. It was shown that a pressure node and a pressure antinode above the nozzle result in fundamentally different helical modes in the flow field. For a pressure node (OP), $m = \pm 1$ modes were dominant throughout the flowfield with $m = +1$ becoming dominant at further downstream distances. The pressure antinode (IP) forcing, on the other hand, resulted in a dominant $m = 0$ mode throughout the flow field and showed a strong response in the global and local heat release measurements. These findings are in agreement with previous work that contains axial

coupling as well as theory predicting the flame response based on the G-equation. When the axial to transverse coupling was corrected for by eliminating the axial velocity fluctuations at the nozzle exit, the coherent $m = 0$ modes disappeared. The heat release response for this purely transverse forcing was also non-existent while measurements of the axial acoustic energy inside of the mixing pipe showed that the acoustic energy was not minimized. This strongly suggests that the flow field and flame response to the axial acoustics is dependent on the axial mode shape, specifically whether there is an axial velocity antinode at the nozzle exit. This strongly supports the hypothesis that the axial acoustics induced in the inlet section of the rig are responsible for the axisymmetric vortical structures and the heat release response of the flame.

Therefore there are two practical strategies for eliminating the flame response to a transverse acoustic wave: 1) eliminate the induced axial acoustics and 2) create an axial velocity antinode at the nozzle exit. The first strategy can be performed by installing nozzles with a high impedance at the problematic frequencies to damp any axial acoustic fields. Another way to achieve this method would be to place Helmholtz resonators at locations corresponding to pressure antinodes within the nozzles, passively canceling the axial acoustic field. However, these two methods could still leave axial acoustics that are strong enough to excite the necessary axisymmetric modes. A third method for cancelling the acoustics is to actuate the flow upstream of the combustor. This method can cancel the axial acoustic field or it could change the axial acoustic mode shape, strategy two.

Care should be exercised when applying these results to non-compact flames. It is not that flames do not have local heat release fluctuations when excited by transverse acoustic waves and/or helical hydrodynamic modes. Rather, these disturbances have

opposite phases on opposing sides of the flame and, consequently, cancel out when calculating the spatially-integrated heat release. However, it is not the spatially-integrated heat release that controls the rate at which the flame adds energy to the acoustic field- it is the spatial integral of the product of the heat release and pressure perturbation. If the flame is acoustically compact, the acoustic pressure is essentially uniform and comes out of the integral. However, if there is an acoustic pressure phase reversal across the flame, it is possible that energy is added to the acoustic field even in cases where the spatially integrated unsteady heat release is zero. Schwing et al. [86, 89, 90, 93] has developed models for high frequency acoustic-flame interactions that couple flame wrinkling and acoustic disturbances. Additionally the author points readers interested in non-compact flame-acoustic interactions to rocket literature, specifically the work of Blackshear [11] and Rogers [9].

The second contribution of this work is the novel interpolation method. The method utilizes a linear least squares approach, multiple r-θ planes, and a single r-z plane to extract helical mode coefficients throughout the volume. Specifically for this flow field, the method uses a curvilinear coordinate system in (r, z) to follow the streamlines of the expanding and contracting annular jet, as the helical modes grow and decay along these lines. The method used helical modes as a basis function for interpolating the Fourier coefficients at the forcing frequency throughout the volume. A caveat on this method is that the method approximates the axial phase speeds of the helical modes from the total disturbance field measured in the r-z plane, which does not allow the phase speeds of non-dominant helical modes to be computed accurately. Additionally the number of r-θ planar

measurements included determines how well the mode shapes can be resolved in the axial direction.

This work used the results of the interpolation to add insight into the understanding of the flow field, namely by spatially reconstructing the complex helical mode coefficients and then radially decomposing them into symmetric and anti-symmetric components about the jet core. It was shown that the flow field response to the transverse forcing was predominantly anti-symmetric regardless of the forcing configuration. This effectively demonstrated that the method is effective at interpolating the volume and allows for additional spatial analysis to be performed on these helical modes.

6.2 Recommended Future Work

The first recommendation for future work is experimental: identify the source of the lack of repeatability in the higher frequency forcing cases. The first recommended step is to implement a phase calibration for the speakers. While the acoustic field may be correct at room temperature conditions, the repeatability disappears as soon as the flame is present. The second recommendation is to install acoustic sensors to measure the axial acoustic velocity at the nozzle exit. This gives a measurement of the axial velocity fluctuations and enables real-time axial minimization to be performed. The author would also recommend performing r-θ sPIV measurements at the nozzle exit simultaneously with chemiluminescence measurements for longer recording times and at more frequencies. This will test the generalization of the finding that the axisymmetric mode correlates strongly with the heat release and test the limits of the acoustically compact flame assumption. For the work presented here, the heat release and $m = 0$ coefficient were not

measured simultaneously, so they needed to be averaged over multiple data cases and then plotted in Figure 75. Simultaneous measurements would allow for more data points with which to calculate a transfer function.

The interpolation method can also be refined. Currently the method uses an axial phase function requiring a-priori knowledge of the phase speed. Unfortunately this can only be measured for the dominant disturbances, and thus the dispersion of different helical modes is lost. To correct for this, the dispersion relations of each helical mode should be modelled and linearized around the dominant mode at the given frequency. This would allow an estimate for each helical mode to be calculated a-priori. The second option is to perform a non-linear least squares method with the phase parameters as an input. This would slow the fit by introducing more variables but would allow for the phases of each helical mode to be calculated separately.

Additionally, several questions emerge from this work for future studies. First, while the flow dynamics appear to remain linear here, it will be of interest to study this configuration over a larger range of forcing amplitudes where strong nonlinearities arise. This raises the questions of if and how nonlinear competition between symmetric and asymmetric modes, co- and counter-rotating modes, or co- or counter-winding modes arise. For example, would one of the modes, say the $m = -1$ be completely eliminated in favour of another mode? A related study of interest would be excitation of additional modes; for example, by exciting the $m = -1$, $m = 0$, and $m = +1$ modes with comparable amplitude (which can be done with a traveling acoustic wave, rather than a standing wave). In addition, exciting other even modes with significant amplitudes, such as $|m| = 2$ will be

of interest, to see how axisymmetric and helical disturbances interact, as well as even and odd modes.

One of the key challenges with measurements of this nature is handling the large volumes of data that are acquired; indeed, transferring data from cameras is one of the main time requirements for the experimental campaigns, and camera memory generally limits the size of data records. While the data acquired here was sufficient to elucidate to high precision key spectral characteristics, the ability to transfer and manipulate much larger data sets will also enable answering additional questions. For example, one interesting question is the degree of interaction between the different modes – as they undergo inherent phase jitter, are their motions phase locked to each other or do they evolve completely independently? This question can be addressed by determining the coherence between these quantities, whose meaningful estimate would require roughly an order of magnitude longer time series. In addition, returning to the nonlinear interactions question, longer data sets will be required to analyse higher order nonlinear correlations (e.g., the degree of interaction for the $m = +1$ mode at ω and the $m = 1$ mode at 2ω), such as the bispectrum.

These studies motivate additional theoretical studies as well. In particular, while the $m = +1$ mode was preferentially amplified, it would be of interest to analyse the relative roles of shear, centrifugal instabilities, baroclinic torque, and dilatation in controlling these results. Such a study could also assess the sensitivity of these results to small variations in, say, relative locations of the shear layer and flame which strongly influences how induced baroclinic vorticity interacts with shear-generated vorticity. Related questions arise for the forced response of a flow, and how the different shear, rotation, and gas expansion terms influence the relative growth rates of different types of modes, and at different frequencies.

APPENDIX A. DETAILED PART DRAWINGS

The next few pages show detailed drawings of the combustor, the nozzle, the windows, and the ceramic liner. The combustor box was water-jetted from 3/8” stainless steel sheets, and the cylindrical geometries were created on a lathe from stainless steel. The exception to this is the swirler which was 3D printed using Inconel. The exact drawings for the swirler are replaced with a generic swirler as the original was designed by a project sponsor and remains proprietary.

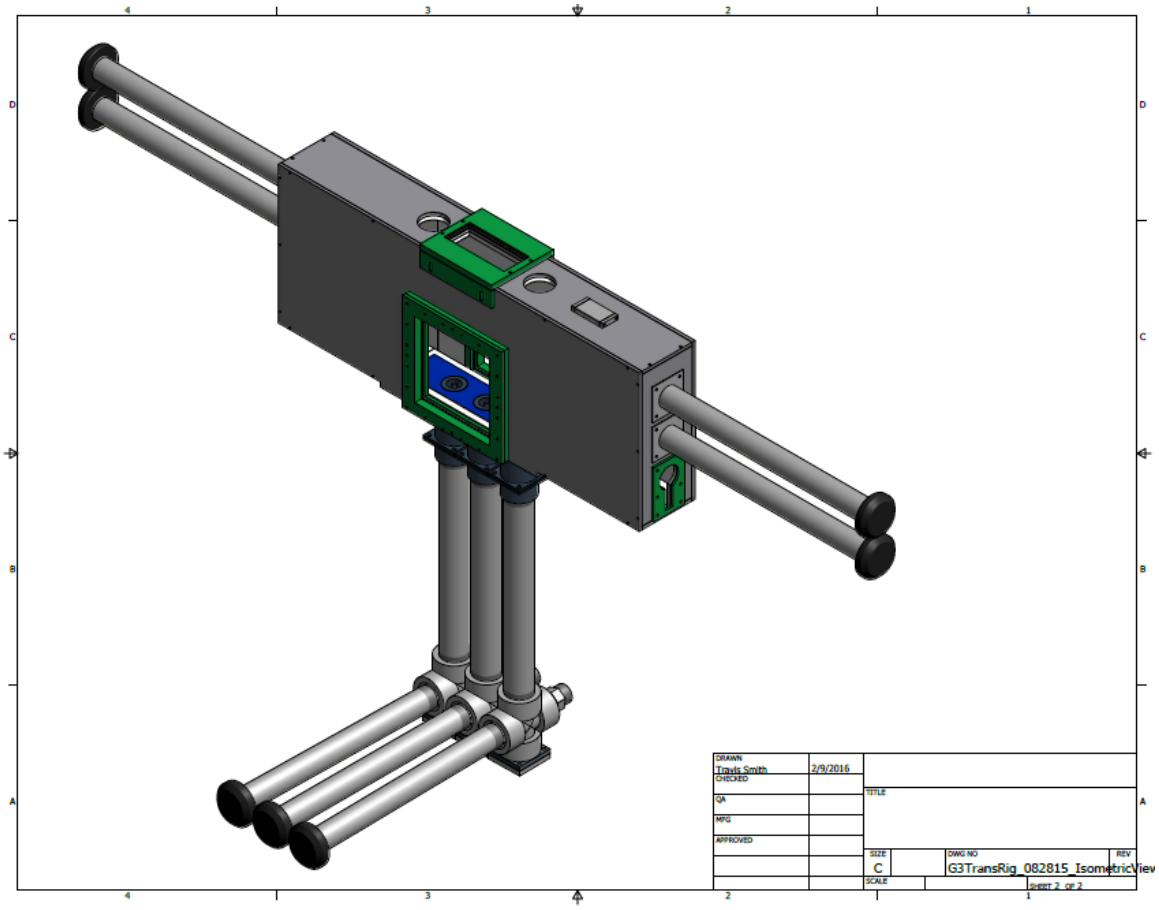

A.1 Combustor Box

The box was water-jetted from 3/8” stainless steel sheets with the exception of the swirler block, which required a more complicated machining process. The acoustic standoff tubes are 26 inches long with the speakers mounted to the ends. The ignitor was moved from the top of the combustor to the plate on the front face. The ignitor mount held two electrodes connected to a transformer that created a spark at 5kHz, and a tube that ejected hydrogen, creating a hydrogen torch to ignite the methane-air mixture.

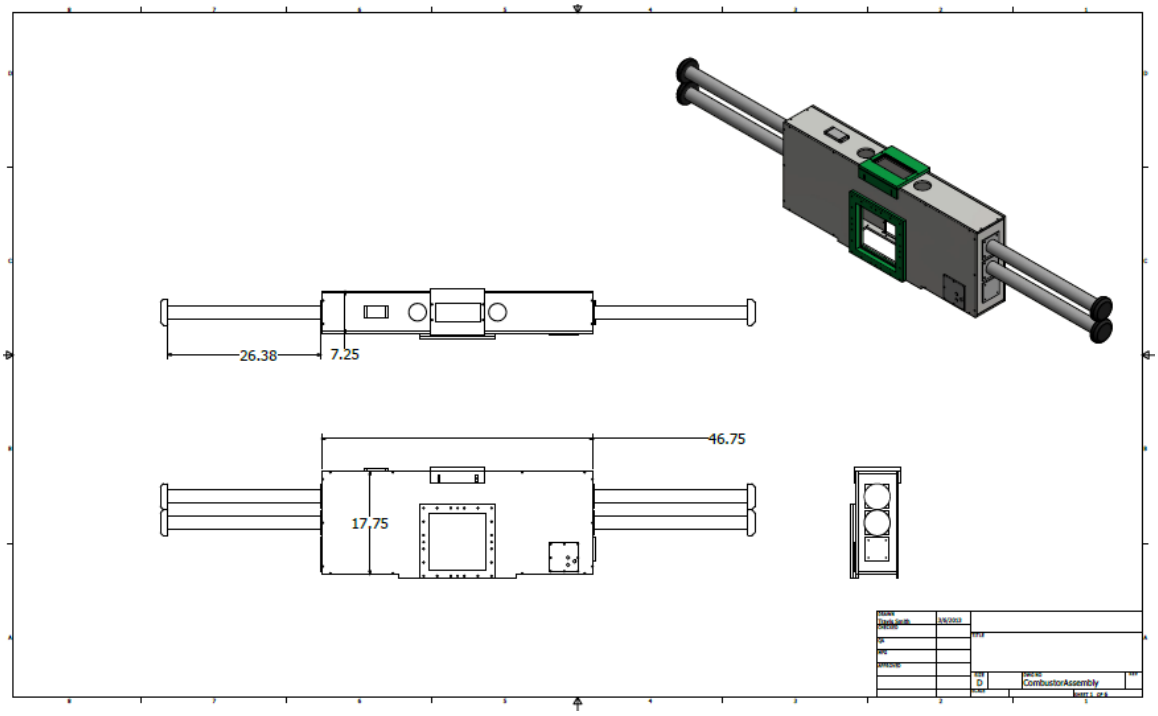

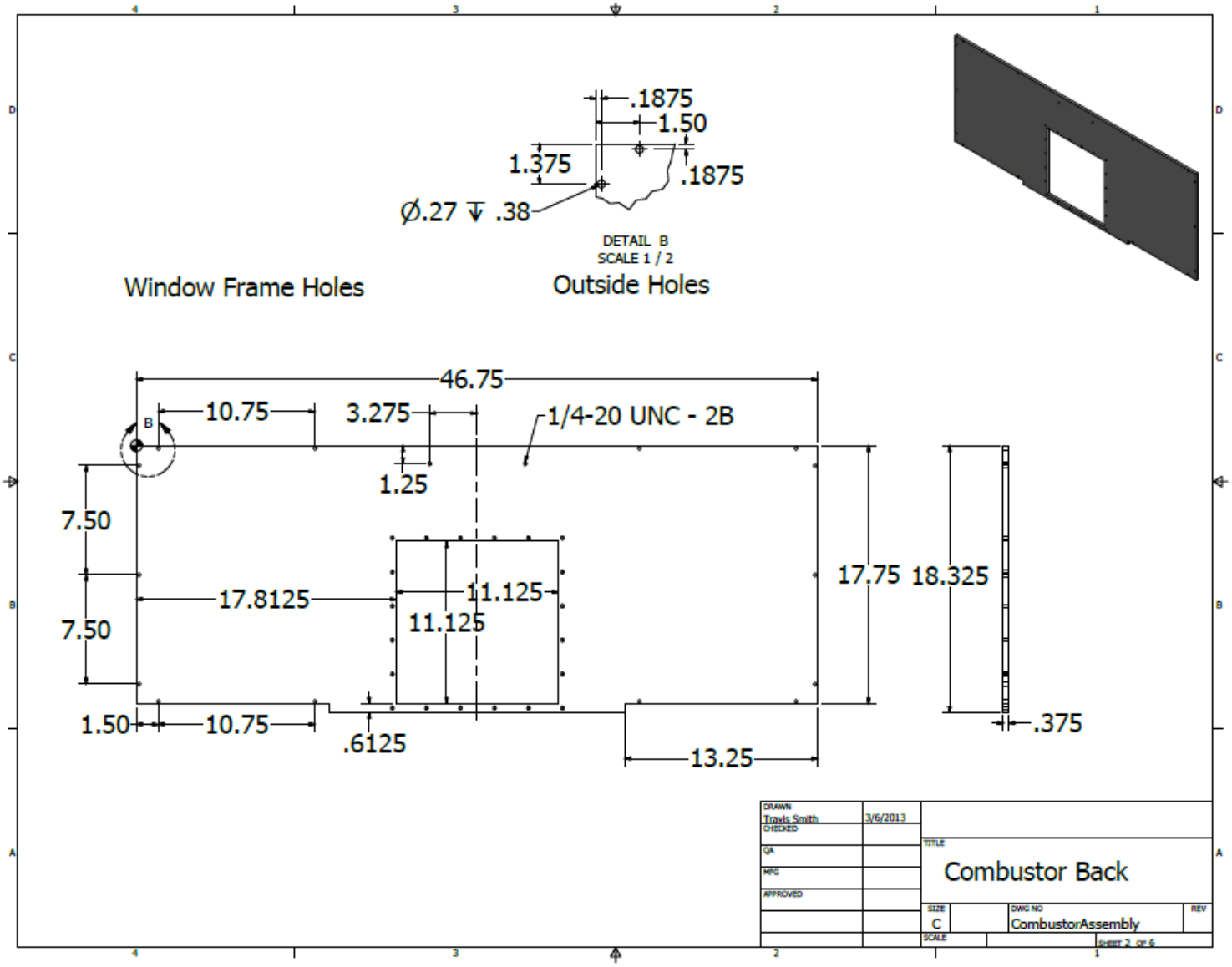
.1875
1.50
1.375
.1875
Ø.27 ↧ .38
DETAIL B
SCALE 1 / 2
Window Frame Holes
Outside Holes
46.75
10.75
3.275
1/4-20 UNC - 2B
B
1.25
7.50
17.8125
11.125
11.125
7.50
17.75
18.325
1.50
10.75
.6125
13.25
.375
DRAWN
Travis Smith
3/6/2013
CHECKED
QA
MFG
APPROVED
TITLE
Combustor Back
SIZE
C
DWG NO
CombustorAssembly
REV
SCALE
SHEET 2 OF 6

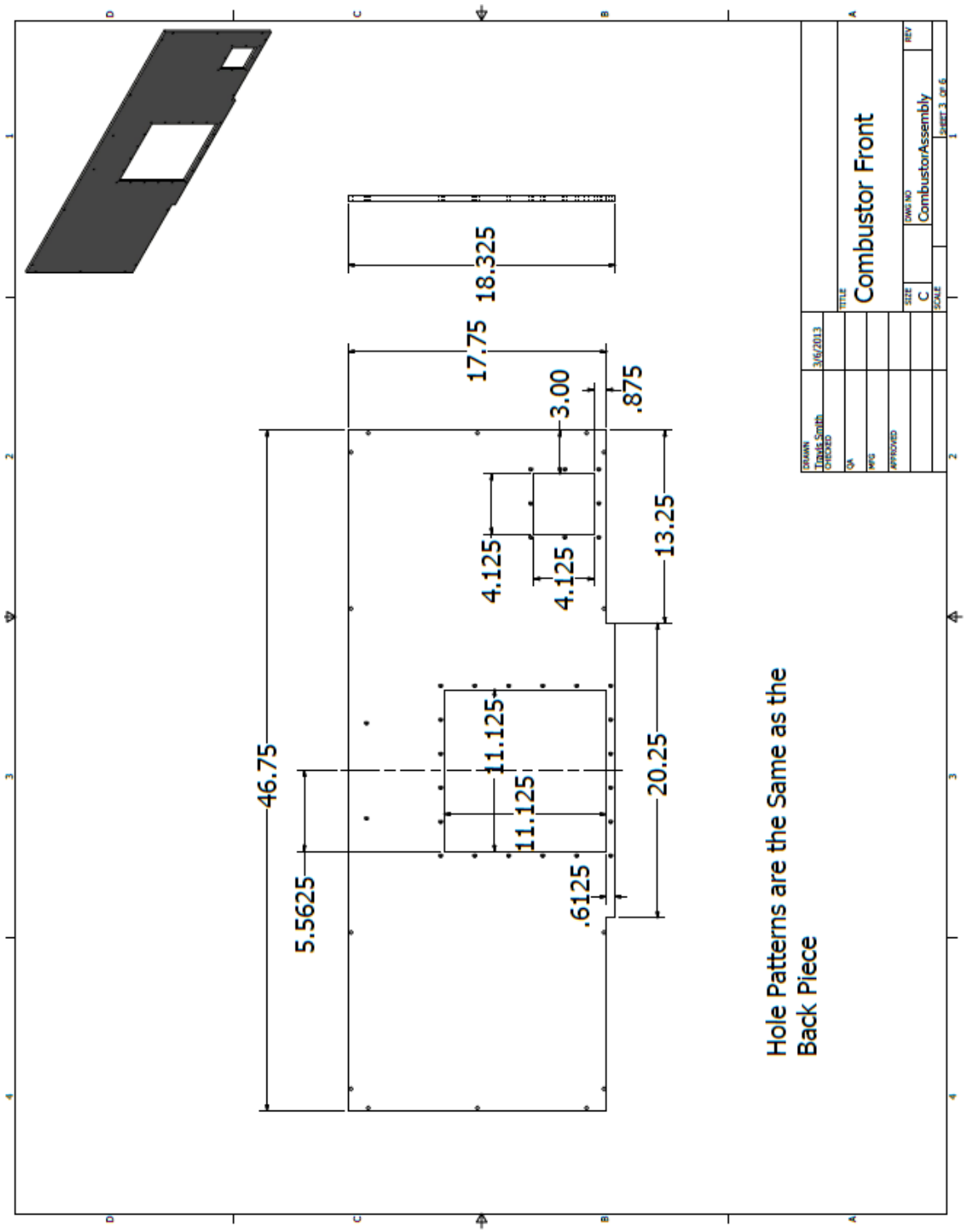
18.325
17.75
3.00
.875
4.125
4.125
13.25
46.75
11.125
11.125
20.25
.6125
5.5625
Hole Patterns are the Same as the Back Piece
Combustor Front
CombustorAssembly
3/6/2013
Travis Smith

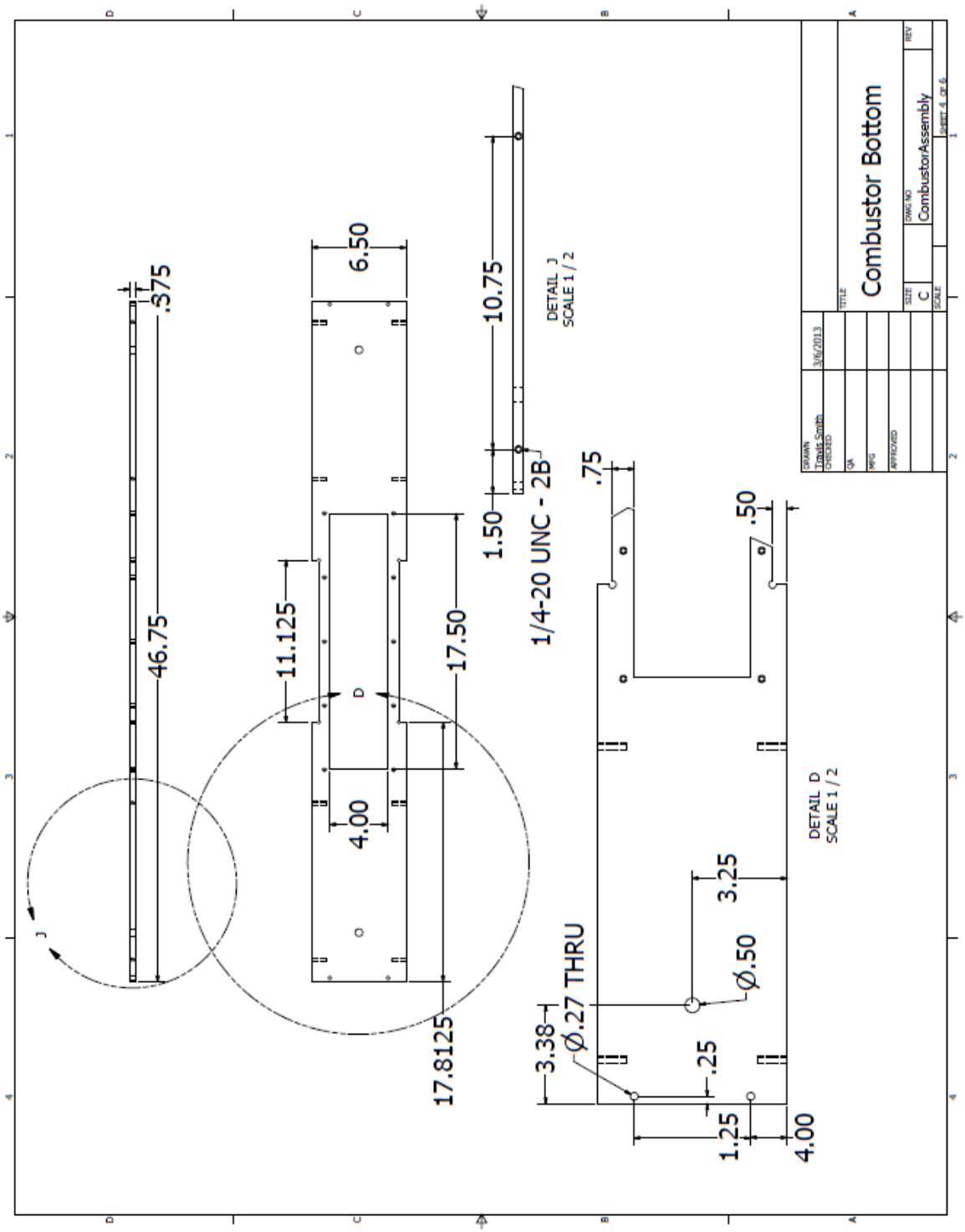
Combustor Bottom
CombustorAssembly
Travis Smith
3/6/2013
C
.375
46.75
6.50
11.125
17.50
4.00
17.8125
10.75
1.50
1/4-20 UNC - 2B
DETAIL J
SCALE 1 / 2
.75
.50
3.25
Ø.50
Ø.27 THRU
3.38
.25
1.25
4.00
DETAIL D
SCALE 1 / 2

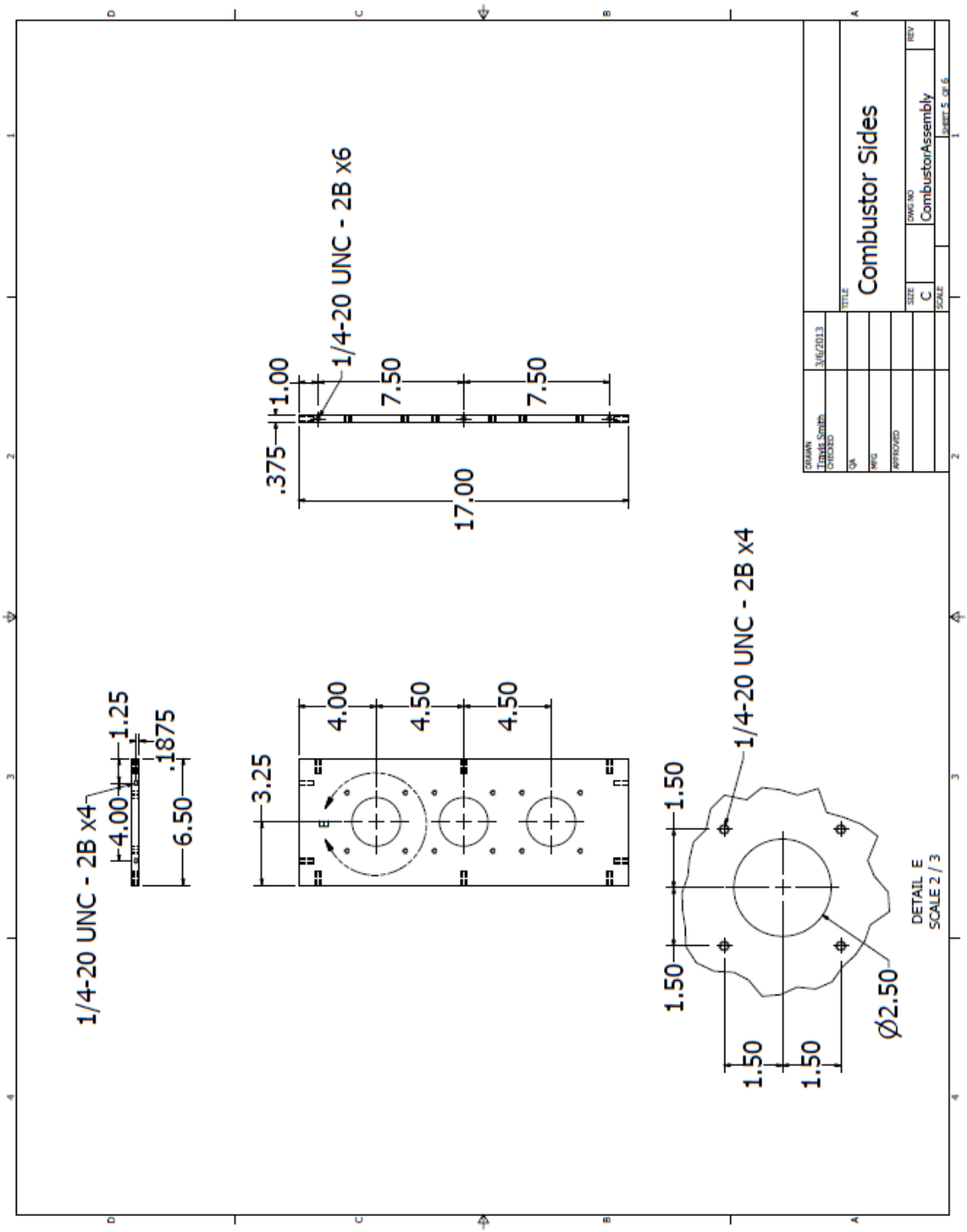
1/4-20 UNC - 2B x6
.375
1.00
7.50
7.50
17.00
1/4-20 UNC - 2B x4
4.00
1.25
.1875
6.50
3.25
4.00
4.50
4.50
1/4-20 UNC - 2B x4
1.50
1.50
1.50
1.50
Ø2.50
DETAIL E
SCALE 2 / 3
DRAWN
Travis Smith
3/6/2013
CHECKED
QA
MFG
APPROVED
TITLE
Combustor Sides
SIZE
C
DWG NO
CombustorAssembly
REV
SCALE
SHEET 5 OF 6

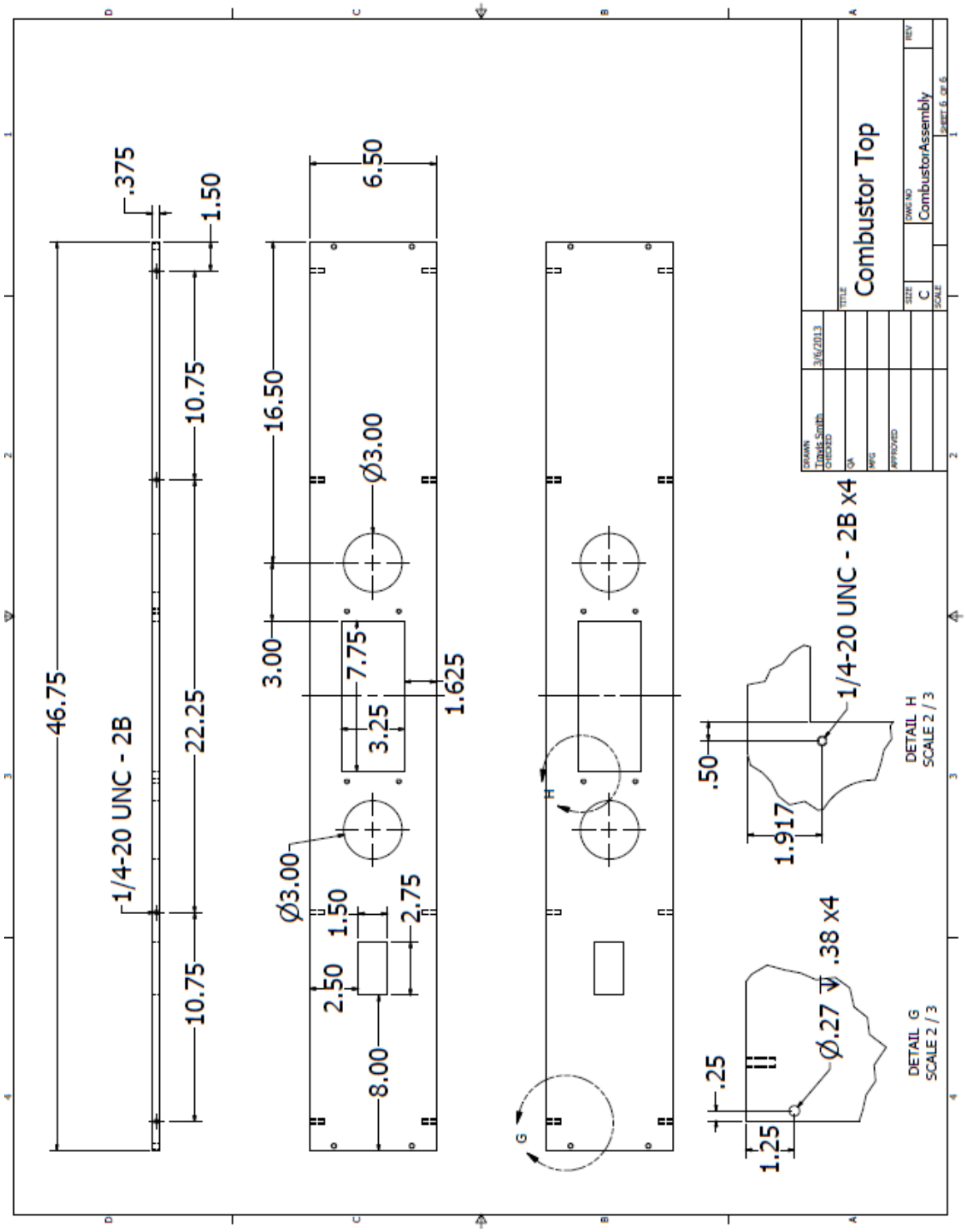
Combustor Top
DWG NO CombustorAssembly
SIZE C
SCALE
REV
DRAWN Travis Smith
CHECKED
QA
MFG
APPROVED
3/6/2013
TITLE
Sheet 6 of 6
46.75
.375
1.50
10.75
22.25
10.75
1/4-20 UNC - 2B
16.50
6.50
3.00
Ø3.00
7.75
3.25
1.625
Ø3.00
1.50
2.50
2.75
8.00
G
H
.50
1/4-20 UNC - 2B x4
1.917
DETAIL H
SCALE 2 / 3
.25
Ø.27 ⌀ .38 x4
1.25
DETAIL G
SCALE 2 / 3

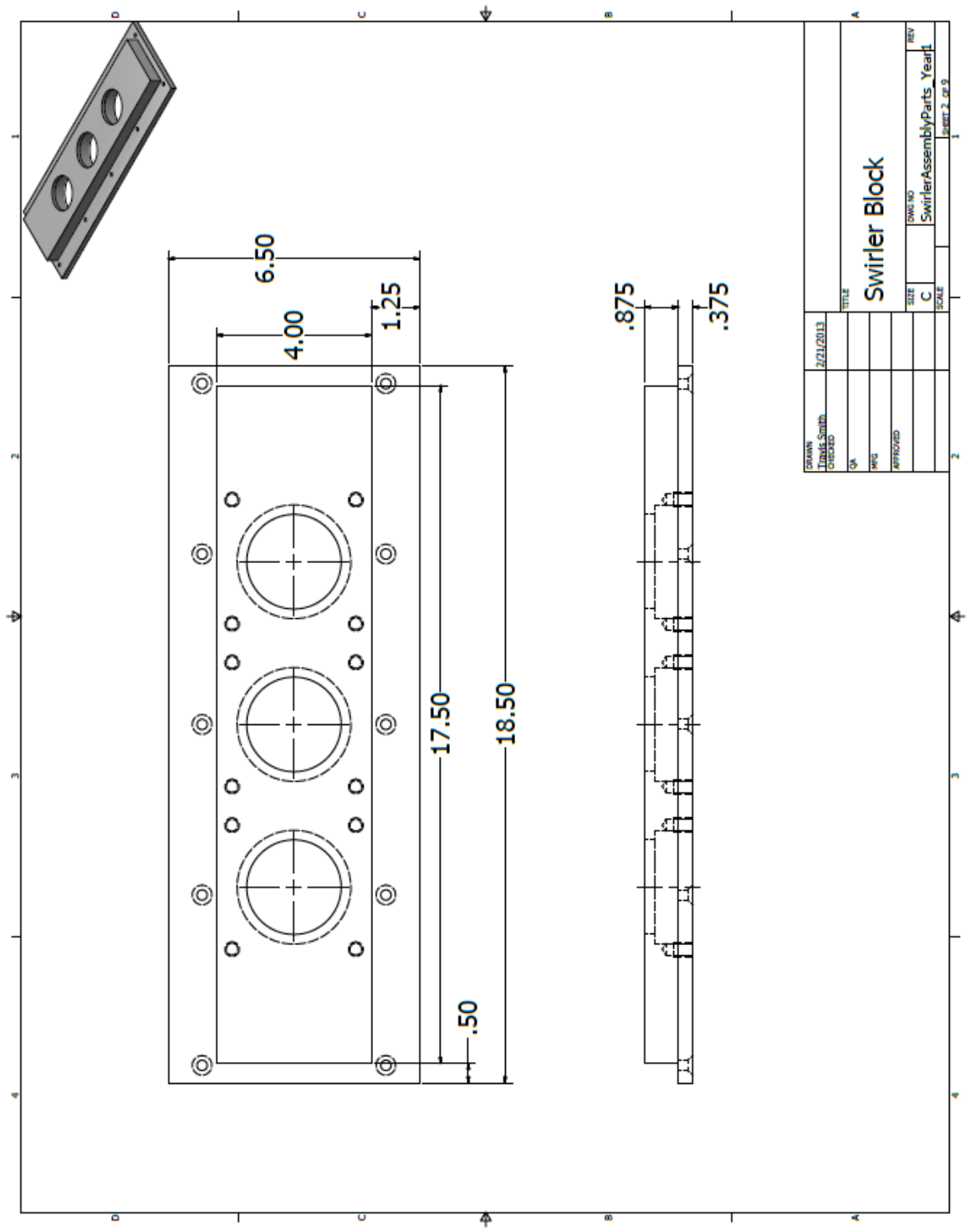
6.50
4.00
1.25
17.50
18.50
.50
.875
.375
Swirler Block
Travis Smith
2/21/2013
SwirlerAssemblyParts_Year1
SHEET 2 OF 9

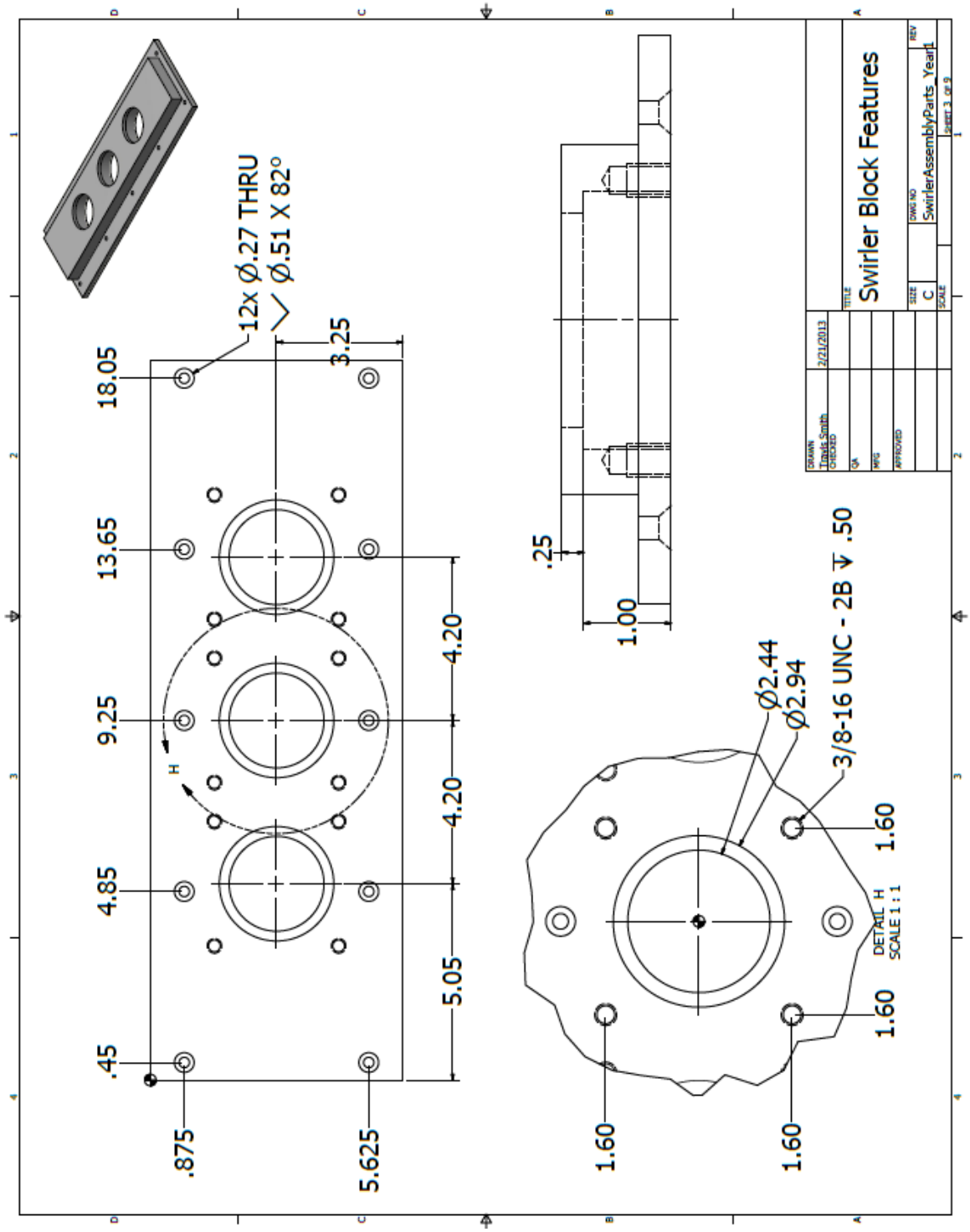
12x Ø.27 THRU
Ø.51 X 82°
3.25
18.05
13.65
9.25
4.85
.45
4.20
4.20
5.05
.875
5.625
.25
1.00
Ø2.44
Ø2.94
3/8-16 UNC - 2B ↧ .50
1.60
1.60
1.60
1.60
DETAIL H
SCALE 1 : 1
Swirler Block Features
SwirlerAssemblyParts_Year1
SIZE
C
SCALE
DWG NO
REV
DRAWN
Travis Smith
2/21/2013
CHECKED
QA
MFG
APPROVED

A.2 Ceramic Box

The ceramic box was designed to fit inside of the metal box without blocking any openings. It was made from Zircar RSLE-57 ceramic with a thickness of 0.5 inches. The bottom plate was designed so that the dump plane would be flush. The ceramic was glued to the metal box using a high temperature sealant.

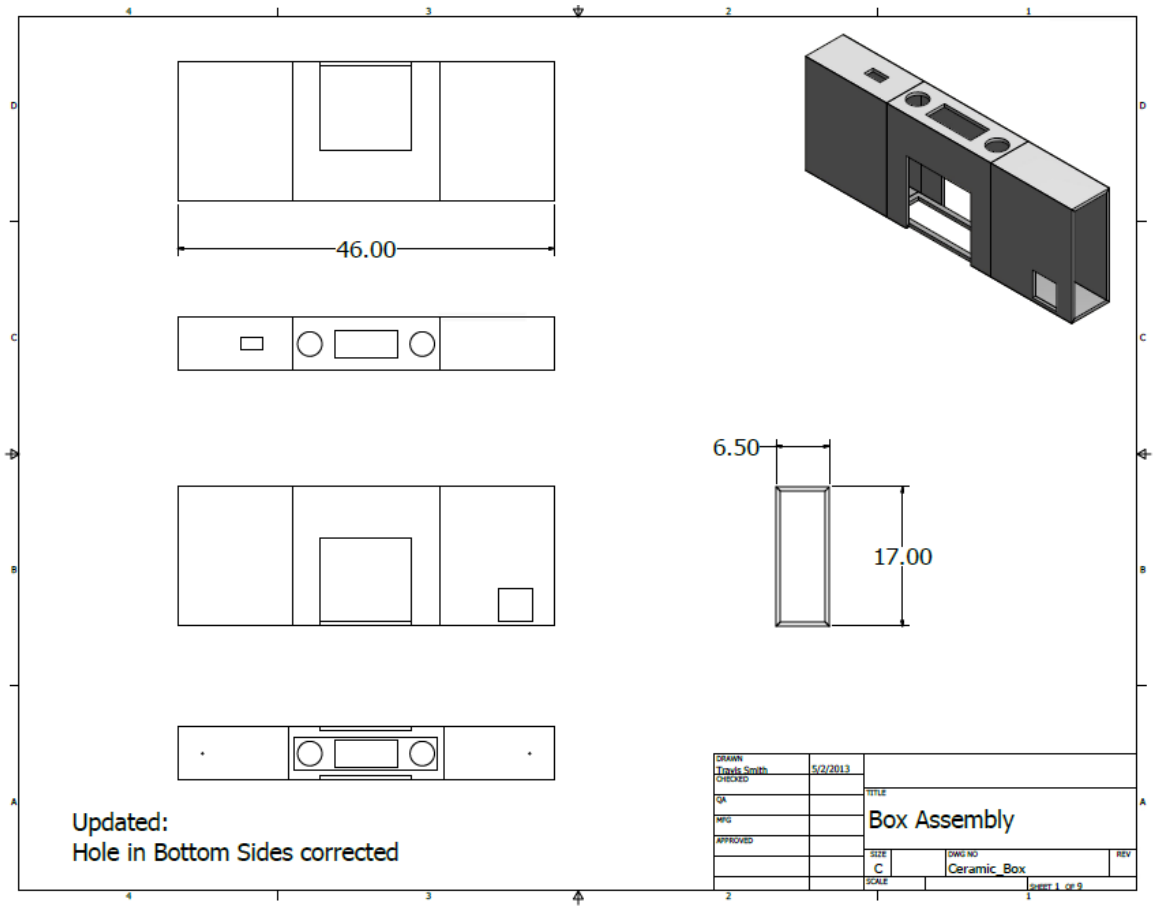

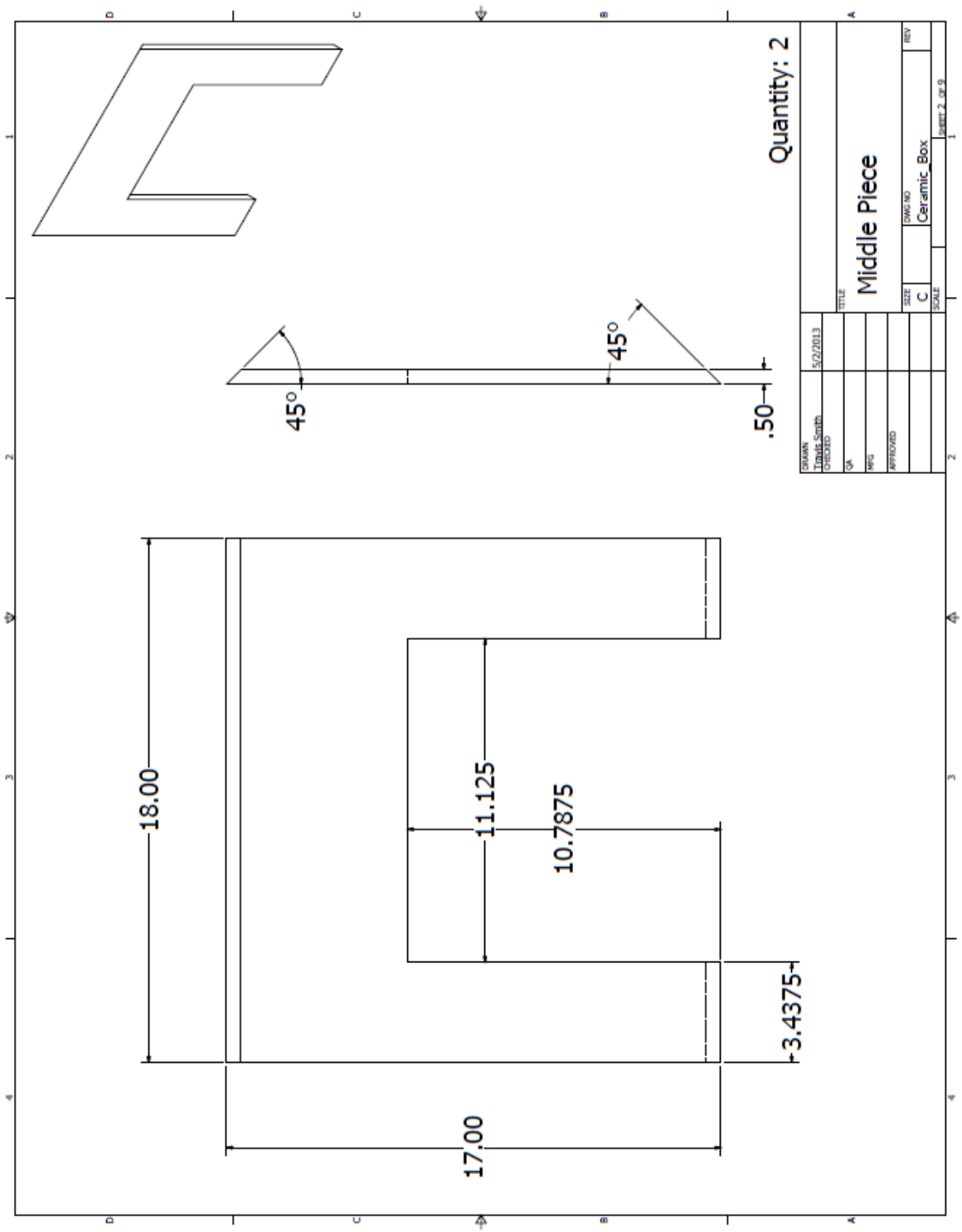
Quantity: 2
Middle Piece
Ceramic_Box
Travis Smith
5/2/2013
45°
45°
.50
18.00
11.125
10.7875
3.4375
17.00

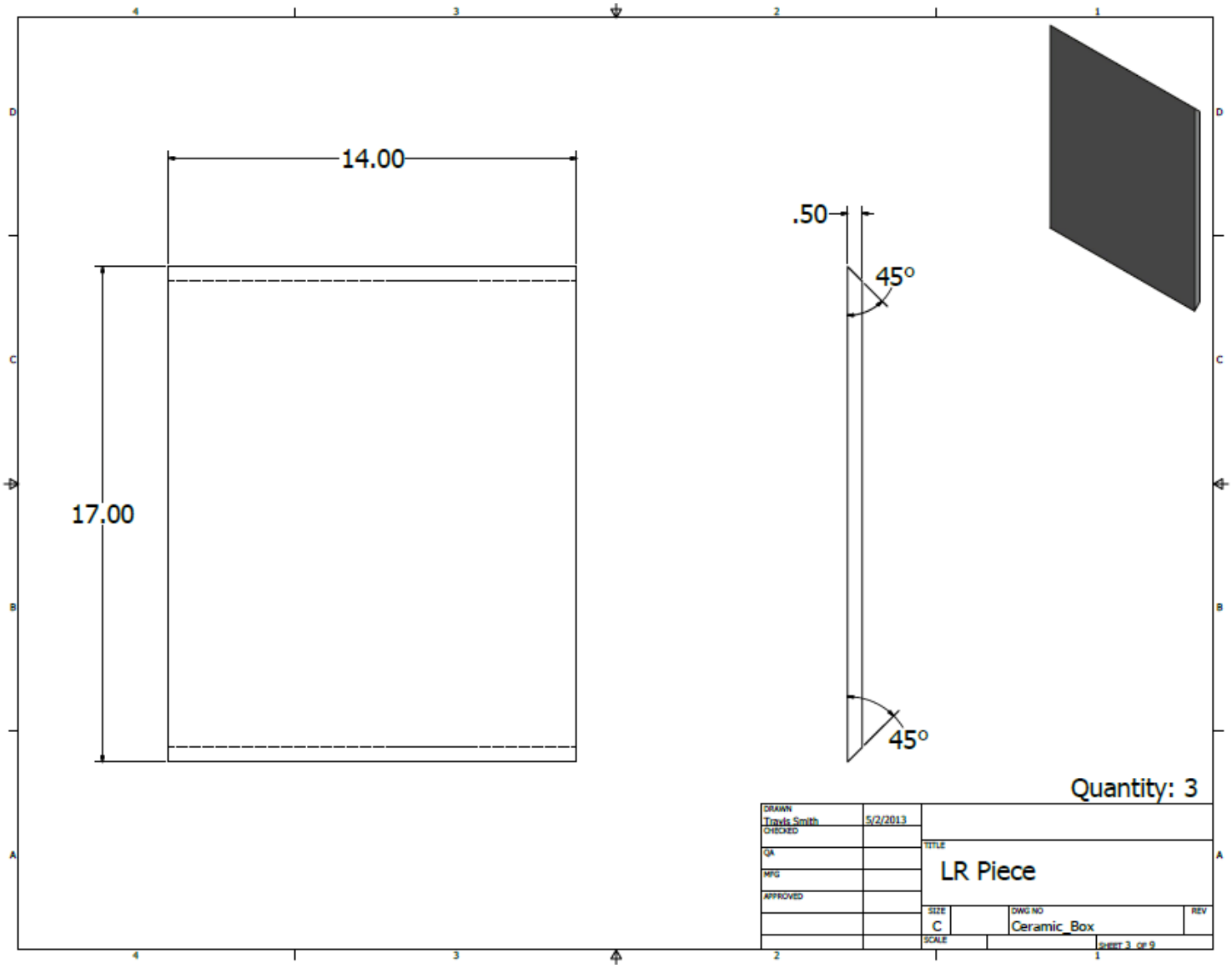
14.00
17.00
.50
45°
45°
Quantity: 3
DRAWN
Trayis Smith
5/2/2013
CHECKED
QA
MFG
APPROVED
TITLE
LR Piece
SIZE
C
DWG NO
Ceramic_Box
REV
SCALE
SHEET 3 OF 9

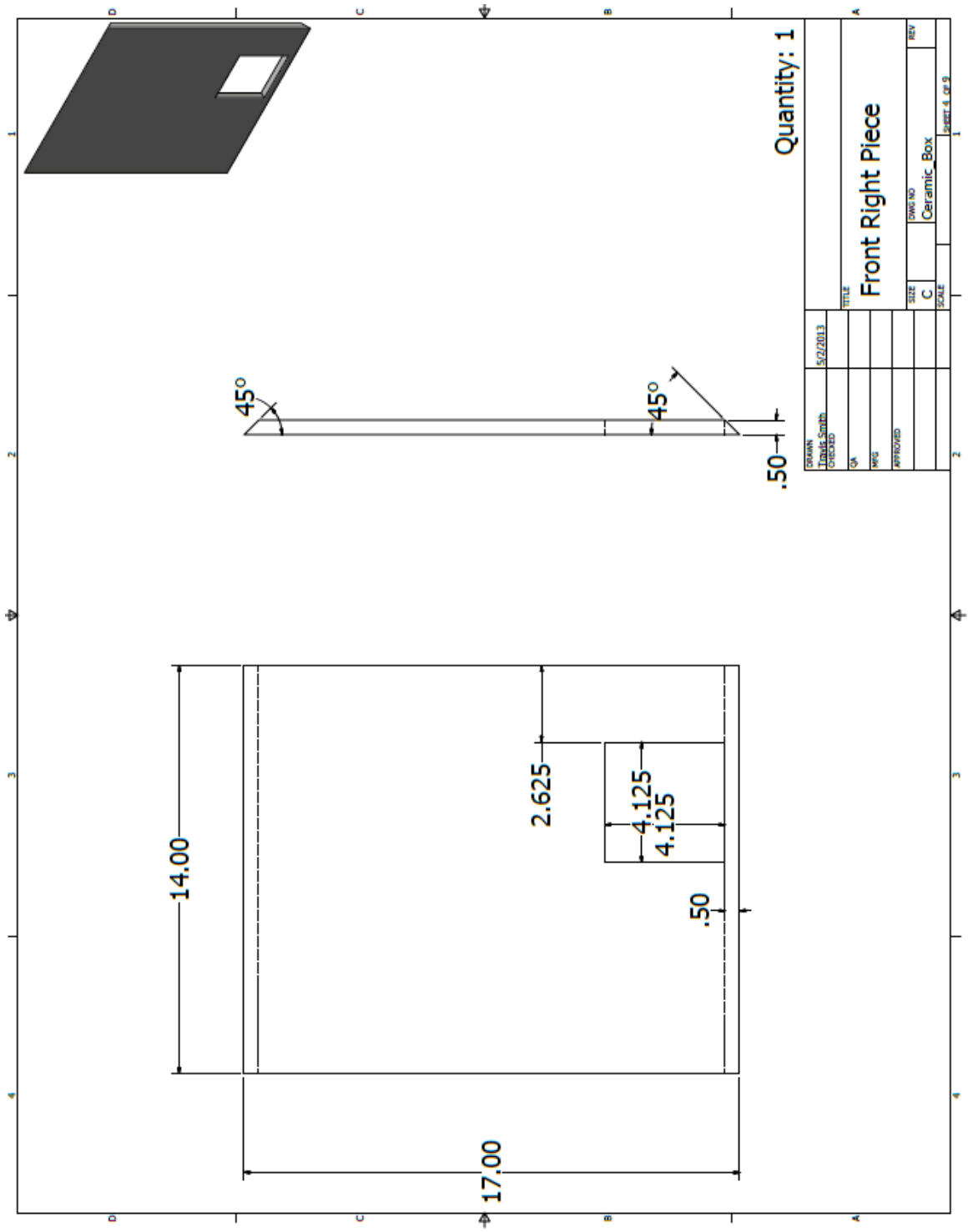
Quantity: 1
Front Right Piece
Ceramic_Box
Sheet 4 of 9
Travis Smith
5/2/2013
45°
45°
.50
14.00
17.00
2.625
4.125
4.125
.50

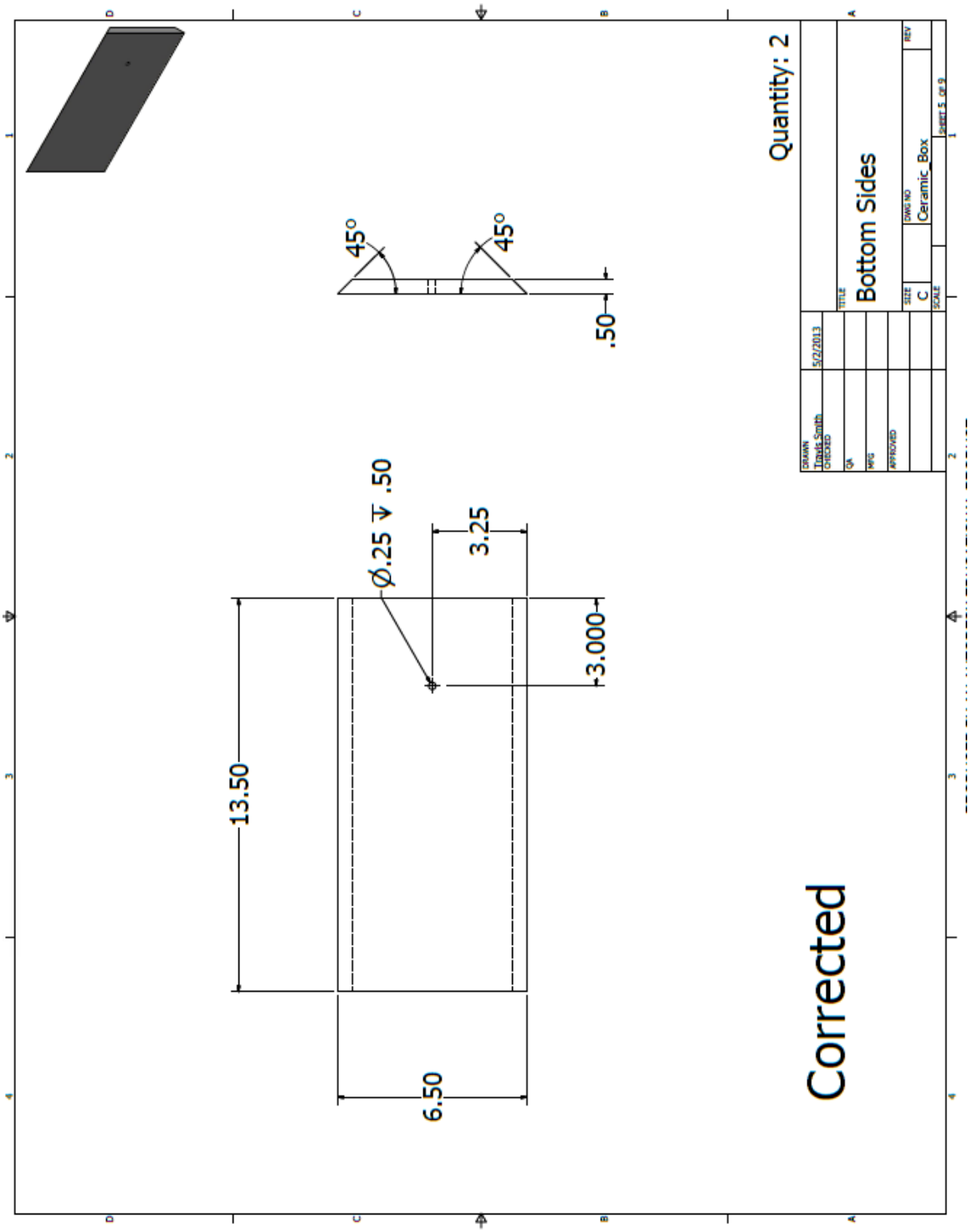
Quantity: 2
Bottom Sides
Ceramic_Box
Corrected
45°
45°
.50
Ø.25 ⌖ .50
3.25
3.000
13.50
6.50

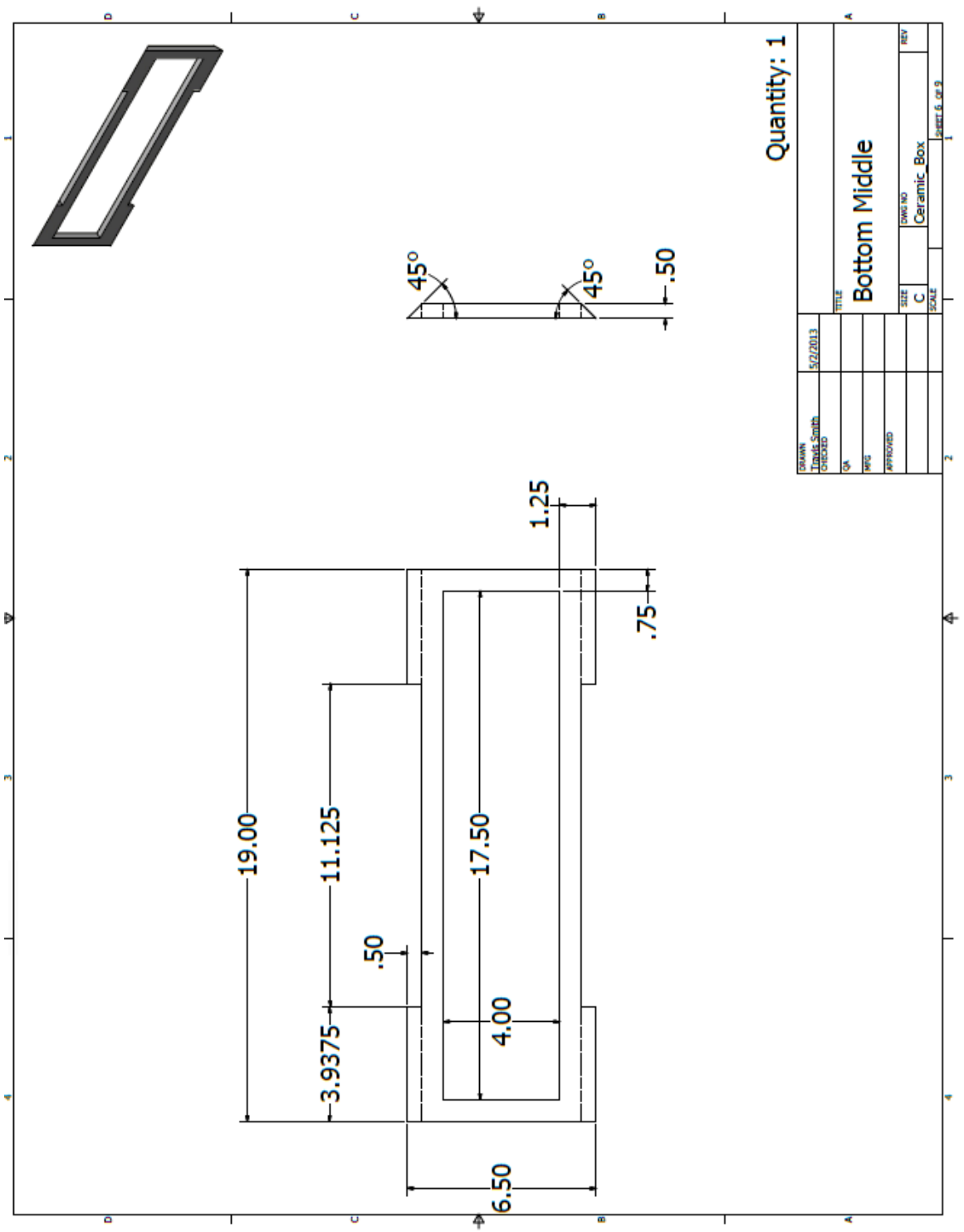
Quantity: 1
Bottom Middle
Ceramic_Box
Travis Smith
5/2/2013
45°
45°
.50
1.25
.75
19.00
11.125
17.50
.50
4.00
3.9375
6.50

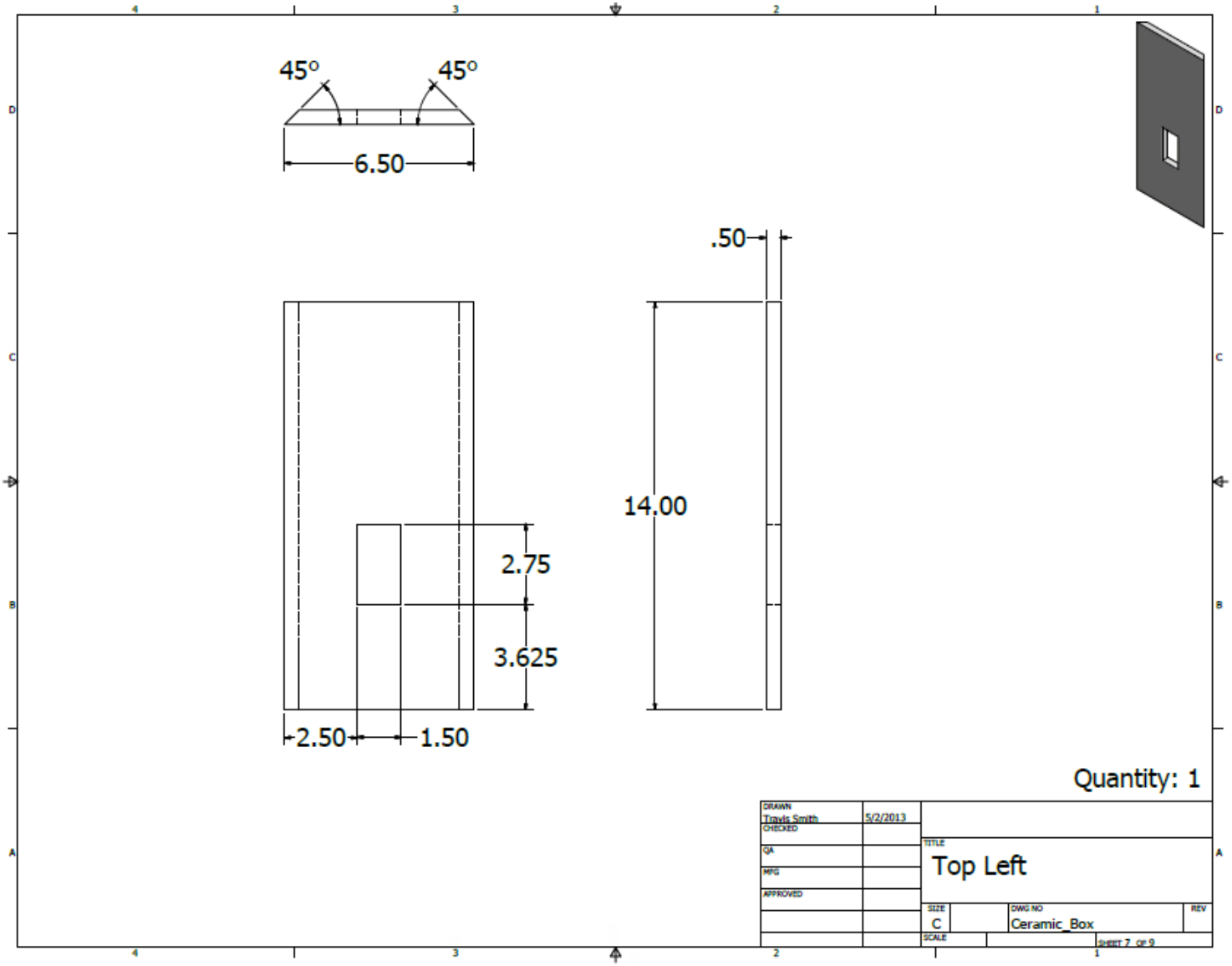
45°
45°
6.50
.50
14.00
2.75
3.625
2.50
1.50
Quantity: 1
DRAWN
Travis Smith
5/2/2013
CHECKED
QA
MFG
APPROVED
TITLE
Top Left
SIZE
C
DWG NO
Ceramic_Box
REV
SCALE
SHEET 7 OF 9

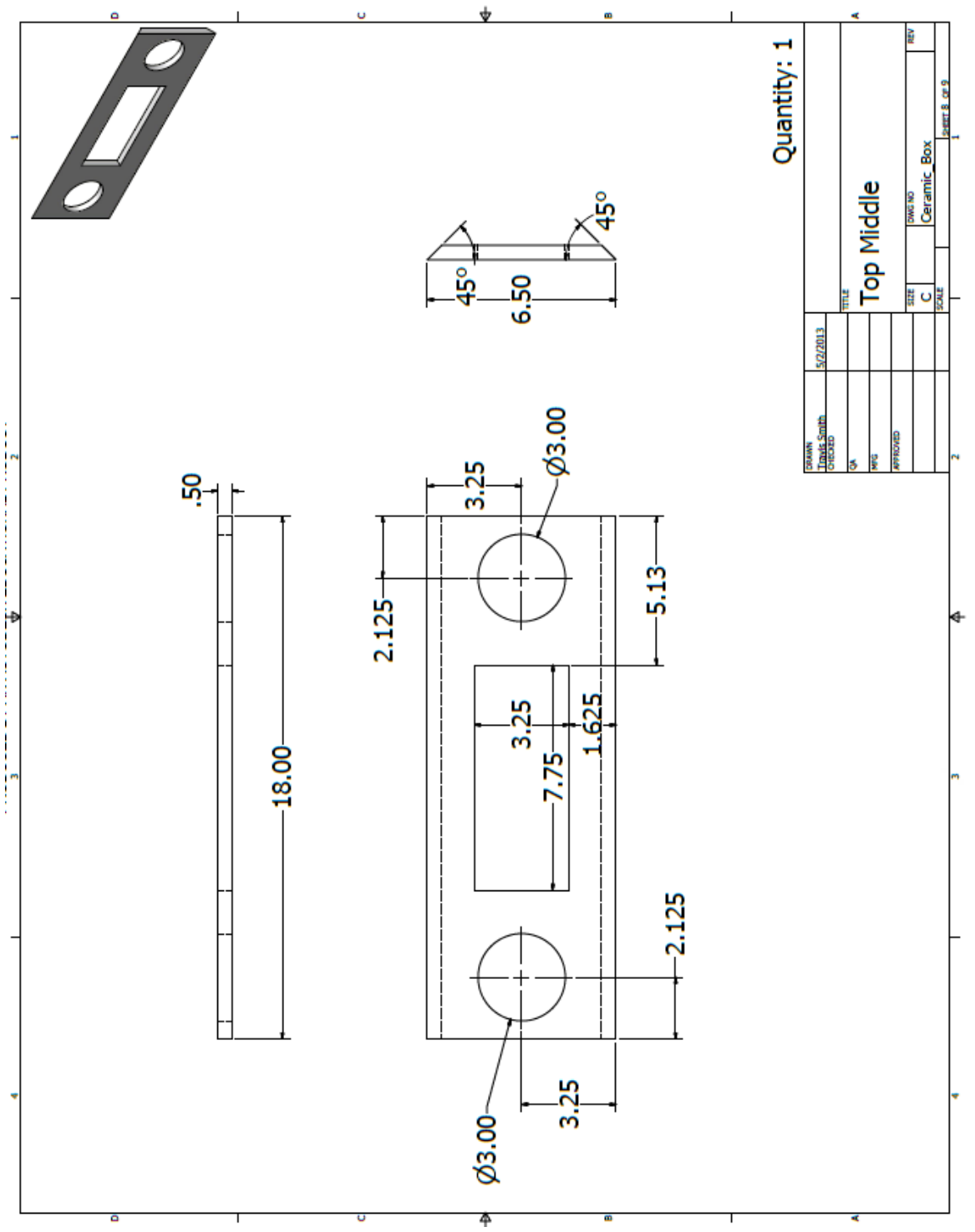
Quantity: 1
Top Middle
Ceramic_Box
DRAWN
Travis Smith
5/2/2013
CHECKED
QA
MFG
APPROVED
SIZE
C
SCALE
REV
SHEET 8 OF 9
45°
45°
6.50
.50
18.00
3.25
Ø3.00
2.125
5.13
3.25
1.625
7.75
2.125
3.25
Ø3.00

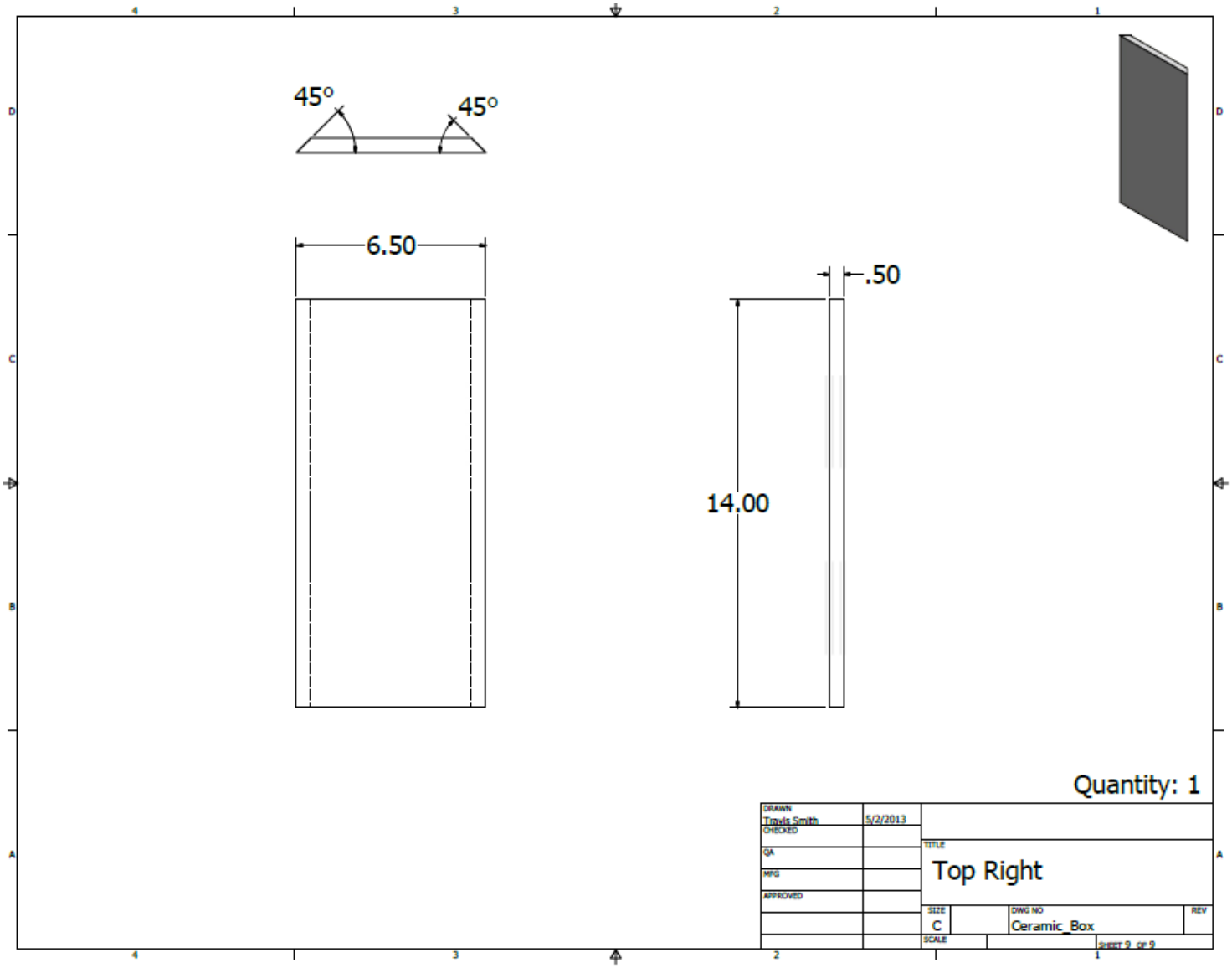
45°
45°
6.50
.50
14.00
Quantity: 1
DRAWN
Travis Smith
5/2/2013
CHECKED
QA
MFG
APPROVED
TITLE
Top Right
SIZE
C
DWG NO
Ceramic_Box
REV
SCALE
SHEET 9 OF 9

A.3 Windows

The front and back windows were repurposed from a previous experiment by Jacqueline O'Connor [128]. Below are shown the drawings for the frames. For the front and back windows, an 1/8" graphite gasket sealed the 0.25" thick quartz glass between the stainless steel window frames. For the top window, a 0.25" window was sealed against the top of the combustor using the same gasket material. A third window frame on the side was added to allow a laser sheet to enter the combustor. The hole pattern of this window was set to match the hole pattern of the side piece, which was also adjusted to allow the laser to enter near the dump plane.

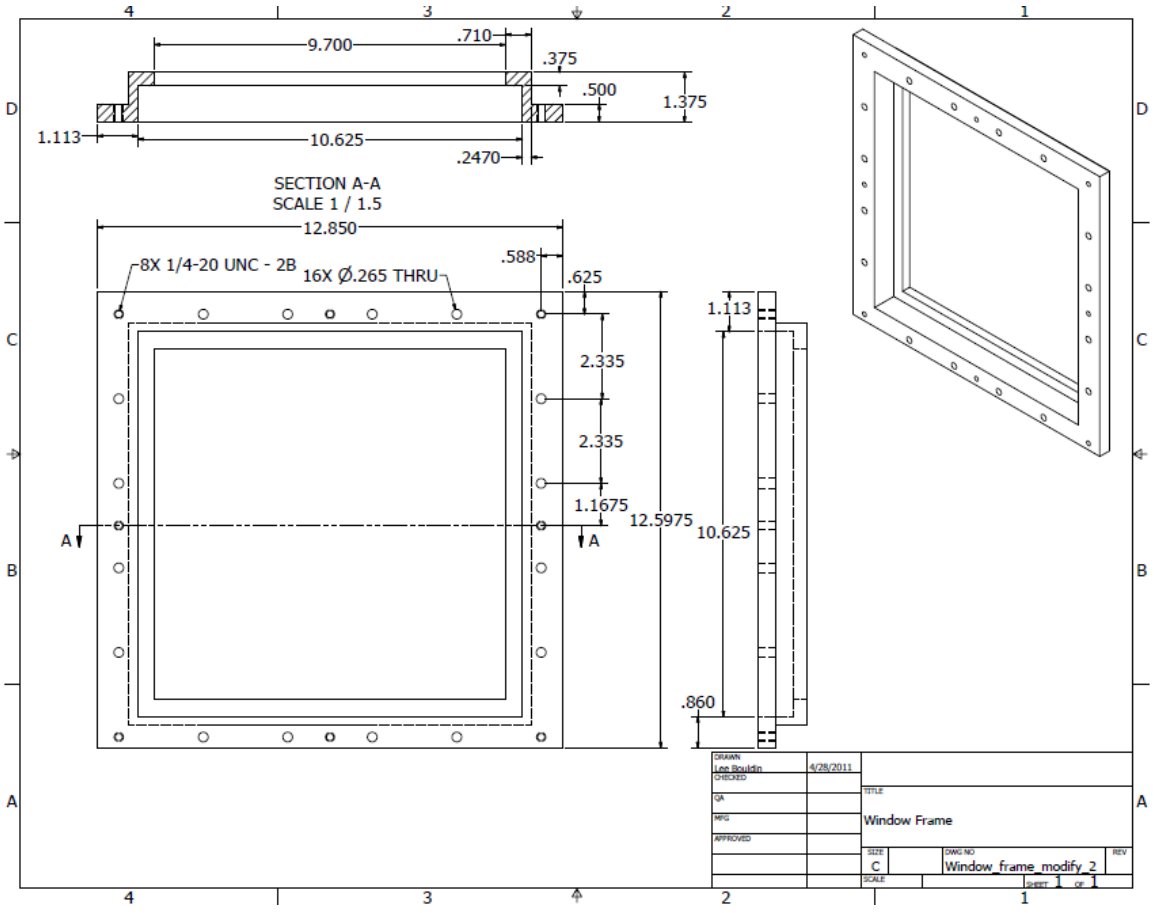

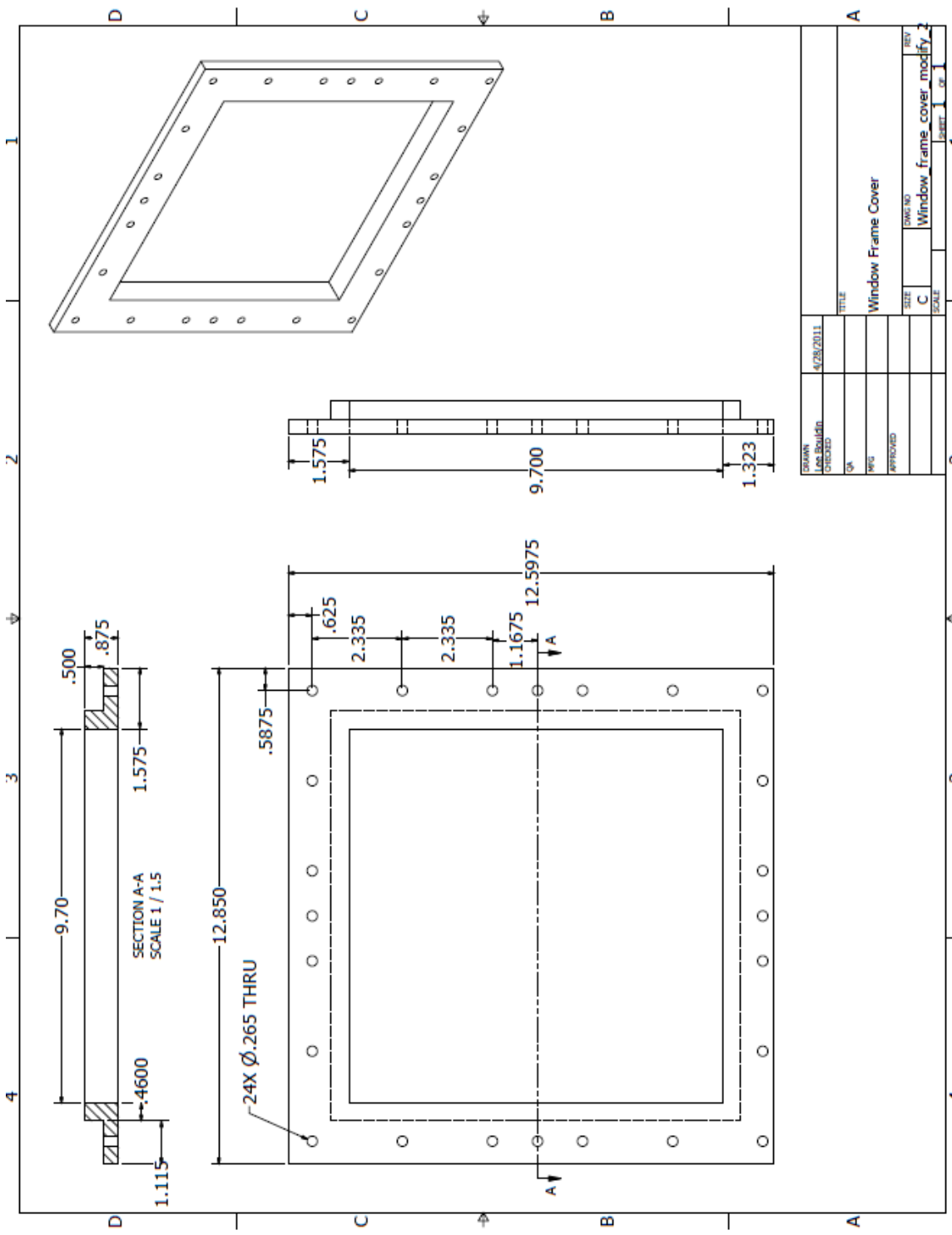
Window Frame Cover
Window_frame_cover_modify_2
4/28/2011
Lee Boulden
SIZE
C
SCALE
SHEET 1 OF 1
1.575
9.700
1.323
12.5975
.625
2.335
2.335
1.1675
.5875
12.850
24X Ø.265 THRU
.500
.875
1.575
9.70
.4600
1.115
SECTION A-A
SCALE 1 / 1.5

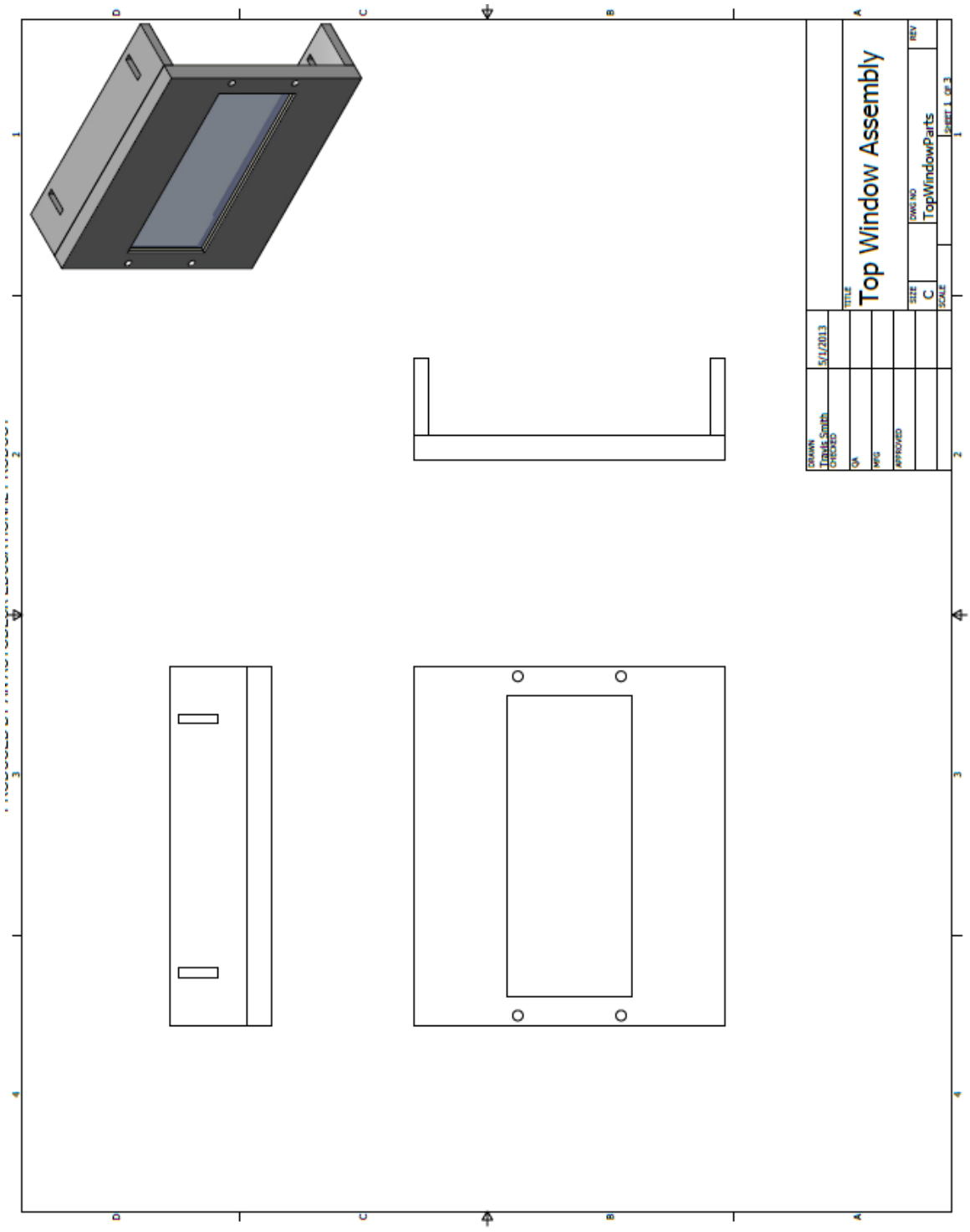
Top Window Assembly
TopWindowParts
C
5/1/2013
Travis Smith

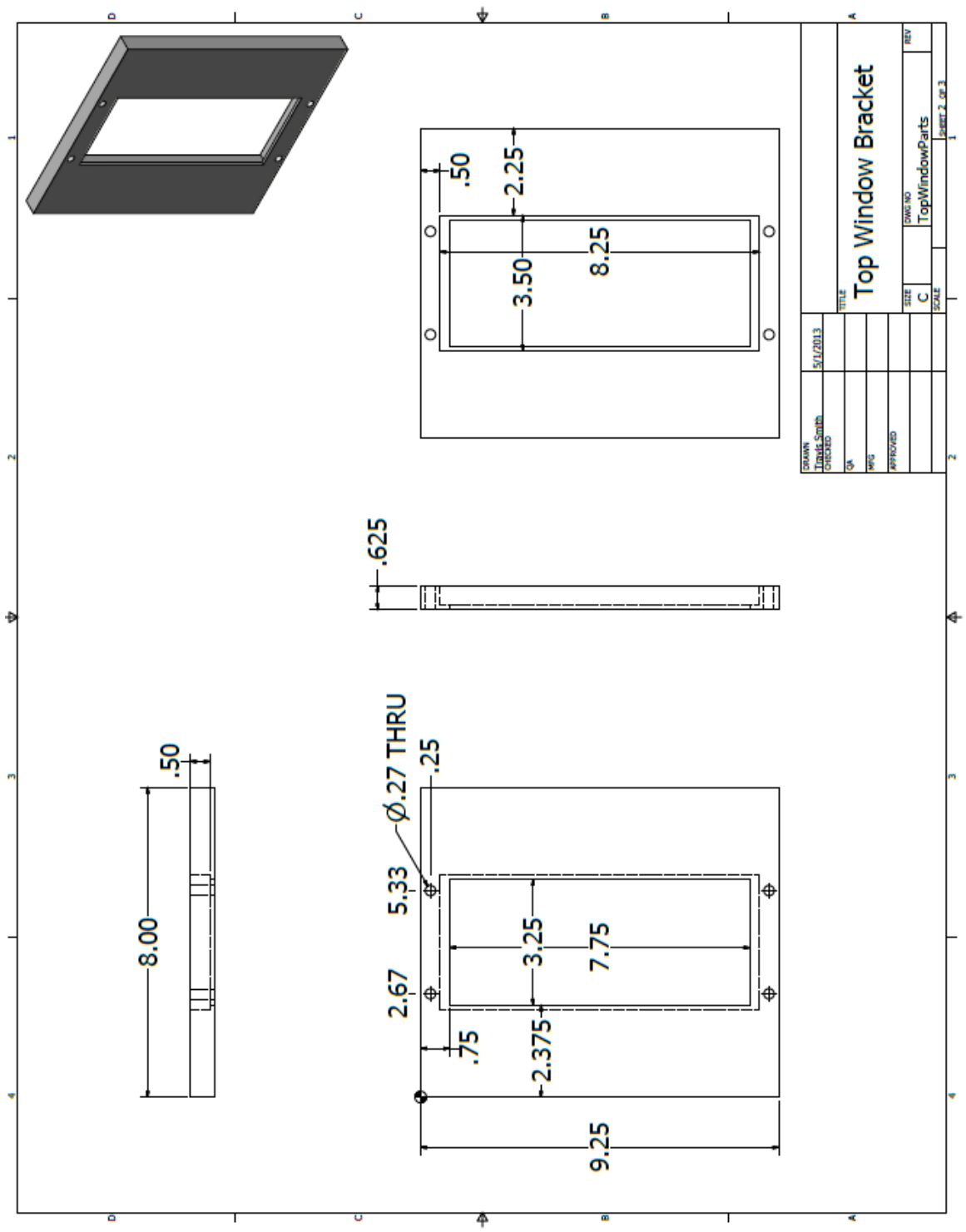
Top Window Bracket
TopWindowParts
Travis Smith
5/1/2013
.50
2.25
8.25
3.50
.625
.50
8.00
Ø.27 THRU
.25
5.33
3.25
7.75
2.67
.75
2.375
9.25

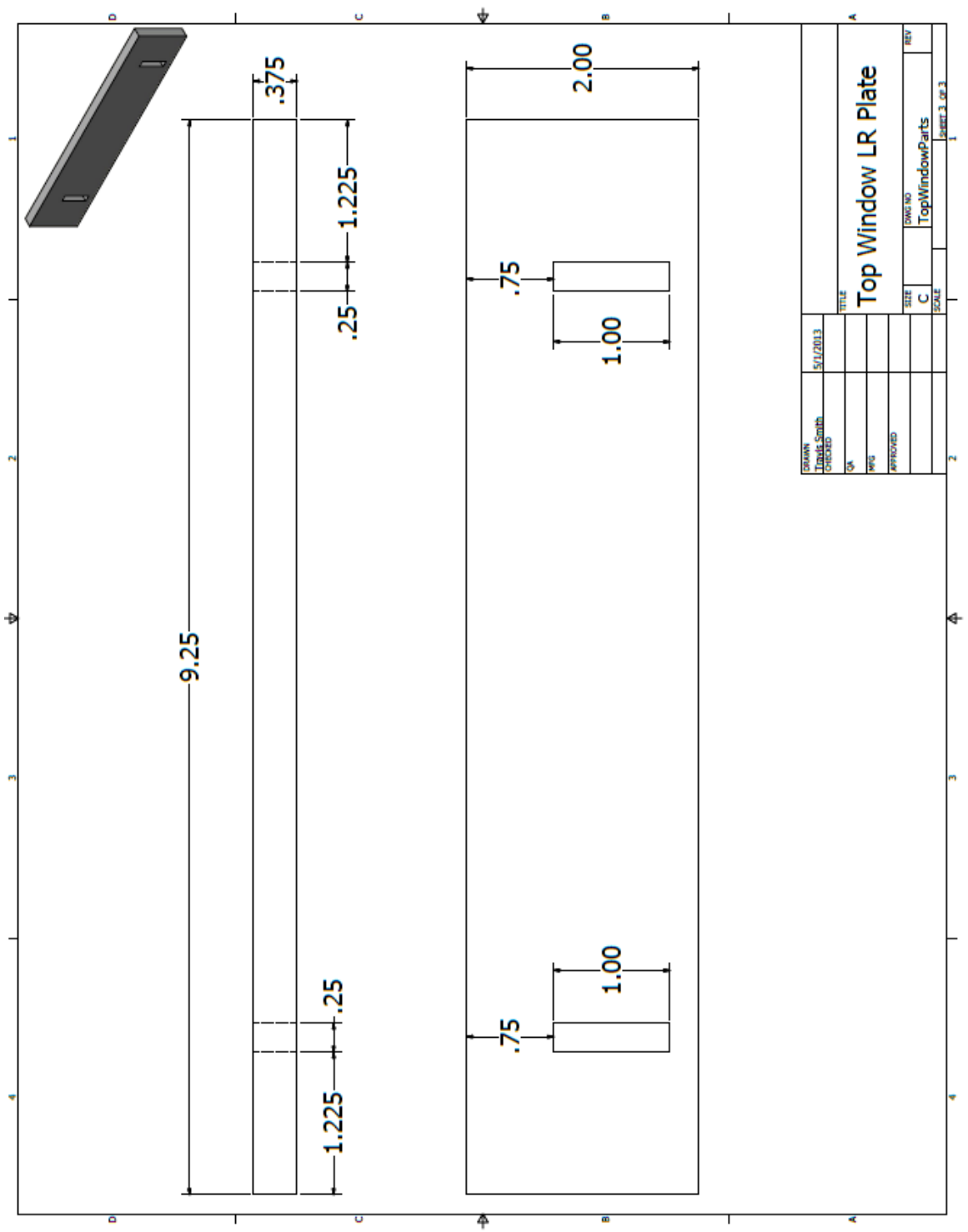
.375
1.225
.25
9.25
.25
1.225
2.00
.75
1.00
.75
1.00
Top Window LR Plate
TopWindowParts
5/1/2013
Travis Smith
C

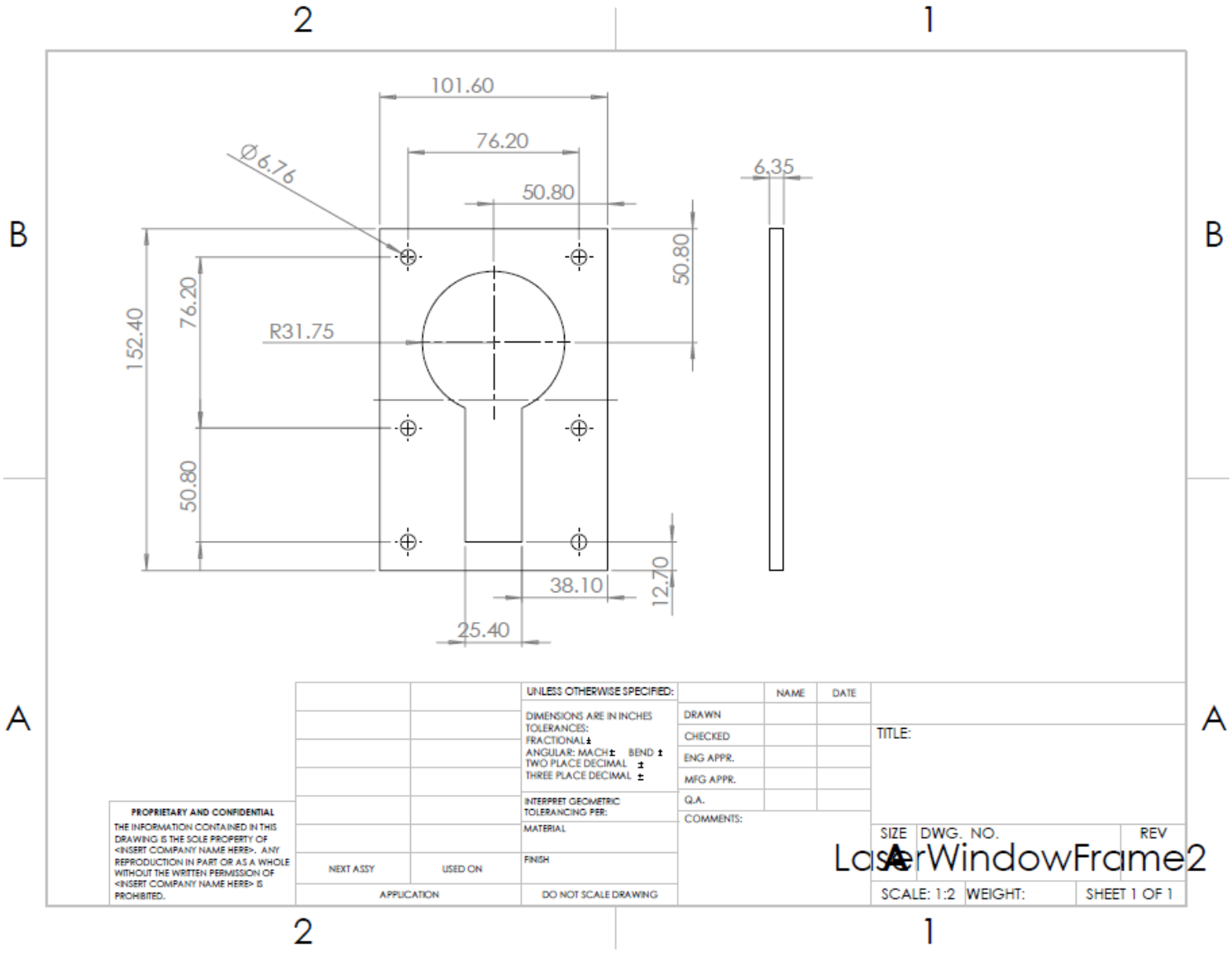
2
1
B
A
101.60
76.20
Ø6.76
50.80
6.35
50.80
76.20
152.40
R31.75
50.80
38.10
12.70
25.40
UNLESS OTHERWISE SPECIFIED:
DIMENSIONS ARE IN INCHES
TOLERANCES:
FRACTIONAL ±
ANGULAR: MACH ± BEND ±
TWO PLACE DECIMAL ±
THREE PLACE DECIMAL ±
INTERPRET GEOMETRIC TOLERANCING PER:
MATERIAL
FINISH
DO NOT SCALE DRAWING
NAME
DATE
DRAWN
CHECKED
ENG APPR.
MFG APPR.
Q.A.
COMMENTS:
TITLE:
SIZE
DWG. NO.
REV
LaserWindowFrame2
SCALE: 1:2
WEIGHT:
SHEET 1 OF 1
NEXT ASSY
USED ON
APPLICATION
PROPRIETARY AND CONFIDENTIAL
THE INFORMATION CONTAINED IN THIS DRAWING IS THE SOLE PROPERTY OF <INSERT COMPANY NAME HERE>. ANY REPRODUCTION IN PART OR AS A WHOLE WITHOUT THE WRITTEN PERMISSION OF <INSERT COMPANY NAME HERE> IS PROHIBITED.

A.4 Nozzle Design

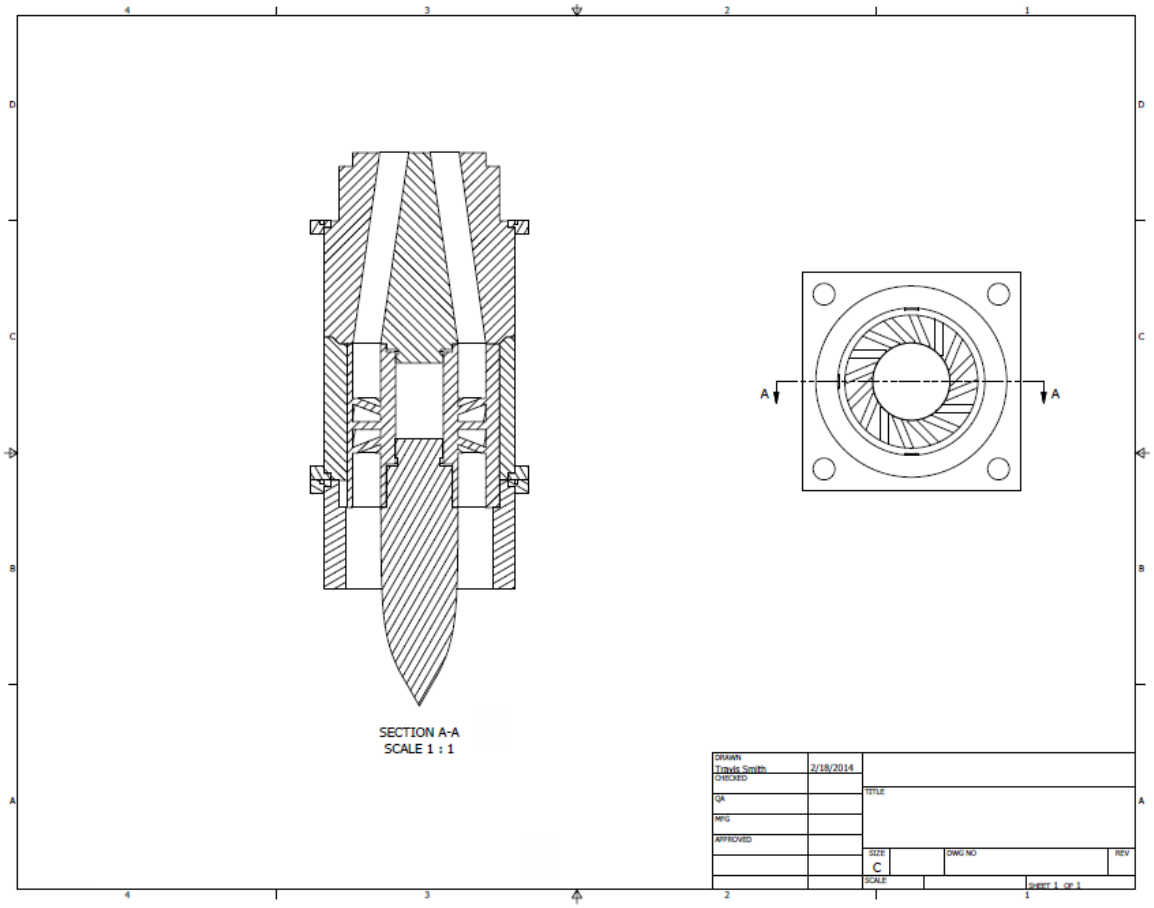

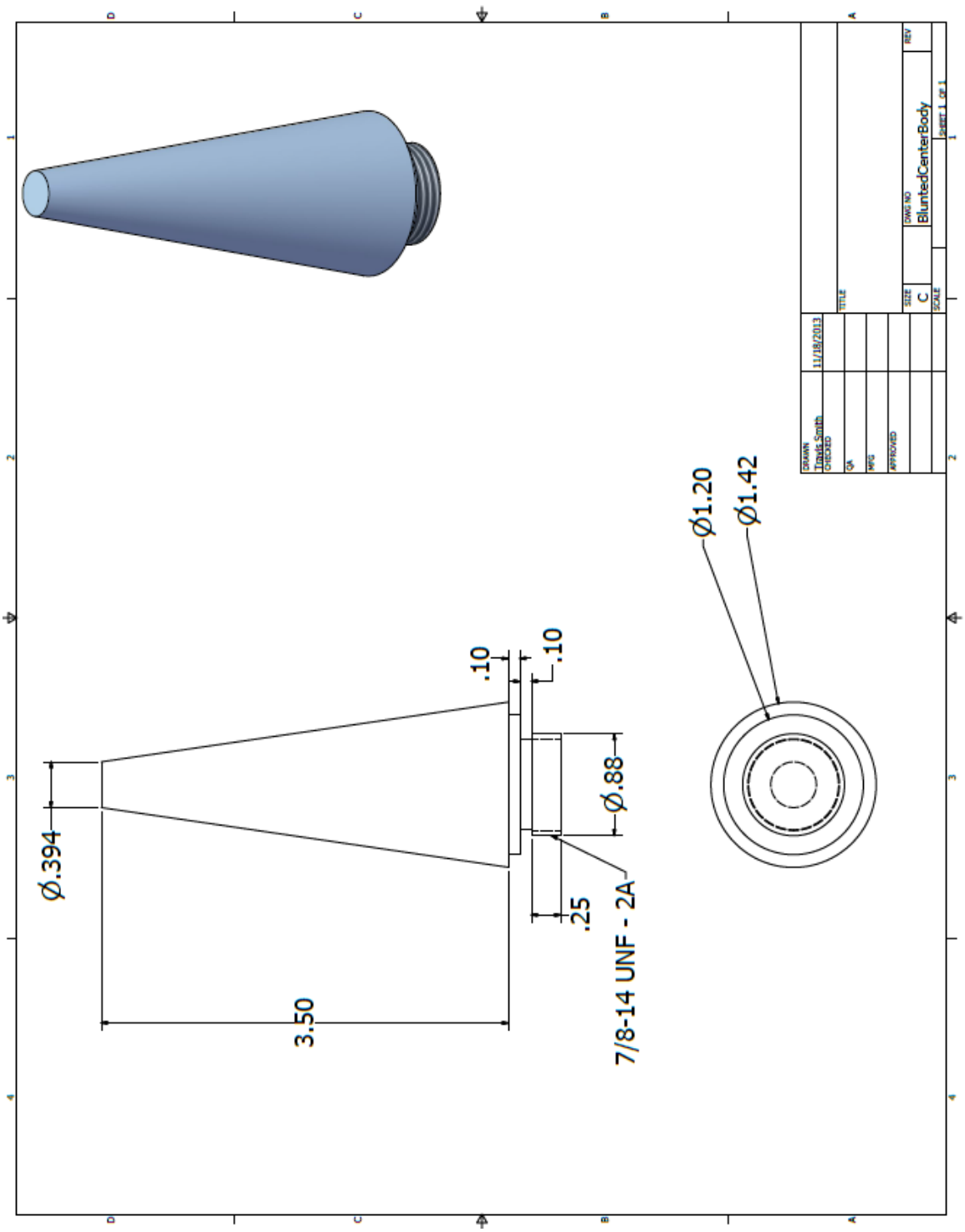
Ø.394
3.50
.10
.10
.25
Ø.88
7/8-14 UNF - 2A
Ø1.20
Ø1.42
DRAWN
Travis Smith
11/18/2013
CHECKED
QA
MFG
APPROVED
TITLE
SIZE
C
DWG NO
BluntedCenterBody
REV
SCALE
SHEET 1 OF 1

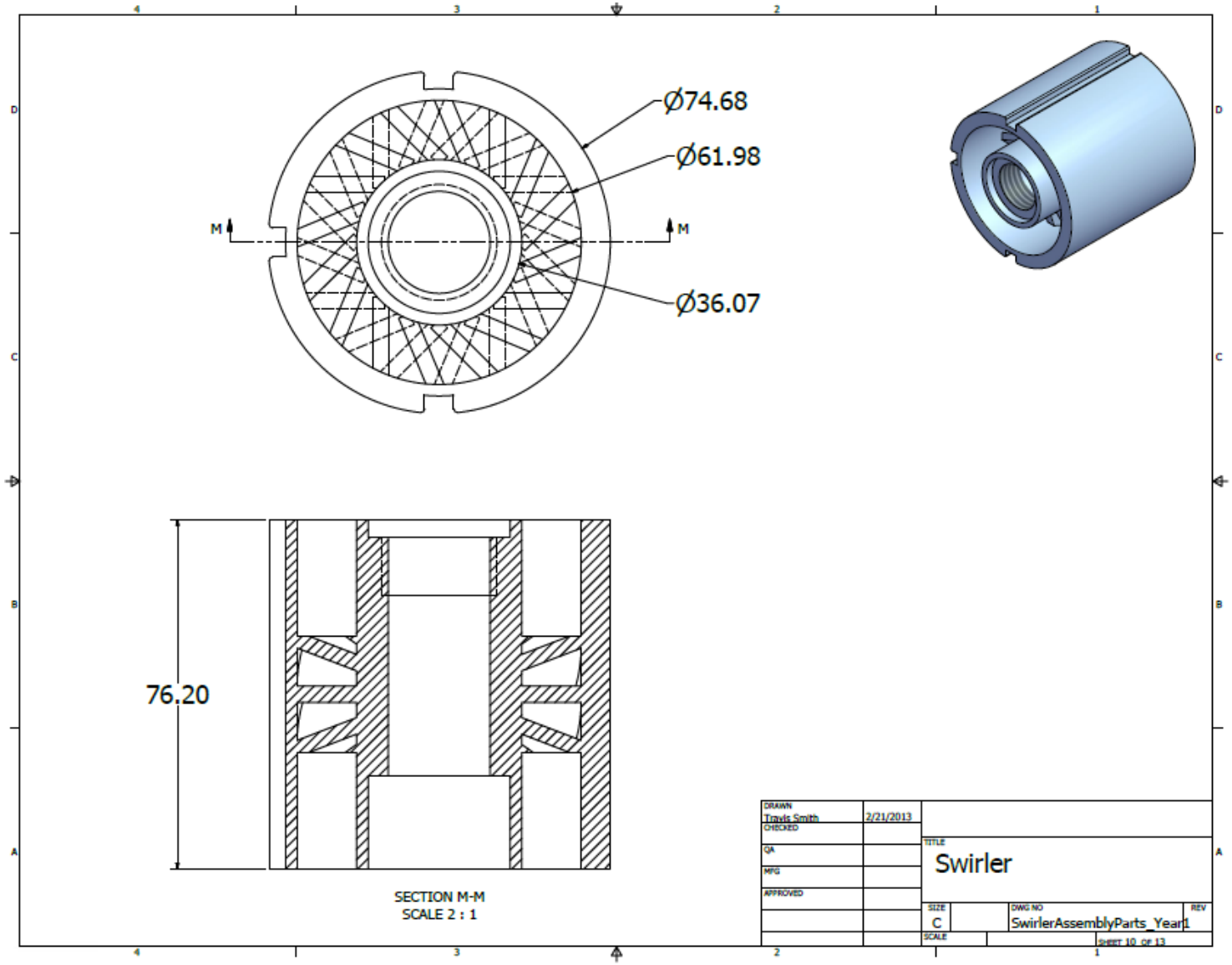
Ø74.68
Ø61.98
Ø36.07
M
M
76.20
SECTION M-M
SCALE 2 : 1
DRAWN
Travis Smith
2/21/2013
CHECKED
QA
MFG
APPROVED
TITLE
Swirler
SIZE
C
DWG NO
SwirlerAssemblyParts_Year1
REV
SCALE
SHEET 10 OF 13

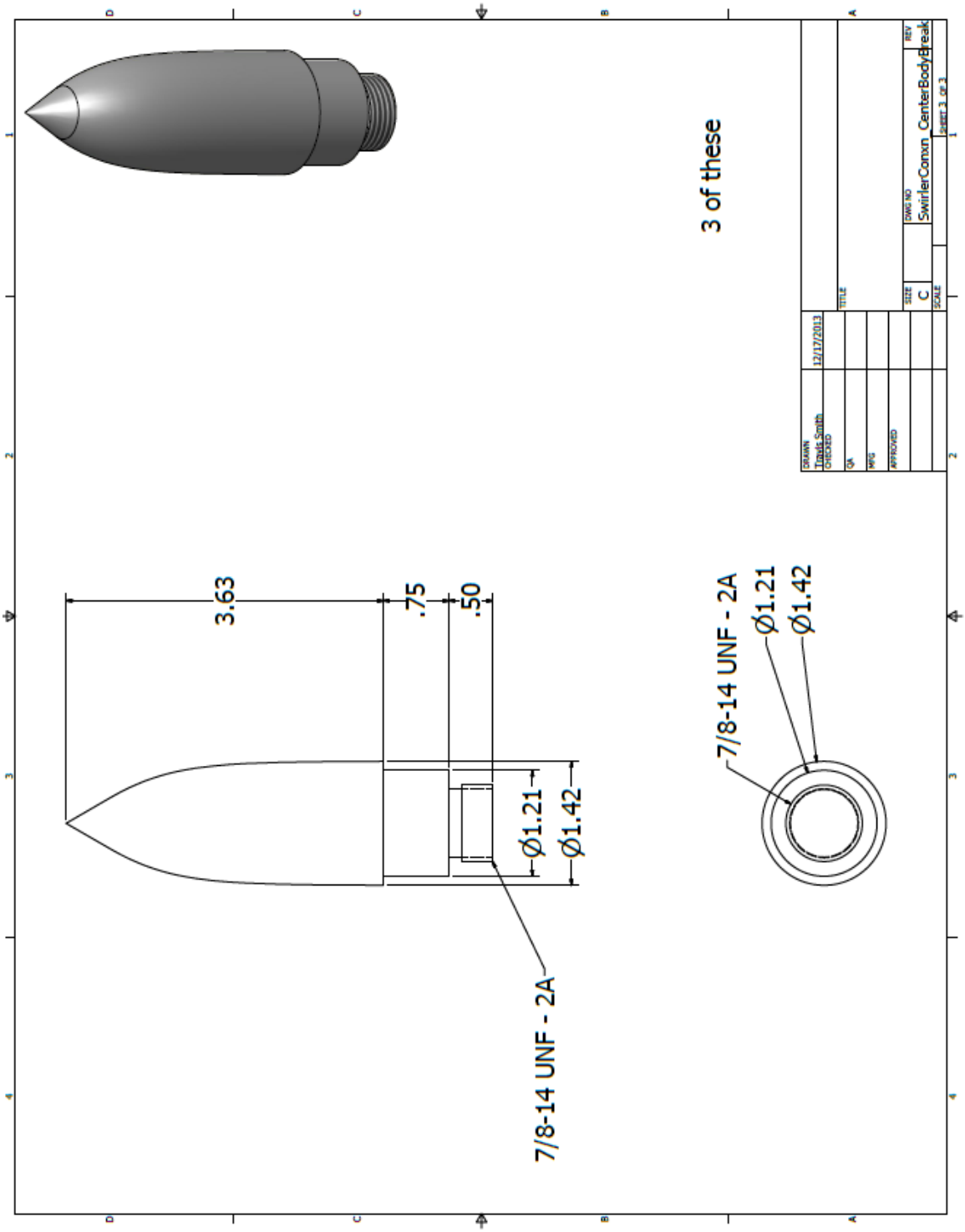
3 of these
3.63
.75
.50
Ø1.21
Ø1.42
7/8-14 UNF - 2A
7/8-14 UNF - 2A
Ø1.21
Ø1.42
DRAWN
Travis Smith
12/17/2013
CHECKED
QA
MFG
APPROVED
TITLE
SIZE
C
DWG NO
SwirlerConxn_CenterBody_Break
REV
SCALE
SHEET 3 OF 3

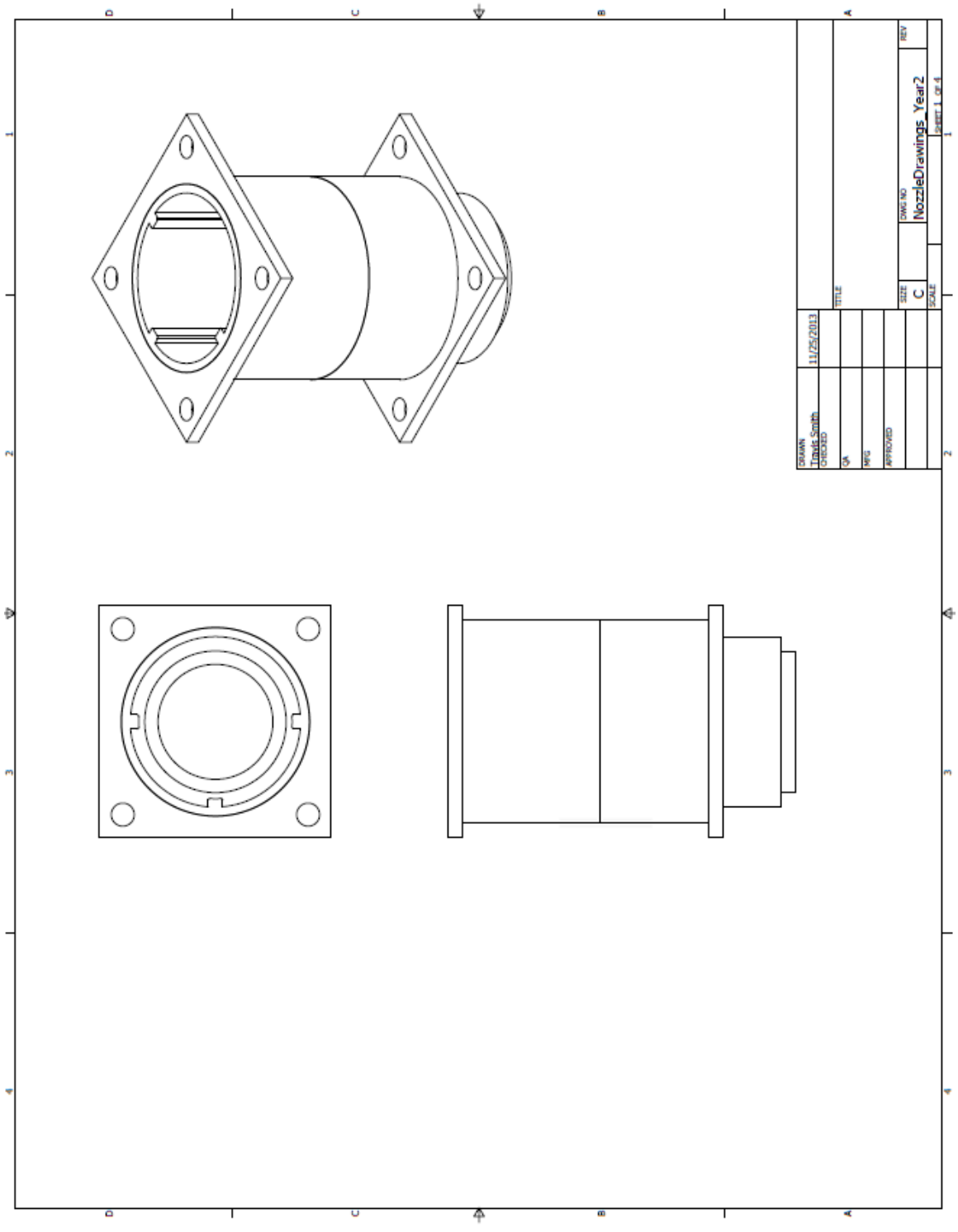
DRAWN
Tayds Smith
11/25/2013
CHECKED
QA
MFG
APPROVED
TITLE
SIZE
C
DWG NO
NozzleDrawings_Year2
REV
SCALE
SHEET 1 OF 4

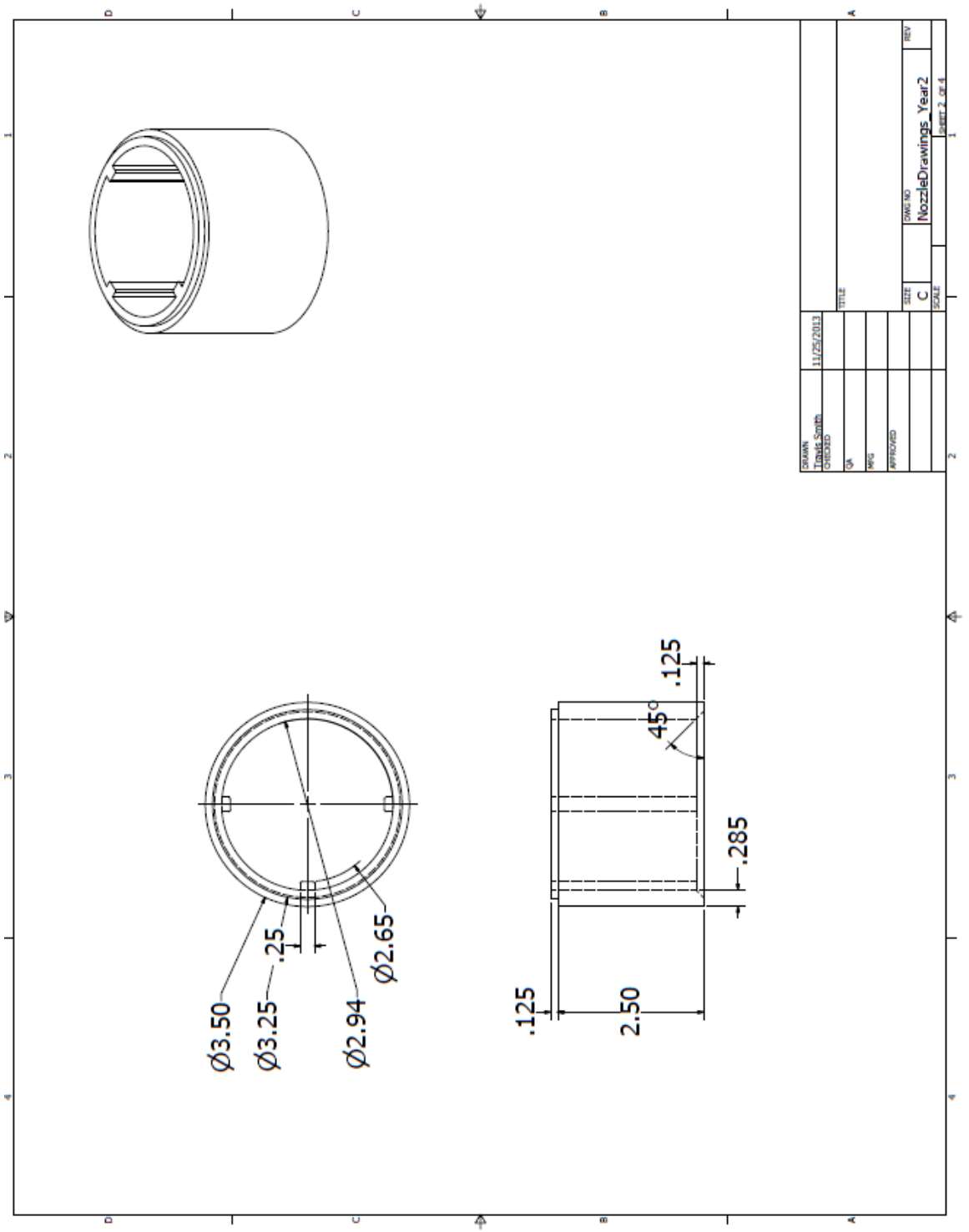
DRAWN
Travis Smith
11/25/2013
CHECKED
QA
MFG
APPROVED
TITLE
SIZE
C
SCALE
DWG NO
NozzleDrawings_Year2
REV
SHEET 2 OF 4
Ø3.50
Ø3.25
.25
Ø2.94
Ø2.65
.125
45°
.285
.125
2.50

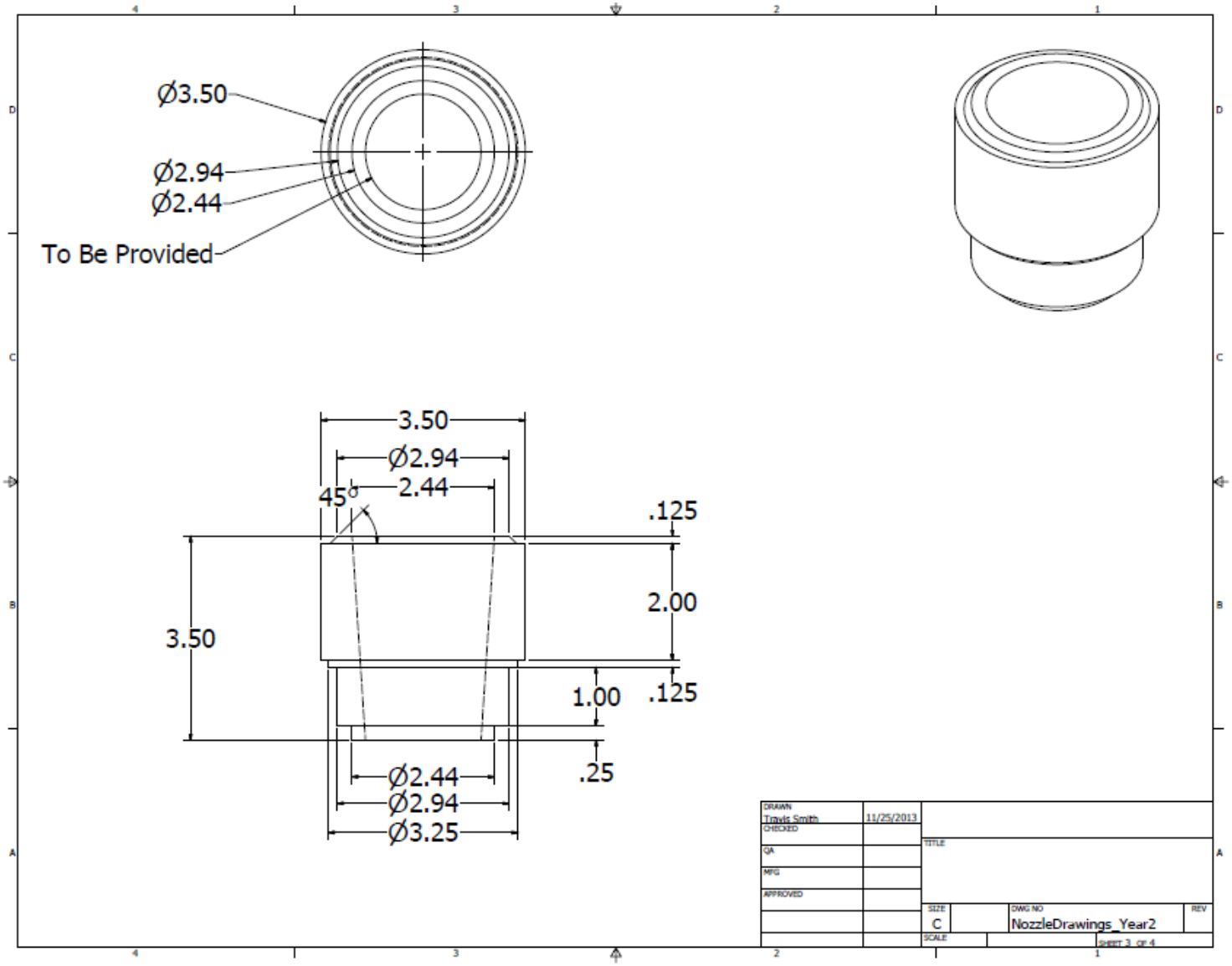
Ø3.50
Ø2.94
Ø2.44
To Be Provided
3.50
Ø2.94
2.44
45°
.125
2.00
3.50
1.00
.125
.25
Ø2.44
Ø2.94
Ø3.25
DRAWN
Travis Smith
11/25/2013
CHECKED
QA
MFG
APPROVED
TITLE
SIZE
C
DWG NO
NozzleDrawings_Year2
REV
SCALE
SHEET 3 OF 4

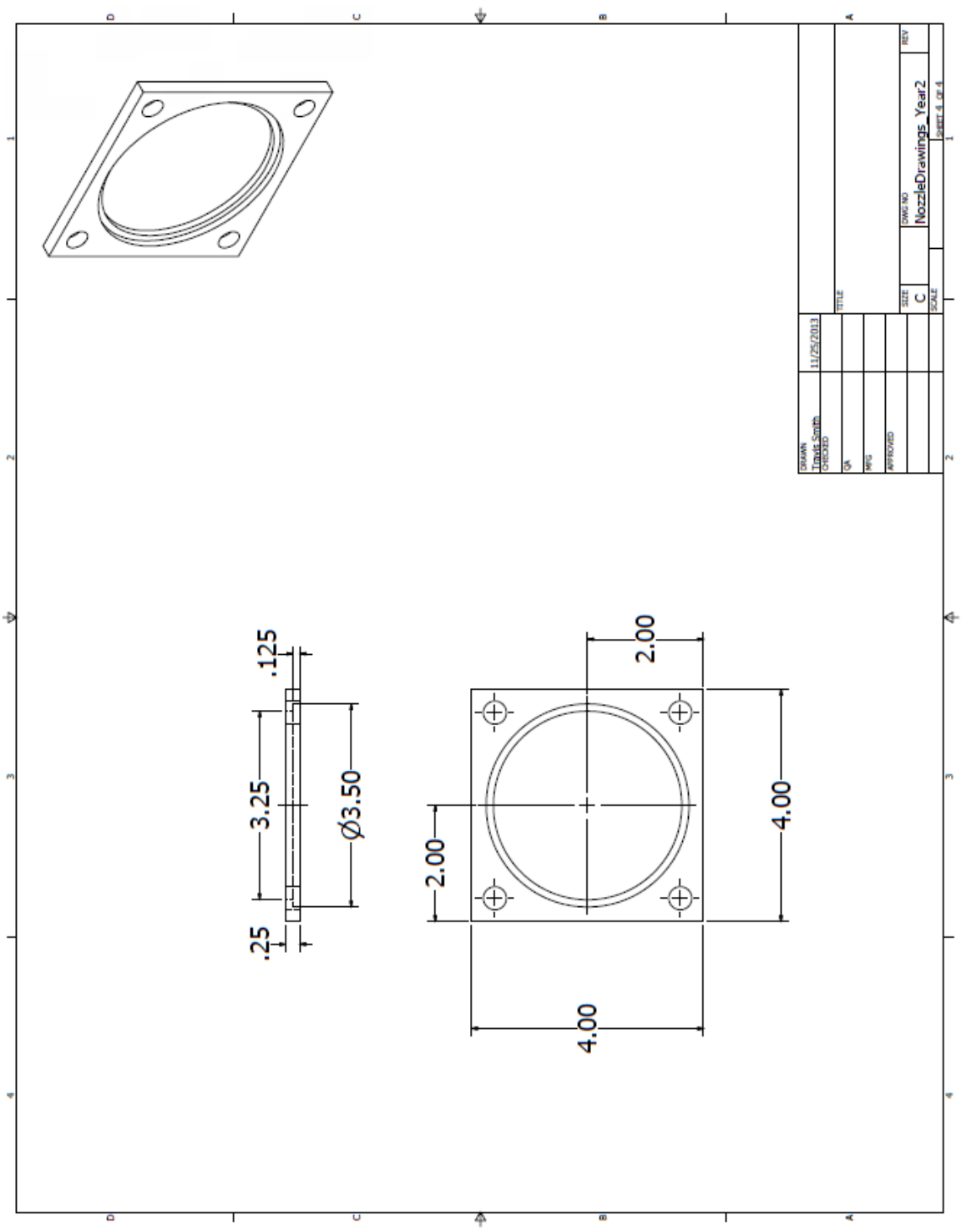
.125
3.25
Ø3.50
.25
2.00
2.00
4.00
4.00
DRAWN
Travis Smith
11/25/2013
CHECKED
QA
MFG
APPROVED
TITLE
SIZE
C
DWG NO
NozzleDrawings_Year2
REV
SCALE
SHEET 4 OF 4

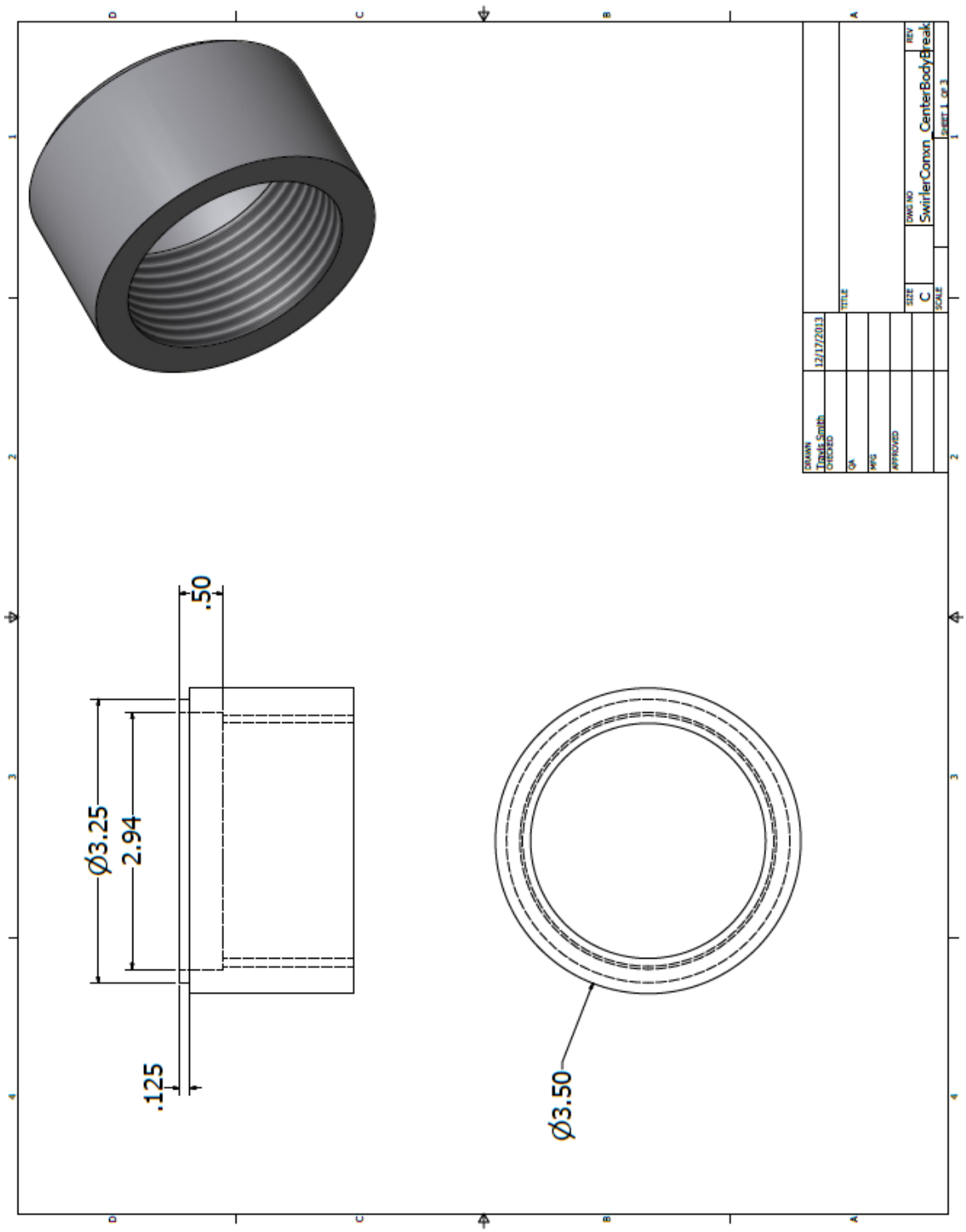
DRAWN
Travis Smith
CHECKED
QA
MFG
APPROVED
12/17/2013
TITLE
SIZE
C
DWG NO
SwirlerComxn_CenterBodyBreak
REV
SCALE
Sheet 1 of 3
.50
Ø3.25
2.94
.125
Ø3.50

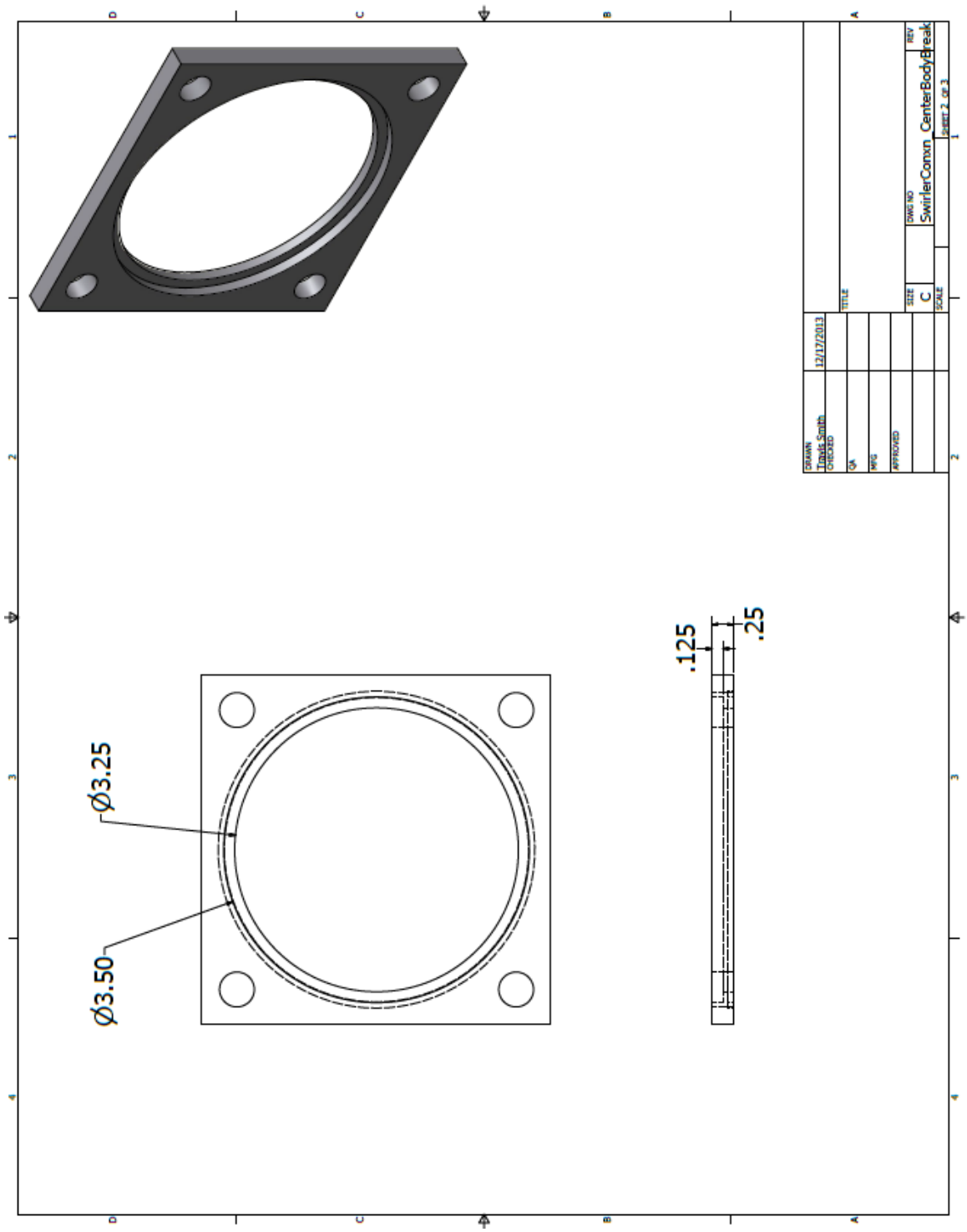
Ø3.25
Ø3.50
.125
.25
DRAWN
Travis Smith
CHECKED
QA
MFG
APPROVED
12/17/2013
TITLE
SIZE
C
DWG NO
SwirlerComxn_CenterBodyBreak
REV
SCALE
SHEET 2 OF 3

A.5 Upstream Critical Orifice Assembly

The upstream critical orifice is shown below with detailed drawings on the next page. Not shown in these drawings are the O-ring grooves used to seal this. The preheated air flows from the side with the smaller opening through the orifice plate and out the larger opening into the mixing pipe. The orifice was calibrated using known flow rates, and the flow rate is metered for temperature and pressure immediately upstream. The plate holders are welded onto the 0.5” pipe and the cross fitting for the 2.5” pipe. The orifice size was chosen to allow the desired flow rates through. Standard choked orifice calculations were performed to size the hole.

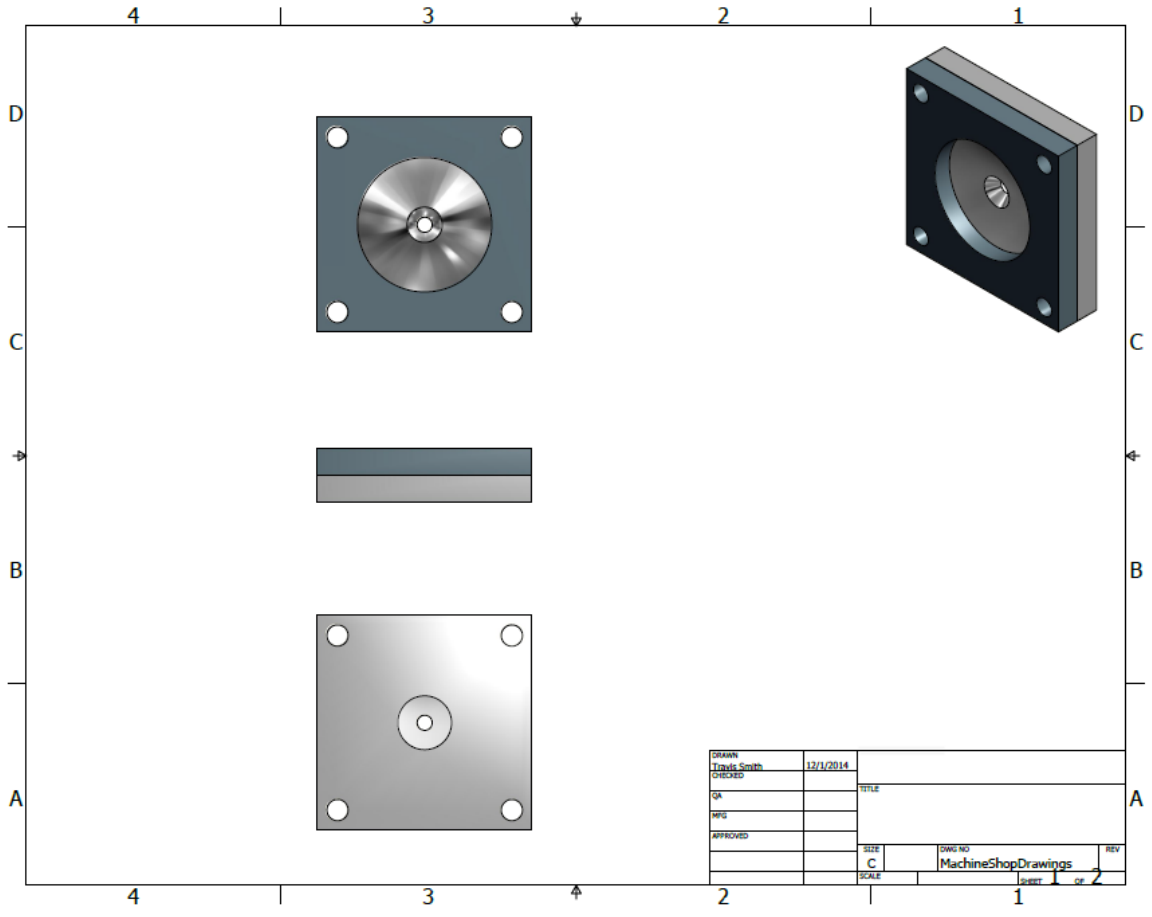

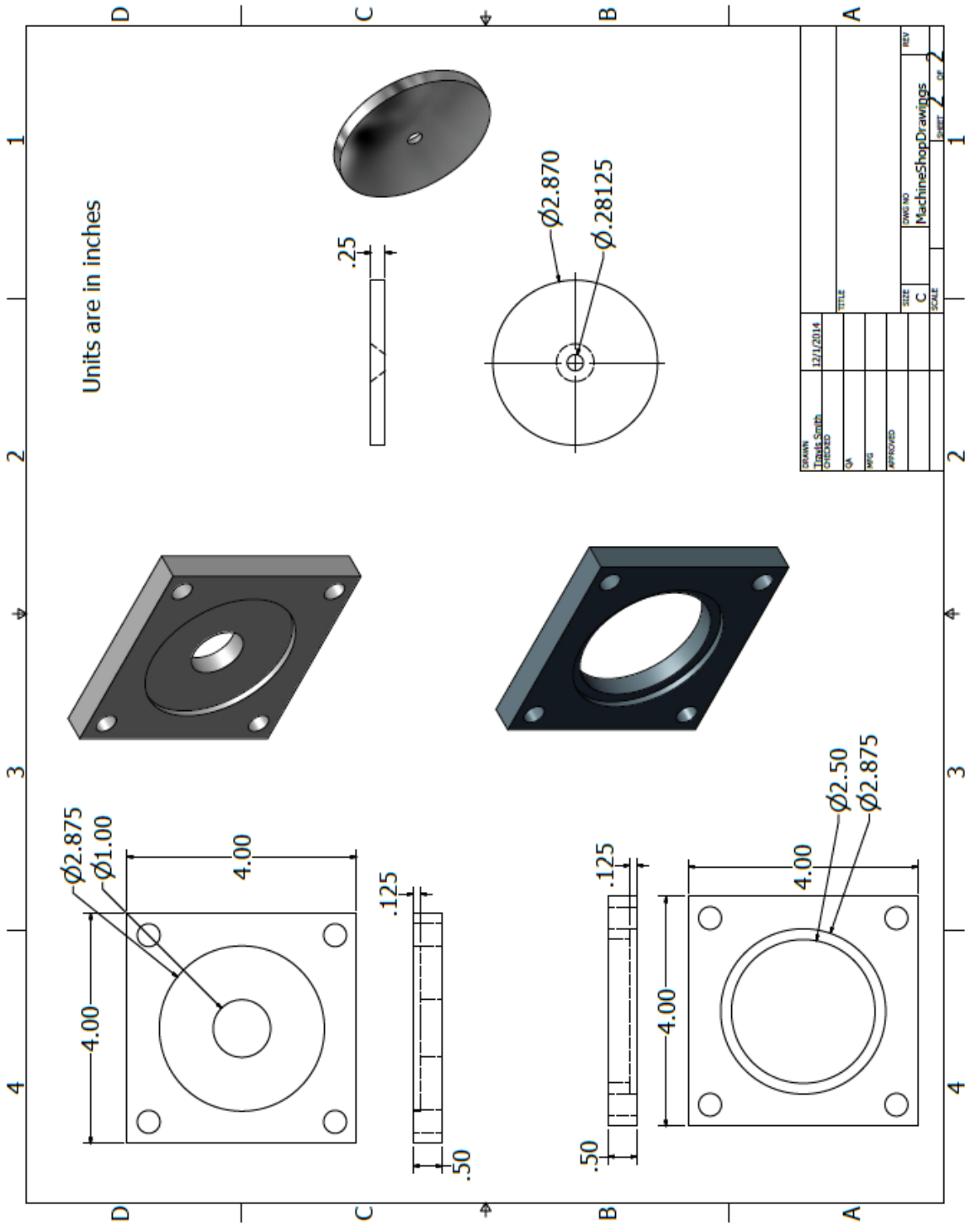
Units are in inches
Ø2.870
Ø.28125
.25
Ø2.875
Ø1.00
4.00
4.00
.125
.50
.125
.50
4.00
4.00
Ø2.50
Ø2.875
DRAWN
Travis Smith
12/1/2014
CHECKED
QA
MFG
APPROVED
TITLE
SIZE
C
DWG NO
MachineShopDrawings
REV
SCALE
SHEET
OF

APPENDIX B. LIST OF AVAILABLE TEST DATA

B.1 Data Set 1: Single Nozzle Spring 2014 (not used in analysis)

For this particular data set, the outer two nozzles were not plugged but were not flowing air or fuel (natural gas). The air preheat temperature for all cases was 505K. The nominal nozzle velocity was 25 and 50 m/s calculated based only on the air. The equivalence ratio was 0.85 regardless of velocity. The air mass flow rates were 0.0168 and 0.034 kg/s. The diagnostics used were sPIV and OH-PLIF at 3kHz in the r-z plane. There were no simultaneous acoustic measurements taken. A total of 2278 sPIV image pairrs and 5405 OH-PLIF images were taken. The dt was set at 14μs and 10μs for the 25 and 50 m/s cases respectively. The camera angles were set at approximately 35 degrees to the normal of the measurement plane and the image resolution was approximately 0.08mm/pixel. This gives a velocity uncertainty of 0.57 m/s and 0.8 m/s for the instantaneous in-plane velocity components for the 25 and 50 m/s cases respectively, based off of a 1/10th pixel sub-grid interpolation uncertainty. The calculated vectors are within $\pm$1.2 r/D and 0 to 1.5 z/D. Table 4 shows the data cases taken for the single nozzle case. All forcing signals were at 1V and had no longitudinal forcing. More details can be found in "SingleNozzle2014_DataGuide.xlsx".

Table 4 - Single Nozzle Spring 2014 Data Cases

CaseName	Velocity (m/s)	Reacting	Forcing
d27	50	Yes	250 IP
d28	50	Yes	390 IP
d29	50	Yes	500 IP
d30	50	Yes	1180 IP
d31	50	Yes	250 OP
d32	50	Yes	390 OP
d33	50	Yes	500 OP
d34	50	Yes	1180 OP
d35	50	No	None
d36	50	Yes	None
d37	25	Yes	250 IP
d38	25	Yes	390 IP
d39	25	Yes	500 IP
d40	25	Yes	1180 IP
d41	25	Yes	250 OP
d42	25	Yes	390 OP
d43	25	Yes	500 OP
d44	25	Yes	1180 OP
d45	25	No	None
d46	25	Yes	None

B.2 Data Set 2: Triple Nozzle Spring 2015 (not used in analysis)

For this data set, all three nozzles were flowing air and fuel (natural gas). The air preheat temperature for all cases was 505K. The nominal bulk nozzle velocities were 25, 35 and 50 m/s calculated based only on the air. The equivalence ratios were set at 0.6, 0.85, 0.6 for the center nozzle regardless of velocity. The diagnostics used were sPIV and OH-PLIF at 5kHz in the r-z and r-θ planes. There were no simultaneous acoustic measurements taken. A total of 3765 sPIV image pairs and 5405 OH-PLIF images were taken. The upstream air pressure was fluctuating during the run, resulting in flow rate fluctuations so that the individual cases may vary by $\pm$5% of the nominal bulk velocity.

Table 5 shows the data cases taken for the triple nozzle configuration in the r-z plane. All forcing signals were at 1V and had no longitudinal forcing. The dt was set at $15\mu s$ and $10\mu s$ for the 25 and 50 m/s cases respectively. The camera angles were set at approximately 35 degrees to the normal of the measurement plane and the image resolution was approximately 0.1mm/pixel. This gives a velocity uncertainty of 0.67 m/s and 1 m/s for the instantaneous in-plane velocity components for the 25 and 50 m/s cases respectively, based off of a $1/10^{th}$ pixel sub-grid interpolation uncertainty.

Table 5 - Triple Nozzle Spring 2015 r-z Data Cases

Case Name	Velocity (m/s)	dt (μs)	Reacting	Forcing
d1	25	15	Yes	None
d2	25	15	Yes	None
d3	25	15	Yes	390 Hz IP
d4	25	15	Yes	390 Hz IP
d5	25	15	Yes	390 Hz OP
d6	25	15	Yes	390 Hz OP
d7	25	15	Yes	1180 Hz IP
d8	25	15	Yes	1180 Hz IP
d9	25	15	Yes	1180 Hz OP
d10	25	15	Yes	1180 Hz OP
d11	25	15	Yes	None
d12	25	15	Yes	390 Hz IP
d13	25	15	Yes	390 Hz OP
d14	25	15	Yes	1180 Hz IP
d17	50	10	Yes	none
d18	50	10	Yes	390 Hz IP
d19	50	10	Yes	390 Hz OP
d20	50	10	Yes	1180 Hz IP
d21	50	10	Yes	1180 Hz OP
d22	50	10	Yes	1180 Hz OP
d23	50	10	Yes	1180 Hz IP
d24	50	10	Yes	390 Hz OP
d25	50	10	Yes	390 Hz IP
d26	50	10	Yes	none

Table 6 shows the data cases taken for the triple nozzle configuration in the r-θ plane. All forcing signals were at 1V and had no longitudinal forcing. The velocities were chosen as 25, 35, and 50 m/s. Four different heights ($\frac{z}{D} = 0.35, 0.5, 1, 2$) were looked at by traversing the laser sheet and cameras vertically. The camera angles were set at approximately 55 degrees to the normal of the measurement plane and the image resolution was approximately 0.094mm/pixel. This gives a velocity uncertainty of 1.18 m/s, 1.86 m/s and 3.03 m/s for the instantaneous in-plane velocity components for the 25, 35, and 50 m/s cases respectively, based off of a 1/10th pixel sub-grid interpolation uncertainty. Out-of-plane velocity has an unquantified bias error. Comparisons between r-θ and r-z time-averaged flow fields agree well, so the bias error is very small for out-of-plane components. More details can be found in "TravisSpring2015LabBook_TripleNozzle.xlsx".

Table 6 - Triple Nozzle Spring 2015 r-θ Data Cases

Case Name	Velocity (m/s)	dt (μs)	Height (z/D)	Forcing
dth9	25	8	0.5	None
dth10	25	8	0.5	None
dth11	25	8	0.5	390 Hz IP
dth12	25	8	0.5	390 Hz OP
dth13	25	8	0.5	390 Hz OP
dth14	25	8	0.5	390 Hz IP
dth15	25	8	0.5	1180 Hz IP
dth16	25	8	0.5	1180 Hz IP
dth17	25	8	0.5	1180 Hz OP
dth18	25	8	0.5	1180 Hz OP
dth29	25	8	1	None
dth30	25	8	1	None
dth31	25	8	1	390 Hz IP
dth32	25	8	1	390 Hz IP
dth33	25	8	1	390 Hz OP
dth34	25	8	1	390 Hz OP
dth35	25	8	1	1180 Hz IP
dth36	25	8	1	1180 Hz IP
dth37	25	8	1	1180 Hz OP

dth38	25	8	1	1180 Hz OP
dth43	25	8	2	None
dth44	25	8	2	None
dth45	25	8	2	390 Hz IP
dth46	25	8	2	390 Hz IP
dth47	25	8	2	390 Hz OP
dth48	25	8	2	390 Hz OP
dth49	25	8	2	1180 Hz IP
dth50	25	8	2	1180 Hz OP
dth51	25	8	2	1180 Hz IP
dth52	25	8	2	1180 Hz OP
dth53	35	5.04	2	None
dth54	35	5.04	2	390 Hz IP
dth55	35	5.04	2	None
dth56	35	5.04	2	390 Hz IP
dth57	35	5.04	2	390 Hz OP
dth58	35	5.04	2	390 Hz OP
dth59	35	5.04	2	1180 Hz IP
dth60	35	5.04	2	1180 Hz OP
dth61	35	5.04	2	1180 Hz OP
dth62	35	5.04	2	1180 Hz IP
dth63	50	3.1	2	None
dth64	50	3.1	2	390 Hz IP
dth65	50	3.1	2	390 Hz IP
dth66	50	3.1	2	390 Hz OP
dth67	50	3.1	2	390 Hz OP
dth68	50	3.1	2	None
dth69	50	3.1	2	1180 Hz IP
dth70	50	3.1	2	1180 Hz OP
dth71	50	3.1	2	1180 Hz OP
dth72	50	3.1	2	1180 Hz IP
dth73	25	8.02	0.35	None
dth74	25	8.02	0.35	390 Hz IP
dth75	25	8.02	0.35	390 Hz OP
dth76	25	8.02	0.35	1180 Hz IP
dth77	25	8.02	0.35	1180 Hz OP
dth78	25	8.02	0.35	1180 Hz OP
dth79	25	8.02	0.35	1180 Hz IP
dth80	25	8.02	0.35	390 Hz OP
dth81	25	8.02	0.35	390 Hz IP
dth82	25	8.02	0.35	None

B.3 Data Set 3: Triple Nozzle Spring 2016

For this data set, all three nozzles were flowing air and fuel (natural gas). The air preheat temperature for all cases was 505K. The nominal bulk nozzle velocity was 25 m/s calculated based only on the air. The equivalence ratios were set at 0.6, 0.95, 0.6 for the center nozzle regardless of velocity. The diagnostics used were sPIV and OH-PLIF at 5kHz in the r-z and r-θ planes. Simultaneous acoustic measurements were taken. A total of 7530 sPIV image pairs and 5405 OH-PLIF images were taken. The flow issues experienced by the previous experiment was fixed for this case so that all velocities are repeatable to within $\pm$0.25 m/s. This particular data set is the first data set that includes longitudinal cancellation. All cases are reacting cases.

Table 7 shows the data cases taken for the triple nozzle configuration in the r-z plane. The camera angles were set at approximately 35 degrees to the normal of the measurement plane and the image resolution was approximately 0.036mm/pixel. This gives a velocity uncertainty of 1.07 m/s for the instantaneous in-plane velocity components, based off of a 1/10th pixel sub-grid interpolation uncertainty.

Table 7 - Triple Nozzle Spring 2016 r-z Data Cases

Case Name	Velocity (m/s)	dt (μs)	Minimization	Forcing
MicroPIV_3Nozzle_0000_no_1	25	3.36	none	None
MicroPIV_3Nozzle_0390IP_no_2	25	3.36	none	390 Hz IP
MicroPIV_3Nozzle_0390IP_yes_1	25	3.36	Yes	390 Hz IP
MicroPIV_3Nozzle_0390IP_yes_2	25	3.36	Yes	390 Hz IP
MicroPIV_3Nozzle_1170IP_no_1	25	3.36	none	1170 Hz IP
MicroPIV_3Nozzle_1170IP_no_2	25	3.36	none	1170 Hz IP
MicroPIV_3Nozzle_1170IP_yes_1	25	3.36	Yes	1170 Hz IP
MicroPIV_3Nozzle_1170IP_yes_2	25	3.36	Yes	1170 Hz IP
MicroPIV_3Nozzle_0390OP_no_1	25	3.36	none	390 Hz OP
MicroPIV_3Nozzle_0390OP_no_2	25	3.36	none	390 Hz OP
MicroPIV_3Nozzle_1170OP_no_1	25	3.36	none	1170 Hz OP
MicroPIV_3Nozzle_1170OP_no_2	25	3.36	none	1170 Hz OP
MicroPIV_3Nozzle_0000_no_3	25	3.36	none	None
MicroPIV_3Nozzle_0390IP_no_3	25	3.36	none	390 Hz IP

Table 8 shows the data cases taken for the triple nozzle configuration in the r-θ plane. All transverse forcing signals were at 1V but the longitudinal amplitudes were varied to minimize axial velocity fluctuations. The flow conditions were the exact same as the r-z experiments. Four different heights ($\frac{z}{D} = 0.15, 0.67, 1.2, 1.7$) were looked at by traversing the laser sheet and cameras vertically. The camera angles were set at approximately 55 degrees to the normal of the measurement plane and the image resolution was approximately 0.09mm/pixel. This gives a velocity uncertainty of 2.67 m/s for the instantaneous in-plane velocity components, based off of a 1/10th pixel sub-grid interpolation uncertainty. More details can be found in "Travis_Feb2016_DataGuide.xlsx".

Table 8 - Triple Nozzle Spring 2016 r-θ Data Cases

Case Name	Velocity (m/s)	dt (μs)	Min.	Height (z/D)	Forcing
3Nozzle_0000_no_h015_1	25	8	none	0.15	None
3Nozzle_0000_no_h015_2	25	8	none	0.15	None
3Nozzle_0390IP_no_h015_1	25	8	none	0.15	390 Hz IP
3Nozzle_0390IP_no_h015_2	25	8	none	0.15	390 Hz IP
3Nozzle_0390IP_yes_h015_1	25	8	Yes	0.15	390 Hz IP
3Nozzle_0390IP_yes_h015_2	25	8	Yes	0.15	390 Hz IP
3Nozzle_1170IP_no_h015_1	25	8	none	0.15	1170 Hz IP
3Nozzle_1170IP_no_h015_2	25	8	none	0.15	1170 Hz IP
3Nozzle_1170IP_yes_h015_1	25	8	Yes	0.15	1170 Hz IP
3Nozzle_1170IP_yes_h015_2	25	8	Yes	0.15	1170 Hz IP
3Nozzle_0390OP_no_h015_1	25	8	none	0.15	390 Hz OP
3Nozzle_0390OP_no_h015_2	25	8	none	0.15	390 Hz OP
3Nozzle_1170OP_no_h015_1	25	8	none	0.15	1170 Hz OP
3Nozzle_1170OP_no_h015_2	25	8	none	0.15	1170 Hz OP
3Nozzle_0000_no_h067_2	25	8	none	0.67	None
3Nozzle_0000_no_h067_3	25	8	none	0.67	None
3Nozzle_0390IP_no_h067_1	25	8	none	0.67	390 Hz IP
3Nozzle_0390IP_no_h067_2	25	8	none	0.67	390 Hz IP
3Nozzle_0390IP_yes_h067_1	25	8	Yes	0.67	390 Hz IP
3Nozzle_0390IP_yes_h067_2	25	8	Yes	0.67	390 Hz IP
3Nozzle_1170IP_no_ h067_1	25	8	none	0.67	1170 Hz IP
3Nozzle_1170IP_no_ h067_2	25	8	none	0.67	1170 Hz IP
3Nozzle_1170IP_yes_ h067_1	25	8	Yes	0.67	1170 Hz IP
3Nozzle_1170IP_yes_ h067_2	25	8	Yes	0.67	1170 Hz IP
3Nozzle_0390OP_no_ h067_1	25	8	none	0.67	390 Hz OP
3Nozzle_0390OP_no_ h067_2	25	8	none	0.67	390 Hz OP
3Nozzle_1170OP_no_ h067_1	25	8	none	0.67	1170 Hz OP
3Nozzle_1170OP_no_ h067_2	25	8	none	0.67	1170 Hz OP
3Nozzle_0000_no_h120_1	25	8	none	1.2	None
3Nozzle_0000_no_h120_2	25	8	none	1.2	None
3Nozzle_0390IP_no_ h120_1	25	8	none	1.2	390 Hz IP
3Nozzle_0390IP_no_ h120_2	25	8	none	1.2	390 Hz IP
3Nozzle_0390IP_yes_ h120_1	25	8	Yes	1.2	390 Hz IP
3Nozzle_0390IP_yes_ h120_2	25	8	Yes	1.2	390 Hz IP
3Nozzle_1170IP_no_ h120_1	25	8	none	1.2	1170 Hz IP
3Nozzle_1170IP_no_ h120_2	25	8	none	1.2	1170 Hz IP
3Nozzle_1170IP_yes_ h120_1	25	8	Yes	1.2	1170 Hz IP
3Nozzle_1170IP_yes_ h120_2	25	8	Yes	1.2	1170 Hz IP
3Nozzle_0390OP_no_ h120_1	25	8	none	1.2	390 Hz OP
3Nozzle_0390OP_no_ h120_2	25	8	none	1.2	390 Hz OP
3Nozzle_1170OP_no_ h120_1	25	8	none	1.2	1170 Hz OP

3Nozzle_1170OP_no_ h120_2	25	8	none	1.2	1170 Hz OP
3Nozzle_0000_no_h170_1	25	8	none	1.7	None
3Nozzle_0000_no_h170_2	25	8	none	1.7	None
3Nozzle_0390IP_no_ h170_1	25	8	none	1.7	390 Hz IP
3Nozzle_0390IP_no_ h170_2	25	8	none	1.7	390 Hz IP
3Nozzle_0390IP_yes_ h170_1	25	8	Yes	1.7	390 Hz IP
3Nozzle_0390IP_yes_ h170_2	25	8	Yes	1.7	390 Hz IP
3Nozzle_1170IP_no_ h170_1	25	8	none	1.7	1170 Hz IP
3Nozzle_1170IP_no_ h170_2	25	8	none	1.7	1170 Hz IP
3Nozzle_1170IP_yes_ h170_1	25	8	Yes	1.7	1170 Hz IP
3Nozzle_1170IP_yes_ h170_2	25	8	Yes	1.7	1170 Hz IP
3Nozzle_0390OP_no_ h170_1	25	8	none	1.7	390 Hz OP
3Nozzle_0390OP_no_ h170_2	25	8	none	1.7	390 Hz OP
3Nozzle_1170OP_no_ h170_1	25	8	none	1.7	1170 Hz OP
3Nozzle_1170OP_no_ h170_2	25	8	none	1.7	1170 Hz OP

B.4 Data Set 4: Triple Nozzle Summer 2016

For this data set, all three nozzles were flowing air and fuel (natural gas). The air preheat temperature for all cases was 505K. The nominal bulk nozzle velocity was 25 m/s calculated based only on the air. The equivalence ratios were set at 0.6, 0.95, 0.6 for the center nozzle regardless of velocity. Seeding air was included in the run. The diagnostics used were sPIV (2xSA5s), OH-PLIF (SA1.1 with HiCatt and UV Circa Lens), and CH* Chemiluminescence (SA3 with IRO and CH* filter) at 5kHz in the r-z plane. Simultaneous acoustic measurements were taken at 50kHz. A total of 7530 sPIV image pairs and 5405 OH-PLIF images were taken. This data set includes longitudinal minimization. All cases are reacting cases.

Table 9 shows the data cases taken for the triple nozzle configuration in the r-z plane. The PIV camera angles were set at approximately 35 degrees to the normal of the measurement plane and the image resolution was approximately 0.13mm/pixel. This gives a velocity uncertainty of 1.3 m/s for the instantaneous in-plane velocity components, based

off of a 1/10th pixel sub-grid interpolation uncertainty. The calculated vectors are within ± 1.5 r/D and 0 to 2.5 z/D. More details can be found in "TripleNozzle_June2016_LabBook.xlsx".

Table 9 - Triple Nozzle Summer 2016 r-z Data Cases

Case Name	Velocity (m/s)	dt (μs)	Min.	Forcing
RZ_3Nozzle_0000_no_1	25	10	none	None
RZ _3Nozzle_0390IP_no_1	25	10	none	390 Hz IP
RZ _3Nozzle_0390IP_yes_1	25	10	Yes	390 Hz IP
RZ _3Nozzle_1170IP_no_1	25	10	none	1170 Hz IP
RZ _3Nozzle_1170IP_yes_1	25	10	Yes	1170 Hz IP
RZ _3Nozzle_1170IP_yes_2	25	10	Yes	1170 Hz IP
RZ _3Nozzle_0390OP_no_1	25	10	none	390 Hz OP
RZ _3Nozzle_1170OP_no_1	25	10	none	1170 Hz OP

B.5 Data Set 5: Triple Nozzle Chemiluminescence Fall 2016

For this data set, all three nozzles were flowing air and fuel (natural gas). The air preheat temperature for all cases was 505K. The nominal bulk nozzle velocity was 25 m/s calculated based only on the air. The equivalence ratios were set at 0.6, 0.95, 0.6 for the center nozzle regardless of velocity. No seeding air was injected for this particular case. CH* Chemiluminescence measurements from an SA-5 camera coupled to the HiCATT intensifier with a 50mm Nikkor lens were taken at 5kHz in the r-z plane simultaneous with acoustics and an OH* PMT measurement at 40kHz. A total of 5405 images were taken. This data set includes longitudinal minimization. All cases are reacting cases. Table 10 summarizes the data cases taken for this setup. More details can be found in "TripleNozzleData_Fall2016.xlsx".

Table 10 - Triple Nozzle 2016 Chemiluminescence Data Cases

Case Name	Velocity (m/s)	Min.	Forcing
3Nozzle_0000_no_1	25	none	None
3Nozzle_0000_no_2	25	none	None
3Nozzle_0390IP_no_1	25	none	390 Hz IP
3Nozzle_0390IP_no_2	25	none	390 Hz IP
3Nozzle_0390IP_yes_1	25	Yes	390 Hz IP
3Nozzle_0390IP_yes_2	25	Yes	390 Hz IP
3Nozzle_1170IP_no_1	25	none	1170 Hz IP
3Nozzle_1170IP_no_2	25	none	1170 Hz IP
3Nozzle_1170IP_yes_1	25	Yes	1170 Hz IP
3Nozzle_1170IP_yes_2	25	Yes	1170 Hz IP
3Nozzle_0390OP_no_1	25	none	390 Hz OP
3Nozzle_0390OP_no_2	25	none	390 Hz OP
3Nozzle_1170OP_no_1	25	none	1170 Hz OP
3Nozzle_1170OP_no_2	25	none	1170 Hz OP

REFERENCES

[1] Lieuwen, T., and Yang, V. 2005. *Combustion Instabilities in Gas Turbine Engines: Operational Experience, Fundamental Mechanism and Modeling*. Washington D.C: AIAA.

[2] Broda, J. C., Seo, S., Santoro, R. J., Shirhattikar, G., and Yang, V. 1998, "An Experimental Study of Combustion Dynamics of a Premixed Swirl Injector," *Twenty-Seventh Symposium (International) on Combustion*. Vol. 27, The Combustion Institute, pp. 1849-1856.

[3] Lieuwen, T. 2012. *Unsteady Combustor Physics*: Cambridge University Press.

[4] Goy, C. J., James, S. R., and Reah, S. 2005, "Monitoring Combustion Instabilities; E.On Uk's Experience," *Combustion Instabilties in Gas Turbine Engines: Operational Experience, Fundamental Mechanisms, and Modeling*. American Institute of Aeronautics and Astronautics, pp. 163-175.

[5] Candel, S. 2002, "Combustion Dynamics and Control: Progress and Challenges," *Proceedings of the Combustion Institute* Vol. 29, pp. 1-28.doi: Doi 10.1016/S1540-7489(02)80007-4

[6] Huang, Y., and Yang, V. 2009, "Dynamics and Stability of Lean-Premixed Swirl-Stabilized Combustion," *Progr. Energy and Combust. Sci.* Vol. 35, No. 4, pp. 293-364.

[7] Rijke, P. L. 1859, "Lxxi. Notice of a New Method of Causing a Vibration of the Air Contained in a Tube Open at Both Ends," *The London, Edinburgh, and Dublin Philosophical Magazine and Journal of Science* Vol. 17, No. 116, pp. 419-422.

[8] Rayleigh, L. 1878, "The Explanation of Certain Acoustic Phenomenon," *Nature* Vol. 18, pp. 319-321.doi: 10.1038/018319a0

[9] Rogers, D. E., and Marble, F. E. 1956, "A Mechanism for High-Frequency Oscillation in Ramjet Combustors and Afterburners," *Jet Propulsion* Vol. 26, No. 6, pp. 456-464.

[10] Elias, I. 1959, "Acoustical Resonances Produced by Combustion of a Fuel-Air Mixture in a Rectangular Duct," *Journal of the Acoustical Society of America* Vol. 31, No. 3, pp. 296-304.doi: Doi 10.1121/1.1907715

[11] Blackshear, P. I., Rayle, W. D., and Tower, L. K. 1955, "Study of Screeching Combustion in a 6-Inch Simulated Afterburner," *National Advisory Committee for Aeronautics*.

[12] Crocco, L. 1965, "Theoretical Studies on Liquid-Propellant Rocket Instability," *Tenth Symposium (International) on Combustion*. The Combustion Institute, pp. 1107-1128.

[13] Crocco, L. 1951, "Aspects of Combustion Stability in Liquid Propellant Rocket Motors .1. Fundamentals - Low Frequency Instability with Monopropellants," *Journal of the American Rocket Society* Vol. 21, No. 6, pp. 163-178.

[14] Nathan, G. J., Mullinger, P. J., Bridger, D., and Martin, B. 2006, "Investigation of a Combustion Driven Oscillation in a Refinery Flare. Part A: Full Scale Assessment," *Experimental Thermal and Fluid Science* Vol. 30, No. 4, pp. 285-295.doi: 10.1016/j.expthermflusci.2005.05.009

[15] Ducruix, S., Schuller, T., Durox, D., and Candel, S. 2003, "Combustion Dynamics and Instabilities: Elementary Coupling and Driving Mechanisms," *Journal of Propulsion and Power* Vol. 19, No. 5, pp. 722-734.doi: Doi 10.2514/2.6182

[16] Lieuwen, T., Neumeier, Y., and Zinn, B. T. 1998, "The Role of Unmixedness and Chemical Kinetics in Driving Combustion Instabilities in Lean Premixed Combustors," *Combustion Science and Technology* Vol. 135, No. 1-6, pp. 193-211.doi: Doi 10.1080/00102209808924157

[17] Lieuwen, T., and Zinn, B. T. 1998, "The Role of Equivalence Ratio Oscillations in Driving Combustion Instabilities in Low Nox Gas Turbines," *Twenty-Seventh Symposium (International) on Combustion, Vols 1 and 2*, pp. 1809-1816.

[18] Lieuwen, T., and Zinn, B. T. 1998, "Theoretical Investigation of Combustion Instability Mechanisms in Lean Premixed Gas Turbines," *36th Aerospace Sciences Meeting & Exhibit*. AIAA, Reno, NV.

[19] Lieuwen, T., Torres, H., Johnson, C., and Zinn, B. T. 2001, "A Mechanism of Combustion Instability in Lean Premixed Gas Turbine Combustors," *Journal of Engineering for Gas Turbines and Power-Transactions of the Asme* Vol. 123, No. 1, pp. 182-189.doi: Doi 10.1115/1.1339002

[20] Acharya, V., Shreekrishna, Shin, D. H., and Lieuwen, T. 2012, "Swirl Effects on Harmonically Excited, Premixed Flame Kinematics," *Combustion and Flame* Vol. 159, No. 3, pp. 1139-1150.doi: 10.1016/j.combustflame.2011.09.015

[21] Silva, C. F., Emmert, T., Jaensch, S., and Polifke, W. 2015, "Numerical Study on Intrinsic Thermoacoustic Instability of a Laminar Premixed Flame," *Combustion and Flame* Vol. 162, No. 9, pp. 3370-3378.doi: 10.1016/j.combustflame.2015.06.003

[22] Worth, N. A., and Dawson, J. R. 2013, "Modal Dynamics of Self-Excited Azimuthal Instabilities in an Annular Combustion Chamber," *Combustion and Flame* Vol. 160, No. 11, pp. 2476-2489.doi: 10.1016/j.combustflame.2013.04.031

[23] Worth, N. A., and Dawson, J. R. 2013, "Self-Excited Circumferential Instabilities in a Model Annular Gas Turbine Combustor: Global Flame Dynamics," *Proceedings of the Combustion Institute*. Vol. 34, pp. 3127-3134.

[24] Dawson, J. R., and Worth, N. A. 2014, "Flame Dynamics and Unsteady Heat Release Rate of Self-Excited Azimuthal Modes in an Annular Combustor," *Combustion and Flame* Vol. 161, No. 10, pp. 2565-2578.doi: 10.1016/j.combustflame.2014.03.021

[25] Staffelbach, G., Gicquel, L. Y. M., Boudier, G., and Poinsot, T. 2009, "Large Eddy Simulation of Self Excited Azimuthal Modes in Annular Combustors," *Proceedings of the Combustion Institute* Vol. 32, pp. 2909-2916.doi: 10.1016/j.proci.2008.05.033

[26] O'Connor, J., Acharya, V., and Lieuwen, T. 2015, "Transverse Combustion Instabilities: Acoustics, Hydrodynamics, and Flame Dynamics," *Progress in Energy and Combustion Sciences* Vol. 49, pp. 1-39.

[27] Blimbaum, J., Zanchetta, M., Akin, T., Acharya, V., O'Connor, J., Noble, D. R., and Lieuwen, T. 2012, "Transverse to Longitudinal Acoustic Coupling Processes in Annular Combustion Chambers," *International Journal of Spray and Combustion Dynamics* Vol. 4, No. 4, pp. 275-297.

[28] Saurabh, A., and Paschereit, C. O. 2013, "Combustion Instability in a Swirl Flow Combustor with Transverse Extensions," *Proceedings of the Asme Turbo Expo: Turbine Technical Conference and Exposition, 2013, Vol 1b*.

[29] Saurabh, A., Steinert, R., Moeck, J. P., and Paschereit, C. O. 2014, "Swirl Flame Response to Traveling Acoustic Waves," *Proceedings of the Asme Turbo Expo: Turbine Technical Conference and Exposition, 2014, Vol 4b*.

[30] Lieuwen, T. 2003, "Modeling Premixed Combustion-Acoustic Wave Interactions: A Review," *Journal of Propulsion and Power* Vol. 19, No. 5, pp. 765-781.doi: Doi 10.2514/2.6193

[31] Dowling, A. P., and Stow, S. R. 2003, "Acoustic Analysis of Gas Turbine Combustors," *Journal of Propulsion and Power* Vol. 19, No. 5, pp. 751-764.doi: Doi 10.2514/2.6192

[32] Noiray, N., Durox, D., Schuller, T., and Candel, S. 2008, "A Unified Framework for Nonlinear Combustion Instability Analysis Based on the Flame Describing Function," *Journal of Fluid Mechanics* Vol. 615, pp. 139-167.doi: 10.1017/S0022112008003613

[33] Palies, P., Durox, D., Schuller, T., and Candel, S. 2011, "Nonlinear Combustion Instability Analysis Based on the Flame Describing Function Applied to Turbulent Premixed Swirling Flames," *Combustion and Flame* Vol. 158, No. 10, pp. 1980-1991.doi: 10.1016/j.combustflame.2011.02.012

[34] Lieuwen, T., and Neumeier, Y. 2002, "Nonlinear Pressure-Heat Release Transfer Function Measurements in a Premixed Combustor," *Proceedings of the Combustion Institute*. Vol. 29, pp. 99-105.

[35] Bellows, B. D., Neumeier, Y., and Lieuwen, T. 2006, "Forced Response of a Swirling, Premixed Flame to Flow Disturbances," *Journal of Propulsion and Power* Vol. 22, No. 5, pp. 1075-1084.doi: Doi 10.2514/1.17426

[36] Armitage, C. A., Balachandran, R., Mastorakos, E., and Cant, R. S. 2006, "Investigation of the Nonlinear Response of Turbulent Premixed Flames to Imposed Inlet Velocity Oscillations," *Combustion and Flame* Vol. 146, No. 3, pp. 419-436.doi: 10.1016/j.combustflame.2006.06.002

[37] Bellows, B. D., Bobba, M. K., Forte, A., Seltzman, J. M., and Lieuwen, T. 2007, "Flame Transfer Function Saturation Mechanisms in a Swirl-Stabilized Combustor," *Proceedings of the Combustion Institute*. Vol. 31, pp. 3181-3188.

[38] Balachandran, R., Ayoola, B. O., Kaminski, C. F., Dowling, A. P., and Mastorakos, E. 2005, "Experimental Investigation of the Nonlinear Response of Turbulent Premixed Flames to Imposed Inlet Velocity Oscillations," *Combustion and Flame* Vol. 143, No. 1-2, pp. 37-55.doi: 10.1016/j.combustflame.2005.04.009

[39] Palies, P., Durox, D., Schuller, T., Morenton, P., and Candel, S. 2009, "Dynamics of Premixed Confined Swirling Flames," *Comptes Rendus Mecanique* Vol. 337, No. 6-7, pp. 395-405.doi: 10.1016/j.crme.2009.06.001

[40] Schuller, T., Ducruix, S., Durox, D., and Candel, S. 2002, "Modeling Tools for the Prediction of Premixed Flame Transfer Functions," *Proceedings of the Combustion Institute* Vol. 29, pp. 107-113.doi: Doi 10.1016/S1540-7489(02)80018-9

[41] Durox, D., Schuller, T., and Candel, S. 2005, "Combustion Dynamics of Inverted Conical Flames," *Proceedings of the Combustion Institute* Vol. 30, pp. 1717-1724.doi: 10.1016/j.proci.2004.08.067

[42] Preetham, R., Santosh, H., and Lieuwen, T. 2008, "Dynamics of Laminar Premixed Flames Forced by Harmonic Velocity Disturbances," *Journal of Propulsion and Power* Vol. 24, No. 6, pp. 1390-1402.doi: 10.2514/1.35432

[43] Wang, H. Y., Law, C. K., and Lieuwen, T. 2009, "Linear Response of Stretch-Affected Premixed Flames to Flow Oscillations," *Combustion and Flame* Vol. 156, No. 4, pp. 889-895.doi: 10.1016/j.combustflame.2009.01.012

[44] Preetham, Thumuluru, S. K., Santosh, H., and Lieuwen, T. 2010, "Linear Response of Laminar Premixed Flames to Flow Oscillations: Unsteady Stretch Effects," *Journal of Propulsion and Power* Vol. 26, No. 3, pp. 524-532.doi: 10.2514/1.41559

[45] Palies, P., Schuller, T., Durox, D., and Candel, S. 2011, "Modeling of Premixed Swirling Flames Transfer Functions," *Proceedings of the Combustion Institute* Vol. 33, pp. 2967-2974.doi: 10.1016/j.proci.2010.06.059

[46] Moeck, J. P., Bourgouin, J. F., Durox, D., Schuller, T., and Candel, S. 2012, "Nonlinear Interaction between a Precessing Vortex Core and Acoustic Oscillations in a Turbulent Swirling Flame," *Combustion and Flame* Vol. 159, No. 8, pp. 2650-2668.doi: 10.1016/j.combustflame.2012.04.002

[47] Acharya, V. S., Shin, D. H., and Lieuwen, T. 2013, "Premixed Flames Excited by Helical Disturbances: Flame Wrinkling and Heat Release Oscillations," *Journal of Propulsion and Power* Vol. 29, No. 6, pp. 1282-1291.doi: 10.2514/1.B34883

[48] Acharya, V., and Lieuwen, T. 2014, "Response of Non-Axisymmetric Premixed, Swirl Flames to Helical Disturbances," *Proceedings of the Asme Turbo Expo: Turbine Technical Conference and Exposition, 2014, Vol 4b*.

[49] Acharya, V., and Lieuwen, T. 2015, "Premixed Flame Response to Helical Flow Disturbances: Non-Linear Effects," *9th U. S. National Combustion Meeting*.

[50] Lee, H. J., Kim, K. T., Lee, J. G., Quay, B. D., and Santavicca, D. A. 2009, "An Experimental Study on the Coupling of Combustio Instability Mechanisms in a Lean Premixed Gas Turbine Combustor," *ASME Turbo Expo 2009: Power for Land, Sea and Air*. Orlando, FL.

[51] Paschereit, C. O., Gutmark, E., and Weisenstein, W. 2000, "Excitation of Thermoacoustic Instabilities by Interaction of Acoustics and Unstable Swirling Flow," *AIAA Journal* Vol. 38, No. 6, pp. 1025-1034.doi: Doi 10.2514/2.1063

[52] Cohen, J., and Proscia, W. 2005, "Characterization and Control of Aeroengine Combustion Instability: Pratt & Whitney and Nasa Experience," *Combustion Instabilities in Gas Turbine Engines*. AIAA, Washington D.C., pp. 113-146.

[53] Szedlmayer, M., Quay, B. D., Samarasinghe, J., De Rosa, A., Lee, J. G., and Santavicca, D. A. 2011, "Forced Flame Response of a Lean Premixed Multi-Nozzle Can Combustor," *ASME 2011 Turbo Expo: Turbine Technical Conference and Exposition.*, Vancouver, British Columbia, pp. 883-891.

[54] Rosa, A. J. D., Samarasinghe, J., Peluso, S. J., Quay, B. D., and Santavicca, D. A. 2016, "Flame Area Fluctuation Measurements in Velocity-Forced Premixed Gas Turbine Flames," *Journal of Engineering for Gas Turbines and Power* Vol. 138.4.

[55] Samarasinghe, J., Peluso, S. J., Quay, B. D., and Santavicca, D. A. 2016, "The Three-Dimensional Structure of Swirl-Stabilized Flames in a Lean Premixed Multinozzle Can Combustor," *Journal of Engineering for Gas Turbines and Power*.

[56] O'Connor, J., Worth, N. A., and Dawson, J. R. 2013, "Flame and Flow Dynamics of a Self-Excited, Standing Wave Circumferential Instability in a Model Annular Gas

Turbine Combustor," *ASME 2013 Turbo Expo: Turbine Technical Conference and Exposition*. San Antonio, TX.

[57] Malanoski, M., Aguilar, M., Acharya, V., and Lieuwen, T. 2013, "Dynamics of a Transversely Excited Swirling Lifted Flame Part 1: Experiments and Data Analysis," *ASME TurboExpo 2013*. San Antonio, Texas.

[58] Crocco, L., and Sirignano, W. A. 1966, "Effect of the Transverse Velocity Component on the Nonlinear Behavior of Short Nozzles," *AIAA Journal* Vol. 4, No. 8, pp. 1428-1430.

[59] Faler, J. H., and Leibovich, S. 1977, "Disrupted States of Vortex Fow and Vortex Breakdown," *Phys. Fluids* Vol. 20, pp. 1385-1400.

[60] Faler, J. H., and Leibovich, S. 1978, "An Experimental Map of the Internal Structure of a Vortex Breakdown," *J. Fluid Mech.* Vol. 86, No. 2, pp. 313-335.

[61] Hall, M. G. 1972, "Vortex Breakdown," *Annual review of fluid mechanics* Vol. 4, No. 1, pp. 195-218.

[62] Benjamin, T. B. 1962, "Theory of the Vortex Breakdown Phenomenon," *Journal of Fluid Mechanics* Vol. 14, No. 4, pp. 593-629.doi: Doi 10.1017/S0022112062001482

[63] Steinberg, A., Boxx, I., Stöhr, M., Meier, W., and Carter, C. 2012, "Effects of Flow Structure Dynamics on Thermoacoustic Instabilities in Swirl-Stabilized Combustion," *AIAA* Vol. 50, No. 4.

[64] Arndt, C., Steinberg, A., Boxx, I., Meier, W., Aigner, M., and Carter, C. 2010, "Flow-Field and Flame Dynamics of a Gas Turbine Model Combustor During Transition between Thermo-Acoustically Stable and Unstable States," *Turbo Expo*. ASME, Glasgow, UK.

[65] Fanaca, D., Alemela, P. R., Hirsch, C., and Sattelmayer, T. 2010, "Comparison of the Flow Field of a Swirl Stabilized Premixed Burner in an Annular and a Single Burner Combustion Chamber," *Eng. Gas Turbines Power* Vol. 132, No. 7.

[66] Syred, N. 2006, "A Review of Oscillation Mechanisms and the Role of the Precessing Vortex Core (Pvc) in Swirl Combustion Systems," *Progr. Energy and Combust. Sci.* Vol. 32, pp. 93-161.

[67] Plessing, T., Kortschik, C., Peters, N., Mansour, M. S., and Cheng, R. K. 2000, "Measurements of the Turbulent Burning Velocity and the Structure of Premixed Flames on a Low-Swirl Burner," *Int. Symp. on Combustion*. Vol. 28, pp. 359-366.

[68] Day, M., Tachibana, S., Bell, J., Lijewski, M., Beckner, V., and Cheng, R. K. 2012, "A Combined Computational and Experimental Characterization of Lean Premixed

Turbulent Low Swirl Laboratory Flames: I. Methane Flames," *Combust. Flame* Vol. 159, No. 1, pp. 275-290.

[69] Oberleithner, K., Sieber, M., Nayeri, C. N., Paschereit, C. O., Petz, C., Hege, H.-C., Noack, B. R., and Wygnanski, I. 2011, "Three-Dimensional Coherent Structures in a Swirling Jet Undergoing Vortex Breakdown: Stability Analysis and Empirical Mode Construction," *Fluid Mech.* Vol. 679, pp. 383-414.

[70] Terhaar, S., Oberleithner, K., and Paschereit, C. O. 2015, "Key Parameters Governing the Precessing Vortex Core in Reacting Flows: An Experimental and Analytical Study," *Proc. Comb. Institute* Vol. 35, No. 3, pp. 3347-3354.

[71] Qadri, U. A., Mistry, D., and Juniper, M. P. 2013, "Structural Sensitivity of Spiral Vortex Breakdown," *Fluid Mech.* Vol. 720, pp. 558-581.

[72] Candel, S., Durox, D., Schuller, T., and Palies, P. 2012, "Progress and Challenges in Swirling Flame Dynamics," *C. R. Mecanique* Vol. 340, pp. 758-768.

[73] Liang, H. Z., and Maxworthy, T. 2005, "An Experimental Investigation of Swirling Jets," *Journal of Fluid Mechanics* Vol. 525, pp. 115-159.doi: 10.1017/S0022112004002629

[74] Huang, Y., Wang, S. W., and Yang, V. 2006, "Systematic Analysis of Lean-Premixed Swirl-Stabilized Combustion," *AIAA Journal* Vol. 44, No. 4, pp. 724-740.doi: Doi 10.2514/1.15382

[75] Oberleithner, K., Paschereit, C. O., and Wygnanski, I. 2014, "On the Impact of Swirl on the Growth of Coherent Structures," *Journal of Fluid Mechanics* Vol. 741, pp. 156-199.doi: 10.1017/jfm.2013.669

[76] Lacarelle, A., Faustmann, T., Greenblatt, D., Paschereit, C. O., Lehmann, O., Luchtenburg, D. M., and Noack, B. R. 2009, "Spatiotemporal Characterization of a Conical Swirler Flow Field under Strong Forcing," *Journal of Engineering for Gas Turbines and Power-Transactions of the Asme* Vol. 131, No. 3.doi: 10.1115/1.2982139

[77] Aguilar, M., Malanoski, M., Adhitya, G., Emerson, B., Acharya, V., Noble, D., and Lieuwen, T. 2015, "Helical Flow Disturbances in a Multinozzle Combustor," *Journal of Engineering for Gas Turbines and Power-Transactions of the ASME* Vol. 137, No. 9.doi: 10.1115/1.4029696

[78] Lee, J. G., and Santavicca, D. A. 2003, "Experimental Diagnostics for the Study of Combustion Instabilities in Lean Premixed Combustors," *Journal of Propulsion and Power* Vol. 19, No. 5, pp. 735-750.doi: Doi 10.2514/2.6191

[79] Schuller, T., Durox, D., and Candel, S. 2003, "A Unified Model for the Prediction of Laminar Flame Transfer Functions: Comparisons between Conical and V-Flame

Dynamics," *Combustion and Flame* Vol. 134, No. 1-2, pp. 21-34.doi: 10.1016/S0010-2180(03)00042-7

[80] Baillot, F., Durox, D., and Prudhomme, R. 1992, "Experimental and Theoretical-Study of a Premixed Vibrating Flame," *Combustion and Flame* Vol. 88, No. 2, pp. 149-168.doi: Doi 10.1016/0010-2180(92)90049-U

[81] Preetham, S. H., and Lieuwen, T. C. 2007, "Response of Turbulent Premixed Flames to Harmonic Acoustic Forcing," *Proceedings of the Combustion Institute* Vol. 31, pp. 1427-1434.doi: 10.1016/j.proci.2006.07.198

[82] Acharya, V., and Lieuwen, T. 2015, "Effect of Azimuthal Flow Fluctuations on Flow and Flame Dynamics of Axisymmetric Swirling Flames," *Physics of Fluids* Vol. 27, No. 10, p. 105106.doi: 10.1063/1.4933135

[83] Acharya, V., and Lieuwen, T. 2016, "Premixed Flame Response to Helical Disturbances: Mean Flame Non-Axisymmetry Effects," *Combustion and Flame* Vol. 165, pp. 188-197.doi: 10.1016/j.combustflame.2015.12.003

[84] Preetham, R., Santosh, H., and Lieuwen, T. 2008, "Forced Response of Premixed Flames: Effect of Flow Non-Uniformity," *46th AIAA Aersopace Sciences Meeting and Exhibit*. AIAA, Reno, Nevada.

[85] Acharya, V., Malanoski, M., Aguilar, M., and Lieuwen, T. 2013, "Dynamics of a Transversely Excited Swirling, Lifted Flame Part Ii: Flame Response Modeling and Comparison with Experiments," *Proceedings of the Asme Turbo Expo: Turbine Technical Conference and Exposition, 2013, Vol 1b*.

[86] Schwing, J., Sattelmayer, T., and Noiray, N. 2011, "Interaction of Vortex Shedding and Transverse High-Frequency Pressure Oscillations in a Tubular Combustion Chamber," *ASME 2011 Turbo Expo: Turbine Technical Conference and Exposition. American Society of Mechanical Engineers*. Vancouver, Canada, pp. 259-268.

[87] Steinberg, A. M., Arndt, C. M., and Meier, W. 2013, "Parametric Study of Vortex Structures and Their Dynamics in Swirl-Stabilized Combustion," *Proceedings of the Combustion Institute*. Vol. 34, pp. 3117-3125.

[88] Bourgouin, J. F., Durox, D., Moeck, J. P., Schuller, T., and Candel, S. 2015, "A New Pattern of Instability Observed in an Annular Combustor: The Slanted Mode," *Proceedings of the Combustion Institute*. Vol. 35, pp. 3237-3244.

[89] Schwing, J., Grimm, F., and Sattelmayer, T. 2012, "A Model for the Thermo-Acoustic Feedback of Transverse Acoustic Modes and Periodic Oscillations in Flame Position in Cylindrical Flame Tubes," *Proceedings of the Asme Turbo Expo 2012, Vol 2, Pts a and B*. pp. 553-566.

[90] Schwing, J., and Sattelmayer, T. 2013, "High-Frequency Instabilities in Cylindrical Flame Tubes: Feedback Mechanism and Damping," *Proceedings of the Asme Turbo Expo: Turbine Technical Conference and Exposition, 2013, Vol 1a*.

[91] Baillot, F., and Lespinasse, F. 2013, "Response of a Laminar Premixed V-Flame to a High-Frequency Transverse Acoustic Field," *Combustion and Flame*.

[92] Lespinasse, F., Baillot, F., and Boushaki, T. 2013, "Responses of V-Flames Placed in an Hf Transverse Acoustic Field from a Velocity to Pressure Antinode," *Comptes Rendus Mecanique* Vol. 341, No. 1-2, pp. 110-120.doi: 10.1016/j.crme.2012.10.015

[93] Zellhuber, M., Schwing, J., Schuermans, B., Sattelmayer, T., and Polifke, W. 2014, "Experimental and Numerical Investigation of Thermoacoustic Sources Related to High-Frequency Instabilities," *International Journal of Spray and Combustion Dynamics* Vol. 6, No. 1, pp. 1-34.

[94] Dawson, J. R., and Worth, N. A. 2014, "The Effect of Baffles on Self-Excited Azimuthal Modes in an Annular Combustor," *Proc. Comb. Inst.*

[95] Bourgouin, J. F., Durox, D., Moeck, J. P., Schuller, T., and Candel, S. 2013, "Self-Sustained Instabilities in an Annular Combustor Coupled by Azimuthal and Longitudinal Acoustic Modes.," *ASME Turbo Expo*. San Antonio, TX.

[96] Durox, D., Prieur, K., Schuller, T., and Candel, S. 2015, "Different Flame Patterns Linked with Swirling Injector Interactions in an Annular Combustor," *Proceedings of ASME Turbo Expo 2015: Turbine Technical Conference and Exposition*.

[97] Bourgouin, J. F., Durox, D., Moeck, J. P., Schuller, T., and Candel, S. 2014, "Characterization and Modeling of a Spinning Thermoacoustic Instability in an Annular Combustor Equipped with Multiple Matrix Injectors," *Proceedings of the Asme Turbo Expo: Turbine Technical Conference and Exposition, 2014, Vol 4a*.

[98] Moeck, J. P., and Paschereit, C. O. 2009, "Modeling Thermoacoustic Instabilities in an Annular Rijke Tube: Asymmetries and Standing and Spinning Modes," *ICSV 16th Proc.*, Poland, Krakow.

[99] Moeck, J. P., Paul, M., and Paschereit, C. O. 2010, "Thermoacoustic Instabilities in an Annular Rijke Tube," *ASME Turbo Expo*. ASME, Glasgow, Scotland.

[100] O'Connor, J., and Lieuwen, T. 2011, "Disturbance Field Characteristics of a Transversely Excited Burner," *Combustion Science and Technology* Vol. 183, No. 5, pp. 427-443.

[101] O'Connor, J., Kolb, M., and Lieuwen, T. 2011, "Visualization of Shear Layer Dynamics in a Transversely Excited, Annular Premixing Nozzle," *49th AIAA Aerospace Sciences Meeting*. Orlando, FL.

[102] O'Connor, J., Mannino, J., Vanatta, C., and Lieuwen, T. 2011, "Mechanisms for Flame Response in a Transversely Forced Flame," *7th US National Technical Meeting of the Combustion Institute*. Atlanta, GA.

[103] O'Connor, J., and Lieuwen, T. 2012, "Recirculation Zone Dynamics of a Transversely Excited Swirl Flow and Flame," *Physics of Fluids* Vol. 24, No. 7.doi: Artn 075107 10.1063/1.4731300

[104] O'Connor, J., and Lieuwen, T. 2012, "Further Characterization of the Disturbance Field in a Transversely Excited Swirl-Stabilized Flame," *Journal of Engineering for Gas Turbines and Power-Transactions of the Asme* Vol. 134, No. 1.doi: Artn 011501 10.1115/1.4004186

[105] O'Connor, J., and Lieuwen, T. 2012, "Influence of Transverse Acoustic Modal Structure on the Forced Response of a Swirling Nozzle Flow," *ASME Turbo Expo 2012*. Copenhagen, Denmark.

[106] O'Connor, J., and Acharya, V. 2013, "Development of a Flame Transfer Function Description for Transversely Forced Flames," *ASME Turbo Expo*. San Antonio TX.

[107] Malanoski, M., Aguilar, M., Shin, D. H., and Lieuwen, T. 2014, "Flame Leading Edge and Flow Dynamics in a Swirling, Lifted Flame," *Combustion Science and Technology* Vol. 186, No. 12, pp. 1816-1843.doi: 10.1080/00102202.2014.923410

[108] Acharya, V., Emerson, B., Mondragon, U., Shin, D. H., Brown, C., McDonell, V., and Lieuwen, T. 2013, "Velocity and Flame Wrinkling Characteristics of a Transversely Forced, Bluff-Body Stabilized Flame, Part Ii: Flame Response Modeling and Comparison with Measurements," *Combustion Science and Technology* Vol. 185, No. 7, pp. 1077-1097.doi: 10.1080/00102202.2013.777715

[109] Emerson, B., Mondragon, U., Acharya, V., Shin, D. H., Brown, C., McDonell, V., and Lieuwen, T. 2013, "Velocity and Flame Wrinkling Characteristics of a Transversely Forced, Bluff-Body Stabilized Flame, Part I: Experiments and Data Analysis," *Combustion Science and Technology* Vol. 185, No. 7, pp. 1056-1076.doi: 10.1080/00102202.2013.777714

[110] Hauser, M., Lorenz, M., and Sattelmayer, T. 2011, "Influence of Transversal Acoustic Excitation of the Burner Approach Flow on the Flame Structure," *Journal of Engineering for Gas Turbines and Power* Vol. 133, No. 4.

[111] Hauser, M., Wagner, M., and Sattelmayer, T. 2012, "Transformation of Transverse Acoustic Velocity of the Burner Approach Flow into Flame Dynamics," *ASME Turbo Expo*. Copenhagen, Denmark.

[112] Saurabh, A., and Paschereit, C. O. 2017, "Dynamics of Premixed Swirl Flames under the Influence of Transverse Acoustic Fluctuations," *Combustion and Flame* Vol. 182, pp. 298-312.doi: 10.1016/j.combustflame.2017.04.014

[113] Lespinasse, F., and Baillot, F. 2013, "Subharmonic Frequency Bifurcation of a Flame in Response to Jet Dynamics Modulated by a Transverse Acoustic Field.," *24th ICDERS*. Taipei, Taiwan.

[114] Gupta, A. K., Lilley, D. G., and Syred, N. 1984. *Swirl Flows*: Abacus Press.

[115] Sciacchitano, A., Neal, D. R., Smith, B. L., Warner, S. O., Vlachos, P. P., Wieneke, B., and Scarano, F. 2015, "Collaborative Framework for Piv Uncertainty Quantification: Comparative Assessment of Methods," *Measurement Science and Technology* Vol. 26, No. 7.doi: 10.1088/0957-0233/26/7/074004

[116] Sciacchitano, A., and Wieneke, B. 2016, "Piv Uncertainty Propagation," *Measurement Science and Technology* Vol. 27, No. 8.doi: 10.1088/0957-0233/27/8/084006

[117] Lauer, M., and Sattelmayer, T. 2010, "On the Adequacy of Chemiluminescence as a Measure for Heat Release in Turbulent Flames with Mixture Gradients," *Journal of Engineering for Gas Turbines and Power-Transactions of the Asme* Vol. 132, No. 6.doi: 10.1115/1.4000126

[118] Guyot, D., Guethe, F., Schuermans, B., Lacarelle, A., and Paschereit, C. O. 2010, "Ch*/Oh* Chemiluminescence Response of an Atmospheric Premixed Flame under Varying Operating Conditions," *Proceedings of ASME Turbo Expo 2010: Power for Land, Sea and Air*. Glasgow, UK.

[119] Boehm, B., Dreizier, A., Gnirss, M., Tropea, C., Findelsen, J., and Schiffer, H. P. 2007, "Experimental Investigation of Turbulence Structure in a Three-Nozzle Combustor," *Proceedings of the Asme Turbo Expo, Vol 2*. pp. 55-64.

[120] Caux-Brisebois, V., Steinberg, A. M., Arndt, C. M., and Meier, W. 2013, "Thermoacoustic Coupling in Swirl-Stabilized Flames with Helical Vortices," *49th Joint Propulsion Conference, AIAA/ASME/SAE/ASEE*. San Jose, CA.

[121] Pruvost, J., Legrand, J., and Legentilhomme, P. 2001, "Three-Dimensional Swirl Flow Velocity-Field Reconstruction Using a Neural Network with Radial Basis Functions," *Journal of Fluids Engineering-Transactions of the Asme* Vol. 123, No. 4, pp. 920-927.doi: Doi 10.1115/1.1412847

[122] Ahmed, S., El Kadi, H., and AlSharif, A. 2014, "Three-Dimensional Turbulent Swirling Flow Reconstruction Using Artificial Neural Networks," *Journal of Mechanical Engineering and Automation* Vol. 4, No. 1, pp. 1-9.doi: 10.5923/j.jmea.20140401.01

[123] Manoharan, K., Emerson, B., Smith, T. E., Douglas, C. M., Lieuwen, T., and Hemchandra, S. 2017, "Velocity Field Response of a Forced Swirl Stabilized Premixed Flame," *ASME Turbo Expo 2017: Turbine Technical Conference and Exposition*. Charlotte, NC, USA.

[124] Smith, T. E., Emerson, B., Proscia, W., and Lieuwen, T. 2017, "Flame Response to Transverse Acoustic Forcing with Minimal Axial Coupling," *ASME Turbo Expo 2017: Turbomachinery Technical Conference and Exposition*. Charlotte, NC.

[125] Rukes, L., Sieber, M., Paschereit, C. O., and Oberleithner, K. 2016, "The Impact of Heating the Breakdown Bubble on the Global Mode of a Swirling Jet: Experiments and Linear Stability Analysis," *Physics of Fluids* Vol. 28, No. 10.doi: 10.1063/1.4963274

[126] Billant, P., Chomaz, J. M., and Huerre, P. 1998, "Experimental Study of Vortex Breakdown in Swirling Jets," *Journal of Fluid Mechanics* Vol. 376, pp. 183-219.doi: Doi 10.1017/S0022112098002870

[127] Tammisola, O., and Juniper, M. P. 2016, "Coherent Structures in a Swirl Injector at Re = 4800 by Nonlinear Simulations and Linear Global Modes," *Journal of Fluid Mechanics* Vol. 792, pp. 620-657.doi: 10.1017/jfm.2016.86

[128] O'Connor, J. 2012, "Response of a Swirl-Stabilized Flame to Transverse Acoustic Excitation." Vol. Ph.D., Georgia Institute of Technology, Atlanta, GA.